eman ta zabal zazu

Universidad del País Vasco
Euskal Herriko Unibertsitatea

University of the Basque Country
Department of Material Physics

PhD thesis

Morphology and dynamics of ice crystals and the effect of proteins

Presented by

María Cascajo Castresana

Supervised by

Prof. Alexander M. Bittner
& Prof. Silvina Cerdeny

Donostia/San Sebastián, 2017

This PhD thesis has been performed at,

Self –Assembly Group
CIC nanoGUNE
Donostia/San Sebastián

Polymers and Soft Matter Group
Materials Physics Center (CFM)
Donostia/San Sebastián

Institute for Atmospheric
and Climate Science
ETH Zürich

To the memory of my grandparents, Ricardo and Amelia

Contents

Summary

The thesis "Morphology and dynamics of ice crystals and the effect of proteins" is based on a wide range of themes, from the basics of ice structure (such as ice surface and ice morphology), over the interaction of proteins with ice, to environmental science (which encompasses cloud formation and glacier dynamics). The focus is on interfaces, namely ice/vapour and ice/water.

By extending environmental scanning electron microscopy (ESEM) to unusually low temperatures, areas in the pressure-temperature landscape of ice morphologies were accessed in-situ. This means recording real time ESEM images and movies under full humidity control in a dynamic ice-vapour equilibrium. Besides reproducing known morphologies of single crystalline and of polycrystalline ice, the high time resolution (frame rate ≤ 1 Hz) gives access to dynamic growth and sublimation events.

During these processes, well-known forms of ice crystallites and polycrystalline ice were found. The time-resolved growth of ice is generally rather difficult to control, especially on the microscale. However, difficulties with the method for studying the growth of ice crystals, such as the effect of the electron beam-gas ionization and charging effects, the problem of facilitating repeated and localized ice growth are discussed and successfully overcome.

Sublimation events at small undersaturation of water vapour are better accessible. The sublimation rates fit to natural phenomena on ice fields, e.g. in the Antarctica or on Mars. The dynamically evolving shapes are complex: From hexagonal single crystal columns,

but also from smooth polycrystalline surfaces, sharp sub-microscale ridges develop, and finally dominate the overall structure.

A new geometry are the so-called "pools", circular features of some µm diameter, into which grain boundaries on polycrystalline ice surfaces decompose during slow sublimation.

The very top surface layers of ice exhibit premelting to a highly disordered so-called "quasi-liquid layer" (QLL). At high temperatures, some K below melting, the QLL is very thick. Here it is shown that such layers form shallow, large droplets, which until now had been characterised locally only by laser confocal microscopy. Below -10°C, the ice morphologies found by ESEM correspond to earlier findings, so the QLL cannot be detected directly. However, it is possible to prove the fluidity of the QLL (the top ice layers) by tracking the path of gold nanoparticles (NPs). This requires again recording movies, but also additional tracking and evaluation software, adapted to the selectively low ESEM contrast.

Plots of single particle mean square displacement (MSD) as function of the time lag show two types of movement, Brownian and "biased" drag. From the first, a diffusion coefficient can be extracted, and the viscosity of the QLL can be calculated. Depending on the particle track, the viscosity value is valid for a specific microscale area, for example the smooth surface of polycrystalline ice or a grain boundary.

In clouds, ice can nucleate directly from vapour water, but more common is nucleation from supercooled water. The process is usually based on the presence of inorganic particles (nuclei). Only recently also organic particles, such as proteins and viruses are being considered. Eight different protein solutions were tested under supercooling

conditions using a drop freezing techniques (optical ice detection systems) and calorimetric measurements. Only (apo)ferritin, ferritin and casein showed good ice nucleation abilities, i.e. freezing already under small supercooling (only some degrees below 0 ºC), while most protein solutions freeze below -15 °C, just like pure water. The performance of (apo)ferritin is independent on large variations of the pH (protonation/deprotonation), which means that surface charge plays a surprisingly small role in ice nucleation.

Resumen

La tesis “morfología y dinámica de los cristales de hielo y su efecto en las proteínas” se basa en una amplia gama de temas que abarcan el fundamento de la estructura del hielo (tanto su superficie como su morfología), la interacción de las proteínas con el hielo y las ciencias ambientales (formación de las nubes y la dinámica de los glaciares). El enfoque se centra en las interfaces hielo/vapor e hielo/agua.

Al extender el rango de temperaturas del microscopio electrónico de barrido ambiental (ESEM) a temperaturas inusualmente bajas, se ha logrado acceder a estudiar la morfología del hielo in-situ en diversas áreas del diagrama de fases (presión-temperatura). Esto significa observar a tiempo real, imágenes por medio de ESEM en condiciones de humedad controladas y en equilibrio dinámico del hielo/agua. Además de reproducir las morfologías ya conocidas de cristales individuales e hielo poli-cristalino, la alta resolución en tiempo (fotogramas por segundo $\leq$ 1 Hz) da acceso al estudio del crecimiento dinámico y a eventos de sublimación.

Durante estos procesos, se han observado formas ya conocidas de hielo, así como hielo poli-cristalino (ver figura 1). El crecimiento de hielo con resolución temporal es muy difícil de controlar, especialmente en la micro escala y durante este estudio se han encontrado dificultades relacionadas con el método para estudiar el crecimiento de cristales de hielo, tal como el efecto de la ionización del haz-gas de electrones y los efectos de carga, o el problema de facilitar el crecimiento repetido y localizado del hielo. Sin embargo, todas estas dificultades se han superado con éxito en esta tesis.

Los eventos de sublimación bajo pequeña saturación de vapor de agua son más accesibles. La tasa de sublimación se ajusta con los fenómenos naturales en el campo del hielo, e. g. en Antártica o en Marte. Las formas del hielo, que evolucionan de manera dinámica, son complejas: no sólo desde columnas hexagonales de un solo cristal, sino también desde superficies lisas poli-cristalinas, se desarrollan crestas afiladas en la escala sub-micrométrica.

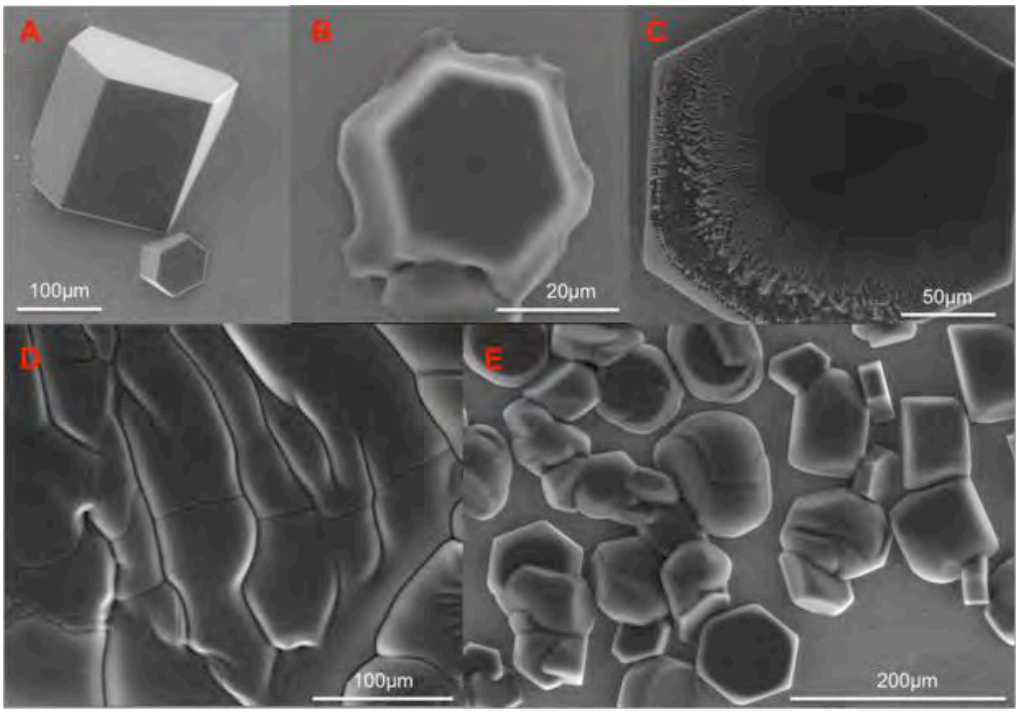

Figura 1. Ejemplos de crecimiento de hielo en el ESEM. Imágenes (a), (b) y (c) muestran cristales de hielo individuales. En la imagen (d) aparece hielo poli-cristalino con bordes de grano bien definidos y la imagen (e) aparecen cristales de hielo individuales junto a hielo poli-cristalino.

Las nuevas geometrías llamadas "*pools*", son formas circulares de algunos µm de diámetro, en las que los límites del grano de la superficie del hielo poli-cristalino se descomponen durante un proceso de sublimación lento (ver figura 2).

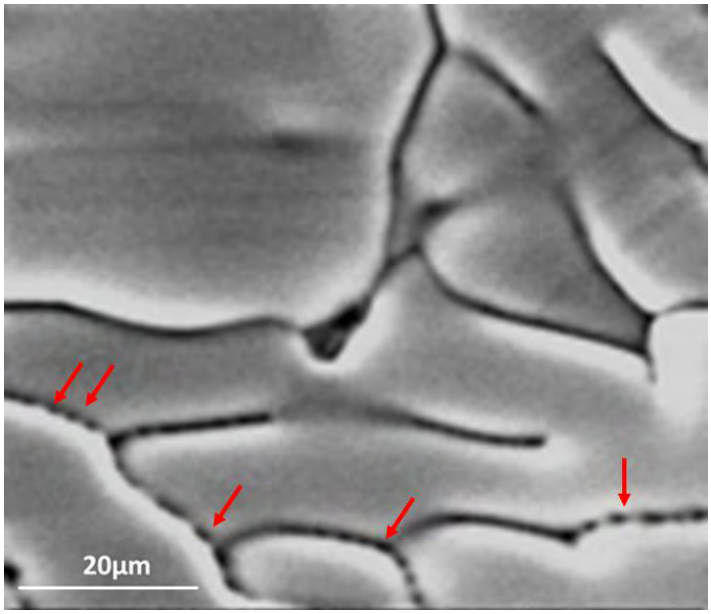

Figura 2. Hielo poli-cristalino durante un proceso de sublimación. Formas circulares designadas como "pools" (marcadas con flechas rojas) aparecen alineadas a lo largo de algunos bordes de grano

Las capas superficiales superiores del hielo, presentan una fusión de forma altamente desordenada denominada "*quasi-liquid layer*" (QLL). A altas temperaturas, algunos grados por debajo de la fusión, la QLL es muy gruesa. En esta tesis, se muestra como dichas capas forman grandes gotas de poca profundidad las cuales hasta ahora se han caracterizado localmente y sólo por medio de la microscopía confocal láser. Por debajo de -10 ºC las morfologías del hielo encontradas por ESEM corresponden a hallazgos anteriores, por lo que la QLL no se puede detectar directamente. Sin embargo, es posible probar la fluidez de QLL (las capas superiores de hielo) mediante el seguimiento de la ruta de nanopartículas de oro (NPs). Esto ha requerido además de la grabación de películas, el desarrollo de un software para el seguimiento y la evaluación, adaptado selectivamente al contraste bajo del ESEM.

El desplazamiento cuadrático medio de las partículas individuales en función del "*time lag*" muestra dos tipos de movimientos: Browniano y "*biased drag*". Del primero, se

puede extraer el coeficiente de difusión y la viscosidad de la QLL. Dependiendo de la trayectoria de cada partícula, el valor de la viscosidad solo es válido para un área específica en la micro-escala como por ejemplo una superficie lisa de hielo poli-cristalino o un límite de grano.

En las nubes, el hielo se puede nuclear desde el vapor de agua, pero es más común la nucleación a partir del agua súper-enfriada. El proceso se basa generalmente en la presencia de partículas inorgánicas (aerosoles, denominados como INPs, *ice nucleating particles*). Solo recientemente se está considerando como posibles INPs las partículas orgánicas, como las proteínas y los virus. La tercera fuente principal de partículas atmosféricas en la atmósfera son las emisiones de los océanos, siendo el fenómeno dominante de dicha emisión conocido como *bubble bursting*. Como el océano es un hábitat para una variedad de organismos, una gran fracción de aerosol marino es también biológica (ver imagen 3), lo que pone de relieve el creciente interés en la investigación de INPs biológicos.

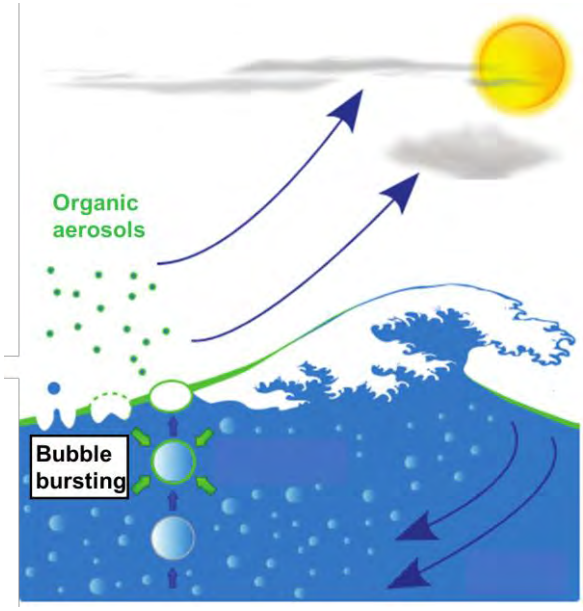

Figura 3. Emisión de INPs de origen orgánico procedentes del océano a la atmósfera

En esta tesis, se han estudiado ocho soluciones diferentes de proteínas en condiciones de súper-enfriamiento mediante las técnicas de congelación de gota (*drop freezing technique*) y calorimetría diferencial de barrido (DSC). Únicamente, la (apo)ferritina y la ferritina han mostrado buenas características para la nucleación de hielo, es decir, la congelación bajo pequeño súper-enfriamiento (solo algunos grados debajo de 0 ºC), mientras que la mayoría de las soluciones de proteínas estudiadas se congelan por debajo de -15 ºC, como el agua pura. El rendimiento de la (apo)ferritina es independiente de las grandes variaciones de pH (protonación/desprotonación), lo que significa que la carga superficial juega un papel sorprendentemente pequeño en la nucleación del hielo.

Una comprensión detallada del proceso de formación de hielo debido a los INPs no sólo es de interés para la comunidad científica de la atmósfera, sino también para la aviación, la conservación de alimentos, la crio-conservación con fines médicos y el estudio de fuentes de agua extraterrestre.

Chapter 1: Introduction

1. Motivation and objectives

Simplicity is the beauty of science.

Sometimes it comes with a theory, like Einstein's equation $E = mc^2$*;*

Sometimes it lies in an experiment, like Young's double-slit setup;

And sometimes it is just about a matter, like ***water****.* [1]

The behaviour and role of water on Earth was already described by the Greek philosopher Aristotle in the fourth century BC [2], but even now we can only partially answer many questions concerning water in its gas, liquid or solid forms. Water is a unique natural substance since it co-exists in its three phases in the typical temperature range at the Earth's surface. Water is the most important substance for our life, but there is also continuous scientific interest due to its unique and unusual properties, e.g. very high surface tension, high specific heat capacity, density maximum at 4ºC (at standard pressure), lower viscosity under high pressure, etc. [3] Water is also the most abundant compound on Earth's surface. In fact, about 70.8% of the surface – which works out to 361 million km – is covered by water, with much of the continental shelf below sea level. The remaining 148 million km are above sea level (see figure 1.1).

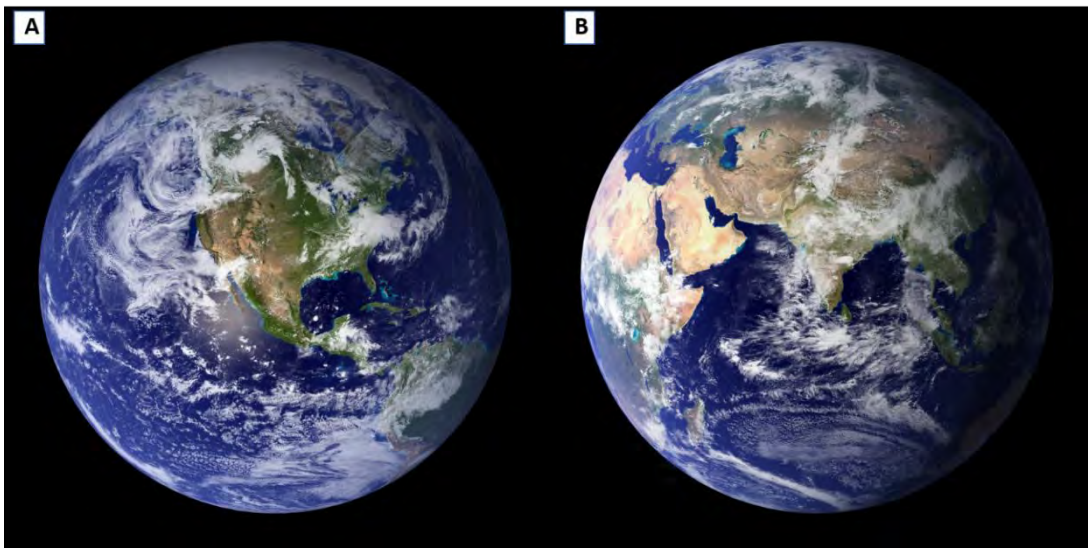

Figure 1.1. The "Blue Planet" A) Western hemisphere: Europe (west of London), western part of Africa, Atlantic Ocean, and a large part of the Pacific. **B) Eastern hemisphere:** Europe (east of London), eastern part of Africa, Asia, Australia, Indian Ocean and some part of the Pacific. (https://www.universetoday.com/14367/planet-earth/)

Solid water covers a much smaller area, with big seasonal variations. It makes up snow, glaciers, sea ice (figure 1.2) and clouds (frequently mixed with water droplets). In each case, the ice crystal morphology (habit) and its dynamical changes during formation, dissolution and movements are of great importance. For example, glaciers and ice sheets store over two-thirds of the Earth's freshwater and are presently contributing to rising sea levels. If the ice sheet in Antarctica were to melt entirely, global sea level would rise about 57 m. [4] Glaciers reach an equilibrium within the present climate by various mechanisms, which include melting, sublimation (evaporation), and also ice flow. This work considers mainly sublimation, which has a decisive influence at low temperatures and at low humidity, which prevents re-precipitation (re-deposition) of water vapour. Sublimation depends strongly on the microstructure of the ice surface, but necessarily changes this structure constantly. On the glacier surface, and generally in snow, ice crystals are randomly oriented because snowflakes settle randomly, and experiments have to reproduce such a polycrystalline morphology. This work does not focus on the ice microstructure in the bulk, but conclusions from the surface studies can in some cases easily be extended. This is important for glacier flow, a process that must obviously be based on plastic deformation under large stress. The stress acts on the many individual small ice crystals that are packed closely together (in the Greenland ice sheet the size of the ice crystals range from 1 mm to 10 cm in diameter, but much smaller crystals can be found, too). When the ice flows and deforms, the ice crystals are deformed and rotated, and they acquire a preferred mutual orientation, which in turn changes the flow properties of the ice. Thus, the "flow history" of the ice can be studied from crystal structure measurements carried out at different depths in a glacier.

Snow covers, although much smaller in volume than glaciers, strongly affect our lives on a local and on a global scale. The snow surface has become a subject of great recent scientific interest, owing to its role in global warming, its ability to release pollution to the aqueous environment, its potential to modify the atmospheric composition, and also as fresh-water supply and environmental archive. *In this thesis, the morphology of freshly grown pure ice is followed on the microscale in real time, during growth and during sublimation. The experiments and results are compiled in chapter 2.*

Figure 1.2. A large iceberg has grounded off Canada's East coast recently (April 2017). (Taken from Greg Locke (Reuters)).

Ice crystals surfaces have another property, which is more interesting on a smaller scale, they are "slippery". Why do solid ice crystals allow to ski, skate and slide so easily at temperatures far below the bulk melting point (the optimum temperature for figure skating is -5.5 ºC, for ice hockey -9 ºC [5])? This question has always been and still is (!) popular and appealing. The most obvious answers, pressure melting [5] and/or frictional heating [6] both fail to explain skating at very low temperatures (down to -30 ºC and below), and slipperiness without friction (ice surfaces are slippery also in absence of movement). Indeed, trying to explain the fact that two pieces of ice, when put together, adhere and become one [7]**,** Faraday in the 19th century proposed that a liquid-like layer exists on ice surface already below the melting temperature. Such a layer has been confirmed [8] and named "disordered" or "quasi-liquid layer" (QLL). For many years scientists have tried to understand the unique properties of ice in terms of the behaviour of the molecules in the topmost layer. However, despite extensive studies, the exact structure and dynamical motion of the individual water molecules at the ice surface have remained elusive. Effects of the micro- and nanoscale morphology have probably never been considered. The q*uantification of the mobility (i.e. viscosity) of the QLL on the complex surface of polycrystalline ice is the objective of chapter 3.*

Ice, liquid water and of course water vapour are essential ingredients of clouds. The transition between the various phases is far from trivial. For example, already Aristotle observed that “warm water could freeze faster than cold water” in his "Meteorology", though his explanation is more philosophic than scientific. Similar findings have been reported in our time [9], [10]. The examination of the phenomenon in a scientific way has to invoke the complexity and sensitivity of the water/ice phase transition [11] for temperature, pressure, cooling rate, fluid turbulence, traces of other substances, and particles. Indeed, clouds can only form when water vapour or liquid nucleates at existing solids, such as ice or mineral dust particles. Since liquid (supercooled water) is present in clouds, experiments should consider liquid water and the experiments in chapter 4 are carried out in presence of supercooled liquid water. Only recently also biogenic particles start to be considered as material that can nucleate water and ice. Proteins, with their enormous chemical and structural variability, appear to play a big role, but there is no general understanding of this phenomenon.

Chapter 4 concentrates on the influence of various proteins on ice nucleation in supercooled water.

In summary, this work contributes to the fundamental understanding of growing and sublimating (evaporating) ice surfaces, in the light of their relevance for processes in the environment, and more generally for all types of ice layers. Nucleation experiments were carried out on flat solid surfaces, and with a range of proteins in supercooled water. This contributes to the understanding of biological aerosols, which are suspected to alter the formation, life cycle and properties of clouds. The general approach in this work is from the nanoscale science view, which suggests methods and research strategies that are based more in Surface Science than in Atmospheric Science, hopefully paving new ways of interdisciplinary approaches.

1.1 Basic concepts

1.1.1 Phase diagrams

A phase diagram shows the preferred physical states of matter at different temperatures and pressure. At ambient temperature and pressure (1 atm = 1.013 bar, marked by ‘E’ in figure 1.3) water is a liquid, but it becomes solid (i.e. ice) if its temperature is lowered below 0 ºC, and gaseous (i.e. vapour) if its temperature is raised above 100 ºC. Each line

in figure 1.3 gives the conditions for the coexistence of two phases, but a change in temperature or pressure may cause the phases to abruptly change from one to the other. Three lines meet at a triple point, where three phases coexist. They may abruptly and totally change into each other upon changing temperature or pressure. A line can end in a critical point, where the properties of two phases become indistinguishable. As usual for solids, ice exhibits polymorphism. In the context of the thesis, the high-pressure phases are not relevant, and the (low-pressure) cubic ice-XI requires extremely low temperatures. Hence the usual ice, the hexagonal phase I_h, is the only one considered.

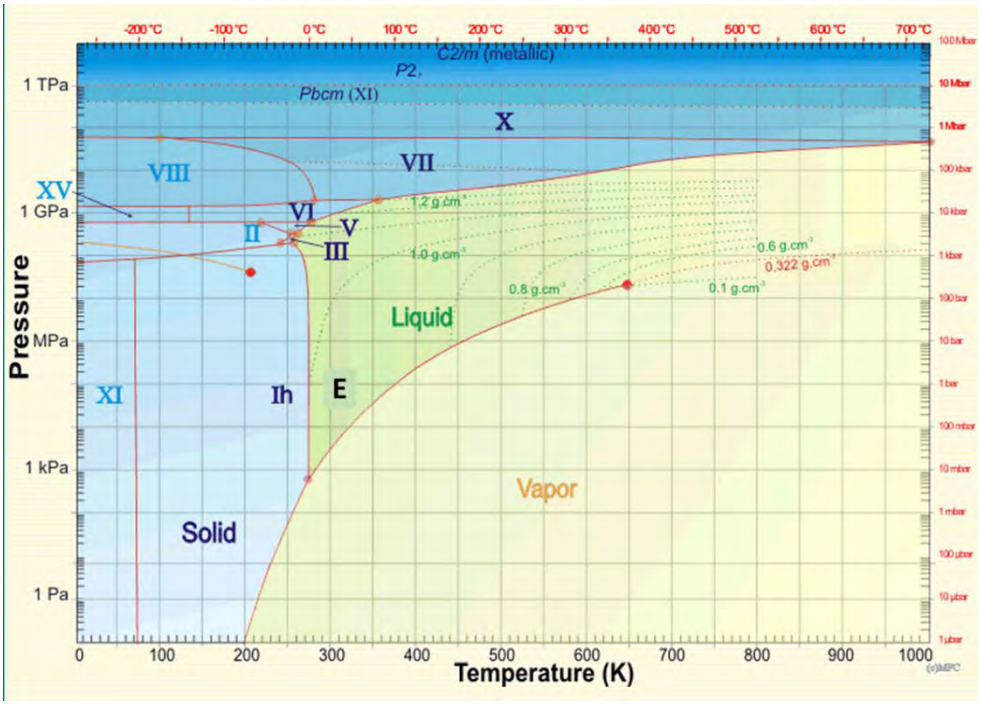

Figure 1.3. Water phase diagram. Source: http://www1.lsbu.ac.uk

1.1.2. Vapour pressure

The water vapour pressure P_{ice} over ice describes the pressure the water vapour reaches when a closed system of ice and vapour is in thermodynamic equilibrium at a certain temperature. Similarly, the water vapour pressure over a liquid interface, $P_{water,}$ is defined and referred to as water vapour pressure [12]. The vapour pressure of both ice and liquid water at the triple point is P_t = 611.657±0.01 Pa at T_t = 0.01 ºC. The vapour pressure may be extended down in temperature from the triple point using the Clapeyron equation:

$$\frac{dP_{ice}}{dT} = \frac{\Delta s}{\Delta V}\frac{dP_{ice}}{dT} = \frac{\Delta s}{\Delta V} \qquad (1.1)$$

where Δs and ΔV are the molar entropy and molar volume changes upon sublimation, respectively.

Assuming that the molar volume of ice is much smaller than that of the vapour, and that the vapour is an ideal gas, one reaches a very good approximation in the Clausius–Clapeyron equation:

$$\frac{dlnP_{ice}}{dT} = \frac{L_{ice}(T)}{RT^2} \qquad (1.2)$$

Here $L_{ice}(T)$ is the molar latent heat of sublimation as a function of temperature, and R is the molar gas constant (8.31447 J mol^{-1}K^{-1}). The parametrization used throughout is based on the Clausius-Clapeyron equation [13]**,** but an improved version was published by Murphy and Koop in 2005 [14]. Here it is used to calculate the water vapour pressure over ice and water (figure 1.4; note that this includes also supercooled water below 0ºC):

$$P_{ice}(T) = exp(9.550426 - 5723.265/T + 3.53068\ln(T) - 0.00728332T);$$

for T >110K (1.3)

$$P_{water}(T) = exp\left(54.842763 - \frac{6763.22}{T} - 4.210\ln(T) + 0.000367T + \tanh[0.0415 \cdot (T - 218.8)] \cdot \left(53.878 - \frac{1331.22}{T} - 9.44523\ln(T) + 0.014025T\right)\right);$$

for 123<T<332 K (1.4)

where the temperature T is in Kelvin, and the pressures P are in Pascal.

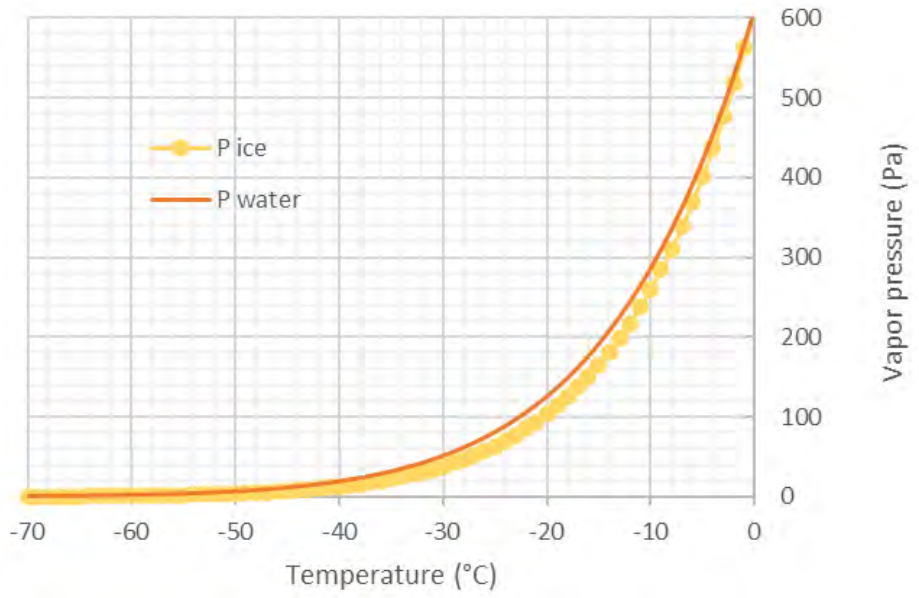

Figure 1.4. The water vapour pressures for ice and supercooled water **(**calculated from [14]**)**

There is a small difference in the vapour pressures of ice and (supercooled) water for a given temperature (see figure 1.5). Note that supercooled water is thermodynamically unstable, but that it is metastable when nucleation of ice can be suppressed; this requires clean and dust-free conditions, which are indeed encountered in clouds.

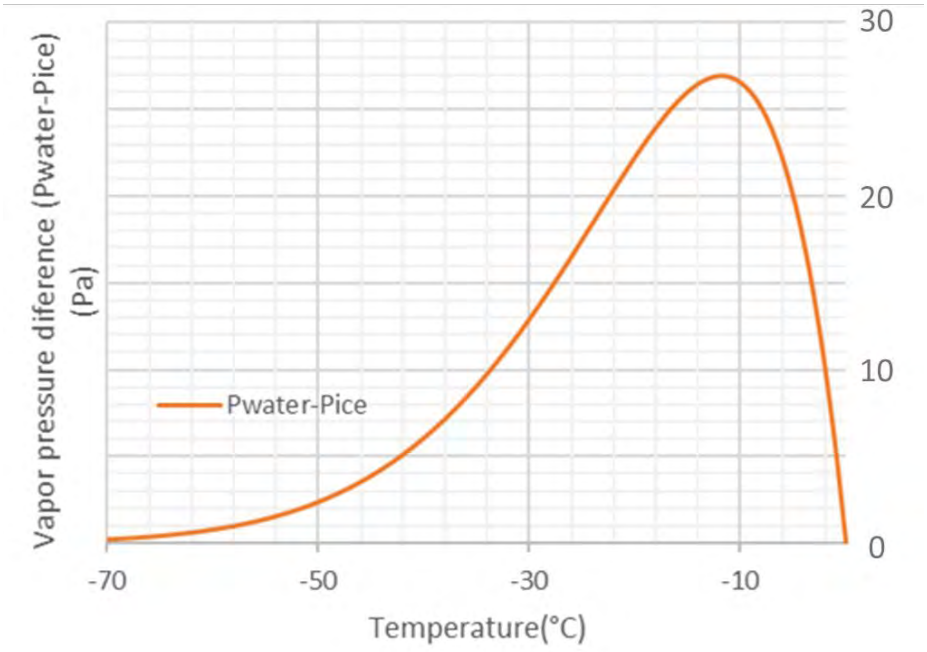

Figure 1.5. Difference in vapour pressures for ice and supercooled water (calculated from [14])

If supercooled droplets and ice crystals coexist in a so-called "mixed-phase" cloud, the ice crystals can grow rapidly via the Wegener-Bergeron-Findeisen process. This process takes place if the saturation vapour pressure over water, P_{water}^{sat} , is higher than the water vapour pressure in the cloud, P_{water}, which in turns needs to be higher than the saturation vapour pressure over ice, P_{ice}^{sat} [15]: $P_{water}^{sat} > P_{water} > P_{ice}^{sat}$ (1.5)

Under these conditions, ice crystals grow and deplete the water vapour, causing the liquid droplets to evaporate.

For small droplets or particles, the vapour pressure is increased to P_{curv} due to the highly curved surface. This can be quantified with the Thomson (or Kelvin) equation, here for the ice/vapour interface:

$$\ln\left({}^{P_{curv}}/_{P_{water}}\right) = \frac{2 \cdot \sigma_{sg} \cdot V_s}{R \cdot T \cdot r} \quad (1.6)$$

with a curvature $1/r$, where σ_{sg} is the interfacial tension between the solid and the vapour, V_s is the molar volume of the ice, R the gas constant, and T the temperature. An analogous expression is valid for the liquid/vapour interface, e.g. for small droplets.

Another curvature effect concerns melting: The phase diagram (figure 1.3) shows that the melting temperature of ice depends only weakly on pressure, but it can be lowered for negatively curved surfaces, i.e. in pores or capillaries. Here the Gibbs-Thomson equation

$$\frac{\Delta T}{T} = \frac{2 \cdot \sigma_{sl} \cdot V_s}{\Delta H_{melt} \cdot r} \quad (1.7)$$

quantifies the (negative) melting point depression, ΔT, at the temperature T, due to the (negative) curvature $1/r$ of the interface, where σ_{sl} denotes the interfacial tension between the solid and the liquid phase, V_s the molar volume of the ice, and ΔH_{melt} the molar enthalpy of melting.

1.1.3. Humidity

The surfaces of ice and liquid water are some of the most important features on our planet. The existence of ice requires temperatures below the triple point (0.01 ºC). At

water vapour pressures below the triple pressure (611.7 Pa), ice cannot melt, but its surface will lose material by sublimation. This process depends sensitively on the vapour pressure or on the relative humidity, h:

$$h = {P_{water}}/{P_{water}^{sat}} \qquad (1.8)$$

where P_{water} is the partial pressure of water vapour, and P_{water}^{sat} the saturated vapour pressure at the given temperature. A humidity $h > 1$ is called supersaturation; it results in ice growth from the vapour, while $h < 1$ causes sublimation. Analogous considerations are valid for the liquid surface.

For atmospheric conditions one has to consider also other gases that are present, i.e. dry air, made up mainly from nitrogen and oxygen. Its pressure at standard conditions (25 ºC) is 101325 Pa (1 atm). In wet air, the partial pressure of water vapour is P_{water}, and its overall fraction is P_{water}/101325 Pa at standard conditions. The humidity definition remains the same given above. This also means that a wet atmosphere can be "simulated" by pure water vapour without inert gases (see the experimental setup in chapters 2 and 3).

1.1.4 Quasi-liquid layers

Molecular solids, but also metals and semiconductors, contain a liquid-like "quasi-liquid" layer (QLL) on their surfaces, in a limited temperature range just below the bulk melting temperature T_{melt}. It has been estimated that van der Waals solids premelt at $\approx 0.9\, T_{melt}$ [16], which would be around -30 °C for water, a surprisingly good estimate (see below). Premelting is based on lowering the energy of the solid surface by the presence of the QLL [17], and it can be rationalized as follows: Crystals melt upon heating because the thermal driving force toward disorder (entropic) overcomes the energy associated with chemical bonding. [18] Atoms or molecules at the surface of a material tend to form fewer bonds with their neighbours, so they are less resistant to thermal disordering. Consequently, the surface (the topmost layer of atoms or molecules) can melt (or disorder) below T_{melt}. The next (subsurface) layer of atoms or molecules has now again fewer (or at least less ordered) bonds to the disordered surface layer, and also this subsurface layer can melt below T_{melt}. Depending on the temperature, the phenomenon can proceed gradually to further subsurface layers, but will stop at a certain depth, which is the thickness of the QLL.

Michael Faraday [19], [7], [20] was the first to propose that water ice is not an absolutely rigid solid, as assumed by most scientists of his era, and in 1850 suggested that the ice surface consists of a thin wet film (see figure 1.6). His experiment was "that a particle of water which could retain the liquid state whilst touching ice on only one side, could not retain the liquid if it were touched by ice on both sides". The existence of a QLL on the surface of ice crystals at temperatures down to around -30 °C is now widely accepted, based on many experimental and theoretical studies, and on simulations. It is probably amongst the better documented cases of premelting.

Figure 1.6. Schematic representation of the quasi liquid layer (QLL) on ice.

Still, a further understanding of premelting on ice is far from trivial. This concerns the QLL thickness, its evolution with temperature, possible dependence on the crystal face, dynamics, amorphous nature and also the spatial uniformity of the QLL. Furthermore, obtaining molecular level information requires sophisticated surface-sensitive techniques and extreme levels of cleanliness. [18]

Experimental evidence

The thickness of the QLL on ice as a function of temperature has been quantified both experimentally [21], [22], [23], [24], [25], [26], [27], [28], [29], [30] and theoretically [31], [32], [33], [34], [35], [36]. Using atomic force microscopy *Doppenschmidt* and *Butt* reported the thickness of the QLL as 11 nm at -10°C [25]. *Elbaum et al.* [3] reported that the QLL thickness increases with introducing a small amount of air to the surface of ice. *Bluhm et al.* measured the QLL thickness by means of the photoelectron spectroscopy technique and its value at -10°C was reported as 0.5 nm [27]. More recently, *Goertz* and co-workers investigated the QLL on the ice surface over the range -10°C to -30°C using interfacial force microscopy and they found a value of 45 nm for the thickness of the QLL at -10°C [30]

A way to increase the QLL thickness is the addition of impurities (see below, solutions and melting point depression). Of greater interest is the influence of temperature on pure QLLs. All relevant studies have shown a significant increase in the thickness of the QLL layer with increasing temperature, reaching macroscopic dimensions at the melting point. As the melting point is approached, the QLL appears to be indistinguishable from the liquid phase in its uppermost layers. However, the QLL changes to an apparent crystalline order within several molecular layers below the surface (1 molecular layer ~ 0.3 nm) [37].

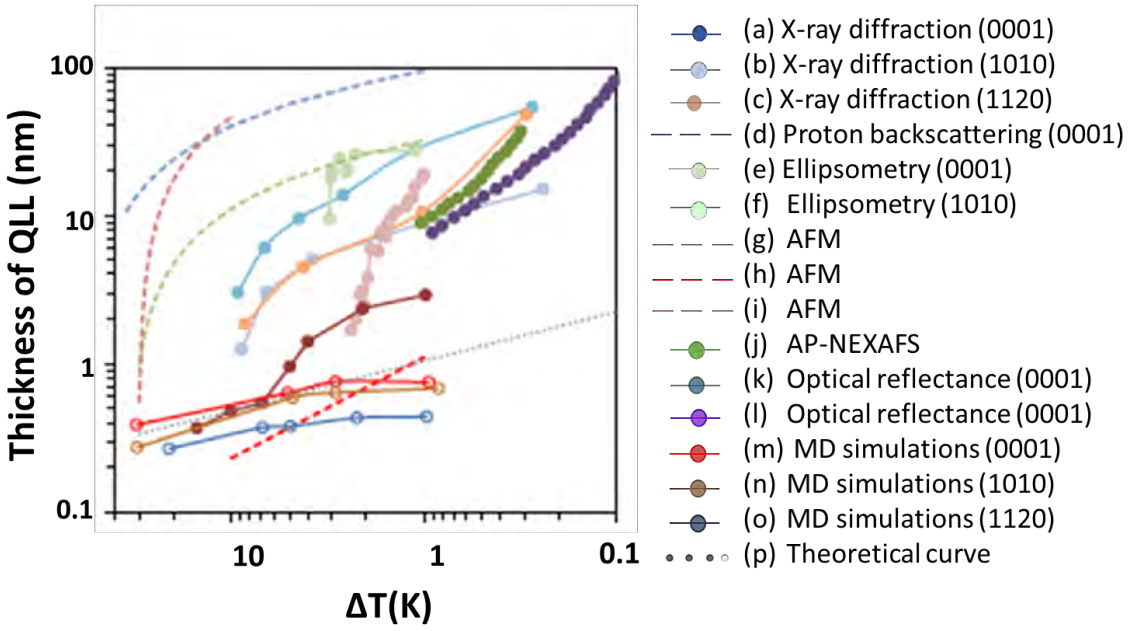

Figure 1.7. Comparison of different methods to derive the thickness of the QLL at the free ice surface versus $\Delta T = T_m - T$ obtained using different methods (redrawn from [38]).

Depending on the methods, experimental studies, molecular dynamics simulations, and thermodynamic calculations on the pure QLL vary as much as two orders of magnitude, as shown in figure 1.7. The uncertainties in the reported results are attributed to the use of different experimental techniques, the ice sample preparation procedure and to the fact that the thickness is not a directly observed in any of the experimental studies. The derivation of the QLL thicknesses from the various observations shown in figure 1.7 may also explain values below 0.3 nm, which fix the lower limit of a physically meaningful thickness, since it is the diameter of a water molecule.

Simulations

As mentioned above, the behaviour of the ice quasi-liquid layer (QLL) has been the subject of several different theoretical studies.

Molecular dynamics (MD) simulations are certainly a useful tool for the study of QLLs. With resolution at the molecular level it is possible to follow the development of this disordered layer from onset up to the macroscopic range, molecule by molecule. Simulations are space (thicknesses below 1nm) and time-limited (timescales up to several microseconds). However, using periodic boundary conditions simulations are performed for infinite flat surfaces of single crystals.

Molecular dynamics simulations show that the QLL develops spontaneously at the free surface of ice at temperatures below the melting point (see figure 1.8), independently of the water model and the crystallographic plane exposed to the vapour phase [39], [40], [41], [42],[43].The onset temperature of the QLL differs with the crystal facet exposed to the vapour phase, being about 100 K and 80 K below the melting point on the basal plane and the prism plane, respectively [36]. The thickness of the QLL also shows slight differences for different crystal facets [36], [44]. It appears that the QLL on the basal plane is somewhat thicker.

Pfalzgraff and co-workers [44] obtained values of 0.67, 0.61, 0.63, 0.84 nm for the thickness of the QLL on the basal, prismatic, 28º pyramidal and 14º pyramidal faces of ice, around ~40 K below the melting point of their water model. The QLL on all faces consisted of two sublayers.

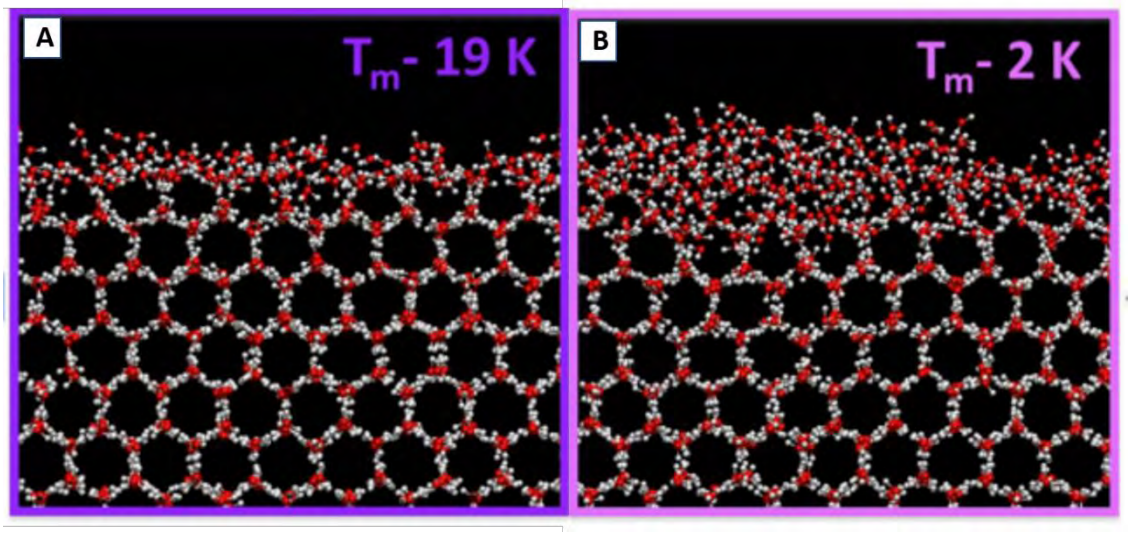

Figure 1.8. Snapshots of the prismatic ice/vapor interface in simulations performed at temperatures correspond to undercooling of −19K **(A)** and −2K **(B)** relative to the melting point of the water model (NE6, T_m =289K). (Redrawn from [45])

In a recent study, *Sanchez et al.* [46], combining surface specific vibrational sum frequency generation (SFG) spectroscopy and molecular dynamics simulations, quantify the change in the interaction between water molecules directly at the interface between ice and air. The authors show that the first molecular layer at the ice surface is already molten at temperatures as low as -38° C, and at -16° C the second layer becomes liquid. The structural ordering decreases continuously. SFG spectroscopy is an example for one of the most powerful experimental methods. This technique provides unique information on the vibrational response of only the topmost surface atoms. For ice, SFG can probe intermolecular interactions and allow to determine the hydrogen bond strength at the surface. The orientational disorder of the QLL can reduce the intensity of the SFG signal for free O-H bonds [8]. Even with such advanced techniques, revealing the dynamic behaviour of QLLs and imaging QLLs in situ remains an experimental challenge, and it is one of the objectives of this thesis.

The QLL on ice has a crucial role in environmental phenomena such as soil freezing or permafrost formation, sliding of glaciers, friction of ice and snow. In fact, the slipperiness of ice and snow implies a thin (quasi-)liquid film, which reduces friction [6], [47], [48], [49], [50], [51]. The QLL also influences the behaviour of atmospheric ice. It was suggested to lead to the electrification of the thunder clouds via charge transfer at the liquid-ice interface [52], [53]. *Abbatt et al.* [54] even proposed that polar stratospheric clouds are able to accommodate HCl by dissolution the QLL, where they can efficiently participate in ozone destruction during winter and spring at and around the poles.

However, one should distinguish such cases of dissolved substances (impurities) from the true QLL on pure ice. The normal melting point of a bulk solid will be altered by the inclusion of impurities as defined by Raoult's law:

$$T_f = T_0 \left(1 - \frac{RT_0 n_{solute}}{q n_{solvent}}\right) \qquad (1.9)$$

where T_f is the freezing temperature, R is the gas constant, q is the molar heat of fusion of the solvent, n_{solute} is the number of moles of solute and $n_{solvent}$ is the number of moles of solvent. This effect can easily cause melting point depression of several Kelvin, even tens of Kelvin! An instructive example is given by Fukazawa et al. [55], who demonstrated by micro-Raman spectroscopy that inorganic salts in ice accumulate in the liquid internal water-vein system at grain intersections [56], [57]. This phase is liquid down to at least -35 ºC.

1.1.5 Diffusional dynamics and its analysis

The word diffusion derives from the Latin word, “diffundere”, which means "to spread out" and is widely used in physics, chemistry, biology, sociology, economics, and finance. In each case, the object that is undergoing diffusion is “spreading out” from a point or location at which there is a higher concentration of that object.

For example, diffusion of lipids and proteins takes place in the cell membrane and is important for cell function and stability. Diffusion in cell membranes is complex, and a subset of diffusion models is therefore required to describe the diffusion (see figure 1.9). The most relevant processes are hindered diffusion (Figure 1.9.A), confined diffusion (Figure 1.9.B), directed motion (Figure 1.9.C), and free diffusion or Brownian motion (Figure 1.9.D). The effects imposed on the diffusion behaviour are transient for the first two cases: For instance, in the middle section of trajectory A (hindered diffusion) in Figure 1.9., the particle diffuses freely. This means that the measured diffusion coefficient depends on the time scale on which it is measured.

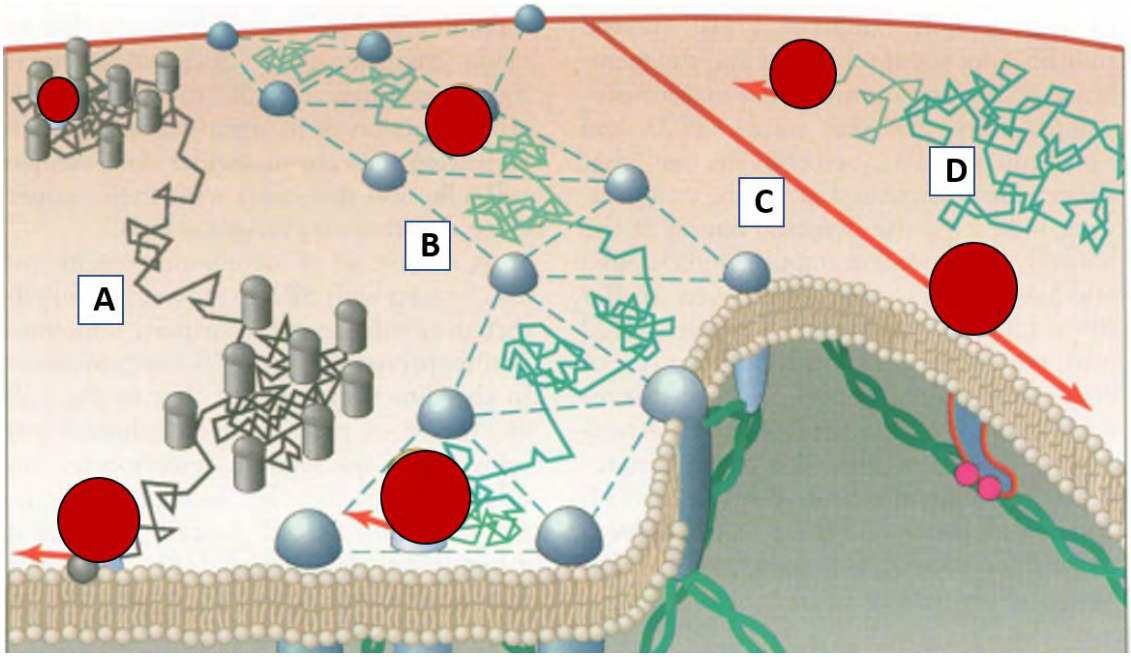

Figure 1.9. Diffusion modes on the cell surface. **(A)** Transient confinement by obstacle clusters **(B)** or by the cytoskeleton, **(C)** directed motion, and **(D)** free random diffusion. Redrawn from [58]

In 1905, Einstein formulated a statistical treatment of Brownian diffusion based on the mean square displacement (MSD) $< x^2 >$ of a particle in one dimension [59]

$$< x^2 >= 2Dt \quad (1.10)$$

This solution is valid for a long observation time t compared to the time of individual particle movements. In two dimensions, where $r^2 = x^2 + y^2$, the MSD becomes:

$$< r^2 >= 4Dt \quad (1.11)$$

In a classic paper from 1905, Einstein derived the well-known diffusion equation for microscopic spheres in liquid solution, relating the diffusion coefficient to the friction coefficient, f:

$$D = \frac{k_B T}{f} = \frac{k_B T}{6\pi\eta R_H} \quad (1.12)$$

Here k_B is the Boltzmann constant, T is the temperature, η is the viscosity of the solution, and R_H is the hydrodynamic radius of the particle. Einstein's diffusion equation presumes a homogenous environment surrounding the diffusing particle. This is not always the case in real systems, where diffusion may be hindered by impediments or barriers, and/or confined within sub-compartments [58]. There are several studies [60], [61], [62] that describe in detail the possible inhomogeneities that a particle can experience in two-dimensional systems.

In two dimensions the MSD for this "anomalous diffusion" becomes

$$< r^2(\tau) >= 4D'\tau^{\alpha} \quad (1.13)$$

For $\alpha = 1$ the diffusion is normal, $D' = D$, while for $0 < \alpha < 1$ it becomes the so-called sub-diffusion (confined diffusion), and for $\alpha > 1$, super-diffusion (biased diffusion). For these types of anomalous diffusion, it turns out that the measured diffusion coefficient D' depends on the observation time. For instance, in case of hindered diffusion, at long times the effect of obstruction is averaged out, and apparent normal diffusion is again observed, but the observed diffusion coefficient is lower than at shorter times [62].

The MSD, $< r^2 >$, is of crucial importance in colloidal studies and biophysics to determine the mode of displacement of particles. It can help to determine whether the particle is freely diffusing, transported, or bound and limited in its movement. Besides an estimation of the parameters of the movement, the diffusion coefficient can be calculated.

Figure 1.10 suggests that plotting the logarithm of the MSD as a function of time might result in a straight line. Its slope α provides the diffusion type: The red curve for α < 1 signifies impeded movement, particles cannot freely diffuse away from their starting point; if the MSD increases faster than linear (α > 1, light-blue curve), the particle should be transported (or "biased"), because Brownian motion could not entrain it that fast.

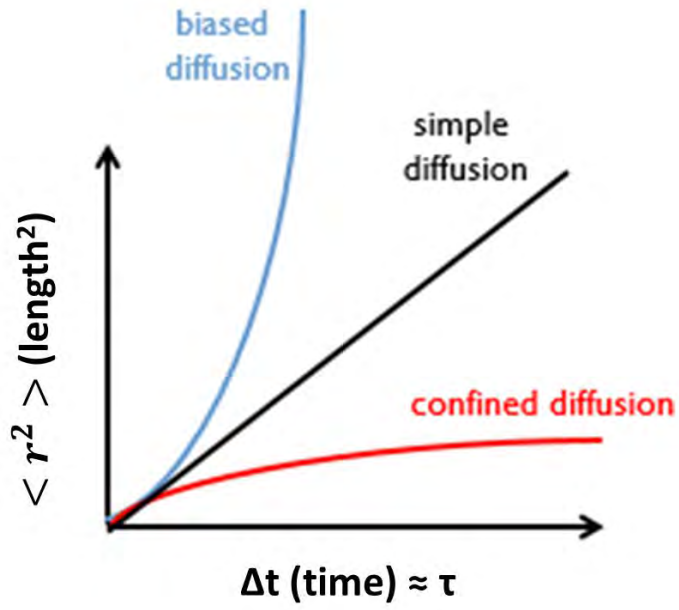

Figure 1.10. Types of diffusion

The second goal of the MSD analysis is the extraction of the diffusion coefficient value D', which is in the logarithmic plot the intercept of the vertical axis. It is important to note that since a *single* diffusion constant is extracted from such an analysis, if the diffusing particle is undergoing multiple types of diffusion during the observed trajectory, the extracted value will only be an average [63]. For example, if the particle undergoes fast diffusion during the first half of the trajectory, followed by slower diffusion during the second half, the measured average diffusion constant will be biased towards the larger

value and provide no information about the underlying two very different diffusion coefficients. At this point one question could arise: How well can the diffusion coefficient D' of a single trajectory be measured?

Several methods have been proposed and described exhaustively to analyse trajectories obtained from tracking data, for example the weighted mean square displacement, developed by Saxton [64], and the cumulative distribution function, by Schütz et al. [65]. The principle for both methods is that the diffusion constant is best characterised at short diffusion times. In Saxton's method, the individual trajectories ($< r^2 >$ vs. t) are analysed, but with the displacement over short-time intervals weighted heavily:

$$< r^2(\tau) >= \frac{1}{N_{T-\tau+1}} \sum_{i=0}^{N_{T-\tau+1}} (\overrightarrow{r}(i+\tau) - \overrightarrow{r}(i)) \quad (1.14)$$

where $< r^2(\tau) >$ is the mean square distance for the time lag τ, N_T is the total number of time steps (= data points in the trajectory). A note on the time lag: "The time interval τ can cause confusion to those unaccustomed to it, as one may think that there is only a single datum per time interval. For example, using a frame rate of 1 s^{-1}, the squared displacement for τ = 1 can be calculated not only from the difference in particle position between frames 1 and 2 but also frames 2 and 3, 3 and 4, 4 and 5... In this way the number of squared displacements that can be calculated for each time interval is n-(τ × frame rate). The mean of these squared displacements can then be calculated to find the mean-squared displacement"[66].

There are two ways to calculate the MSD for a given time lag τ, by averaging over all pairs of points τ time steps apart, or by averaging over independent pairs of points τ time steps apart. Most researchers use the average over all pairs, as also in this work; this can be exemplified as follows: Consider a trajectory of eleven steps. Now the MSDs for time lags τ = 2 are determined for all pairs separated by two time steps resulting in eleven individual values for MSD (τ = 2) and thus eleven diffusion coefficients (see figure 1.11). For time lag τ = 3, ten individual diffusion coefficients are obtained, and so forth. Finally, for time lag τ = 11 (where the diffusion coefficient is the least well characterised) only one value for D is obtained.

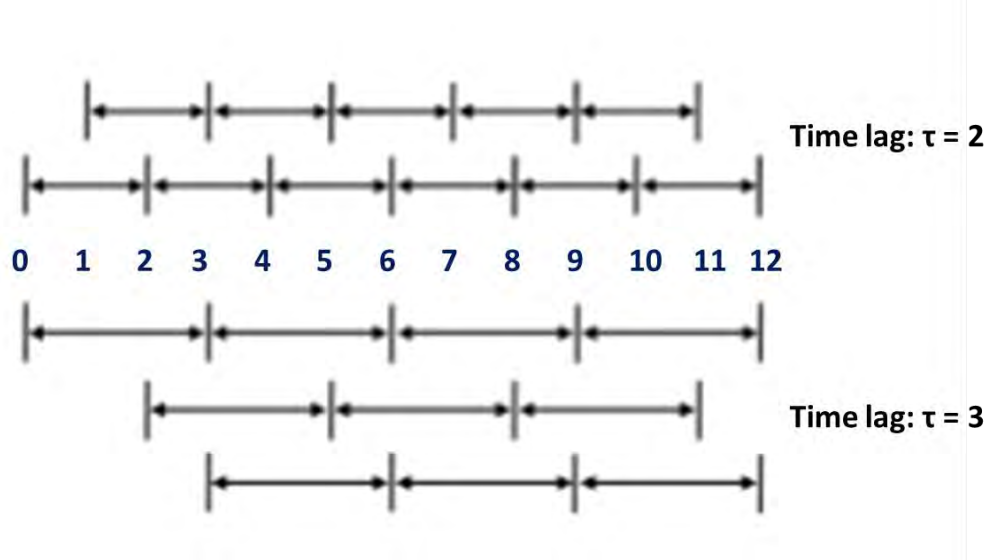

Figure 1.11. The basis for the weighting method. Redrawn from [64]

On the other hand, the MSD at different time lags for multiple trajectories are analysed collectively in the method by *Schütz et al.* The result is given as a single probability function $P(r^2, \tau)$ which describes the probability of finding a particle within a circle of a given radius r after a time lag τ :

$$P(r^2, \tau) = 1 - \exp(\frac{r^2(\tau)}{<r^2(\tau)>}) \quad (1.15)$$

where $\tau = \Delta t$ is the time between two consecutive images.

The two methods of analysis have each their strengths and deficiencies. The cumulative distribution function method yields better statistics, especially when many short trajectories are known [64], but the method proposed by Saxton is the most intuitive, and clearly shows if the diffusion behaviour of a single particle changes during a trajectory. Here the Saxton method was used for data analysis in this work.

1.2 Properties of ice

The unique and unusual properties of water originate mainly from the structure of the molecules and their H-bonding. One important aspect is that ice is less dense than liquid

water. The thermal expansivity for water has its minimum at 4 °C, below which it is increasing again [67]. The volume of ice is 9% larger than water at ambient pressure and approximately 17% larger at 2 kbar [68]. The molecular arrangement for a single water molecule, with molecular formula H_2O, is shown in figure 1.12.

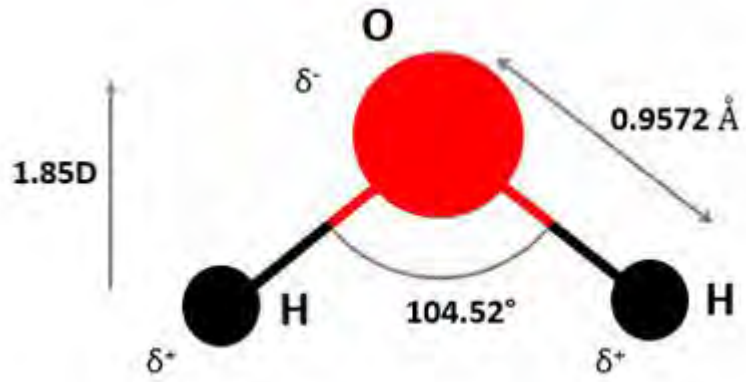

Figure 1.12. The geometry of a free H_2O molecule: Two hydrogen atoms are covalently bonded to an oxygen atom. The partial charges δ cause a large dipole moment. Redrawn from [69]

The equilibrium distance between the oxygen and hydrogen atoms is 0.0957 nm and the angle between the oxygen and hydrogen bonds is 104.52°[69]. Water is a polar molecule. The high electronegativity of the oxygen atom leads to an uneven electron density distribution in a water molecule (the average electron density around the oxygen atom is about ten times that around the hydrogen atoms). Consequently, there is a partial negative charge, δ^-, near the oxygen atom and partial positive charges, δ^+, on the hydrogen atoms. This asymmetrical distribution of electronic charge results in the bent configuration of the water molecule and induces an electric dipole moment of 1.85 Debye in the gas phase [70].

Due to the mentioned uneven electron density of water molecules, a dynamic attractive interaction between neighbouring water molecules involving one hydrogen atom located between the two oxygen atoms occurs; this is known as hydrogen bonding. The tetrahedral structure of water and other uncommon properties of the distinct phases of water, such as the temperature of the maximum density, the lower density of ice relative to water, the high boiling temperature, are all a consequence of the hydrogen bonds. The

simplest example is the water dimer, in which one water molecule is oriented with its positively charged hydrogen atom between two negatively charged oxygen atoms, one from the same molecule and one from another water molecule (see figure 1.13).

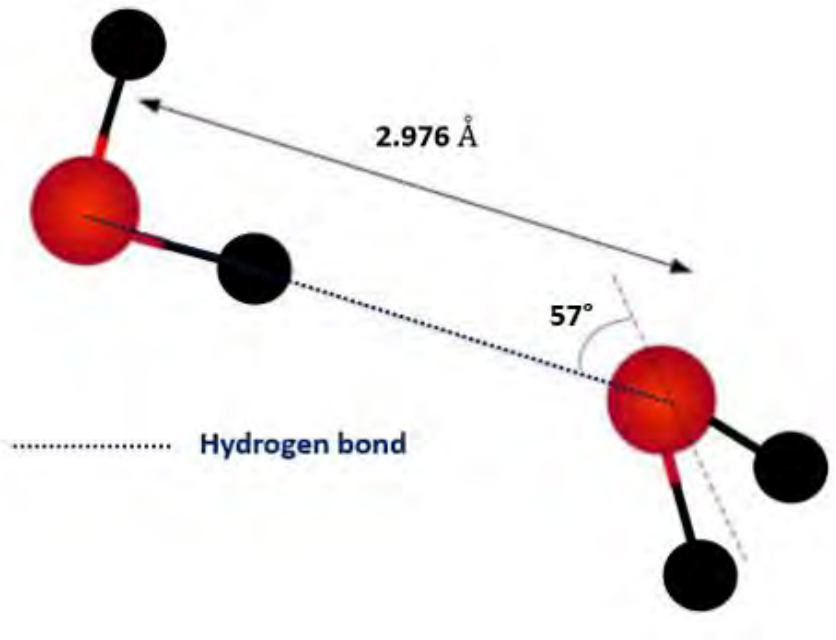

Figure 1.13. Schematic representation of hydrogen bonding between two water molecules. Redrawn from [71]

The water hydrogen bond is a weak bond, but strong enough to be maintained during thermal fluctuations at, and below, ambient temperatures. The energy of a hydrogen bond is generally considered to consist of different contributions (about 90% electrostatic and about 10% electron sharing). By bringing together two water molecules, electrostatic interactions between their partial charges occur and they also polarize each other, generating a distortion of their charge distributions. These effects strengthen the hydrogen bond. On the other hand, there is a repulsive force that prevents the violation of the Pauli exclusion principle due to interpenetration of the charge clouds. The energy of a hydrogen bond in ordinary ice is about 23 kJ/mol [72]. Each water molecule can form two hydrogen bonds involving their hydrogen atoms, while its oxygen atom accepts two hydrogen bonds from two other neighbours, meaning that there can be up to four hydrogen bonds formed by one water molecule.

1.2.1 Hexagonal ice I_h

Ice I_h is by far the most common ice crystal polymorph on earth, which is already obvious from the six-fold symmetry of ice crystals (and snowflakes) formed from liquid water [73]. Each water molecule of ice I_h establishes the maximally possible four hydrogen bonds with the molecules surrounding it. The tetrahedral structures arrange in a hexagonal lattice. One of the consequences of the ice I_h structure and tetrahedral arrangement of the water molecules is the low density of ice in comparison with liquid water (at ambient pressure). The positions of the atoms in ice I_h obey the Bernal-Fowler rules [74]:

- Each oxygen atom is directly attached to two hydrogen atoms forming a water molecule.

- Two hydrogen atoms of one molecule are directed towards two other oxygen atoms in neighbouring molecules.

- Only one hydrogen atom is located between two oxygen atoms in the lattice structure.

The crystal structure of I_h is shown in figure 1.14. The unit cell of the ice I_h lattice consists of four water molecules. There are two possible sites for each hydrogen atom, meaning a proton-disordered behaviour of hexagonal ice.

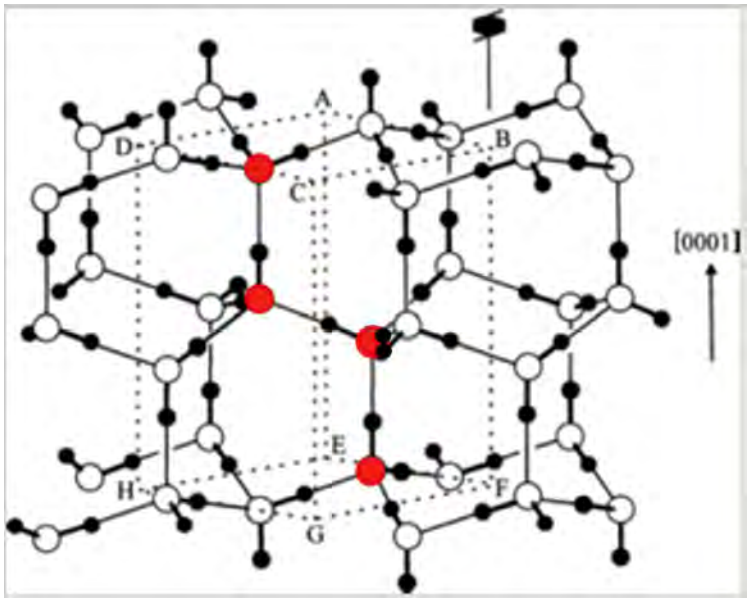

Figure 1.14. The crystal structure of ice I_h. The unit cell of the average structure is marked ABCDEFGH, and the four oxygen atoms contained within this cell are shown in red. The c-axis of this structure lies along BF as indicated. Redrawn from [74]

The unit cells pack into a hexagonal super cell as shown in figure 1.15. Hexagonal ice crystals form hexagonal plates and columns where the top and bottom faces are the basal planes. These faces that are perpendicular to the c-axis, identified with a (0001) notation, are known as the basal faces or planes. Faces which are parallel to the c-axis are called prism or prismatic faces. There are two sets of prismatic faces, primary and secondary, and they are represented by (1010) and (1210), respectively. The basal and the primary prismatic faces are the ones exposed to the water vapour and constitute the surface of the growing crystal. Another set of planes in ice I_h are known as pyramidal faces (see figure 2.14.A, chapter two). They are beveled facets associated with each prismatic surface [75]

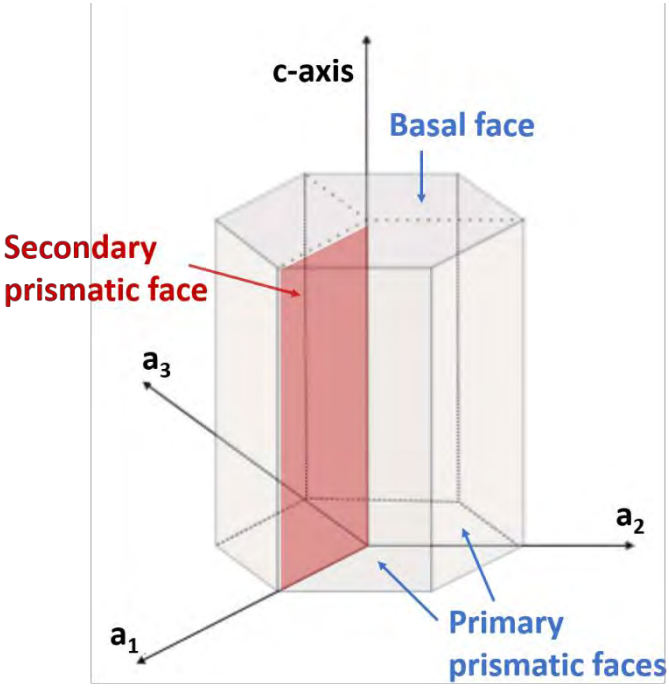

Figure 1.15. Hexagonal super cell of ice I_h. Redrawn from [69]

1.2.2 Ice crystals

The size and shape of ice crystals vary with atmospheric conditions, and in turn the ice morphology has a strong impact on its geophysical effects, from radiative properties to its tendency to agglomerate [4].

As shown in figure 1.16, crystals can grow as hexagonal plates and columns or have more complex geometrical shapes like bullet rosettes and dendrites. The habit is dominated by

poly-crystals of various forms with two distinct habit regimes: plate-like from -20°C to -40°C and columnar from -40°C to -70°C.

Below -20°C the crystal habit is dominated by columnar crystals, in addition to plates, depending on supersaturation. Between -20°C and -10°C plates and dendritic snowflake crystals are observed. Above -10°C crystals form columns or needles, before transitioning back to plates and dendrites close to the melting temperature.

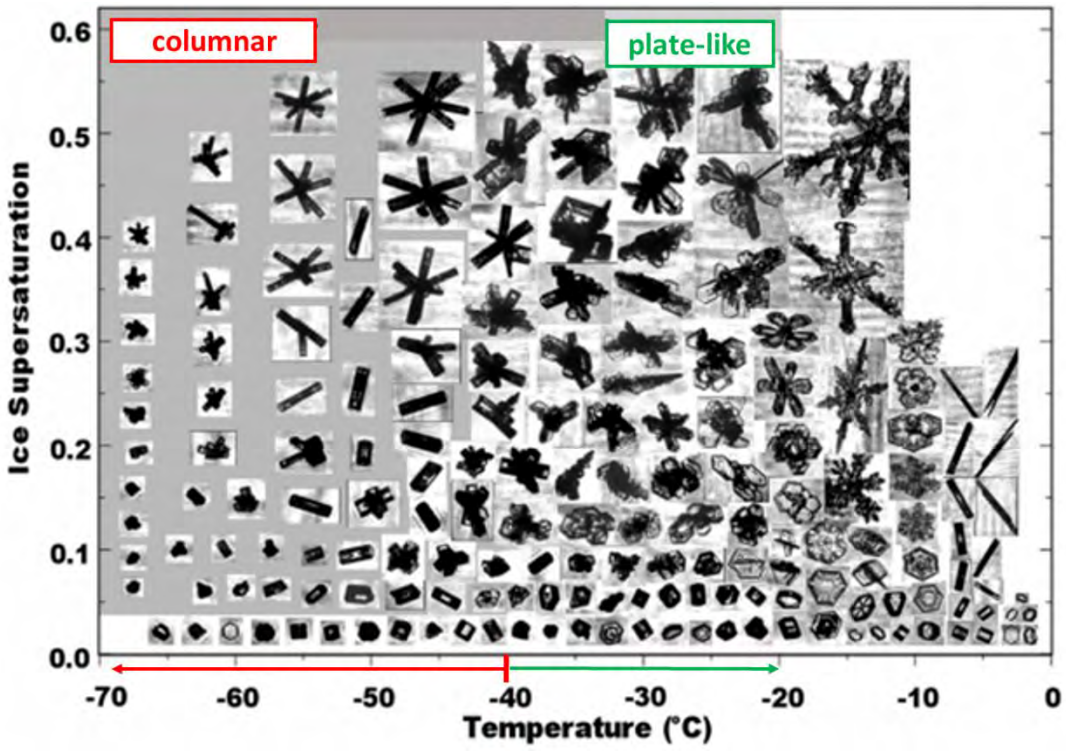

Figure 1.16. Habit diagram from ice crystals grown between 0°C and -70°C. Redrawn from [76]

There are two principal features that one can conclude from figure 1.16: the morphology change with temperature, which is known as habit change, and the increase of complexity with supersaturation.

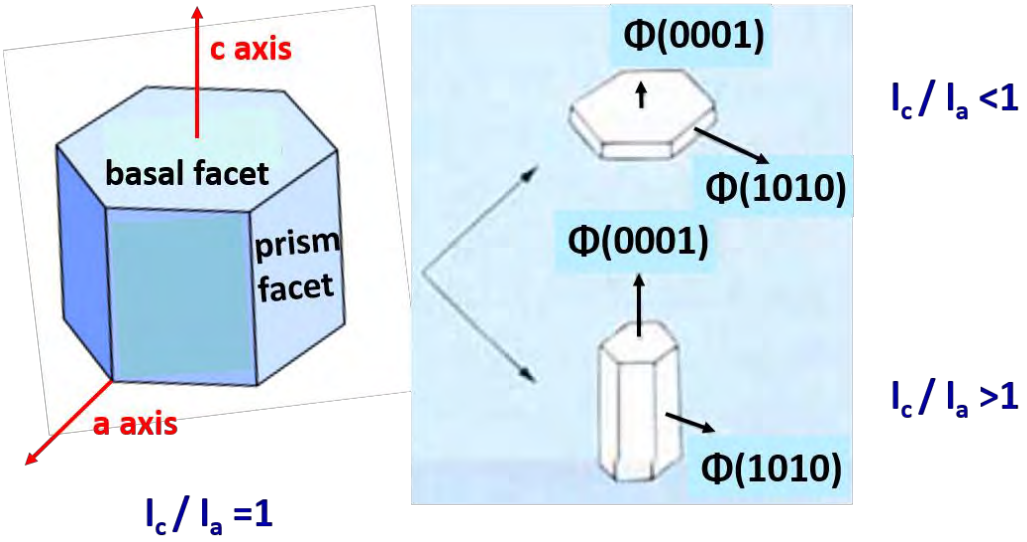

Figure 1.17. Hexagonal prism and the change of habit phenomenon (adapted from [29]) based on the growth rate, Φ, at the different facets.

The habit is determined by the growth rate in the different directions (see figure 1.17). Therefore, if water condenses preferentially on basal faces, the ice crystals adopt a prismatic shape. On the other hand, plates are formed if prismatic faces are preferred areas for water condensation.

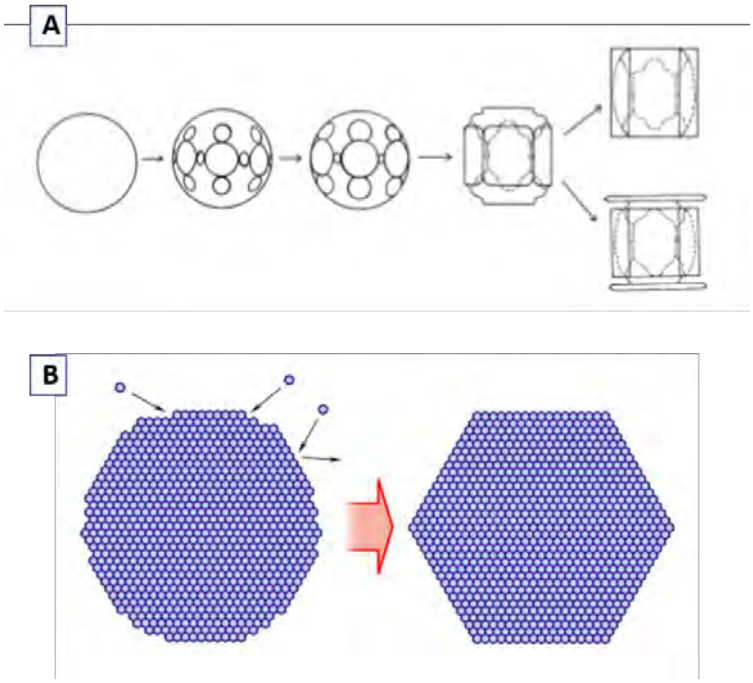

Figure 1.18. A) Phases of crystal growth on the way from a spherical ice crystal (droxtal) to a hexagonal prism (taken from [77]). **B)** Representation of facetting (from snowcrystals.com)

Small nearly spherical ice crystals with well rounded corners and edges are known as "droxtals" (see figure 1.18.A), a term that combines the words droplet and crystal. During growth, flat facets can appear on ice crystals: Water molecules hit the crystal surface and stick, but they attach more readily to rough areas on the surface, where many possible new bonds are available. They stick less well to smooth areas (facets) with fewer bonds (see figure 1.18.B). As a result, the smooth surfaces accumulate material more slowly than rough surfaces. The rough parts soon fill in, leaving just the smooth, faceted surfaces.

A possibly unexpected effect is the formation of circular flat areas on ice particles of various shapes [77], for various growth process, which is in this work also verified for growth in the ESEM (see figure 1.19).

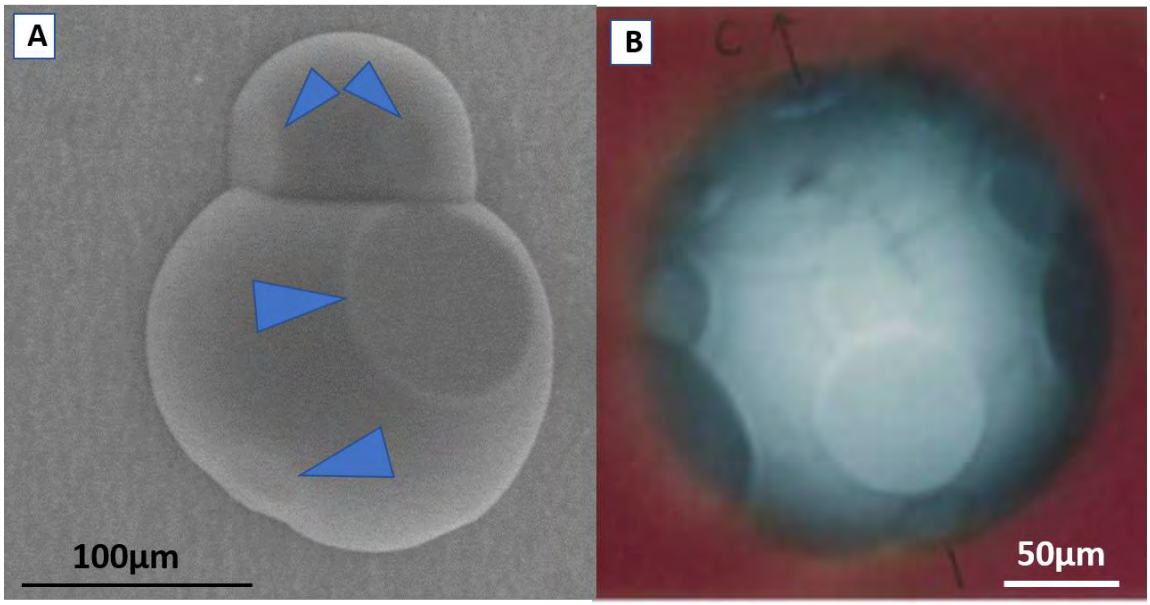

Figure 1.19. A) Two droxtal-like merged ice crystals grown in the ESEM. Blue arrows show circular flat areas on the ice crystals surface (own data). **B)** Ice particle grown from frozen water droplets, accompanied with the development of circular crystal faces (taken from [77])

As reported by Bailey and Hallett [78], mostly symmetric hexagonal crystals with equal length facets were grown, but also “scalene” ice crystals, which are hexagonal plates, whose sides are of different lengths (see figure 1.20). Scalene plates typically have pairs of sides with equal lengths (in the example in figure 1.20.A, one can distinguish two lengths, a short distance between 8 and 9µm, and a longer one, between 11 and 12 µm).

On rare occasions, completely asymmetric plates (six sides with different lengths) are observed (in figure 1.20.B, the lengths of the six facets are all different, from 2.95 µm up to 12.86 µm).

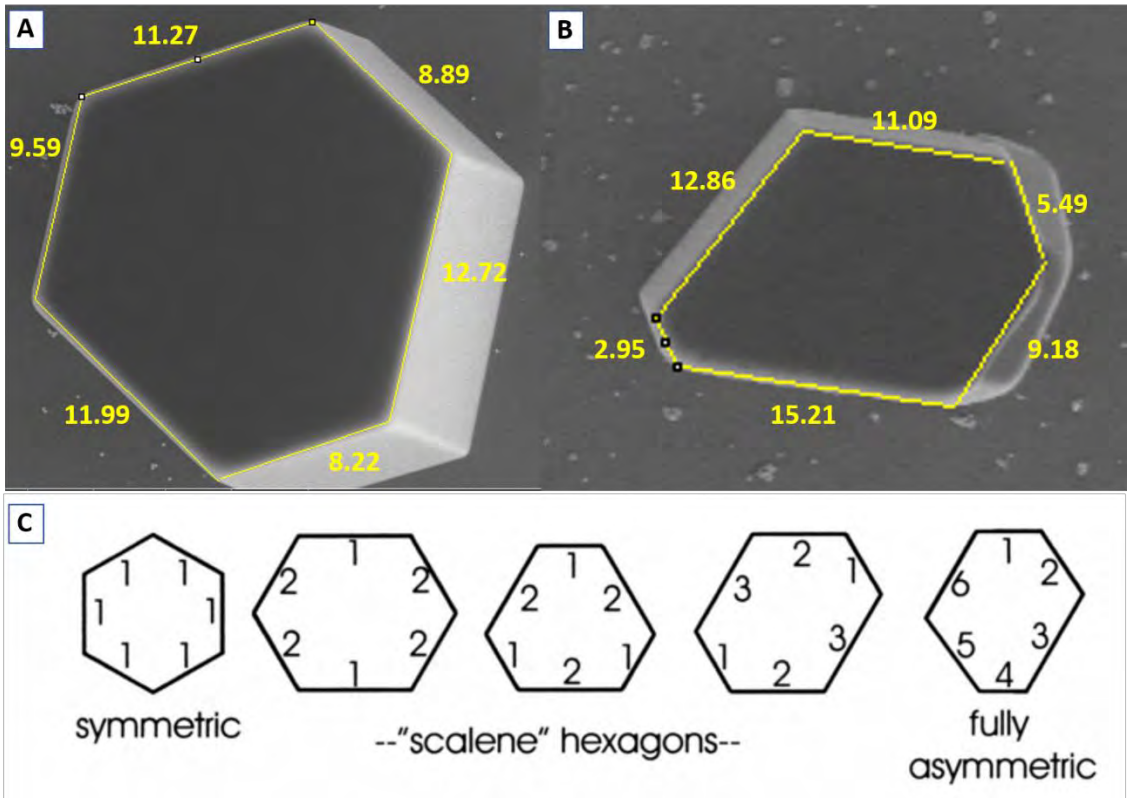

Figure 1.20. Two different ice hexagonal prisms grown in the ESEM. **A)** Scalene hexagon (own data). **B)** Fully asymmetric hexagon (own data). **C)** Asymmetric ice crystal shapes described as scalene plates [78]

The complex behaviour of ice crystal habits is well known, meaning that not only temperature and supersaturation are key factors, but also the initial nucleation process. For example, one can occasionally grow more complex ice crystals (see figure 1.21), with a similar appearance to a bullet rosette, which normally appear at temperatures <-40°C [79].

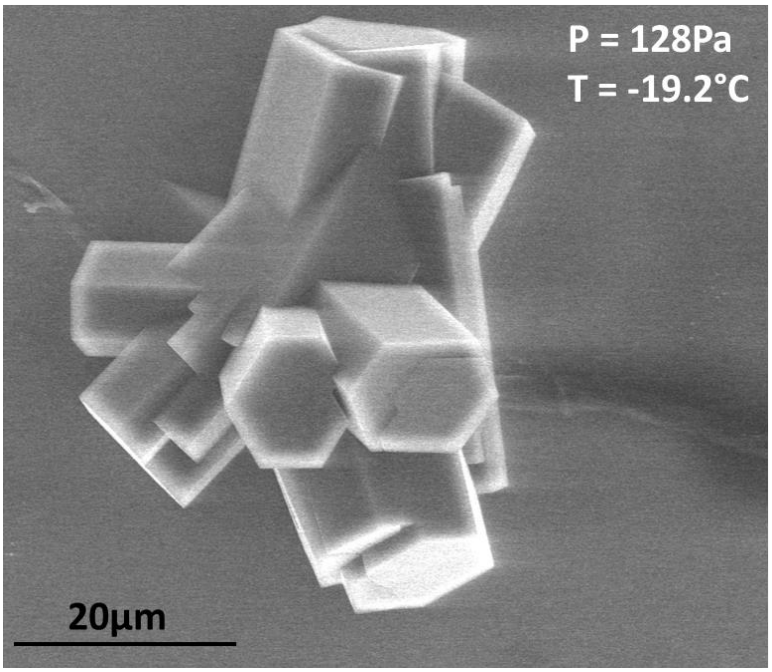

Figure 1.21. Complex ice crystal (bullet rosette) grown in the ESEM (own data).

1.2.3 The ice-vapour interface

Various experimental studies have investigated the ice growth from the water vapor and its dependence on temperature and supersaturation. Kinetic processes, like transport and attachment phenomena, control the ice growth (vapour and liquid can be supercooled), while the reverse process, sublimation, is thermodynamically controlled (there is no superheating)

Attachment kinetics can describe how water molecules are arranged into the ice structure. The ice growth velocity [80] is given by:

$$v(T, S_i) = \alpha_w(T, S_i) \cdot v_{kin}(T) \cdot S_i \quad (1.17)$$

where $v(T, S_i)$ is the growth velocity of ice, α_w is the dimensionless attachment coefficient (also known as the condensation coefficient), v_{kin} is the kinetic velocity of the molecules in the gas phase, and S_i is the supersaturation above the ice surface. The supersaturation is related to the previously defined humidity by

$$S_i = h - 1 \quad (1.18)$$

The growth rates of the prism and basal facets of ice for temperatures ranging from -40°C to -10°C were studied by *Libbrecht* [81]. Surprisingly, they found no significant difference in growth rate between both ice faces over the analysed temperature range.

The temperature and supersaturation dependence of the growth rates of the different faces in an ice crystal was investigated by *Lamb* and *Scott* [82]. According to their results exists a local maximum for each face, which corresponds to -6°C for the basal face, while at the prism face the maximum growth occurs at -13°C. It must be noticed that heating effects might not have been negligible due to the enormous size of the measured ice crystals and also the fact that the supersaturation values may not have been accurate at points close to the observed crystals, as other crystals growing nearby could act as vapor sinks.

Significant discrepancies in the reported values for the growth rates on basal and prism faces of ice grown from water vapor are well known; they are discussed in [83]. They derive mainly from systematic effects (latent heat effects, diffusion effects, substrate interactions), which make it difficult to perform a quantitative analysis. However, some generally accepted rules are: The growth velocity on the prism face is higher at T>-5°C and at -20°C<T<-10°C, on the basal face the rate is faster for -10°C<T<-5°C.

The growth rates of basal and prism faces of ice as a function of supersaturation for a temperature range from -1°C to -30°C have been studied by *Sei* and *Gonda* [84]. The limiting habit of the ice crystals growing on a substrate at 40 Pa changes with decreasing temperature as follows: Hexagonal plates grow at temperature from 0°C to -4°C, hexagonal columns from -4°C to -10°C, again hexagonal plates from -10°C to -21°C, and hexagonal columns below -21°C. However, the authors do not clarify the substrate effect on the growth behavior.

Bailey and *Hallett*, in a more recent study, [76] propose a new habit diagram of ice growth from vapor in air (see figure 1.16) which retains the well-established descriptions of habits from the older diagrams for temperatures above -18°C, that is, from plates (0°C to -4°C) to columns (-4°C to -8°C) to plates (-8°C to -22 °C), but it diverges from the previous habit diagrams for lower temperatures and distinguishes two distinct habit regimes: plate-like from -20°C to -40°C and columnar from -40°C to -70°C.

Libbrecht and *Rickerby* [85] have presented more recent measurements of crystal growth on the principal facets of ice over a broader range of temperatures (2°C to -40°C) that attempt to minimize systematic errors. They have made a careful study of the interactions with the substrate. It has been noted previously that substrate interactions could influence the measurements results, since prism facets intersecting their substrate grew up to five times faster than prism facets not intersecting the substrate.

All these results show that nucleation always requires a solid "substrate". Here, and also in nature, this can be an existing ice crystal (homogeneous) or some solid "dust" particle (heterogeneous), while experiments are best carried out on well-defined flat surfaces. Depending on chemistry, crystallinity, and purity, some ice crystal habits may be preferred: The very first layer of ice and its orientation on the substrate can have a huge influence. A well known example is the epitaxial growth of ice on silver iodide (AgI) [86].

1.3 Ice nucleation in the atmosphere

1.3.1 Homogeneous ice nucleation

Homogeneous ice nucleation involves formation of ice either directly via deposition of water vapour, or via the liquid phase which subsequently freezes. It is highly improbable, except at extremely low temperatures (−100°C), that the first mentioned pathway occurs in the atmosphere, because it would imply transition from a high entropy system (vapour) to a low entropy system (ice crystal)[87]. The process of homogeneous nucleation starts when - by chance - molecules in the liquid droplet form an ordered cluster, known as an embryo. This embryo acquires and loses individual water molecules, leading to fluctuations in its size. If the embryo reaches a critical size, it is termed an ice germ, whereby addition of a further water molecule results in spontaneous growth of the ice germ, and a macroscopic phase change of the droplet.

The energy decreases as a result of the phase change from liquid to ice, proportional to the number of added water molecules, but at small sizes the energy increases due to formation of the ice embryo surface, which depends on the surface tension. There is a

maximum, hence an energy barrier ΔE*, at a certain size, the critical size of the ice germ, r* (see figure 1.22).

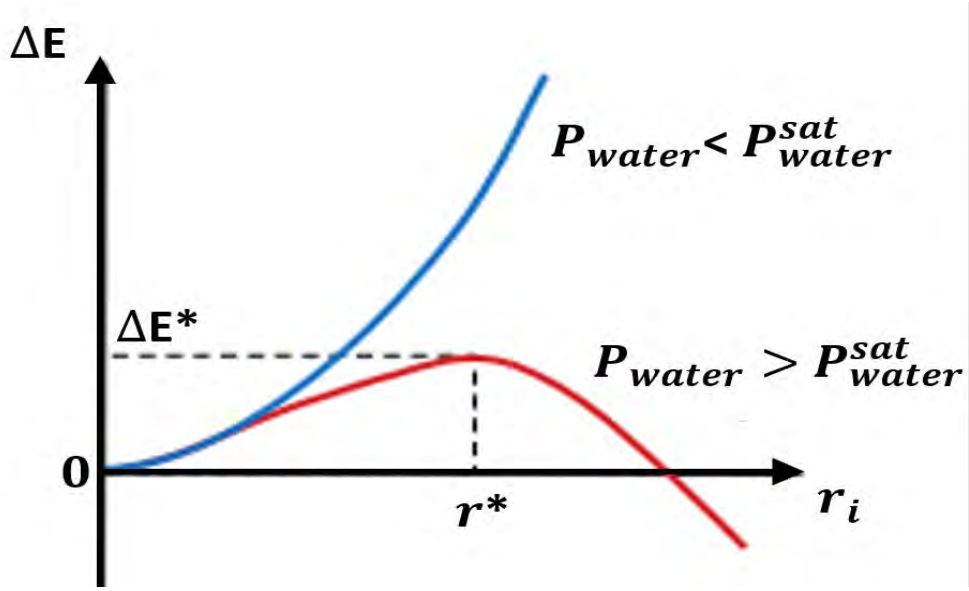

Figure 1.22. Energy change of a water droplet upon increase of radius by condensation. The critical radius is marked as r*. Redrawn from [88]

Median freezing temperatures of −41°C and -35°C for 1 µm and 100 µm sized water droplets, respectively, have been reported in the literature [89]. These temperatures are reached in the upper troposphere at 8-16 km. In the atmosphere, droplets may contain dissolved salts, which cause a melting point depression (see section 1.1.4, equation 1.9) and therefore a lower homogeneous nucleation temperature [90].

1.3.2 Heterogeneous ice nucleation and its mechanisms

Ice nucleation in the atmosphere might take place at higher temperatures than that of homogeneous nucleation [91] due to the availability of certain aerosol particles, since nucleation particles (INPs), which lower the energy barrier for ice formation.

Four different mechanisms of heterogeneous ice nucleation have been identified [99], [90]. All heterogeneous pathways, shown in figure 1.23 together with homogeneous freezing of pure water and of solution droplets, require supercooled water in the vicinity of the ice embryo, and of course supersaturation conditions.

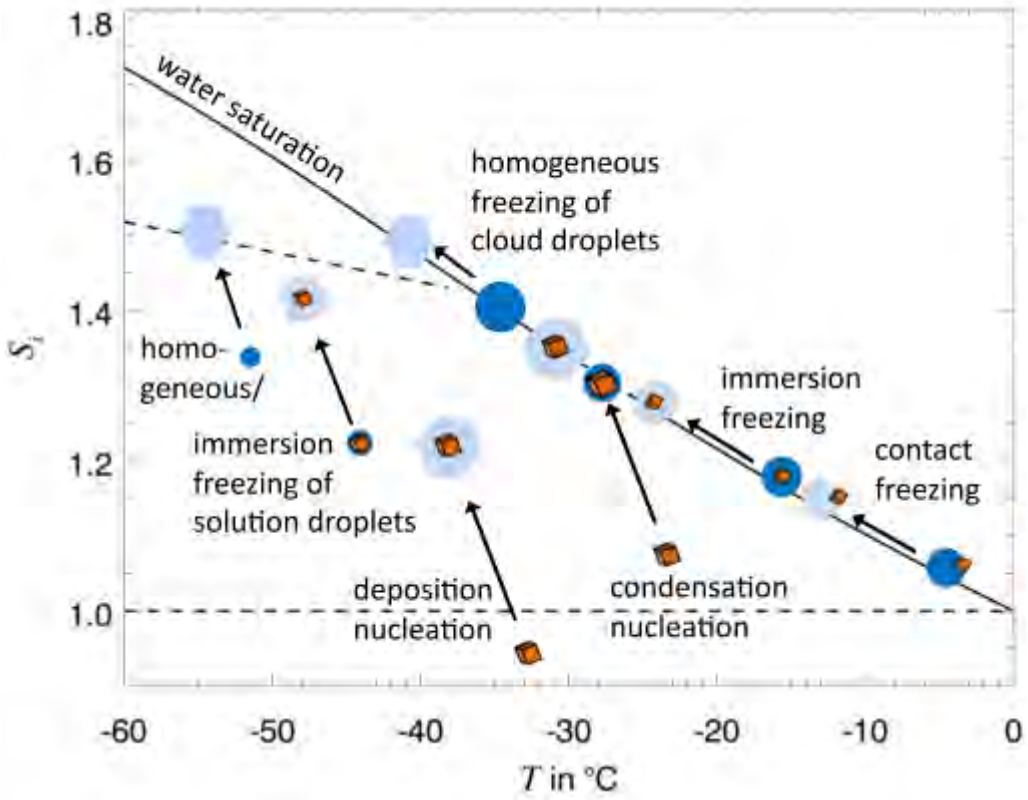

Figure 1.23. Ice nucleation pathways of a rising air parcel showing atmospheric trajectories of temperature and ice saturation. Droplets are represented by circles, hexagons indicate ice crystals, and cubes ice nucleation particles (INPs). [100]

Contact nucleation refers to the initiation of ice nucleation by an INP OR CCN??? which contacts the surface of a supercooled droplet, either from the outside, by colliding with the droplet, or by touching the surface from the inside, if it is immersed in the droplet. It has been observed that contact nucleation occurs at higher temperatures than freezing initiated by other processes [101].

Deposition nucleation occurs when a sufficient amount of water vapour deposits directly on an INP to form a critical ice embryo without an intermittent liquid phase. This requires the vapour to be saturated with respect to ice but not necessarily with respect to water. This is the mechanism operating in the experiments shown in chapter two.

If the relative humidity exceeds saturation with respect to water, **condensation freezing** becomes more probable. Water condenses on an INP, and an ice germ forms during condensation, i.e. without further supercooling.

As already explained in section 1.3.1, atmospheric saturation ratios with respect to water are never sufficiently high for homogeneous cloud droplet formation, which would require cloud condensation nuclei (CCN). If the CCN is liquid or soluble, the droplet may freeze homogeneously at sufficiently low temperatures [102], as typically in cirrus clouds. If the immersed CCN is solid and insoluble it can initiate **immersion freezing**.

The latter two scenarios, condensation and immersion freezing, are the most common mechanism for the formation of ice in mixed-phase clouds [103]. A topic of continuing debate and ongoing research is whether the underlying physical processes of ice nucleation in the condensation and immersion mode are the same [93], [104], [105]. Furthermore, it has been hypothesized that true deposition nucleation does not take place in the atmosphere, but that it is rather a homogeneous or immersion freezing process of water in pores [96].

1.3.3 Biological aerosols and their role in ice nucleation

Very different types of aerosol particles exist in the Earth's atmosphere: Solid particles such as crystalline sea salt, pollen, mineral dust particles, soot from combustion processes, and liquid particles such as water droplets with dissolved sulfuric acid or salts. Primary aerosol particles are mainly emitted from the Earth's surface while secondary aerosols are formed directly in the atmosphere by gas-to-particle conversion processes. [106] These processes include nucleation, condensation, as well as heterogeneous and multiphase chemical reactions [107]. Atmospheric aerosol particles vary in size over several orders of magnitude and have lifetimes from a few seconds up to more than a year [108]. They differ not only in size distribution, but also in shape, particle density, optical properties, etc. Aerosols can transport material over long distances (thousands of km), owing to atmospheric lifetimes of up to several weeks. This is relevant for instance in the biogeochemical cycle of iron, where dust is a major source of iron in the ocean [109], [110].

Aerosols have multiple effects on our environment. A rather direct effect is the influence on the Earth's radiative budget, by scattering and by absorbing radiation. Indirect effects are for example based on the formation of CCNs (see section 1.3.2), which, in a cloud with fixed liquid water content, lead to an increase in the number of cloud droplets and a

decrease in their size. This so-called "Twomey effect" [111] increases the cloud albedo. Smaller cloud particles also decrease the precipitation efficiency, i.e. they induce a longer cloud lifetime [112].

Besides participating in a variety of processes that influence our environment, aerosols are infamous for potentially negative effects on human health [90]. They can transport biological matter such as viruses and organisms, including pathogens and fragments of pathogens [113]. Respiratory diseases such as allergies [114], cardiovascular diseases and lung cancer, [115] have been linked to exposure to biological and inorganic fine particulate matter. Generally, fine particles can penetrate deeper into the respiratory system and thus be more relevant for health effects, while biological matter can interfere directly with cell biochemistry.

Organic compounds in the atmosphere influence climate and air quality in various ways. On the other hand, atmospheric organics largely participate in aerosol formation to produce secondary organic aerosols (SOAs) and coatings on existing particles [107]. Figure 1.24 shows the global aerosol distribution with a classification of aerosol types. A large portion of sulfate particles (marked in white colour in figure 1.24) is emitted by anthropogenic sources, and strongly correlates with organic compounds.

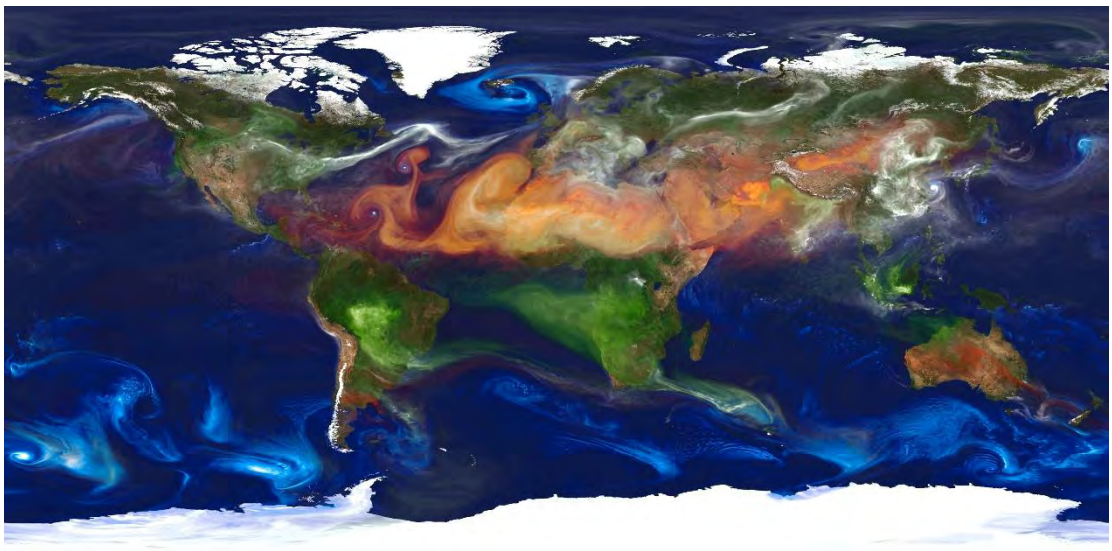

Figure 1.24. Portrait of global aerosols: Sea salt in blue, mineral dust in red, smoke from fire in green, sulfate particles from natural sources and fossil fuel emissions in white. From http://www.nasa.gov/multimedia/imagegallery

In this work, the focus is on a subclass of organics, primary biological aerosol particles (PBAPs), which are defined as "solid airborne particles derived from biological organisms, including microorganisms and fragments of biological materials such as plant debris and animal dander" [116], [117]. Some PBAPs can give rise to significant ice nucleation in mixed-phase clouds at extremely high temperatures (-1°C) [118], [100]. Also all other processes previously mentioned regarding ice particle formation and growth can be influenced by the presence of PBAPs, but their effects are not well documented. This is for a good part due to the wide range of the material: Spores, bacteria, viruses, biomolecules, and also aggregates of biological and non-biological particles. The size of the PBAPs ranges from over hundred µm down to a few nm [119], as shown by the following examples:

Pollen are amongst the largest PBAPs, with grain sizes of 10 - 100 µm. There are many studies on the ice efficiency of pollen: Water droplets are found to freeze at $T \leq -9°C$ (and at $T \leq -5°C$ by contact freezing) when they collide with pollen [120]. Non-proteinaceous macromolecules located on pollen have been found to nucleate ice at $T \leq -17°C$ [121], [122].

Fungal spores are at least several µm in size. Together with the slightly smaller bacteria, they are among the most common PBAPs in the atmosphere, with residence times of several days and transport distances up to thousands of kilometers [117]. Spores often contain surface layers that influence ice nucleation. E.g., hydrophobic proteins that coat the *Cladosporium fungal spore*, a common type of spore in the atmosphere, has been found to cause low freezing temperatures of $\leq -28°C$ [123]; a proteinaceous INP on *Mortierella alpine mycelium* from top-soils in southeast Wyoming has been found to cause freezing of droplets already at -5°C.

Of the µm-sized bacteria, *Pseudomonas syringae* is especially well studied. It contains an ice-nucleating protein (INP) in its outer cell wall [100]. Its hydrogen bond strengths and polarities are similar to those of ice [124], which probably makes this protein especially efficient [90].

Viruses, made up from nucleic acid and protein, cover size ranges from 1000 to 10 nm. Virus aerosols concern not only humans, but also animals and plants. Their transport is

rather a topic in health than in physics. Both viruses and bacteria often attach to other aerosol particles [125].

As is clear from the role of viruses and bacteria, proteins must play an important, if not the most important role in the 1 nm range. In fact, the protein Snowmax® is so effective that it is in widespread use as biodegradable INP for the production of artificial snow. For this reason, it is worthwhile to explore the nature of proteins in some detail.

Proteins are made of amino acids linked into linear chains, called polypeptide chains. Proteins differ in sequence and number of amino acids. A polypeptide chain is made up of a polypeptide backbone with attached side chains (see figure 1.25). There are 20 different amino acids and, consequently, 20 different side chains. One chain end, the amino terminus or N-terminus, carries a free amino group (NH_3^+), and the other, the carboxyl terminus or C-terminus, carries a free carboxylate group (COO^-). The amino acids are classified into categories according to the type of their side chains, which are either charged positively or negatively (necessarily polar), or uncharged polar, or uncharged non-polar.

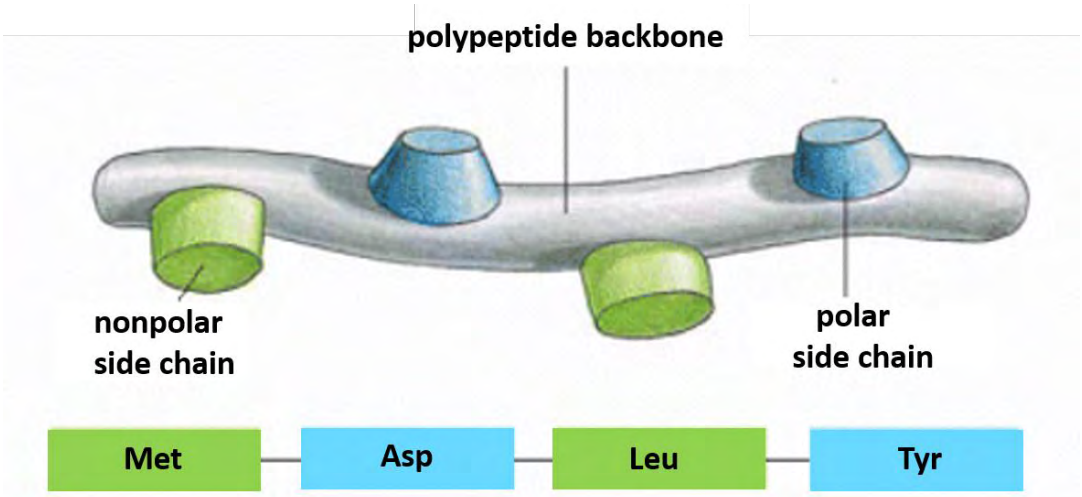

Figure 1.25. Schematic representation of a polypeptide chain. This example shows a sequence of four amino acids, represented by their three-letters abbreviations: Met (methionine, non-polar), Asp (aspartic acid, polar, negatively charged), Leu (leucine, non-polar) and Tyr (tyrosine, polar, uncharged). Redrawn from [126].

The extreme number of possible sequences and the 3D folding of the chain determine protein structure and function. The hydrogen-bonding properties of water have important effects on the folding; most chains fold into compact conformations (see figure 1.26). The

polar amino acid side chains now make up the outer surface, which interacts with water, while the non-polar groups are buried inside to form a hydrophobic core.

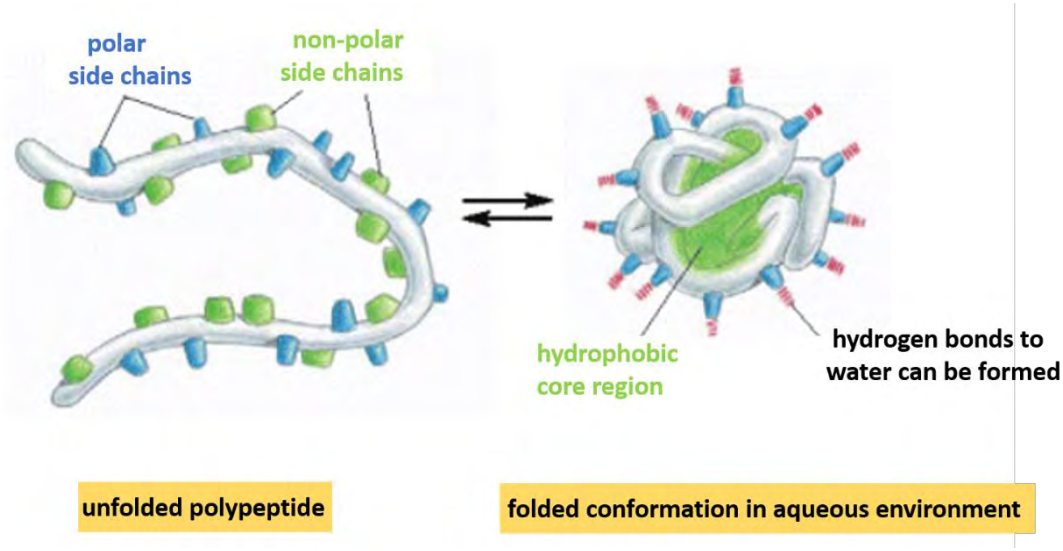

Figure 1.26 Schematic representation of the protein folding process in aqueous environment. Redrawn from [126]

What is the source of the PBAPs? As implied by using the word "dust", the Earth's landmass is a very potent producer of all types of aerosols, including PBAPs. However, given the surface of the oceans and their role for the climate, emissions from the oceans do play a role, too. Sea-spray aerosol is produced by bubble bursting [104], [105] (figure 1.28), and organic material from the sea surface microlayer can concentrate in sub-micrometer film droplets [128]. The organic matter contains PBAPs since the ocean is a habitat for a variety of organisms, and also very rich in bacteria and viruses.

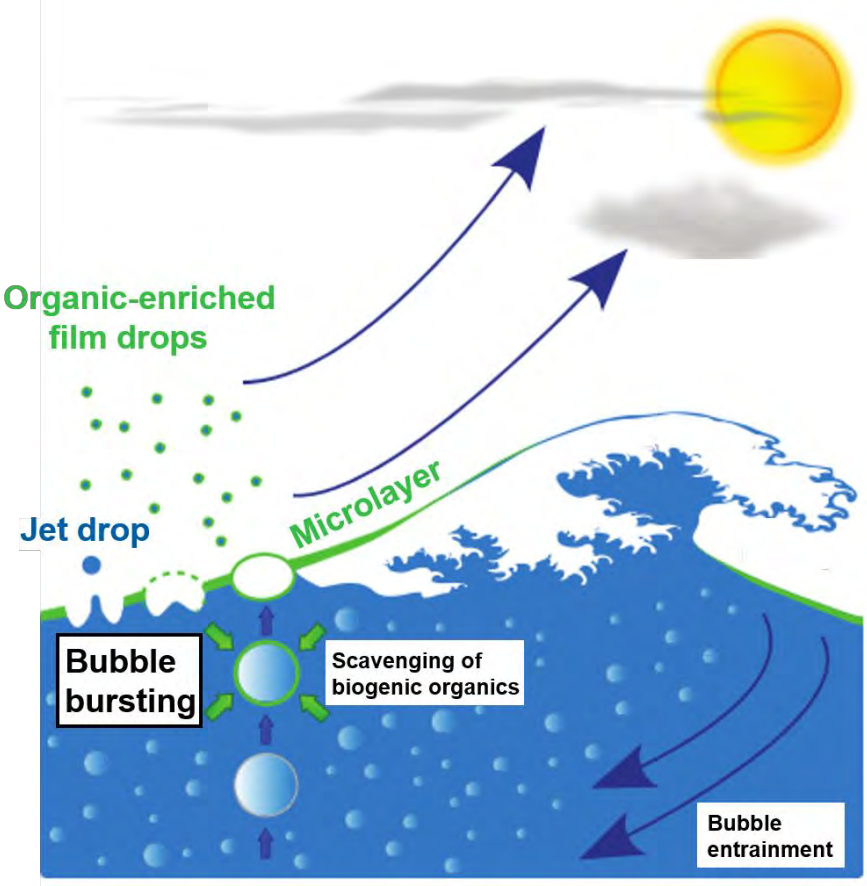

Figure 1.27. Sea-spray aerosol particles enriched in organic material are generated when bubbles burst at the air–sea interface. Redrawn from [129].

The role of bacteria and viruses is little known. Marine particles from the Southern Ocean have been suggested to play a considerable role in glaciation of mixed-phase clouds in this region by *Bigg* already in 1967 [130], and later by *Rosinski et al.* in 1986 [131]. But only in recent years marine INPs were tested systematically. For example, the planktonic diatom species *Thalassiosira pseudonana* increases the freezing temperature of water and salt water [132], phytoplankton cell exudates from the sea-surface microlayer can nucleate ice [129], and organic-coated sea salt is a rather common type of INP [133].

1.4. The geo- and astrophysical relevance of ice

Water ice is not restricted to Earth. Indeed, observations of interstellar clouds show that the building blocks of water, hydrogen and oxygen, are some of the most abundant

elements in the Universe. In the following, some examples for ice in our solar system are discussed.

The geophysics of ice was already touched at the beginning of this chapter. Although ice is spread over all continents (and the oceans), two giant ice sheets contain more than 99 % of the freshwater ice on Earth: The Antarctic ice sheet extends almost 14 million km (even larger area than whole Europe, which extends about 10 million km), while the Greenland ice sheet extends about 1.7 million km , covering most of the island of Greenland. The sheets contain enormous quantities of frozen water. If the Greenland ice sheet and the Antarctic ice sheet were to melt, the sea level would rise about 6 m and 57 m, respectively. The influence on the climate, but also on the weather is substantial; for instance, large high-altitude plateaus on the ice caps alter storm tracks and create cold downslope winds.

Both ice sheets are in contact with air of low humidity, based on temperatures well below those of most glaciers on other continents. This means that sublimation is here of special relevance. The sublimation rate (and the redeposition by snow) ultimately determines whether ice fields can exist at all.

The same argument applies to ice reservoirs on the Moon, and on other planets and their moons. Some of these reservoirs, for example the closest one to Earth, on the Moon, are probably small, and poorly characterized. The situation is much better for Mars with its large polar ice caps. For both Moon and Mars, water from ice reservoirs might be essential for running a permanently inhabited station.

1.4.1. Excursus: Ice on Mars

Mars is the only planet that could permit a landing mission with today's space technology. A certain similarity of the conditions and landscapes on Mars with those in the Arctic and Antarctic on Earth has already spurred mission simulations. However, the atmosphere on Mars has a pressure of merely around 600 Pa, and it is mainly composed of CO_2. It contains only 0.05% water (Earth: around 1 %). This does not allow (pure) liquid water to exist, but Mars is the only other planet that features surface ice (see figure 1.28).

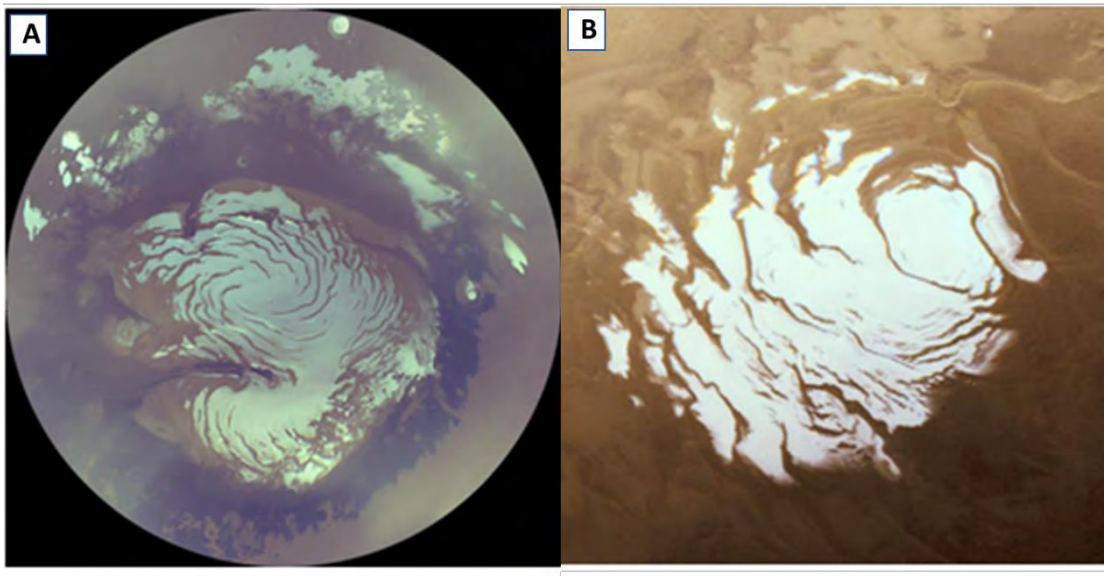

Figure 1.28. A) The North Polar Layered Deposits (PLD) on Mars. The white is water ice. **B)** The South Polar Layered Deposits (PLD) on Mars. The white is CO_2 ice, under which water ice is located. Source: https://www.nasa.gov/mission_pages/mars/images/index.html

Observations and measurements from satellites have shown that in the present climate on Mars, water mainly exists in large ice caps at the poles, the Polar Layered Deposits (PLD). There is also permafrost in the mid- and high latitudes, and there are frost patches and ancient glaciers, scattered all over the surface of the planet, but the two PLDs are currently the largest known water reservoirs on the planet. The North PLD (see figure 1.28.A) has a diameter of around 1000 km and the South PLD (see figure 1.28. B) is around 1500 km, comparable to the size of the Greenland ice sheet on Earth. Both PLDs consist of layers of water ice, dust and CO_2 ice.

Each PLD has a distinctive upper layer: in the North, this layer consists of water ice, which covers the underlying deposits. In the south, it consists of a layer of CO_2 ice with a thickness of several meters that only covers a small part of the underlying water ice, which is else covered by a layer of dust. This makes the South PLD appear much smaller than it actually is. The atmosphere is quite dusty, it contains cirrus-like ice (water and CO2) clouds. Ice can rain down on Mars, and the PLDs partially sublimate in their respective summers - this could be seen as analogous to the equilibrium between snow and sublimation on Earth, and to the seasons

In contrast to the ice-covered areas at high latitudes, the glaciers on the low latitudes do not originate from the current climate period, since the temperatures currently are too high for glaciers to form. They are remnants from older periods with different climate conditions caused by shifts in the rotation axis of the planet. The ice is now stored underneath a layer of dust and rocks that protects it from sublimation or melting, despite elevated temperatures on the surface. Even for the exposed North polar cap, a sublimation rate of merely 5 cm/year has recently been reported [134].

The Martian ground ice is deposited inside the porous soil in various depths, mainly depending on the latitude. In some areas at high latitude, around 50% of the mass in the underground is ice, and the ground ice lies very close to the surface. The origin of the ground ice is still being discussed in the scientific community. Many theories consider the origin of the ice as a combination of frozen ancient oceans, upwelling from subsurface water reservoirs, and the ice being deposited under current climate conditions, where water is exchanged with the other water reservoirs through the atmosphere.

1.4.2. Excursus: Ice on three moons

The existence of water on the Moon has been debated for well over a hundred years and at least three explanations for its origin have been formulated [135]. The water could be primordial, existing since the Moon formed and now trapped in the regolith; it could be deposited when icy comets strike the Moon; or it could form when solar-wind protons interact with oxygen in the minerals near the Moon’s surface.

The latest results based on the analysis of debris following an impact on the lunar surface provide a proof for the presence of water [136], but ice has not yet been detected [4]. The reservoirs are much smaller than on Mars, and because of the low atmospheric pressure (comparable to ultrahigh vacuum) restricted to cold areas inside permanently shaded craters. However, in principle they could be used for a permanent station.

Leaving our "near vicinity" in the solar system, we encounter the outer hydrogen planets. On these planets, ice is likely present in clouds and very deep in the cores, but many of their moons do contain surface ice. Moreover, the surfaces of at least two moons do not simply contain ice, but they are completely *dominated* by very thick ice layers.

First, Jupiter's moon Europa is slightly smaller than our own Moon with a diameter of around 3000 km. This moon is covered by a several kilometre-thick ice layer, dominated by beautiful ridges and cracks, and probably lying on top of a deep-water ocean (see figure 1.29)

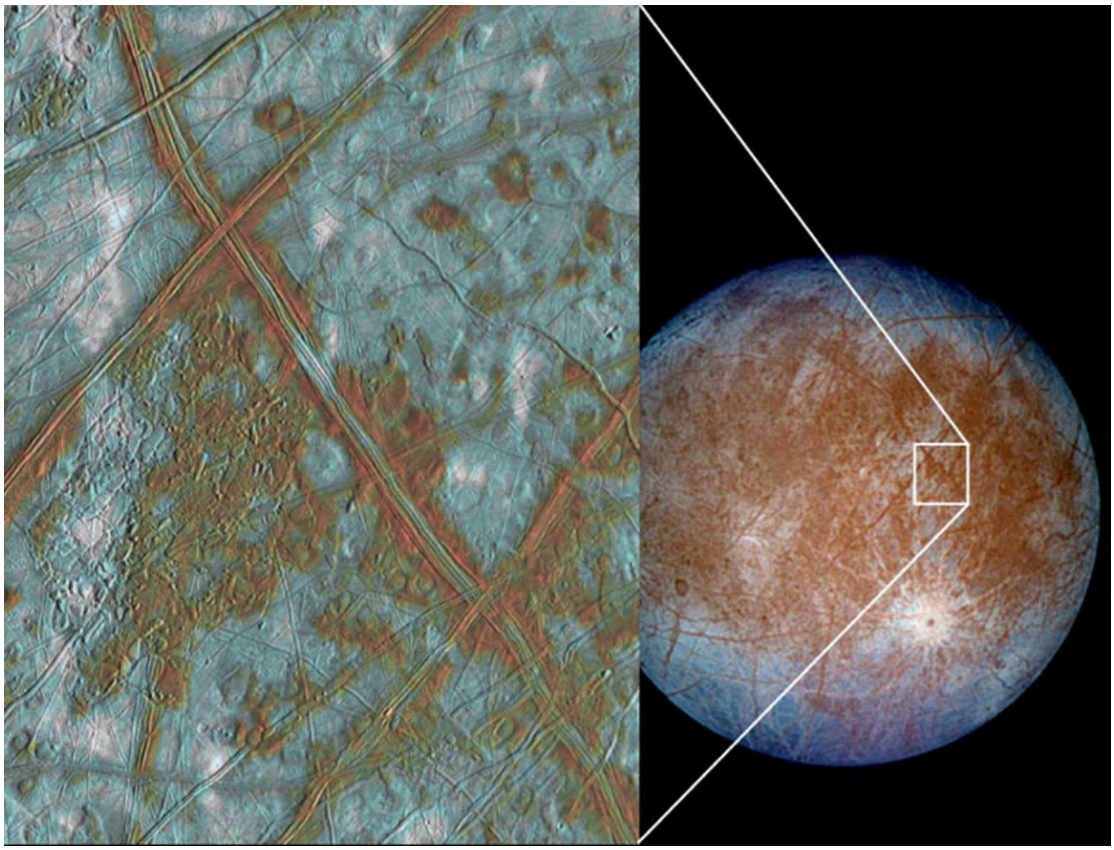

Figure 1.29. The icy surface of Jupiter's moon Europa is filled with beautiful ridges and cracks, probably created by tidal stresses, maybe in connection with a subsurface ocean. Source: https://solarsystem.nasa.gov/planets/jupiter/galleries

Second, the Saturn moon Enceladus is much smaller, with a diameter of around 500 km. It also has an icy surface with various cracks and ridges, but the most interesting features are the geysers in the south polar area (see figure 1.30). The geysers are powered by so-called cryovolcanoes that work exactly like "real" volcanoes, just with ice instead of magma. In the cryovolcanoes, the ice deep below the surface is heated by tidal forces and turned into vapour that expands to form a geyser or an explosion. The geysers eject ice particles 500 km into space.

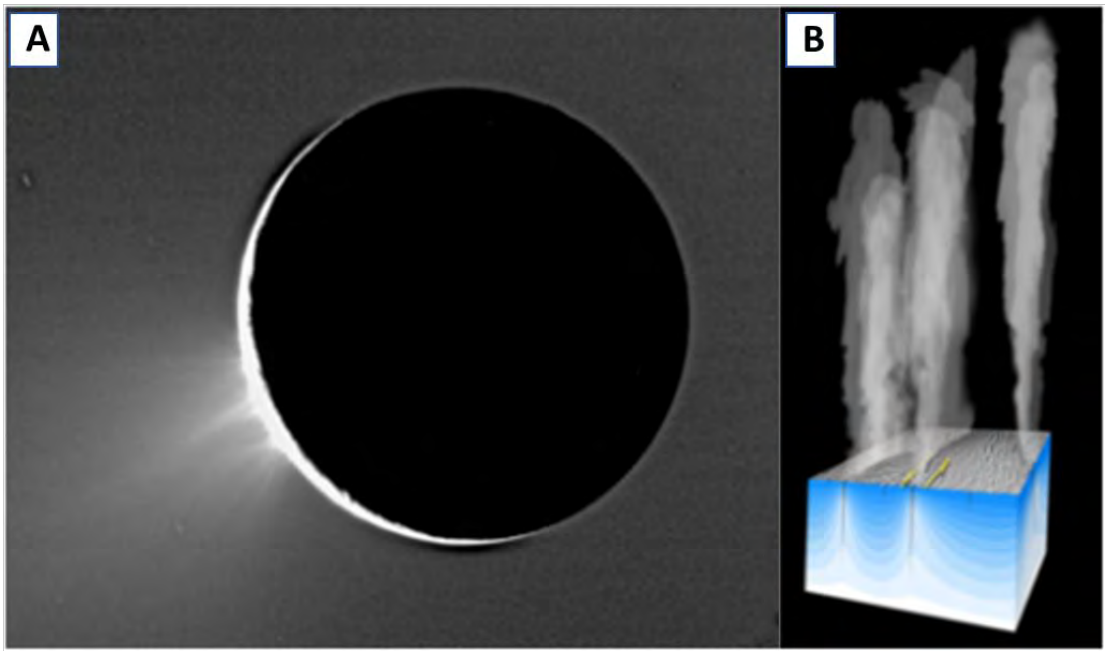

Figure 1.30. A) Saturn's icy moon Enceladus has immense cryo-volcanism. This can be seen on the lower left side of the moon. **B)** Schematic drawing describing how the cryo-volcanism works. Source: https://solarsystem.jpl.nasa.gov/galleries/search&target=enceladus

1.5 References

[1] X. Kong, “Molecular Investigations of Atmospherically Relevant Interface Processes Ice Formation and Water Accommodation on Ice and Organic Surfaces,” 2014.

[2] Aristotle, *Meteorologica, translated by H.D.P. Lee (harvard U.P., LOndon, 1962), Book I, Chap.XII, pp.85-87*.

[3] F. Stradling, “Physical section - Recent advances in the physics of water,” *J. Frankl. Inst. 152*, pp. 257–268, 1901.

[4] T. Bartels-Rausch *et al.*, “Ice structures, patterns, and processes: A view across the icefields,” *Rev. Mod. Phys.*, vol. 84, no. 2, pp. 885–944, 2012.

[5] R. Rosenberg, “Why is Ice Slppery,” *Phys. Today*, vol. 58, no. 12, pp. 50–55, 2005.

[6] F. P. Bowden and T. P. Hughes, “The Mechanism of Sliding on Ice and Snow,” *Proc. R. Soc. A Math. Phys. Eng. Sci.*, vol. 172, no. 949, pp. 280–298, 1939.

[7] M. Faraday, “Michael Faraday’s Diary,” no. 79. 1833.

[8] Y. Li and G. A. Somorjai, “Surface Premelting of Ice,” *J. Phys. Chem. C*, vol. 111, no. 27, pp. 23–36, 2007.

[9] I. Firth, “Cooler? ”, *Phys. Educ.*, vol. 6, no. 32, 1971.

[10] E. B. Mpemba and D. G. Osborne, “Cool?,” *Phys. Educ.*, vol. 4, 1969.

[11] M. Jeng, “The Mpemba effect: When can hot water freeze faster than cold?,” *Am. J. Phys.*, vol. 74, no. 6, p. 514, 2006.

[12] G. Ritter, “The Growth and Morphology of Small Ice Crystals in a Diffusion Chamber,” 2014.

[13] A. Wexler, “Vapor pressure formulation for ice,” *J. Res. Natl. Bur. Stand.*, vol. 81A, no. February, p. 5, 1977.

[14] D. M. Murphy and T. Koop, “Review of the vapour pressures of ice and

supercooled water for atmospheric applications," *Q. J. R. Meteorol. Soc.*, vol. 131, no. 608, pp. 1539–1565, 2005.

[15] A. Korolev, "Limitations of the Wegener–Bergeron–Findeisen Mechanism in the Evolution of Mixed-Phase Clouds," *J. Atmos. Sci.*, vol. 64, pp. 3372–3375, 2007.

[16] J. Dash, "History of the search for continuous melting," *Rev. Mod. Phys.*, vol. 71, no. 5, pp. 1737–1743, 1999.

[17] J. G. Dash, H. Fu, and J. S. Wettlaufer, "The premelting of ice and its environmental consequences," *Reports Prog. Phys.*, vol. 58, no. 1, pp. 115–167, 1995.

[18] A. Michaelides and B. Slater, "Melting the ice one layer at a time," *Proc. Natl. Acad. Sci.*, vol. 114, no. 2, p. 201619259, 2017.

[19] M. L. before the R. I. reported in the A. 1850 Faraday, "Lecture before the Royal Institution reported in the Athaneum," no. 640. 1850.

[20] M. Faraday, "Faraday, M., 10, 152.," in *Proc. R. Soc. London*, 1860, vol. 10, no. 152.

[21] I. Golecki and C. Jaccard, "Intrinsic surface disorder in ice near the melting point," *J. Phys. C Solid State Phys.*, vol. 11, pp. 4229–4237, 1978.

[22] R. R. Gilpin, "Wire regelation at low temperatures," *J. Colloid Interface Sci.*, vol. 77, no. 2, pp. 435–448, 1980.

[23] M. Elbaum, S. G. Lipson, and J. G. Dash, "Optical study of surface melting on ice," *J. Cryst. Growth*, vol. 129, no. 3–4, pp. 491–505, 1993.

[24] V. Sadtchenko and G. E. Ewing, "Interfacial melting of thin ice films: An infrared study," *J. Chem. Phys.*, vol. 116, no. 11, pp. 4686–4697, 2002.

[25] A. Döppenschmidt and H. J. Butt, "Measuring the thickness of the liquid-like layer on ice surfaces with atomic force microscopy," *Langmuir*, vol. 16, no. 16, pp. 6709–6714, 2000.

[26] D. Beaglehole and D. Nason, "Transition layer on the surface on ice," *Surf. Sci.*,

vol. 96, pp. 357–363, 1980.

[27] H. Bluhm, D. F. R. a. N. K. Ogletree, C. Fadley, Z. Hussain, and M. Salmeron, "The premelting of ice studied with photoelectron spectroscopy," *J. Phys. Condens. Matter*, vol. 14, no. 8, pp. L227--L233, 2002.

[28] B. Pittenger *et al.*, "Premelting at ice-solid interfaces studied via velocity-dependent indentation with force microscope tips," *Phys. Rev. B*, vol. 63, no. 13, p. 134102, 2001.

[29] Y. Furukawa and H. Nada, "Anisotropic surface melting of an ice crystal and its relationship to growth forms," *J. Phys. Chem. B*, vol. 101, no. 32, pp. 6167–6170, 1997.

[30] M. P. Goertz, X. Y. Zhu, and J. E. Houston, "Exploring the liquid-like layer on the ice surface," *Langmuir*, vol. 25, no. 12, pp. 6905–6908, 2009.

[31] R. Ohnesorge, H. Löwen, and H. Wagner, "Density functional theory of crystal-fluid interfaces and surface melting," *Physical Review E*, vol. 50, no. 6. pp. 4801–4809, 1994.

[32] A. Landa, P. Wynblatt, H. Hakkinen, N. Barnett, and U. Landman, "Equilibrium interphase interfaces and premelting of the Pb(110) surface," *Phys. Rev. B*, vol. 51, no. 16, 1995.

[33] J. M. Phillips, "Layer by Layer Melting of Argon Films on Graphite - a Computer-Simulation Study," *Phys. Lett. A*, vol. 147, no. 1, pp. 54–58, 1990.

[34] H. Hakkinen and M. Manninen, "Computer simulation of disordering and premelting of low-index faces of copper," *Phys. Rev. B*, vol. 46, no. 3, 1992.

[35] H. Löwen, "Melting, freezing and colloidal suspensions," *Phys. Rep.*, vol. 237, no. 5, pp. 249–324, 1994.

[36] M. M. Conde, C. Vega, and A. Patrykiejew, "The thickness of a liquid layer on the free surface of ice as obtained from computer simulation," *J. Chem. Phys.*, vol. 129, no. 1, 2008.

[37] D.-M. Zhu, D. Pengra, and J. G. Dash, "Edge melting in two-dimensional solid

films," *Phys. Rev. B*, vol. 37, no. 10, 1988.

[38] T. Bartels-Rausch *et al.*, "A review of air-ice chemical and physical interactions (AICI): Liquids, quasi-liquids, and solids in snow," *Atmos. Chem. Phys.*, vol. 14, no. 3, pp. 1587–1633, 2014.

[39] C. L. Bishop *et al.*, "On thin ice: surface order and disorder during pre-melting," *Faraday Discuss.*, vol. 141, pp. 9–30, 2009.

[40] K. Bolton and J. B. C. Pettersson, "A Molecular Dynamics Study of the Long-Time Ice Ih Surface Dynamics," *J. Phys. Chem. B*, vol. 104, no. 7, pp. 1590–1595, 2000.

[41] R. G. Pereyra and M. A. Carignano, "Ice nanocolumns: A molecular dynamics study," *J. Phys. Chem. C*, vol. 113, no. 29, pp. 12699–12705, 2009.

[42] S. Neshyba, E. Nugent, M. Roeselová, and P. Jungwirth, "Molecular dynamics study of ice-vapor interactions via the quasi-liquid layer," *J. Phys. Chem. C*, vol. 113, no. 11, pp. 4597–4604, 2009.

[43] T. D. Shepherd, M. A. Koc, and V. Molinero, "The quasi-liquid layer of ice under conditions of methane clathrate formation," *J. Phys. Chem. C*, vol. 116, no. 22, pp. 12172–12180, 2012.

[44] W. Pfalzgraff, S. Neshyba, and M. Roeselova, "Comparative molecular dynamics study of vapor-exposed basal, prismatic, and pyramidal surfaces of ice," *J. Phys. Chem. A*, vol. 115, no. 23, pp. 6184–6193, 2011.

[45] I. Gladich, W. Pfalzgraff, O. Maršálek, P. Jungwirth, M. Roeselová, and S. Neshyba, "Arrhenius analysis of anisotropic surface self-diffusion on the prismatic facet of ice," *Phys. Chem. Chem. Phys.*, vol. 13, no. 44, p. 19960, 2011.

[46] M. A. Sánchez *et al.*, "Experimental and theoretical evidence for bilayer-by-bilayer surface melting of crystalline ice," *Proc. Natl. Acad. Sci.*, p. 201612893, 2016.

[47] F. P. Bowden, "Friction on Snow and Ice," *Proc. R. Soc. London. Ser. A Math. Phys. Eng. Sci.*, vol. 217, no. 1131, pp. 462–478, 1953.

[48] D. C. B. Evans, J. F. Nye, and K. J. Cheeseman, “The kinetic friction of ice,” *Proc. R. Soc. Lond. A*, vol. 347, pp. 493–512, 1976.

[49] S. C. Colbeck, “The kinetic friction of snow,” *J. Glaciol.*, vol. 34, no. 116, pp. 78–86, 1988.

[50] S. C. Colbeck, “The layered character of snow covers,” *Rev. Geophys.*, vol. 29, no. 1, pp. 81–96, 1991.

[51] B. N. J. Persson, “Ice friction: Role of non-uniform frictional heating and ice premelting,” *J. Chem. Phys.*, vol. 143, no. 22, pp. 1–9, 2015.

[52] G. J. Turner and C. D. Stow, “The quasi-liquid film on ice evidence from , and implications for contact charging events,” *Philos. Mag.*, vol. 49, no. 4, 1984.

[53] M. B. Baker and J. G. Dash, “Mechanism of charge transfer between colliding ice particles in thunderstorms,” *J. Geophys. Res. Atmos.*, vol. 99, no. D5, pp. 10621–10626, 1994.

[54] J. Abatt, K.D. Beyer, A. F. Fucaloro, P. J. Wooldridge, R. Zhang, and Molina.M.J., “Interaction of HCl Vapor with Water-ice: Implications for the Stratosphere,” *J. Geophys. Res.*, vol. 97, pp. 819–826, 1992.

[55] H. Fukazawa, K. Sugiyama, S. Mae, H. Narita, and T. Hondoh, “Acid ions at triple junction of Antarctic ice observed by Raman scattering,” *Geophys. Res. Lett.*, vol. 25, no. 15, pp. 2845–2848, 1998.

[56] R. Mulvaney, E. W. Wolff, and K. Oates, “Sulphuric acid at grain boundaries in Antarctic ice,” *Nature*, vol. 331, no. 6153, pp. 247–249, 1988.

[57] J. F. Nye, “The geometry of water veins and nodes in polycrystalline ice,” *J. Glaciol.*, vol. 35, no. 119, pp. 17–22, 1989.

[58] K. Jacobson, E. D. Sheets, and R. Simson, “Revisiting the fluid mosaic model of membranes.,” *Science*, vol. 268, no. 5, pp. 1441–1442, 1995.

[59] A. Einstein, “‘The motion of elements suspended in static liquids as claimed in the molecular kinetic theory of heat.,’” *Ann. d. Phys.*, vol. 322, no. 8, pp. 549–560, 1905.

[60] M. J. Saxton, “Anomalous diffusion due to obstacles: a Monte Carlo study.,” *Biophys. J.*, vol. 66, no. 2 Pt 1, pp. 394–401, 1994.

[61] P. F. F. Almeida and W. L. C. Vaz, “Lateral diffusion in membranes.,” in *Handbook of Biological Physics*, Elsevier B.V., 1995.

[62] M. J. Saxton, “A Biological Interpretation of Transient Anomalous Subdiffusion. I. Qualitative Model,” *Biophysj*, vol. 92, no. 4, pp. 1178–1191, 2007.

[63] X. Michalet, “Mean square displacement analysis of single-particle trajectories with localization error: Brownian motion in an isotropic medium,” *Phys. Rev. E - Stat. Nonlinear, Soft Matter Phys.*, vol. 82, no. 4, pp. 1–13, 2010.

[64] M. J. Saxton, “Single-particle tracking: the distribution of diffusion coefficients.,” *Biophys. J.*, vol. 72, no. 4, pp. 1744–53, 1997.

[65] G. J. Schütz, H. Schindler, and T. Schmidt, “Single-molecule microscopy on model membranes reveals anomalous diffusion.,” *Biophys. J.*, vol. 73, no. 2, pp. 1073–1080, 1997.

[66] G. Dunderdale, S. Ebbens, P. Fairclough, and J. Howse, “Importance of particle tracking and calculating the mean-squared displacement in distinguishing nanopropulsion from other processes,” *Langmuir*, vol. 28, no. 30, pp. 10997–11006, 2012.

[67] D. H. Rasmussen, “Clustering in supercooled water,” *J. Chem. Phys.*, vol. 59, no. 9, p. 5003, 1973.

[68] G. M. Marion and S. D. Jakubowski, “The compressibility of ice to 2.0 kbar,” *Cold Reg. Sci. Technol.*, vol. 38, no. 2–3, pp. 211–218, 2004.

[69] V. F. Petrenko and R. W. Whitworth, *Physics of Ice*. 1999.

[70] S. a. Clough, Y. Beers, G. P. Klein, and L. S. Rothman, “Dipole moment of water from Stark measurements of H2O, HDO, and D2O,” *J. Chem. Phys.*, vol. 59, no. 5, pp. 2254–2259, 1973.

[71] A. Mohandesi, “Molecular-Dynamics Simulations of Ice Growth from the Vapour Phase: Demonstration of Proof of Principle,” 2015.

[72] P. G. Debenedetti, “Supercooled and glassy water,” *J. Phys. Condens. Matter*, vol. 15, no. 45, pp. R1669–R1726, 2003.

[73] P. V. Hobbs, *Ice physics*, Oxford Uni. 2010.

[74] V. F. Petrenko and R. W. Whitworth, *Physics of ice*, Oxford Uni. 1999.

[75] W. C. Pfalzgraff, R. M. Hulscher, and S. P. Neshyba, “Scanning electron microscopy and molecular dynamics of surfaces of growing and ablating hexagonal ice crystals,” *Atmos. Chem. Phys. Discuss.*, vol. 9, no. 5, pp. 20739–20763, 2009.

[76] M. P. Bailey and J. Hallett, “A Comprehensive Habit Diagram for Atmospheric Ice Crystals: Confirmation from the Laboratory, AIRS II, and Other Field Studies,” *J. Atmos. Sci.*, vol. 66, no. 9, pp. 2888–2899, 2009.

[77] C. Takahashi and M. Mori, “Growth of snow crystals from frozen water droplets,” *Atmos. Res.*, vol. 82, no. 1–2, pp. 385–390, 2006.

[78] M. Bailey and J. Hallett, “Growth Rates and Habits of Ice Crystals between -20o℃ and -70o℃,” *J. Atmos. Sci.*, vol. 61, pp. 514–544, 2004.

[79] J. Hallett and B. J. Mason, “The Influence of Temperature and Supersaturation on the Habit of Ice Crystals Grown from the Vapour,” *Proc. R. Soc. A*, vol. 247, no. 1251, pp. 440–453, 1958.

[80] K. G. Libbrecht, “The physics of snow crystals,” *Rep. Prog. Phys.*, vol. 68, pp. 855–895, 2005.

[81] K. G. Libbrecht, “Growth rates of the principal facets of ice between -10 °C and -40 °C,” vol. 247, pp. 530–540, 2003.

[82] D. Lamb and W. D. Scott, “The Mechanism of Ice Crystal Growth and Habit Formation,” *Journal of the Atmospheric Sciences*, vol. 31, no. 2. pp. 570–580, 1974.

[83] K. G. Libbrecht, “A Critical Look at Ice Crystal Growth Data,” *eprint arXiv:cond-mat/0411662*, p. 21, 2004.

[84] T. Sei and T. Gonda, "The growth mechanism and the habit change of ice crystals growing from the vapor phase," *J. Cryst. Growth*, vol. 94, no. 3, pp. 697–707, 1989.

[85] K. G. Libbrecht and M. E. Rickerby, "Measurements of surface attachment kinetics for faceted ice crystal growth," *J. Cryst. Growth*, vol. 377, pp. 1–8, 2013.

[86] G. W. Bryant, J. Hallett, and B. J. Mason, "The epitaxial growth of ice on single-crystalline substrates," *J. Phys. Chem. Solids*, vol. 12, no. 2, pp. 189–195, 1960.

[87] D. Lamb and J. Verlinde, *Physics and Chemistry of Clouds*. 2011.

[88] R. Mirza, "Cloud Microphysics," no. 1966, pp. 69–106, 2010.

[89] A. Welti, "Experimental Studies on Deposition and Immersion Mode Ice Nucleation on Mineral Dust," no. 20538, pp. 1–149, 2012.

[90] H. R. Pruppacher and J. D. Klett, *Microphysics of clouds and precipitation*, 2nd editio. New York, Boston, Dordrecht, London, Moscow, 1997.

[91] K. Sassen, "Indirect climate forcing over the western US from Asian dust storms," *Geophys. Res. Lett.*, vol. 29, no. MARCH, pp. 455–456, 2002.

[92] E. J. Langham and B. J. Mason, "The Heterogeneous and Homogeneous Nucleation of Supercooled Water," *Proc. R. Soc. Lond. A. Math. Phys. Sci.*, vol. 247, no. 1251, pp. 493–504, 1958.

[93] G. Vali, "Sizes of Atmospheric Ice Nuclei," *Nature*, vol. 212, pp. 384–385.

[94] N. H. Fletcher, "Active Sites and Ice Crystal Nucleation," *Journal of the Atmospheric Sciences*, vol. 26, no. 6. pp. 1266–1271, 1969.

[95] C. Marcolli, S. Gedamke, T. Peter, and B. Zobrist, "Efficiency of immersion mode ice nucleation on surrogates of mineral dust," *Atmos. Chem. Phys. Discuss.*, vol. 7, no. 4, pp. 9687–9716, 2007.

[96] C. Marcolli, "Deposition nucleation viewed as homogeneous or immersion freezing in pores and cavities," *Atmos. Chem. Phys.*, vol. 14, no. 4, pp. 2071–2104, 2014.

[97] D. Niedermeier *et al.*, “Heterogeneous ice nucleation: Exploring the transition from stochastic to singular freezing behavior,” *Atmos. Chem. Phys.*, vol. 11, no. 16, pp. 8767–8775, 2011.

[98] E. K. Bigg, “The formation of atmospheric ice crystals by the freezing of droplets,” *Q. J. R. Meteorol. Soc.*, vol. 79, no. 342, pp. 510–519, 1953.

[99] R. Rogers and M. Yau, *A Short Course in Cloud Physics*. Pergamon, Tarrytown, NY, 1989.

[100] C. Hoose and O. Möhler, “Heterogeneous ice nucleation on atmospheric aerosols: A review of results from laboratory experiments”, *Atmos. Chem. Phys.*, vol. 12, no. 20. 2012.

[101] R. A. Shaw, A. J. Durant, and Y. Mi, “Heterogeneous surface crystallization observed in undercooled water,” *J. Phys. Chem. B*, vol. 109, no. 20, pp. 9865–9868, 2005.

[102] T. Koop, B. Luo, A. Tsias, and T. Peter, “Water activity as the determinant for homogeneous ice nucleation in aqueous solutions,” *Nature*, vol. 406, no. 6796, pp. 611–4, 2000.

[103] A. Ansmann *et al.*, “Influence of Saharan dust on cloud glaciation in southern Morocco during the Saharan Mineral Dust Experiment,” *J. Geophys. Res. Atmos.*, vol. 113, no. 4, pp. 1–16, 2008.

[104] H. Wex *et al.*, “Intercomparing different devices for the investigation of ice nucleating particles using Snomax as test substance,” *Atmos. Chem. Phys.*, vol. 15, no. 3, pp. 1463–1485, 2015.

[105] G. Vali, P. J. DeMott, O. Möhler, and T. F. Whale, “Technical Note: A proposal for ice nucleation terminology,” *Atmos. Chem. Phys.*, vol. 15, no. 18, pp. 10263–10270, 2015.

[106] Y. Boose, “Field and laboratory studies of atmospheric ice nucleating particles,” 2016.

[107] M. Hallquist *et al.*, “The formation, properties and impact of secondary organic

aerosol: current and emerging issues," *Atmos. Chem. Phys. Atmos. Chem. Phys.*, vol. 9, no. February, pp. 5155–5236, 2009.

[108] W. C. Hinds, "Aerosol technology," *J. Aerosol Sci.*, vol. 14, no. 2, p. 175, 1999.

[109] R. Duce and N. Tindale, "Chemistry and biology of iron and other trace metals," *Limnol. Oceanogr. Ocanography*, vol. 36, no. 8, pp. 1715–1726, 1991.

[110] P. W. Boyd and M. J. Ellwood, "The biogeochemical cycle of iron in the ocean," *Nat. Geosci.*, vol. 3, no. 10, pp. 675–682, 2010.

[111] S. Twomey, "The Influence of Pollution on the Shortwave Albedo of Clouds," *Journal of the Atmospheric Sciences*, vol. 34, no. 7. pp. 1149–1152, 1977.

[112] B. A. Albrecht, "Fractional Cloudiness," *Science Reports.*, vol. 245, pp. 1227–1230, 1989.

[113] P. E. Taylor, R. C. Flagan, A. G. Miguel, R. Valenta, and M. M. Glovsky, "Birch pollen rupture and the release of aerosols of respirable allergens," *Clin. Exp. Allergy*, vol. 34, no. 10, pp. 1591–1596, 2004.

[114] J. A. Bernstein *et al.*, "Health effects of air pollution," *J. Allergy Clin. Immunol.*, vol. 114, no. 5, pp. 1116–1123, 2004.

[115] C. A. Pope *et al.*, "Lung cancer, cardiopulmonary mortality, and long-term exposure to fine particulate air pollution.," *JAMA*, vol. 287, no. 9, pp. 1132–41, 2002.

[116] "IGAP: The International Global Aerosol Program, Deepak Publishing, Hampton, VA, 1992."

[117] V. R. Després *et al.*, "Primary biological aerosol particles in the atmosphere: A review," *Tellus, Ser. B Chem. Phys. Meteorol.*, vol. 64, no. 1, 2012.

[118] R. C. Schnell and G. Vali, "Biogenic Ice Nuclei: Part I. Terrestrial and Marine Sources," *Journal of the Atmospheric Sciences*, vol. 33, no. 8. pp. 1554–1564, 1976.

[119] D. G. Georgakopoulos *et al.*, "Microbiology and atmospheric processes:

biological, physical and chemical characterization of aerosol particles," *Biogeosciences Discuss.*, vol. 5, no. 2, pp. 1469–1510, 2008.

[120] K. Diehl, S. Matthias-Maser, R. Jaenicke, and S. K. Mitra, "The ice nucleating ability of pollen: Part II. Laboratory studies in immersion and contact freezing modes," *Atmos. Res.*, vol. 61, pp. 125–133, 2002.

[121] S. Augustin *et al.*, "Immersion freezing of birch pollen washing water," *Atmos. Chem. Phys.*, vol. 13, no. 21, pp. 10989–11003, 2013.

[122] B. G. Pummer, H. Bauer, J. Bernardi, S. Bleicher, and H. Grothe, "Suspendable macromolecules are responsible for ice nucleation activity of birch and conifer pollen," *Atmos. Chem. Phys.*, vol. 12, no. 5, pp. 2541–2550, 2012.

[123] R. Iannone, D. I. Chernoff, A. Pringle, S. T. Martin, and A. K. Bertram, "The ice nucleation ability of one of the most abundant types of fungal spores found in the atmosphere," *Atmos. Chem. Phys.*, vol. 11, no. 3, pp. 1191–1201, 2011.

[124] A. V. Kajava and S. E. Lindow, "A Model of the Three-dimensional Structure of Ice Nucleation Proteins," *Journal of Molecular Biology*, vol. 232. pp. 709–717, 1993.

[125] W. Yang, S. Elankumaran, and L. C. Marr, "Concentrations and size distributions of airborne influenza A viruses measured indoors at a health centre, a day-care centre and on aeroplanes.," *J. R. Soc. Interface*, vol. 8, no. 61, pp. 1176–84, 2011.

[126] P. W. B. Alberts, A. Johnson, J. Lewis, M. Raff, K. Roberts, *Molecular Biology of The Cell*, 4th editio. Garland Science, New York, 2002.

[127] B. Gantt and N. Meskhidze, "The physical and chemical characteristics of marine primary organic aerosol: A review," *Atmos. Chem. Phys.*, vol. 13, no. 8, pp. 3979–3996, 2013.

[128] J. Y. Aller, M. R. Kuznetsova, C. J. Jahns, and P. F. Kemp, "The sea surface microlayer as a source of viral and bacterial enrichment in marine aerosols," *J. Aerosol Sci.*, vol. 36, no. 5–6, pp. 801–812, 2005.

[129] T. W. Wilson *et al.*, "A marine biogenic source of atmospheric ice-nucleating

particles," *Nature*, vol. 525, no. 7568, pp. 234–238, 2015.

[130] E. K. Bigg, "Cross Sections of Ice Nucleus Concentrations at Altitude over Long Paths," *Journal of the Atmospheric Sciences*, vol. 24, no. 2. pp. 226–229, 1967.

[131] J. Rosinski, P. L. Haagenson, C. T. Nagamoto, and F. Parungo, "Ice-forming nuclei of maritime origin," *J. Aerosol Sci.*, vol. 17, no. 1, pp. 23–46, 1986.

[132] D. A. Knopf, P. A. Alpert, B. Wang, and J. Y. Aller, "Stimulation of ice nucleation by marine diatoms," *Nat. Geosci.*, vol. 4, no. 2, pp. 88–90, 2011.

[133] D. A. Knopf *et al.*, "Journal of Geophysical Research: Atmospheres," pp. 365–381, 2014.

[134] C. S. Hvidberg and H. J. Zwally, "Sublimation of water from the north polar cap on Mars," Workshop "Mars Atmosphere Modelling and Observations" Granada, Spain, pp. 13–15, 2003.

[135] E. L. Andreas, "New estimates for the sublimation rate for ice on the Moon," *Icarus*, vol. 186, no. 1, pp. 24–30, 2007.

[136] A. Colaprete *et al.*, "Detection of water in the LCROSS ejecta plume.," *Science*, vol. 330, no. 6003, pp. 463–468, 2010.

Chapter 2:
Electron microscopy of ice deposition and sublimation

2.1 The Environmental Scanning Electron Microscope (ESEM)

Ice crystals are often probed by optical microscopy [1], but in this work scanning electron microscopy (SEM) was chosen as the imaging method. The advantage is the far greater resolution (<10 nm), compared to optical methods (μm range).

In standard SEM, an electron beam is scanned across the target, and the scattered electrons are collected for image formation. A high vacuum environment (10^{-3} Pa or lower) is necessary to allow the electron beam to reach the target, and specimens need to be coated to be electrically conducting, so any charge deposited by the imaging beam into the specimen can flow off. Strong electric fields build up otherwise and deflect the beam from the target, which distorts the generated image**.** Obviously, the pressure conditions are unsuitable for ice at most temperatures: Water ice reaches a vapor pressure of $5.5 \cdot 10^{-2}$ Pa, which might be just about permissible, only at -80°C [2]. For the temperature ranges of interest (above -80°C), the water vapor pressure is orders of magnitudes higher, see fig. 1.4 (chapter 1).

This problem was solved by Environmental scanning electron microscopy (ESEM). The essential difference to SEM is the ability to operate in a gas atmosphere in the sample chamber. Various commercial implementations have been available since the 1970s (SEM was pioneered by Ernst Ruska already in 1931), and imaging has been demonstrated up to 2700 Pa water vapour (Danilatos (1988)). In this thesis, a FEG (Field Emission Gun) ESEM (Quanta 250, FEI) was used for the experiments (see figure 2.1).

In order to work at non-vacuum conditions, the microscope is equipped with a series of pressure-limiting apertures inside the electron acceleration and focussing column (in-column PLAs) as shown in figure 2.2. A differential pumping system separates the different vacuum levels in the column from the low vacuum in the specimen chamber. This chamber must be especially well separated from the column because the water vapour pressure in the chamber is orders of magnitude higher than what can be tolerated in the column.

Figure 2.1. FEG (Field Emission Gun) ESEM Quanta 250. Top: Column (with cladding), middle: Specimen chamber, bottom: Vibration insulation (clad by grey front panel).

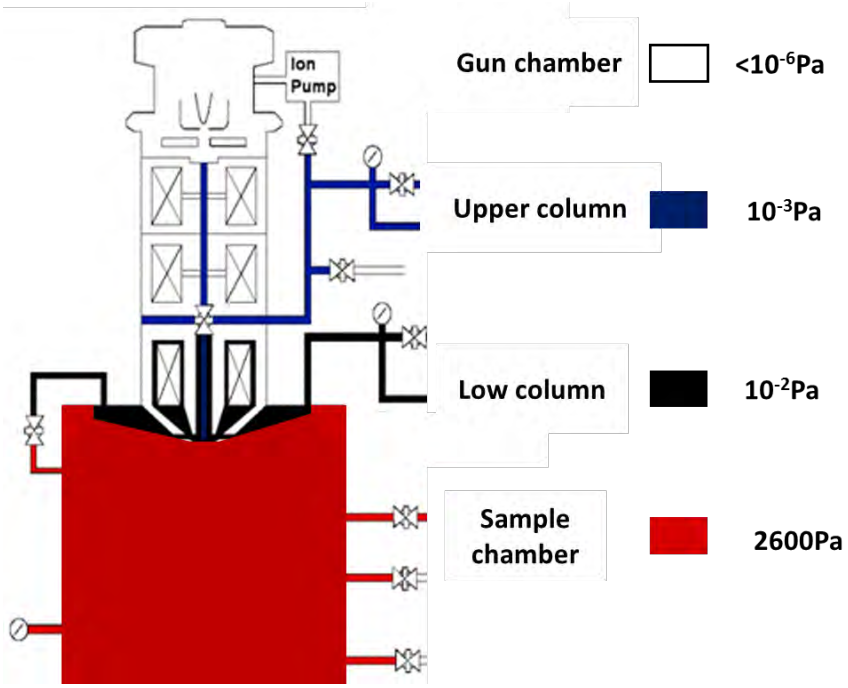

Figure 2.2. Vacuum stages in the ESEM. Black: Pole piece, bottom of the electron column. Redrawn from [5].

The in-column PLAs are discs with small holes in the centre. They are made sufficiently large to let the electron beam pass, but as small as practical to limit leakage from the next (lower) section.[3] The vacuum system consists of a turbo molecular pump (TMP, 250l/s) and two mechanical pre-vacuum pumps (PVP). This assures at the FEG (Field Emission Gun) a very good vacuum ($<10^{-6}$ Pa), at the top of the column $<10^{-3}$ Pa, and at the mid-portion of the column $<10^{-2}$ Pa, while in the specimen chamber up to 2600 Pa are possible (during venting for sample change even ambient pressure). ESEM requires to install the lowest pressure limiting aperture (PLA cone) manually at the bottom of the pole piece [4] (see figure 2.3).

Figure 2.3. PLA cone for the ESEM [2].

The ESEM is equipped with a range of detectors that can be operated at different vacuum conditions (see appendix I). Due to the presence of a gas, mainly water vapour, the principle of signal detection differs from that of a conventional SEM. The primary electron beam is very energetic, and it penetrates the water vapour, scanning across the surface of the sample. Secondary electrons are released from the surface of the sample, as they are in standard SEM, but they encounter water molecules once they leave the surface.

The water molecules, when hit by the secondary electrons, produce additional secondary electrons. The resulting cascade of electrons is accelerated toward the detector, and the positively charged water ions (having lost secondary electrons) are attracted towards the sample surface. Here they recombine with negative charge, and prevent the build-up of static charge on the sample. This process, illustrated in figure 2.4, allows to image insulating materials without applying a conductive coating.

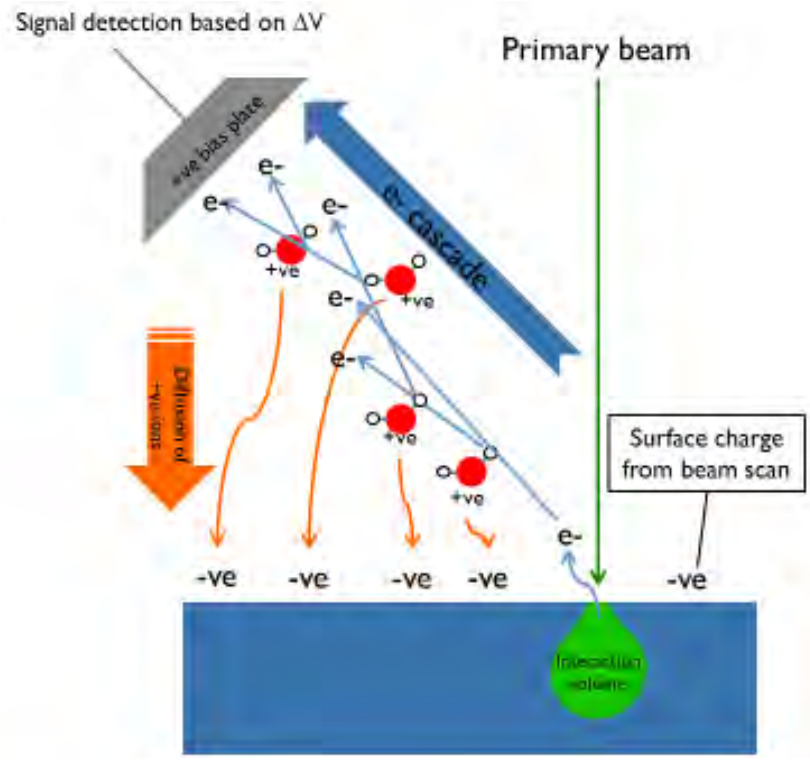

Figure 2.4. Detection principle in ESEM: Secondary electrons are created in the (microscale) interaction volume (green) of the primary beam with the sample (blue). The electrons created close to the surface leave the sample and ionize water molecules in the gas phase. The liberated additional electrons form a cascade, which can be detected at a positively biased plate. The H_2O^+ ions recombine with negative charges on the sample.

Resolution in a SEM depends on its ability to focus the beam of electrons in the smallest possible spot on the sample surface. How can the ESEM resolution closely approach that of SEM in a gaseous environment? Clearly, the gas must scatter the primary electrons. However, this does not necessarily impact the resolution[5] significantly: Most electrons scattered in the column are prevented from reaching the sample by the PLAs in the column, meaning that most scattering that could affect resolution occurs between the lowest PLA (at the pole piece) and the sample surface. Scattering is a discrete process, not a continuous one. Each individual electron is deflected only when it passes within a certain critical distance of a gas molecule. The scattering of electrons by gas molecules follows a Poisson distribution. The average number of collisions provides a basis for defining three different scattering regimes (see figure 2.5). Conventional SEMs operate in the Minimal Scattering Regime where scattering effects on the beam are insignificant. In the Complete Scattering Regime, ≥95% of the electrons are scattered at least once, and therefore the beam is generally broadened and not useful for SEM imaging. ESEM

operates in the Partial Scattering Regime, where 95% to 5% of the electrons pass without scattering. This diminishes the resolution, but for most applications only marginally [5].

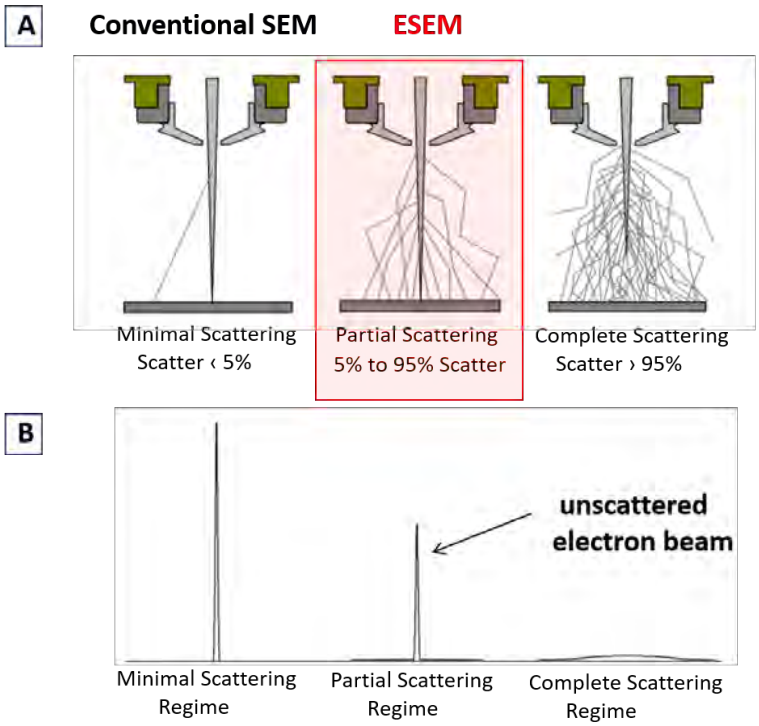

Figure 2.5. A) Scattering regimes based on the average number of scattering events per electron. The ESEM operates in the partial scattering regime. **B)** Shape of the beam intensity profile which depends on the scattering regime. Adapted from [5].

2.2 ESEM imaging

The experiments were carried out with an SiO_2 film grown on an *n*-doped Si wafer (see figure 2.6.A)). The silicon wafer ((111) orientation, thickness 0.27 mm, doped with phosphorus, resistivity 1 Ohm·cm) was cut in 4x4 mm pieces by a wafer dicing saw (Disco DAD321). The pieces were thoroughly cleaned by sonication in an ultrasonicator (VWR Ultrasonic Cleaner) for 15 minutes in a sequence of three solvents: isopropanol (LC-MS chromasolv®, Sigma-Aldrich), acetone (ACS reagent >99.5%, Sigma-Aldrich), water (18 MOhm cm, <5ppb total organic content, Millipore). They were blown dry with nitrogen and surface-oxidized in an oxygen plasma cleaner ("Femto", Diener) for approximately 8 min with a 10 sscm gas flow (0.1 mbar oxygen pressure). This renders the wafers hydrophilic. For an experiment, a wafer piece was placed on a home-made copper stub that fitted nicely into the sample stage (see figure 2.6.B)). Liquid gallium-

indium alloy was employed for bonding the wafer to the stub. The stub was tightly fit into the Peltier stage by an aluminium foil spacer (see Appendix II).

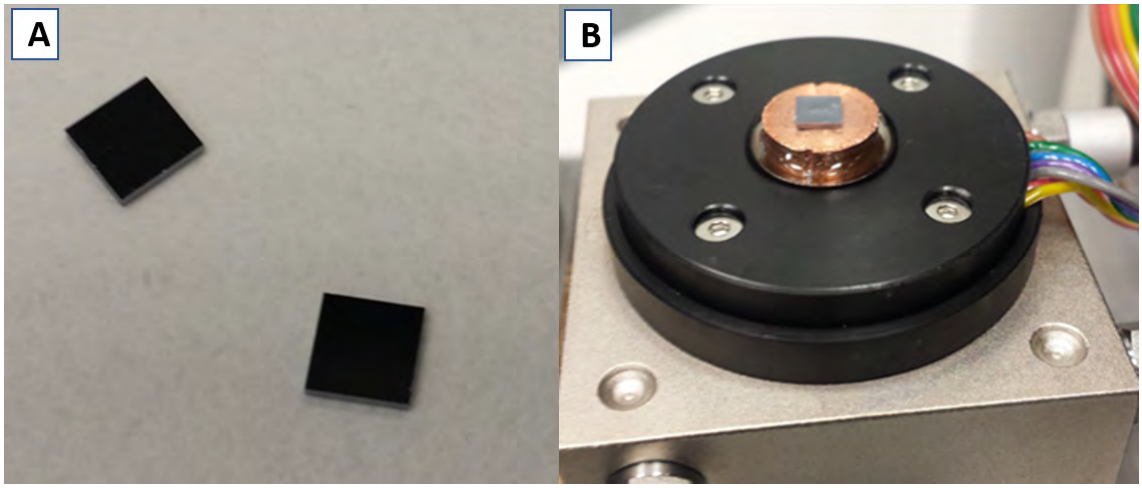

Figure 2.6. A) Silicon wafers used as substrate for growing ice. **B)** Silicon wafer mounted on a copper stub, inserted in the ESEM Peltier stage (black). The copper oxidizes in air, as evident by its reddish colour.

Images and movies of ice crystals during growth and sublimation on the wafer pieces were recorded in a FEG (Field Emission Gun) ESEM (Quanta 250, FEI), operated in the wet mode (see figure 2.7). The sample stage temperature was adjusted between 0 °C and -20 °C by Peltier cooling; resistive heating allowed to reach ambient temperature quickly after the experimental runs. The imaging gas was pure water vapour, introduced via an automated leak valve. The vapour was generated from a heated reservoir of MiliQ-water, containing also a platinum wire for the catalytic decomposition of organic contaminants. The gas phase temperature is not well defined, but given the very slow pressure changes, the water vapour will adjust to the sample temperature when it reaches the cooled surface. The ESEM software shows "100%" as relative humidity value for $h \geq 1$; all values reported here were recalculated according to equation 1.8 (chapter 1).

The relative humidity in the chamber was controlled by increasing or decreasing the pressure in small steps (< 5 Pa), in the range from ca. 50 Pa up to ca. 700 Pa (limit 2600 Pa). Mainly, a beam voltage of 10 kV was used, and spot sizes from 3 to 5 (spot diameters ca. 1 nm to 7 nm). The beam current range ~~was~~ controlled by an aperture in the upper column; it was always kept at its smallest value (setting 7), which assured minimal beam current and thus beam damage.

Electron detection in ESEM is achieved with a positively charged plate (see figure 2.4). This can be either the large field detector (LFD), placed some cm sideways (in the SEM images this is always the right-hand side), and away from the pole piece, or with the gaseous secondary electron detector GSED, a thin brass line, which encircles the lowest PLA. The standard image size was 1024x884 pixels, and the dwell time was in the µs range (mainly 10-30 µs). The dwell time is the amount of time the electron beam illuminates a single pixel [6]. For a sufficiently high signal-to-noise ratio (SNR) image, the required dwell time leads to large data acquisition times. Reducing the dwell time at a given probe current will lead to a lower SNR, and thus limit the information content of the image. Typical doses (current·dwell time/focus area) are about 10^4 e_s^-/nm^2 [7].

For starting an experiment, first ambient temperature was set, and the pressure was lowered to 100 Pa. It was then raised to about 2000 Pa to replace air with water vapour (purge). The purging procedure was repeated twice, and the pressure was then set to 100 Pa. The sample was then cooled to the desired starting temperature, usually -15 °C. At such low pressures ($h < 1$), all water remains in the gas phase. The pressure was then increased slowly until reaching the sublimation line ($h = 1$). The pressure reading corresponds very closely (within 2 Pa) to the sublimation line. Ice started to grow very slowly on the sample, allowing recording images and movies of growth in real time.

However, usually a short excursion to higher pressures was applied to speed up growth. Under such supersaturation conditions ($h > 1$), the Peltier element power limits the temperature adjustment. Hence supersaturation can reach max 100 Pa, but usually only <50 Pa. This is, however, sufficient to induce rather fast ice formation and ice crystal growth (see figure 2.7). After stabilization, the pressure was slowly reduced to sublimation ($h < 1$), again during ESEM imaging. In order to avoid too fast kinetics, h was usually adjusted to a value close to 1 for growth and sublimation. The theoretical equilibrium at $h = 1$ is unstable, meaning that any small deviation from ideal conditions produces either growth or sublimation.

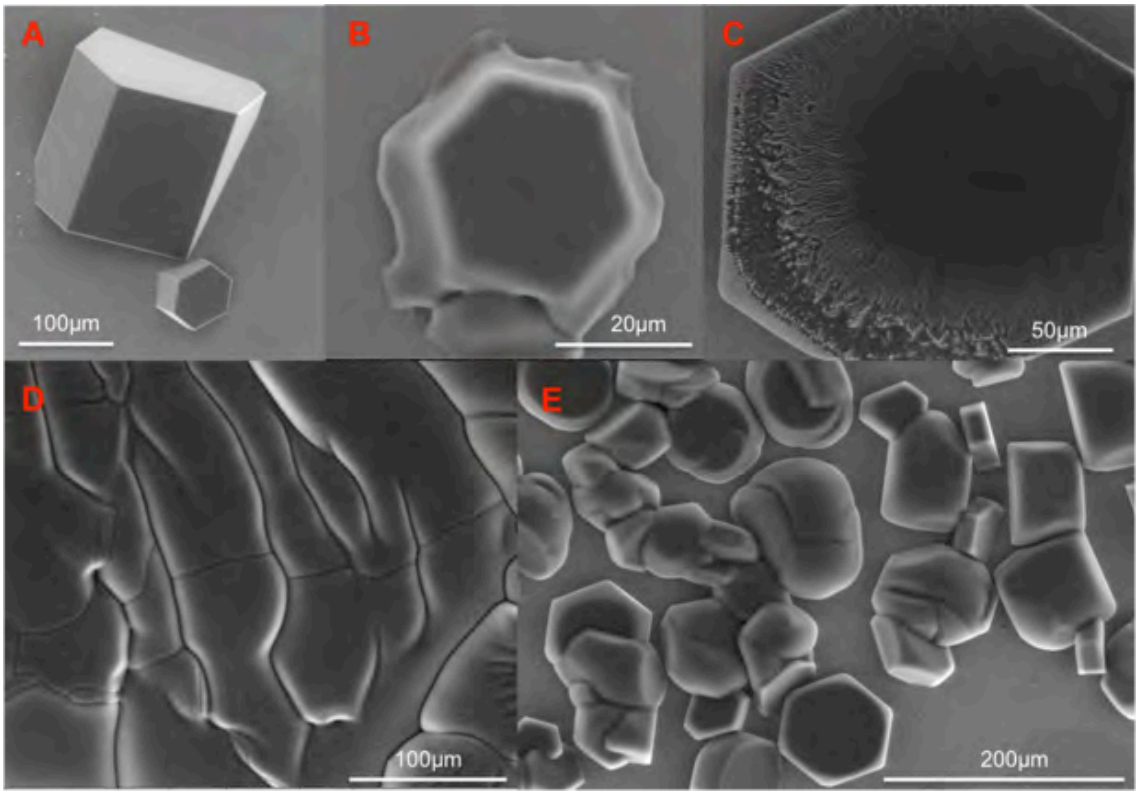

Figure 2.7. Ice growth examples. Images (a) to (c) display the characteristics of crystals produced at high oversaturation. Image (d) shows polycrystalline ice with well-defined grain boundaries (stripes), and (e) single crystals beside polycrystalline ice. Imaging conditions: (a) P = 130 Pa, T = -17.9 °C, h = 0.89; (b) P = 138 Pa, T = -17.0 °C, h = 0.85; (c) P = 136 Pa, T = -18.2 °C, h = 1.10; (d) P = 438 Pa, T = -4.9 °C, h = 1.08; (e) P = 135 Pa, T = -18.4 °C, h = 1,12.

The ice growth proceeds in a similar way on the wafer and on oxidized copper (the stub surface) (see figure 2.8). Epitaxial growth of plates and columns can be induced by AgI [8], which was here not necessary. The morphology of the deposited ice was usually polycrystalline, but single crystals (hexagonal plates or columns, and prisms) were found on all substrates. The ice columns grow in random directions, though, while the basal plane is always horizontal on AgI (i.e. parallel to the AgI surface) [9].

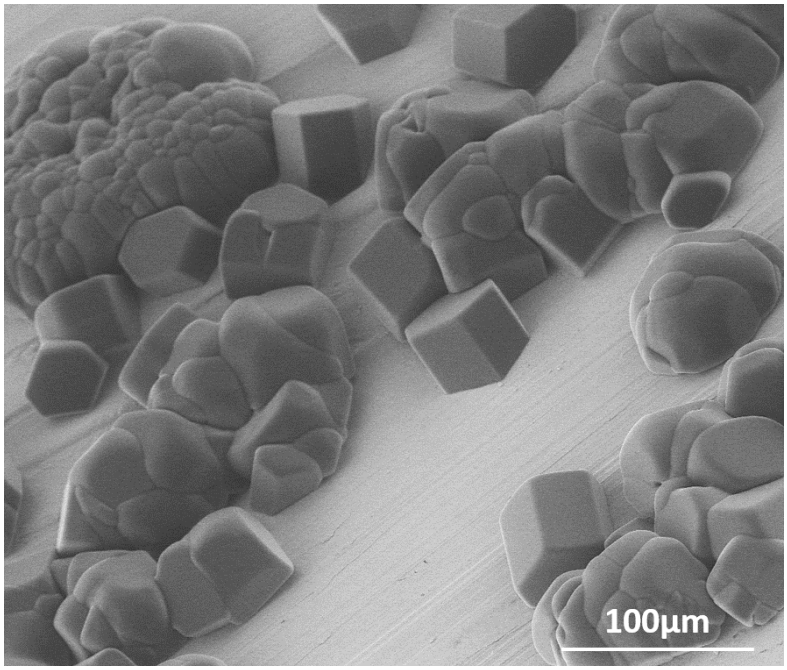

Figure 2.8. Example for rapid growth of ice crystals on the ill-defined (oxidized and rough) surface of the copper stub. In the middle of the image, one can make out several merged single crystals with straight edges and 120° angles. The crystals exhibit smooth edges (roughening). Imaging conditions: P = 135 Pa, T = -17.8 °C, h = 0.92.

2.2.1 Contrast

It is instructive to recall the contrast mechanisms in SEM and ESEM. The detection of the ionization cascade in ESEM is in this respect well comparable to the detection of low energy secondary electrons. Hence the LFD - in its position at the side of the column – is comparable to the Everhart-Thornley detector, which is the standard in high vacuum: Both can induce a shading effect, resulting from shielding secondary electrons produced on surfaces that do not directly face the detector (see figure 2.9).

The axially symmetric GSED should be comparable to an in-lens detector, and produce much less shading. However, electrons impinging on a steep surface induce highly directional emissions, such that shading is always present for GSED images, too, at least to some extent. The effect has a strong dependence on the acceleration voltage in SEM [10]. The voltage in ESEM was found to have a less pronounced effect, but generally optimal imaging required rather high voltages (10-30 kV, see also [11]). More important is that the overall secondary electron yield requires a delicate balance between pressure,

detector distance, and amplifier bias [11], [12]. Hence, the bias was adjusted (i.e. the brightness) whenever the pressure was changed by more than a few Pa.

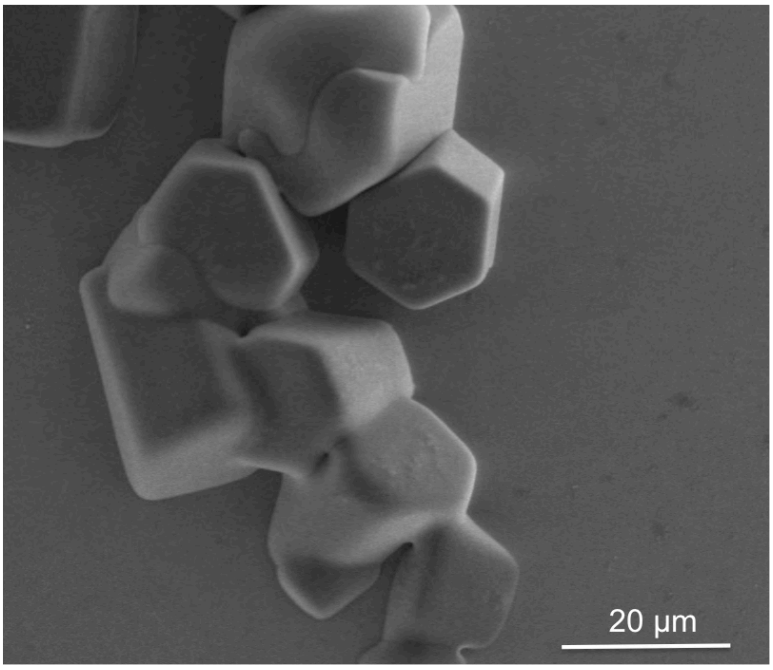

Figure 2.9. Several large single crystals grown on a silicon wafer. Each crystal face displays a brightness, which depends on its angle with the surface, and on its position with respect to the detector. The crystals on the right exhibit prism faces of different contrast. The dark hexagonal basal planes (left) show a huge contrast difference to the very bright prism faces, whose angle with the surface is close to the surface normal. Imaging conditions: P = 158 Pa, T = -17.4 °C, h = 1.19.

These observations are completely in line with other ESEM studies on ice [13], [14]. In addition, there are various other non-topographic effects that modulate the brightness. For example, asperities such as edges and corners can charge up and thus emit electrons more effectively, so they often appear bright, although ESEM offers a very good neutralization of the sample[11] (see figure 2.10). Other charging effects were observed, such as large-scale areas of rapidly changing contrast, only rarely.

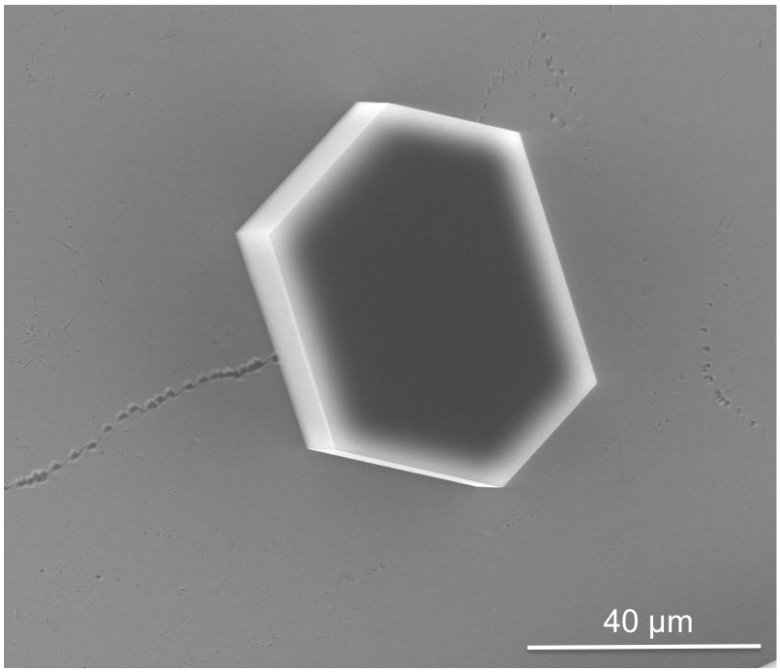

Figure 2.10. Hexagonal crystal of ice. The basal plane is nearly horizontal. The outer rim is bright, an effect that might indicate charging. Imaging conditions: P = 127 Pa, T = -18.7 °C, h = 0.97.

2.2.2 Beam damage

Various mechanisms can cause beam damage[15], [16]; generally, X-rays appear to cause more problems than electrons [17],[18]. Beam damage should be minimized, for which imaging of areas in the micro- rather than in the nano-range was sufficient. Indeed, the standard procedures cause negligible damage. It was, however, difficult to assess damage after longer imaging because the ice surfaces are highly dynamic (see figure 2.11). Given the delicate nature of ice, the absence of damage had to be verified by specific experiments, as detailed in the following.

J.M. Alonso et al. already showed that the conditions employed here are safe for about 1 min even on sensitive proteins [7], hence doses could be increased by zooming in, which was otherwise avoided. Only for image sizes of ca. 10 µm changes became obvious, e.g. darkening of areas (see figure 2.11). Zooming out thereafter allowed imaging the created defect, showing up as dark micro-spot on the grey, rather flat ice surface. The data show nearly complete “healing” of the damaged areas (micro-spots) after several minutes, due to the dynamic nature of the ice.

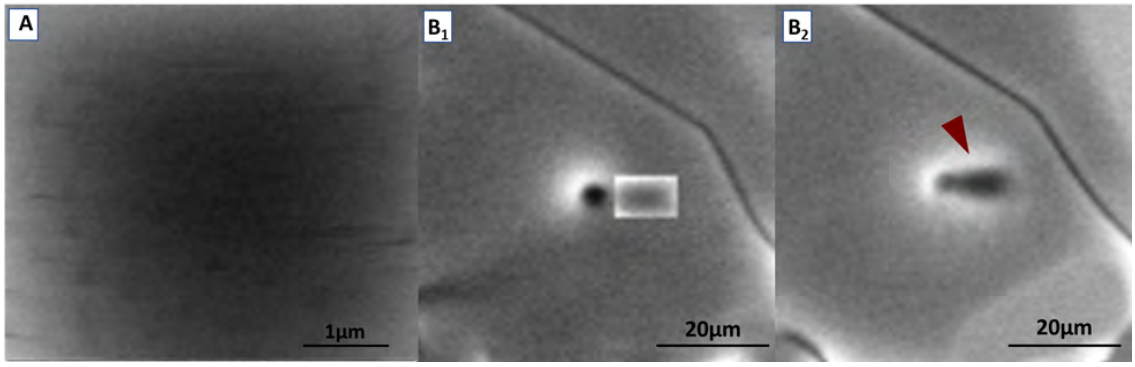

Figure 2.11. Effects of exposing an ice surface to a 10keV beam at constant dwell time (20 µs) for several seconds. **A)** Zooming in a small area shows a dark microspot. The horizontal streaks might be very fast submicrospots. **B_1) B_2)** After two identical consecutive scans of the same area, a deep hole (dark spot) appears. The beam is then zoomed in again on the rectangular window. **B_2)** The small rectangular area has caused more damage (marked with red triangle). Imaging conditions: P = 288 Pa, T = -10.3 °C, h = 1.

Another example for typical scan damage on a polycrystalline ice surface is provided in figure 2.12. Each rectangle corresponds to a smaller image recorded before; after zooming out the damaged area can be detected.

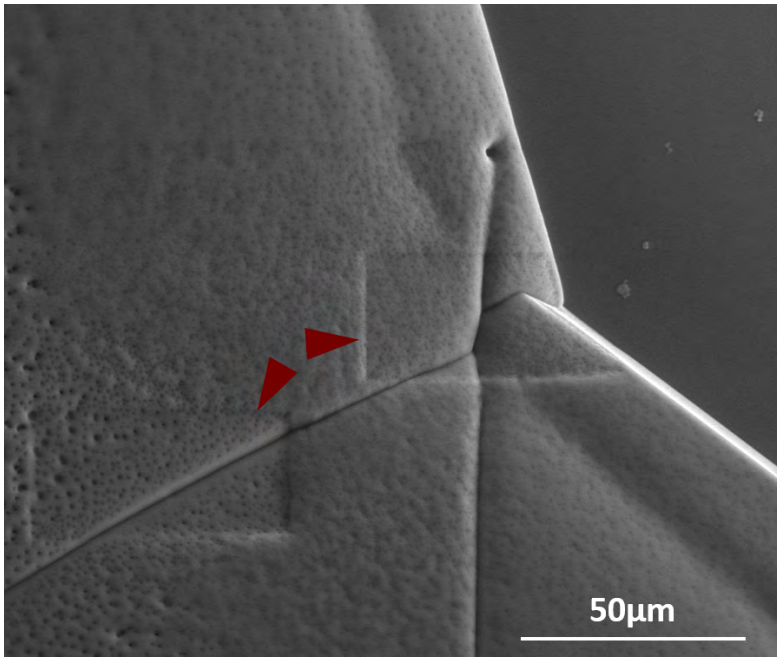

Figure 2.12. Beam damage to a polycrystalline ice surface. Characteristic rectangle structures caused by the beam are marked with red triangles. Imaging conditions: P = 113 Pa, T = -20.0 °C, h = 1.09.

What is the nature of these defects? They must be related to mass loss, for example by sputtering. This is, however, known to occur only at higher voltages [15]. Another possibility would be beating, which is based on various primary processes [15], [16]. The final result should be local sublimation or melting, as found for nanoscale voids in thin layers in TEM [19]. However, in SEM samples the energy can be much better dissipated (in three dimensions). The temperature change for local heating of a stationary beam is [15]

$$\Delta T = \frac{3 \cdot I \cdot U}{2 \cdot \pi \cdot \kappa \cdot R_b} \qquad (2.1)$$

where I is the beam current, U is the beam voltage and κ =1.6 W/(m·K) is the thermal conductivity of ice. When R_b is set to the beam diameter of several nm, one has to include the ratio of dwell time to scan time (>>1000), resulting in negligible temperature changes for the used currents and voltages. Even if repeated scanning of a zoomed-in area (10 µm) is considered as stationary, the temperature would increase by a mere 0.55 K (this would also be expected for heating a µm-sized interaction volume, see figure 2.4). So local melting or temperature-induced sublimation is not expected under any condition.

It is postulated that the damage of ice in ESEM is caused by radiolysis, i.e. based on chemical and not thermal changes. Radiolysis can cause structural changes in ice, which ultimately extend to areas that are much larger than the beam diameter. Scanning at very short dwell times (0.1 µs) revealed constantly forming and dissolving sub-micro-spots of 300-500 nm diameter. These small spots are visualized in figure 2.11A as horizontal streaks. They have low contrast, but they are the precursors of the dark micro-spots, like the one filling the complete image of figure 2.11A. This finding has never been reported before. It should be connected to the stochastic nature of the damage spurs around the beam track[16], although the spots themselves are much larger than spurs (10 nm). The lifetime of spurs is in the ms range. The used fast scans fit well to this estimate (dwell time in the low µs range, ca. 200 pixels per line, one spot ca. 5 lines, hence ≥1 ms are necessary to image a spot as a disk, and not as a streak).

2.3 Growth and sublimation processes

2.3.1 Single crystal growth and merging of crystals

The relevance of this part of the work is first the verification of the reported scenarios, and second, the elucidation of the formation of grain boundaries.

For slow water vapour pressure increase, slow growth of hexagonal single crystal pillars occurs on the oxidized Si wafer, i.e. on an amorphous SiO_2 surface. In contrast to epitaxial growth, the axis of the pillars can take any orientation. Epitaxial growth on AgI would assure a horizontal orientation of the basal plane[9], which is found only statistically (see figure 2.7). Ice grows in the hexagonal I_h phase; other phases would require much higher pressures and/or much lower temperatures (see section 1.1.1 in chapter 1). As usual at low pressure, hexagonal prisms develop (section 1.2.1 in chapter 1) (see figure 2.13). The hexagonal face is the basal plane (0001) of ice I_h. The surface becomes surprisingly inhomogeneous during growth of additional ice. The growth speed observed in this work (measured as horizontal enlargement) is in the same range (100 nm/s) that *Libbrecht* and *Rickerby* found for 0.1% supersaturation [20], which corresponds to <1 Pa above saturation in the ESEM.

The results are in agreement with the studies cited in chapter 1 (section 1.2.3), although this work does not offer a systematic study of the growth rate at the different ice faces with different temperatures; however, the ice growth on the basal face is much faster than on the prismatic face (see figure 2.13).

In the following, two processes will be repeatedly referred to, roughening and facetting. Roughening refers to the gradual disappearance of flat crystal planes (facets) and to the concurrent change of growth kinetics for crystals near equilibrium, which implies a high mobility of surface atoms/molecules [21]. The term can be misleading: Indeed, the surfaces become rough on the nanoscale, based on fast diffusion events. But on the macroscale the morphology becomes smooth: Corners and edges disappear, and the overall shape is nearly spherical. An intermediate state between a crystal habit with sharp edges and a complete rounded sphere is the droxtal ("droplet crystal"), introduced already in section 1.2.2. Facetting can now be envisaged as the reverse process, the gradual growth of low surface energy planes/facets (normally these are densely packed surfaces), thereby removing smooth rounded areas, and creating sharp corners and edges.

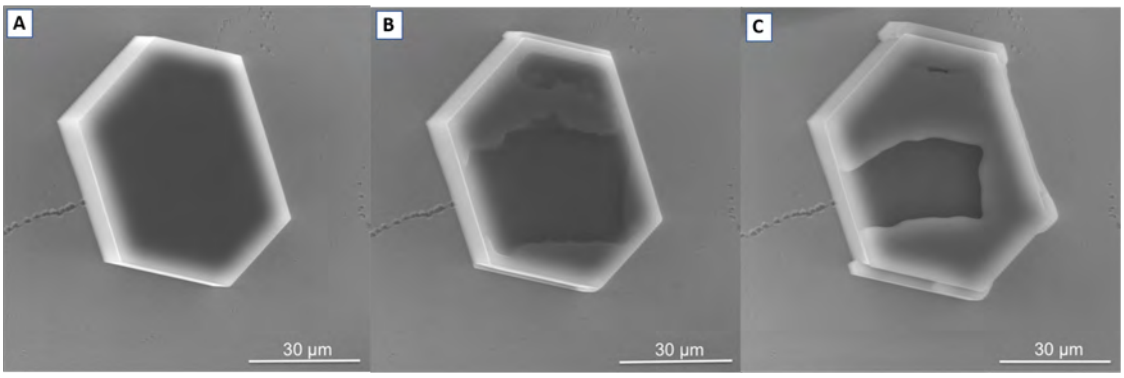

Figure 2.13. Hexagonal single crystal during ice growth. The prismatic faces on top and bottom are overgrown by ice of 3 µm thickness. The basal plane is bright on top and at the bottom, where fresh ice layers have grown. Imaging conditions: (a) P = 127 Pa, T = -18.7 °C, h = 0.97; (b) P = 146 Pa, T = -17.6 °C, h = 1.12; (c) P = 219 Pa, T = -13.6 °C, h = 1.17.

Figure 2.14 presents clearly resolved observations of surfaces of growing hexagonal ice crystals. Many crystals (very clearly number 1,3, and 4) can be related to droxtals, which have changed their shape according to their growth stage [22], see sectionchapter 1.2.2. While *Pfalzgraff et al.* [23] found pyramidal facets and curved (termed by the authors as conical non-facetted) surfaces associated with ice growth (see figure 2.14.A)), pyramidal facets were not found, but many smooth and curved (non-facetted) surfaces (see figure 2.14.B)).

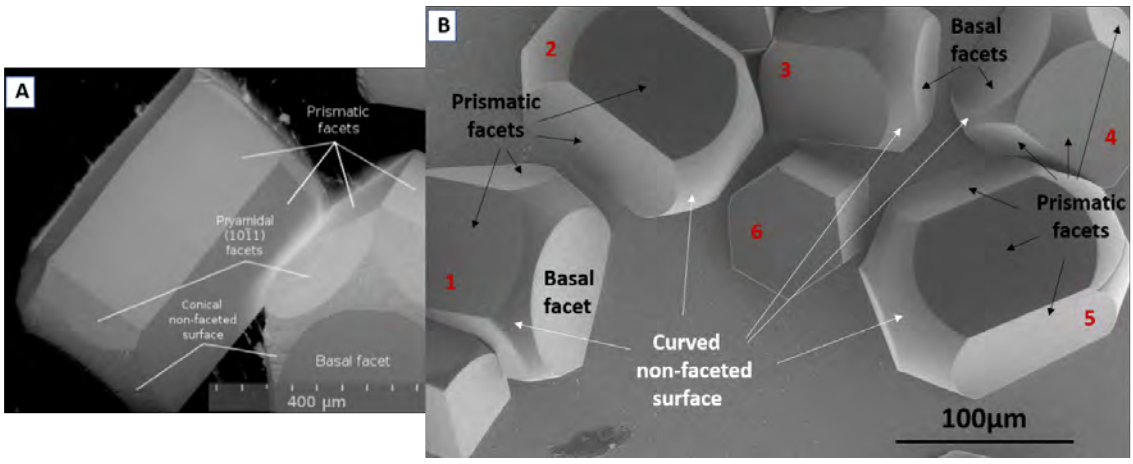

Figure 2.14. ESEM images of growing ice crystals. **A)** Taken from [23]. **B)** Own data. Imaging conditions in B): P = 148 Pa, T = -18.2 °C, h = 1.21.

Crystals number 2 and 5 exhibit prismatic surfaces at a near-normal angle, while their basal planes are tilted away from the detector. In the droxtal-like crystals (1, 3 and 4), the basal planes face the detector, see section 2.2.1. Except for ice crystal number 6, all crystals display non-facetted surfaces, which must be based on roughening. This type of surface is associated with fast growth, and appears during the early stages of the growing process, not at equilibrium. The high mobility of the water molecules is probably assured by fast sublimation and re-deposition.

On a very much larger scale circular areas can be found (see chapter 1), sometimes on the basal face of ice crystals (see figure 2.15), but also on prism faces (see figure 2.14). They appear as circular features of hundreds of μm diameter, with dark contrast, but often with a somewhat blurred border. Crystals with such features can be addressed as the first stage towards development of a droxtal.

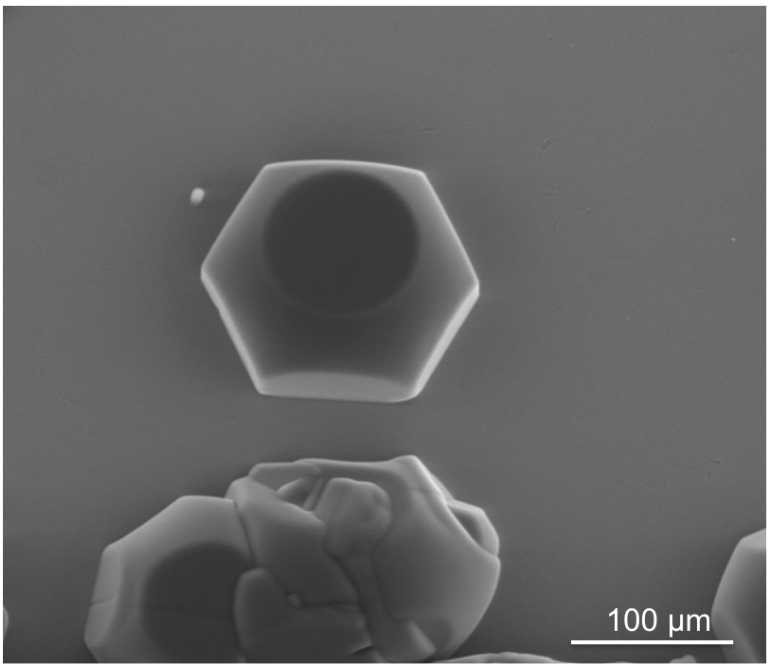

Figure 2.15. Flat circular area of ca. 200 μm diameter on the basal face of a single crystal (top middle). Some grain boundaries between the crystals at the bottom are visible, and more round features. Imaging conditions: P = 104 Pa, T = -20.5 °C, h = 1.06.

When two growing crystals merge, their relative orientation is usually at an angle, and a grain boundary forms. In the top view, it appears as a long dark stripe of some μm

thickness (see figure 2.7D, and 2.16 at right). Smooth surfaces on a single crystal can suddenly develop a large amount of grain boundaries during growth, when they contact another crystal (see figure 2.16). This phenomenon was already found by Magee et al. [13] and by Pedersen et al. [14]. It may be due to an avalanche of dislocations, possibly starting at the new grain boundary [14]. In some cases, it was possible to record growth spirals (macro-steps, see figure 2.16.B)), which were also found by optical microscopy[8], [24]–[26], but not yet by SEM. It is known that they are subject to dynamical changes above -4.4 °C [26], which were not observed.

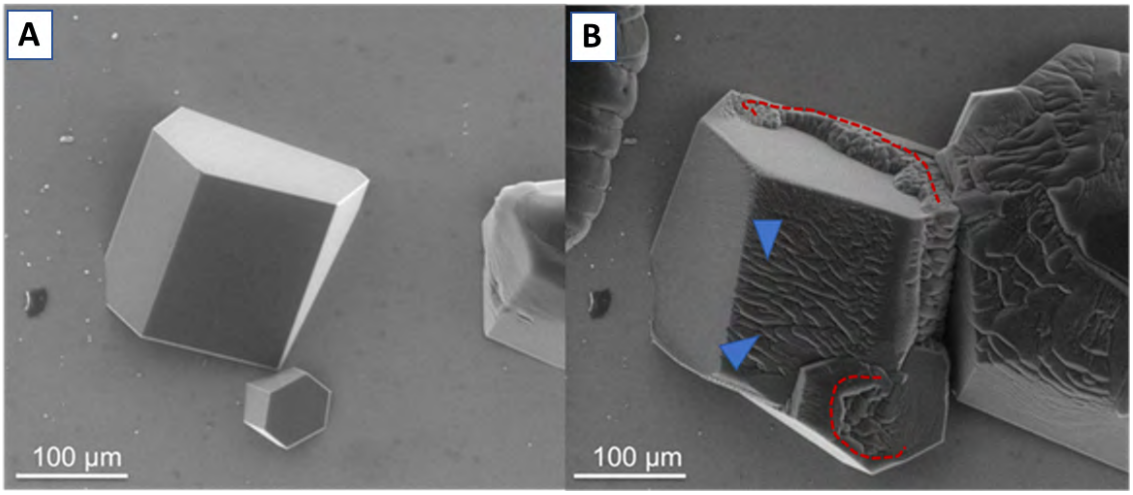

Figure 2.16. Single crystals merging during growth. As soon as the crystals touch, the planes in contact show polycrystalline topography with a large density of grain boundaries (dark stripes, marked by the blue arrows). Two growth spirals are traced by red dotted lines. Imaging conditions: (a) P = 130 Pa, T = -17.9 °C, h = 0.89; (b) P = 127 Pa, T = -18.3 °C, h = 0.97.

The merging of many single crystals ultimately produces a polycrystalline surface, with many grain boundaries, but without any facet (see following section and figure 2.7D). The merging effect is observed also in polycrystalline ice (see figure 2.17). The first micrograph in the series (A) shows smooth ice surfaces, while in the second and third micrographs surface roughness appears - not only in the contact area between ice crystals (marked with red and white triangles in figure 2.17), but also in areas where the different ice surfaces are *not* in contact (blue triangles).

Is difficult to infer and to quantify three-dimensional roughness from two-dimensional images. *Neshyba et al*. have defined a roughness metric for mesoscopically rough ice facets[27], and Butterfield et al. have more recently[28] presented a sophisticated method

for retrieving quantitative, three-dimensional surface morphology of ice from SEM images (based on a functional form for backscattered electron intensity as a function of ice facet orientation).

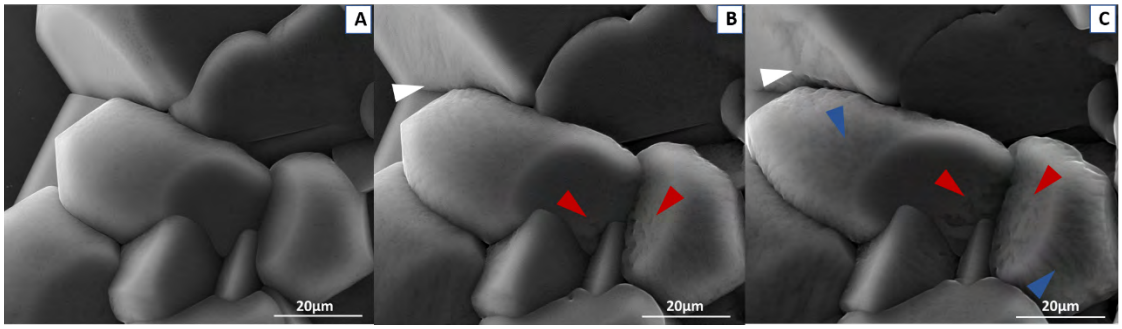

Figure 2.17. Polycrystalline ice during growth. Crystals in contact progressively develop a rough topography, not only in the contact areas (red and white triangles) but also in non-contact areas (blue triangles). Imaging conditions: A), B) P = 110 Pa, T = -20.1 °C, h = 1.06; C) P = 109 Pa, T = -20.1 °C, h = 1.05.

2.3.2 Polycrystalline ice and grain boundaries

Liquids in grain boundaries

Polycrystalline ice at temperatures close to melting exhibits a range of features that are all linked to grain boundaries [29], [30]. Before presenting the data, the presence of liquid water will be shortly reviewed because it is a decisive feature of ice in nature.

Starting with the assumption of pure ice, liquid (supercooled) water can be stabilised at curved solid/liquid interfaces. The Gibbs-Thomson equation

$$\Delta T = \frac{2 \cdot \sigma_{sl}}{\rho_s \cdot \Delta H_{melt} \cdot r} \qquad (2.2)$$

quantifies the melting point depression, ΔT, where σ_{sl} denotes the interfacial tension between the solid and the liquid phase, ρ_s refers to the solid density and ΔH_{melt} to the molar enthalpy of melting. It predicts high curvatures 1/r and thus submicron features, which have been observed for some model systems[7], [30], but - as far as known - not in ice. Another stabilisation mechanism is the application of stress. Wherever two grains meet under stress (e.g. in a flowing glacier), water can be stabilized in microscale lenses at the boundary plane. These lenses can be observed close to the melting point, e.g. by optical microscopy. They attain diameters up to 100 µm [31], [32].

Probably most important in nature are dissolved compounds, which tend to segregate from ice into a liquid aqueous phase. High melting point depressions become possible, and liquid inclusions can reach the μm and mm size, even in absence of stress. As mentioned in chapter 1, the normal melting point of a bulk solid will be altered by the inclusion of impurities (according to the Raoult law, see equation 1.9).

It is well established that natural polycrystalline ice contains "veins" filled by liquid, where three grains meet. The size of the deltoid vein cross-section depends on temperature; detailed characterizations down to a few micrometers have been carried out with optical microscopy, e.g. by Mader [33]. Veins meet at nodes and can thus build up a 3D network of liquid channels inside ice, which is of importance in natural ice: It is in these channels that salts and acids are concentrated, and where microbial life is possible. When a node reaches the ice surface, the deltoid cross-section of one of the veins can be exposed[31]. Barnes et al. were able to image such deltoids by SEM, but they do not directly discuss their origin [34]. However, any vein or node exposed to water vapour of $h < 1$ cannot be completely filled. For pure water, the vein size (r) would be in the low μm range (according to equation (2.2)), and water could only reside in the acute angles, typically 30° to 40° [33], of the deltoid-shaped veins.

In summary, all discussed liquid water structures, lenses and veins, should be in the μm range. Such structures are located in the ice bulk, and are thus not available for SEM characterization. Wherever they might reach the surface, liquid water would evaporate at $h < 1$. The grain boundaries at the temperatures applied here, for pure ice, should not be filled by water. They would be liquid only for extremely small curvatures, as discussed above. One cannot exclude the presence of veins and lenses, filled by liquid water, in the bulk of polycrystalline ice, but the surface shows no indication for liquid water.

Grain boundaries in ESEM

In the ESEM deposition experiments, continuous layers of ice required at least tens of μm thick deposits. Clean flat oxidized Si wafers were always used, but the relatively rough copper stub or any other surface would be suitable, too (see figure 2.8). The required fast growth can be achieved by pressure jumps to $h > 1$, and subsequent stabilization at $h = 1$. Such ice layers were always polycrystalline, appearing bright with typical dark bands, the grain boundaries (see figure 2.18). The 3D structure of these boundaries was

determined by AFM [35]; they are 50-500 nm deep. Hence, one can be confident that the dark colour is of topographic origin. During sublimation, it became possible to further resolve the boundaries as chains of microscale "pools" (see section 2.4).

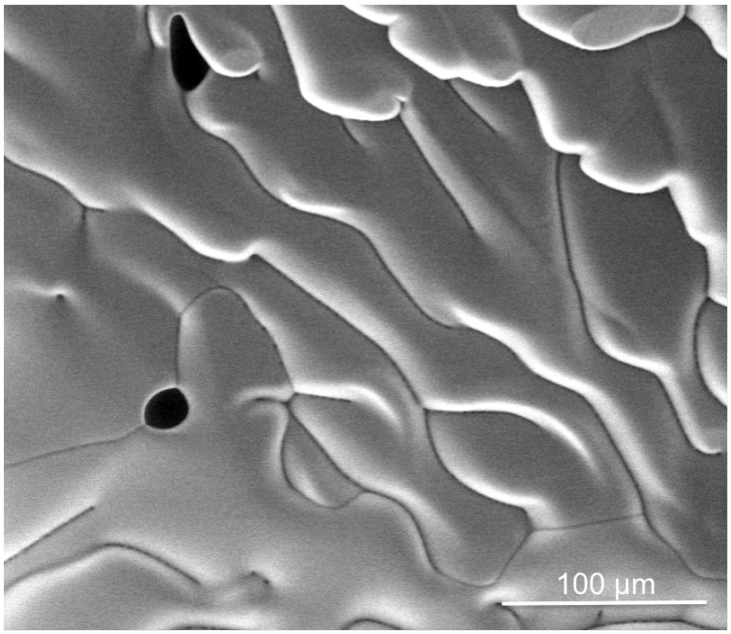

Figure 2.18. Typical polycrystalline ice surface. The grains appear bright, with typical shading effects. They are limited by 1 to 2 µm wide dark bands, the grain boundaries. Three boundaries meet at angles from 90° to 120°. Each grain boundary consists of aligned small dark pools of 1 µm diameter (see section 2.4). Some larger pools up to 10 µm diameter can be observed, too. Imaging conditions: P = 438 Pa, T = -4.8 °C, h = 1.08.

Three grain boundaries often meet at angle from 90° to 120°. This would be expected from nodes, where four veins meet. The fourth vein should then be exposed to show a deltoid-shaped structure, as Nye et al. found for very large veins close to the melting point [31]. However, such structures were found very rarely, and veins should not be present on pure ice surfaces (see above). In some cases, grain boundaries were seen also in ice layers that grew on top of a basal plane. In the example shown in figure 2.19, the grain boundaries do not cover the basal face completely; in the middle of the basal plane a circular dark area appears, in which the grain boundaries converge. The similarity to other circular areas (figure 2.15) is striking, although usually no grain boundaries border the circular areas.

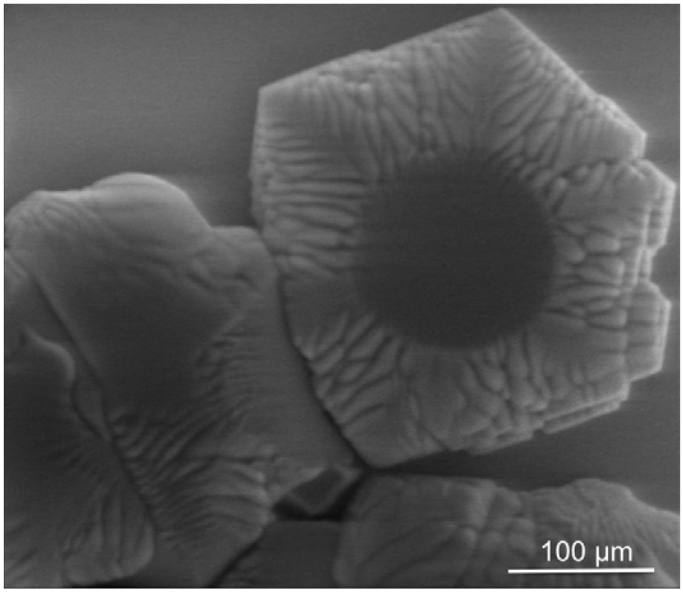

Figure 2.19. Dark circular area in the middle of a basal plane (a sharp 120º edge is visible at top left), on which thick ice layers have been grown. The dark area is surrounded by a plethora of dark lines, grain boundaries in the thick ice layers. Imaging conditions: P = 327 Pa, T = -8.4 °C, h = 1.09.

2.3.3 Sublimation

When a small growth rate is kept ($h \geq 1$), ice attaches in flat layers, and edges remain straight (see above). For $h \leq 1$ the ice sublimates, which requires lowering the pressure by (at least) a few Pa. Several observations of surface structures after a sublimation process have been made [36],[37],[38],[39]. The exact mechanism remains unclear. However, it is obvious that molecules detach from all locations of the crystals, specially also from flat surfaces and not only from the edges, leading to relatively homogeneous roughness of the crystals on all facets.

The high rate of evaporation and re-adsorption (growth) should provide a very effective mechanism for surface transport. One can expect that many structures form by evaporation from high-energy structures, such as kinks and steps, and transport through the gas phase. This should lead to a very effective roughening: Sharp edges and corners will lose molecules and appear smooth and rounded. Figure 2.20 shows a typical result, a hexagonal pillar during sublimation. The outer borders of the crystal have evolved curvatures of tens of µm. The prism faces show similar behaviour (see figure 2.9). In addition, wherever crystals had merged, grain boundaries appeared in the typical network structure.

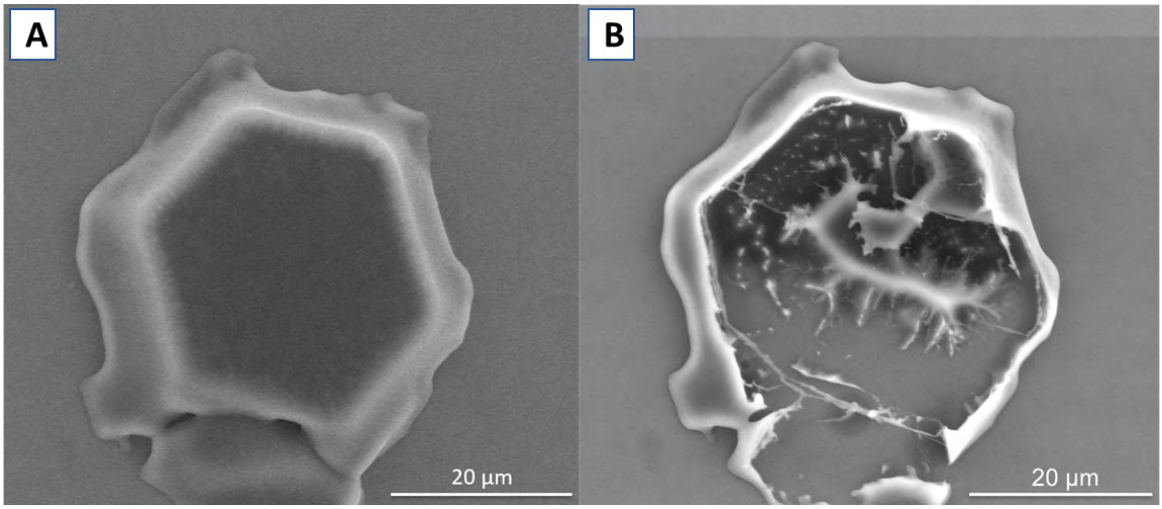

Figure 2.20. A) Hexagonal prism during sublimation. Image conditions: P = 100 Pa, T = -17.0 °C, h = 0.85. The evaporation process has caused substantial roughening, as visible by the rounded edges. The 120 º angle between the edges is preserved. **B)** The area imaged in A) after nearly complete sublimation. The edges of the thin ice sheets charge and thus appear very bright. Imaging conditions: P = 100 Pa, T = -17.0 °C, h = 0.85.

Depending on the pressure change, the brightness requires detector adjustment during sublimation. However, some additional contrast changes are not related to the detector. A typical scenario involves the appearance of very bright small features, often aligned along grain boundaries or edges of ice crystals (see figure 2.21). Baker et al. describe the same for much lower temperature [40], however, they show a relation to contamination (in natural ice samples). This impurity effect has been studied by several authors that suggest that solutes, such as sodium chloride, sulphuric acid or dust particles in the crystals may be the underlying cause for the macroscopic structures that develop during sublimation ([36],[37],[41],[42],[43]). One can exclude all of this for a pure ice system. Here the features should stem from localized high emission currents, and could be linked to asperities that appear during evaporation[40]. The asperities escape imaging (beam damage), so they might well be of nanoscale dimensions. This would mean that some local structures are more strongly bound than the surrounding molecules, which is compatible with the dislocations found at grain boundaries. Similar strings of bright dots were found also on the steep flanks of objects, whose shape is reminiscent of single crystals (see figure 2.22). As already discussed above, these flanks are prism faces, which had - during the merging of crystals - grown very fast, and displayed a high density of grain boundaries. Such structures are often hidden below the apparently smooth surface of polycrystalline ice layers.

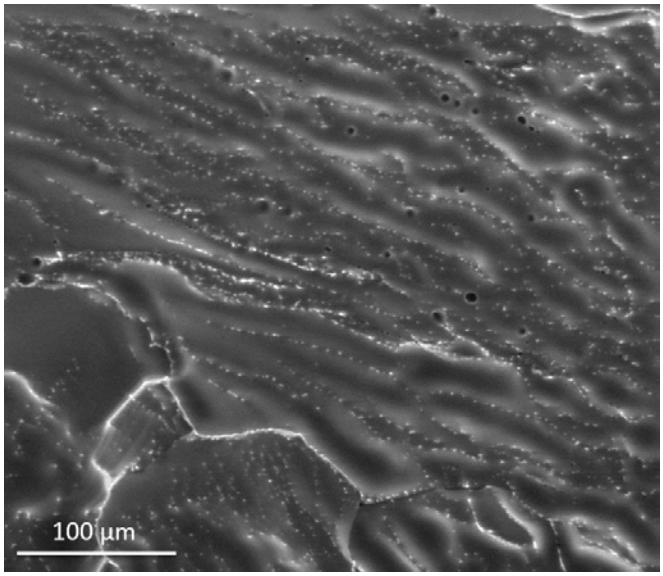

Figure 2.21. Polycrystalline ice surface during sublimation. The complete surface is dotted with small white spots, aligning along grain boundaries. Imaging conditions: P = 400 Pa, T = -5.0 °C, h = 0.92.

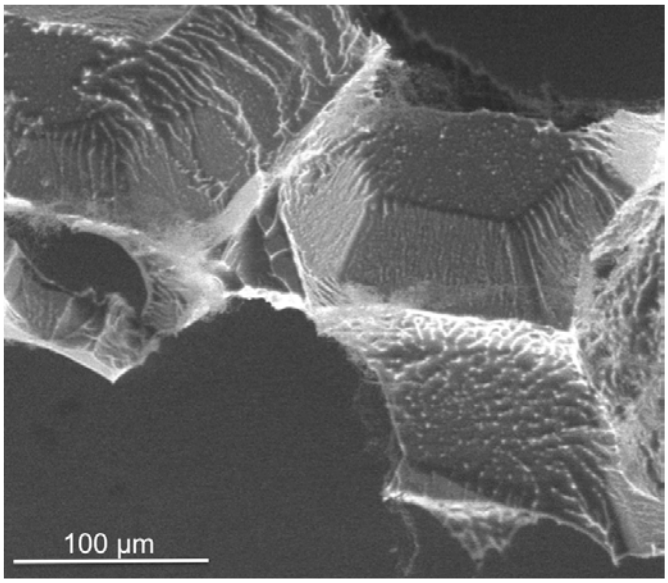

Figure 2.22. Single crystal during sublimation. White spots line up at grain boundaries at the prism faces. Imaging conditions: P = 56 Pa, T = 1.0 °C, h = 0.08.

In the final stages of sublimation, a much-distorted network of polygonal cells shows up (see figure 2.23). Similar structures have been reported by De Micheli and Licenblat [44] with low magnification optical microscopy under similar conditions; unfortunately the authors give no scale. The walls of the cells observed by ESEM are very bright, and they are interpreted as protrusions, in line with the findings for the bright dots. This is indeed

verified when the smooth wafer substrate becomes apparent. Shortly before complete sublimation one can identify some walls as steep faces, originating from single crystals (see figure 2.24). Again, these faces are decorated with strings of bright dots. Features that can be correlated with a potential opening of water-filled veins or lenses were never observed.

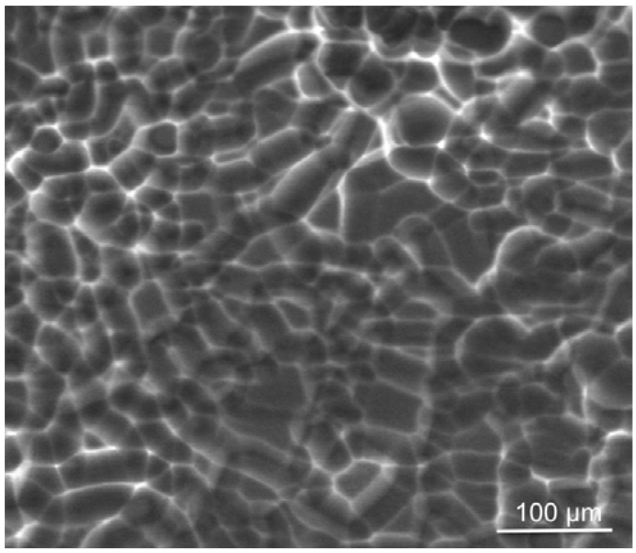

Figure 2.23. Typical cell structure after nearly compete sublimation of polycrystalline ice. Imaging conditions: P = 233 Pa, T = -10.1 °C, h = 0.81.

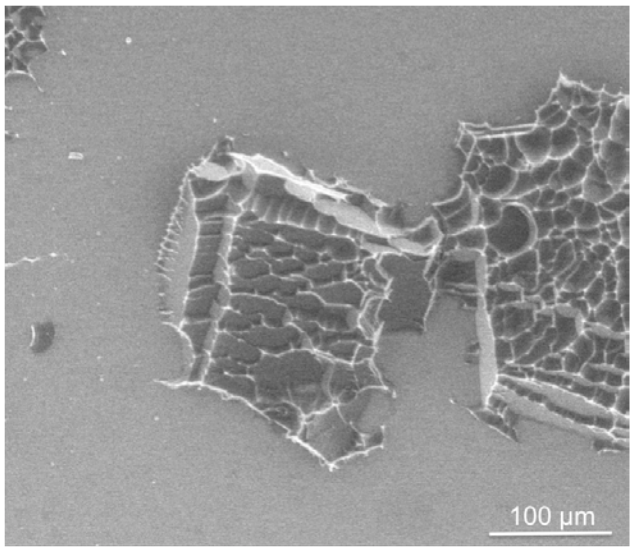

Figure 2.24. The very last stage before complete sublimation. The bright grey background is the pure silicon wafer surface; all other features are ice crystals. Some faces are decorated with bright lines (strings of bright dots). Imaging conditions: P = 100 Pa, T = -17.1 °C, h = 0.89.

"Etching channels"

It is instructive to follow the fate of individual grain boundaries during sublimation. Sublimation preferentially occurs at the grain boundaries because these are regions of high energy[43]. Following the theory by *Barnes et al.*[34], the "etching" of grain boundaries by sublimation should create ever widening channels (see figure 2.25). It was possible to record this widening in real time (figures 2.26, 2.27). The channels simply move vertically down, together with the ice surface. Note that when the grain boundary plane is not exactly normal to the surface, the channels no longer mark the boundary location, but also move horizontally.

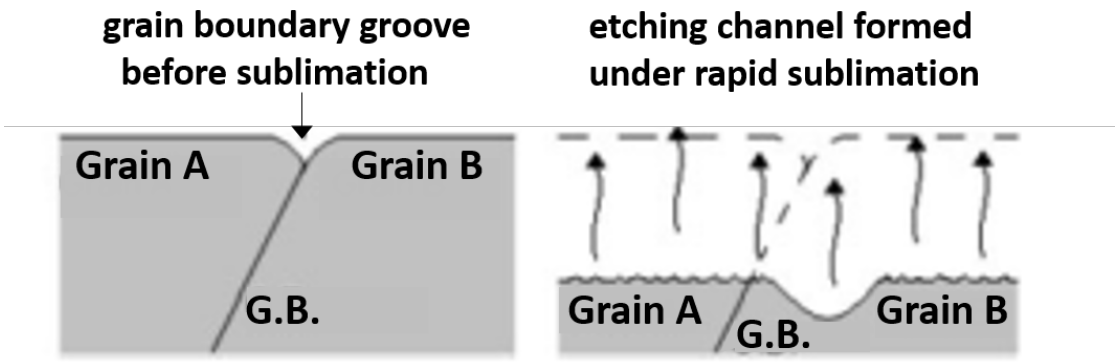

Figure 2.25. Rapid sublimation at grain boundaries. (Redrawn from [34]**).**

The "etched" grain boundary channels are much wider than the boundary itself, an effect used by *Barnes et al.*[34] to easily visualize the boundaries by optical microscopy. In figures 2.26 and 2.27 one can distinguish how the location, shape, and direction of grain boundaries have changed, consistent with the theory. Figure 2.27 additionally shows quantitative data. In the late stages of sublimation, the channels become extremely wide, such that the two crystals that border the boundary appear (see figure 2.28).

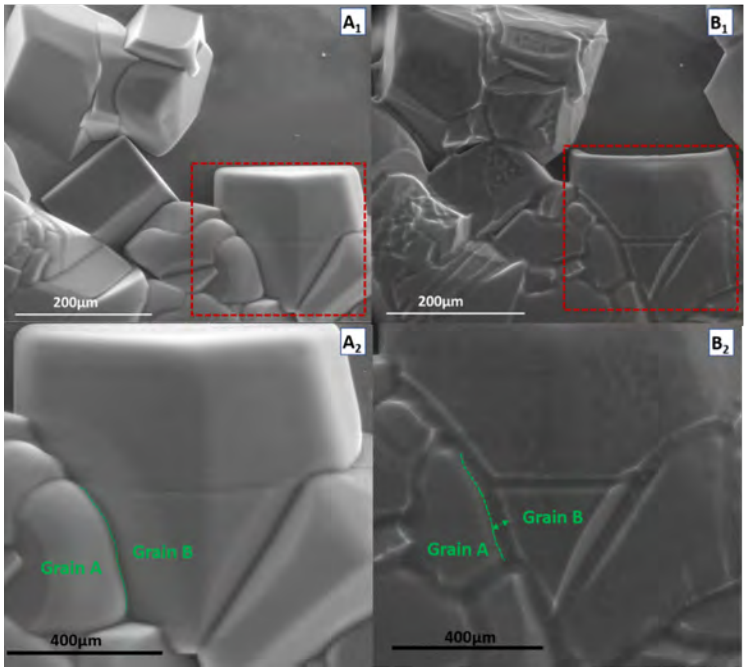

Figure 2.26. Polycrystalline ice during sublimation. **A_1), A_2)** Initial state. One grain boundary is marked with a dashed green line in the zoomed image (A_2). **B_1), B_2)** Image (and zoomed-in region) recorded after 3 min of sublimation**.** The newly formed channel is marked in B_2 with a double arrow. Imaging conditions: (a_1) P = 135 Pa, T = -18.7 °C, h = 1.15; (b_1) P = 113 Pa, T = -18.8 °C, h = 0.86.

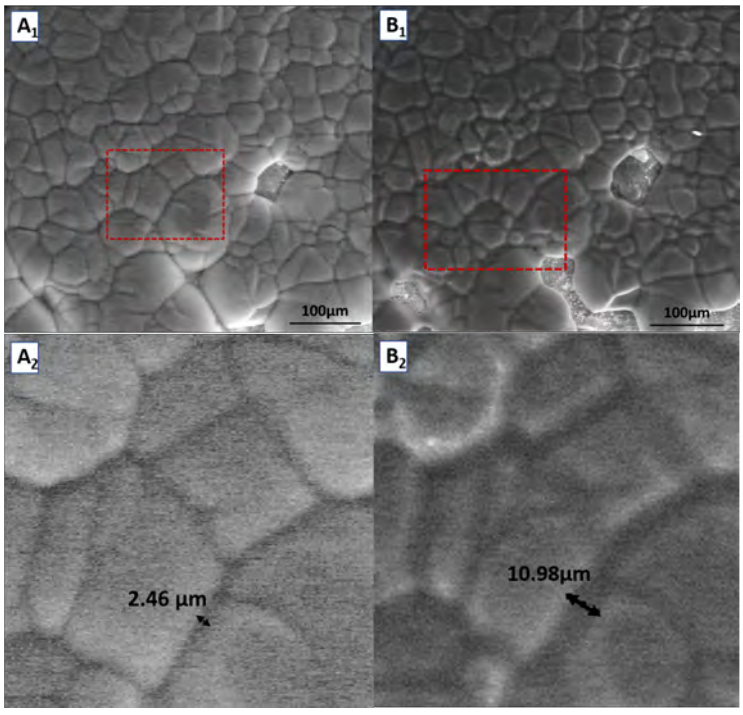

Figure 2.27. Polycrystalline during sublimation. **A_1), A_2)** Initial state. The zoom A_2 allows to measure the width of a grain boundary. **B_1), B_2)** Image recorded after 155 s of sublimation**.** The width of the grain boundary has increased more than fourfold. Imaging conditions: (a_1) P = 181 Pa, T = -14.8 °C, h = 0.93; (b_1) P = 171 Pa, T = -15.1 °C, h = 0.88.

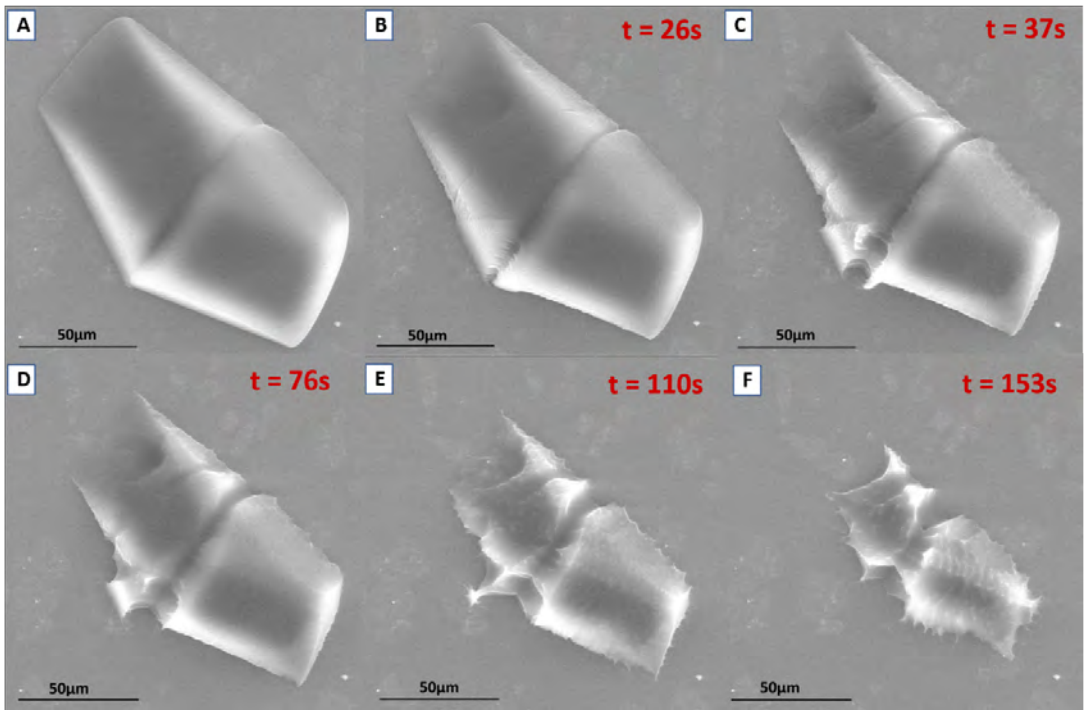

Figure 2.28. Time series of two merged ice crystals during sublimation. Imaging conditions: (a) P = 181 Pa, T = -14.8 °C, h = 0.93; (b) P = 171 Pa, T = -15.1 °C, h = 0.88; (c) P = 171 Pa, T = -15.1 °C, h = 0.88; (d) P = 171 Pa, T = -15.1 °C, h = 0.88; (e) P = 171 Pa, T = -15.1 °C, h = 0.87; (f) P = 171 Pa, T = -15.0 °C, h = 0.88.

Sublimation speed

The images in figures 2.26, 2.27, and 2.28 are extracted from time series of sublimation events. SEM does not allow to measure vertical distances (heights); especially during fast recording, it is practically impossible to tilt the sample stage, in order to obtain a side view. However, lateral distances can be determined with great precision. Receding speeds of edges of ice crystals were around 200 nm/s, at temperatures as low as -19 ºC, and at humidities around 90%. The experimental ESEM setup is not designed for the determination of sublimation rates; it is however instructive to compare this value to values observed in nature at similar temperatures: The North polar ice cap on Mars is estimated to sublimate at a rate above 5 cm/year (1.6 nm/s) [45], in the Martian summer, when extended ice fields at the poles evaporate (see section 1.4.1in chapter 1). This is quite similar to the highest sublimation rates (40 cm/year, 13 nm/s) of Antarctic glaciers [46]. In contrast, sublimation from subsurface ice in dry valleys of Antarctica is maximally of 0.1 mm/year (0.003 nm/s) [47]. Note that a comparison with the situation on the Moon makes no sense because ice is only stable in extremely cold shaded craters, where the rate is calculated to be unmeasurably small [48].

2.4 Unusual microscale features observed during sublimation

Branched structures on the basal plane

Some phenomena (figures 2.29 and 2.30) become observable when a basal plane is (by chance) oriented horizontally and sublimates rather slowly, such that the structure can be zoomed. In figure 2.29 a spiky ice surface develops on the basal plane, as well as on the prismatic planes of the ice crystals, but sublimation seems to start preferentially at the basal planes. The white, highly branched surface structure can again be interpreted as ridges (see section 2.3.3); different from the lines discussed above, they do not appear to be composed of bright spots. Rather, the scenario is reminiscent of sublimation patterns of ice on the wafer, which are of a much larger scale (see figure 2.24).

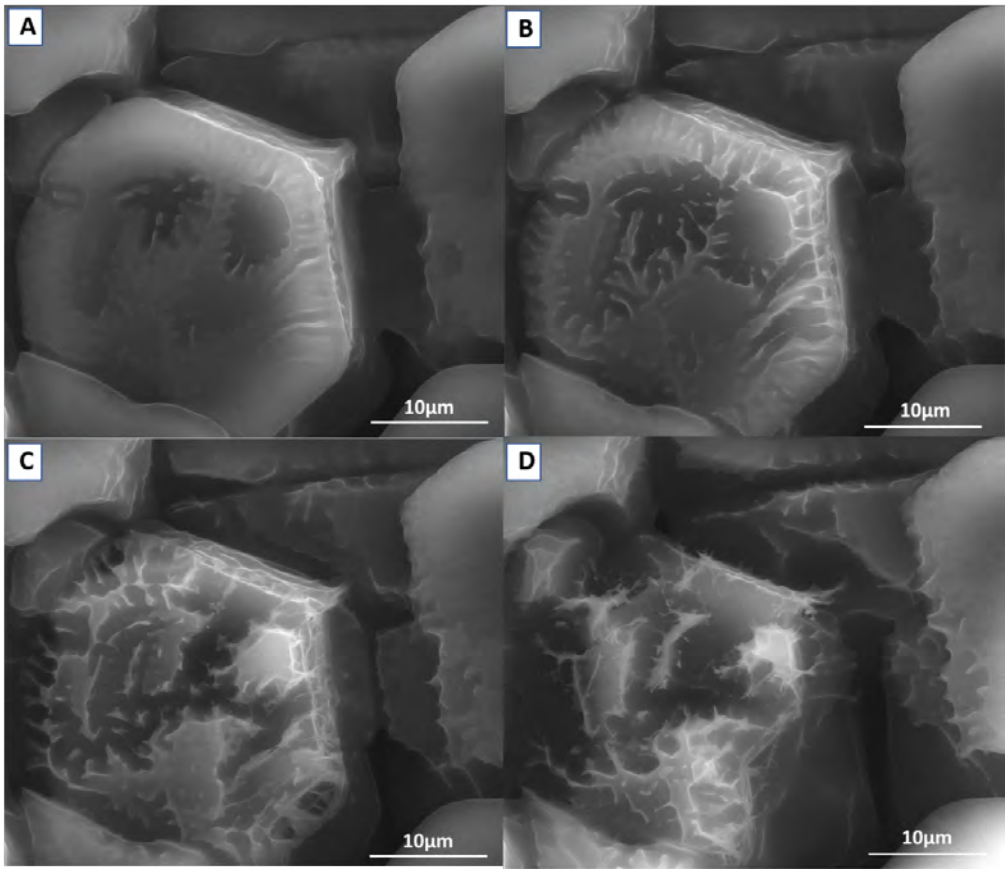

Figure 2.29. Time series of an ice surface during sublimation. Imaging conditions: (a) P = 125 Pa, T = -18.9 °C, h = 1.07; (b) P = 124 Pa, T = -18.9 °C, h = 1.06; (c) P = 123 Pa, T = -19.0 °C, h = 1.08; (d) P = 124 Pa, T = -19.1 °C, h = 1.09.

Holes in the basal plane

In some cases, pressure reduction induced the appearance of deep holes in the basal planes of hexagonal ice crystals (figure 2.30). The first holes appeared when the pressure was lowered by only 10 Pa (see figure 2.30 B). Further decrease produced more holes (see figure 2.30 C)-E)), and finally complete evaporation. Note that the temperature was in this case not constant (it reduced by 3 K). The holes appear statistically, just like the spots observed during beam damage (section 2.2.2). However, they are static and simply enlarge. One can expect that continuous scanning over beam damage spots increases the damage such that the already damaged spots enlarge, probably on the expense of smaller, fresh beam damage spots. This is supported by the observation that all observed scenarios as in figure 2.30 require continuous scanning, of course under the condition of a rather small image (zoom).

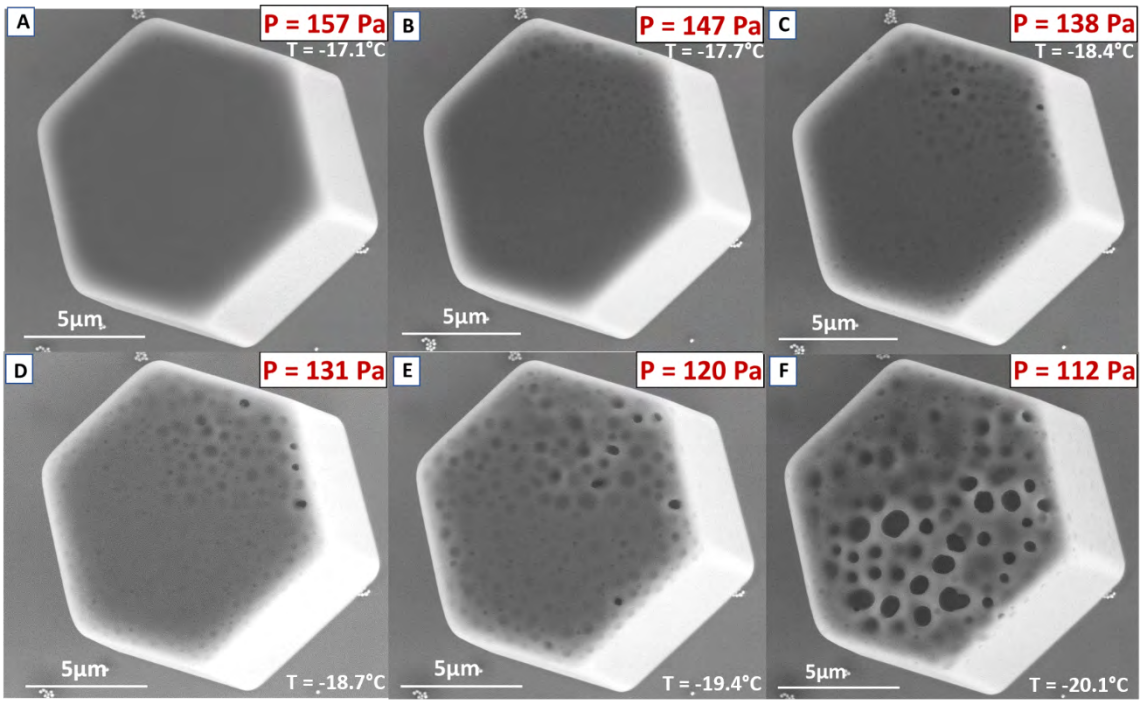

Figure 2.30. Time series of a hexagonal ice crystal during sublimation, which was initiated by reducing the water vapour pressure. Imaging conditions: (a) P = 157 Pa, T = -17.1 °C, h = 1.15; (b) P = 147 Pa, T = -17.7 °C, h = 1.13; (c) P = 138 Pa, T = -18.4 °C, h = 1.12; (d) P = 131 Pa, T = -18.7 °C, h = 1.12; (e) P = 120 Pa, T = -19.4 °C, h = 1.09; (f) P = 112 Pa, T = -20.1 °C, h = 1.08.

"Pools" in grain boundaries

The emergence of dark spots or “pools“ along the grain boundaries was already introduced (figure 2.18, see also figure 2.21); these pools have not been reported yet. A pool is a nearly circular dark structure of a diameter that barely exceeds the grain boundary thickness of 1-3 µm. The observation does not require substantial evaporation, such as the "etching" of channels reported above. Surprisingly, pools also exist directly in grain boundaries – in fact, many grain boundaries appear to consist of a string of pools. The pools do not appear to be equally distributed along grain boundaries (see figure 2.31).

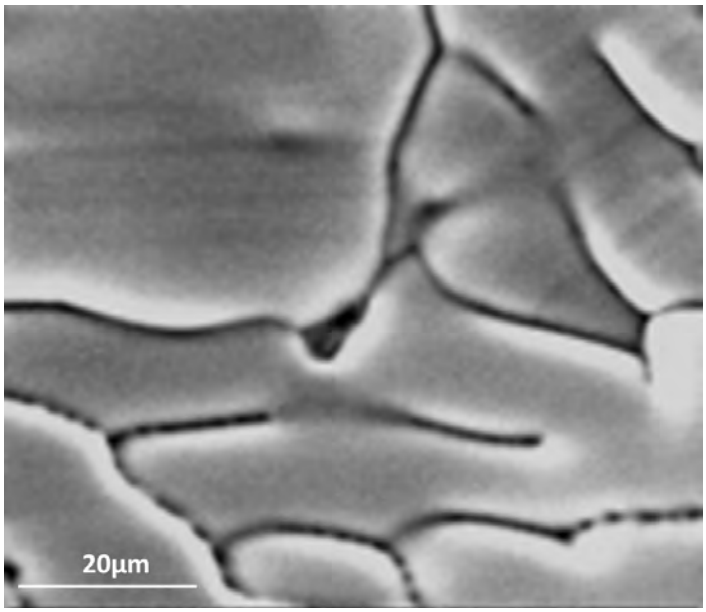

Figure 2.31. Polycrystalline ice surface during sublimation. Circular dark spots or “pools”, aligning along grain boundaries, can be distinguished. Imaging conditions: P = 287 Pa, T = -10.3 °C, h = 1.13.

What is the roughening mechanism for such small structures? With the Gibbs-Thomson equation (2.2), one can safely exclude the presence of liquid water under the conditions of low temperatures, at least for structures above ca. 10 nm size (smaller ones would be hard to resolve), located at the surface. The "pool" curvature is thus far too small to allow (super-cooled) liquid water to exist, as observed e.g. for wedges at curved mica in a surface force apparatus[49]. Another option would be an ultrathin liquid layer: Ice surfaces under the described conditions must feature a quasi-liquid layer (see following chapter) of disordered water molecules, which would offer yet another transport route, but the viscosity is far too high to compete with gas phase transport.

Pools were never found during growth, only during slow sublimation. This suggestes that some form of transport of water molecules from corners or edges, presumably as vapour, is involved. Indeed, stabilizing the system at $h = 1$, exactly balancing growth and sublimation, invariably involves also sublimation events. As shown in the previous section, this condition induces roughening of larger structures, which easily produces rounded shapes. So, one should expect that at some parts of the grain boundaries water molecules are transported from edges and kinks by sublimation, and that these processes smoothen the structure - just as traditional roughening does, which is based on surface diffusion. Such a scenario could finally produce a string of pools. This is reminiscent of the Rayleigh-Plateau instability that explains how a jet of liquid is perturbed into a steady stream of droplets. Ii is thus suggested that the pools are topographic features based on roughening processes.

2.5 Conclusions and furture prospects

An efficient method to image the growth of ice crystals by ESEM was developed, although real time imaging of the growth of ice crystals at low pressures entails a challenge. One cannot achieve an accurate control of pressure and temperatures inside the chamber without re-designing the vacuum system. However, the ESEM allows accessing pressures from 10 Pa (typically 50 Pa) up to 2600 Pa (typically 1000 Pa) and temperatures from -30 °C to +45 ºC. The temperature range can be extended to lower temperatures (-190 °C) relatively easily with the cryoMAT setup (developed by FEI), which is based on nitrogen gas cooling. Processes at much lower temperatures should be accessible if the dynamics is not too slow.

As discussed in this chapter, water vapour decreases resolution and contrast, which makes imaging difficult, especially at high pressures. Regardless of these technical complications, it was demonstrated that ESEM avoids charging, and that it is fully compatible with in situ growth and sublimation, and capable to reveal the surface morphology of ice crystals.

Polycrystalline ice layers were characterized in detail, including growth and sublimation. The observed scenarios are fully compatible with reports based on other SEM studies

(mainly at lower temperatures), and with optical microscopy. A large variety of ice structures was found, e.g. hexagonal prisms and droxtals (droplet crystals).

Understanding and controlling the growth of ice crystals is of interest in many domains, from geophysics to biology or food engineering. In materials science, the growth of ice crystals in colloidal suspensions is used in processing routes called “ice templating” or “freeze-casting”, where the unidirectional growth of the crystals and their successive removal by sublimation are used to template porosity in various materials. The microstructure, architecture, and properties of these materials are related, to some extent, to the morphology of the crystals grown during freezing.

The control of nucleation and ice growth kinetics can improve anti-icing and de-icing performances on a surface. Ice formation is currently a major problem in a wide variety of areas, including solar panels, refrigeration systems, power transmission systems, and aircraft, and studies about ice growth should be done to develop new surfaces which reduce ice build-up in these systems. Superhydrophobic surfaces have been already designed to prevent ice formation. Due to their ability of repelling water, they are also "ice-phobic," exhibiting lower ice adhesion than normal surfaces. However, at very low temperatures most of these surfaces still experience frost formation.

More generally, understanding and controlling ice formation may even help address the problem of melting glaciers. It will add to our knowledge of how cold temperatures may affect both living and non-living systems, including how living cells respond to cold, and how ice forms in clouds at high altitudes. A more precise knowledge of the initial steps of freezing could eventually help to improve weather forecasts and climate models, as well as help to develop better materials for seeding clouds to increase rainfall.

Rather complex micropatterns, including sharp ridges, form during sublimation. The results for ice sublimation give a real time insight into microscopic processes that should be relevant for glaciers. Wherever glaciers contain very pure water, the ice surface morphology should be similar to scenarios presented in figures 2.21-2.28. Sublimation is, besides melting, the second way how glaciers shrink. Given the enormous local, and the potentially large global impact of glaciers on geology and on climate, glacier surfaces merit more attention - they are as yet a rather more empirical field of study. Interestingly, the sublimation scenario should be similar for Martian ice fields during summer. The

"application relevance" of glaciology on Mars might at first appear very remote, but a future permanent station will heavily depend on the availability of water, either from (postulated) streams of brine ("recurrent slope linae"), or from seasonal ice clouds, or from the ice fields, which harbour most water on Mars.

Furthermore, the merging of single crystals, their roughening, development of grain boundaries, etc. were followed in real time. These phenomena had mainly not been detected by SEM (only at lower magnification with optical microscopy). It is especially important to understand how the development of ice crystals over time is linked to the changes in water vapour pressure and temperature. Possibly the most unusual and new discovery is a substructure of the grain boundaries that appears during sublimation, namely small "pools", ascribed to gas phase transport of water molecules. A better understanding of this phenomenon could be relevant in glacier rheology or contaminant transport in glaciers. Another interesting question to address and further investigate in the future could be the effect of repeated growth and sublimation cycles. The influence of the growth history on crystal morphology is little known. It could be interesting to systematically apply repeated cycles of sublimation and growth, in order to analyse if the crystal complexity changes. In some cases of the ESEM experiments it was found that a growth phase following a sublimation phase increased the complexity of the crystals, as they can develop from a single- into a polycrystalline geometry. But to obtain a determining factor that could govern the exact behaviour, an enormous number of experimental runs should be performed.

One further question could be if the growth of the crystals on the silicon wafer is representative for atmospheric application, where the ice crystals are not in contact with a heat reservoir. Besides, it is also ambiguous how the chemical and surface structure of the nucleation material can influence the macroscopic growth results. Crystalline substrates for epitaxy are not required; however, further investigation of various nucleation substrates could be an interesting aspect. It would be ideal to find a material with a single nucleation site, suppressing ice growth elsewhere, since otherwise ice forms at many unwanted places inside the microscope chamber, which leads to a fast depletion of the water vapour reservoir.

2.6 References

[1] G. Sazaki, S. Zepeda, S. Nakatsubo, M. Yokomine, and Y. Furukawa, “Quasi-liquid layers on ice crystal surfaces are made up of two different phases,” *Proc. Natl. Acad. Sci. U. S. A.*, vol. 109, no. 4, pp. 2–5, 2011.

[2] W. Wagner, A. Saul, and A. Pruss, “International Equations for the Pressure along the Melting and along the Sublimation Curve of Ordinary Water Substance,” *J. Phys. Chem.*, vol. 23, 1994.

[3] G. et al. Danilatos, “Integrated electron optical/differential pumping/Imaging signal detection system for an environmental scanning electron microscope,” 1989.

[4] M. Dufek, “The Quanta FEG 250 / 450 / 650 User Operation Manual 5,” no. December, p. 228, 2010.

[5] R. Johnson, “Environmental Scanning Microscopy: An introduction to ESEM®,” pp. 1–56, 1996.

[6] T. Dahmen *et al.*, “Feature Adaptive Sampling for Scanning Electron Microscopy,” *Sci. Rep.*, vol. 6, no. April, p. 25350, 2016.

[7] J. M. Alonso, M. L. Górzny, and A. M. Bittner, “The physics of tobacco mosaic virus and virus-based devices in biotechnology,” *Trends Biotechnol.*, vol. 31, no. 9, pp. 530–538, 2013.

[8] H. Asakawa, G. Sazaki, E. Yokoyama, K. Nagashima, S. Nakatsubo, and Y. Furukawa, “Roles of surface/volume diffusion in the growth kinetics of elementary spiral steps on ice basal faces grown from water vapor,” *Cryst. Growth Des.*, vol. 14, no. 7, pp. 3210–3220, 2014.

[9] G. W. Bryant, J. Hallett, and B. J. Mason, “The epitaxial growth of ice on single-crystalline substrates,” *J. Phys. Chem. Solids*, vol. 12, no. 2, pp. 189–195, 1960.

[10] J. Cazaux, “On some contrast reversals in SEM: Application to metal/insulator systems,” *Ultramicroscopy*, vol. 108, no. 12, pp. 1645–1652, 2008.

[11] M. Toth, B. L. Thiel, and A. M. Donald, “Interpretation of secondary electron images obtained using a low vacuum SEM,” *Ultramicroscopy*, vol. 94, no. 2, pp. 71–87, 2003.

[12] B. L. Thiel, “Master curves for gas amplification in low vacuum and environmental scanning electron microscopy,” *Ultramicroscopy*, vol. 99, no. 1, pp. 35–47, 2004.

[13] N. B. Magee, A. Miller, M. Amaral, and A. Cumiskey, “Mesoscopic surface roughness of ice crystals pervasive across a wide range of ice crystal conditions,” *Atmos. Chem. Phys.*, vol. 14, no. 22, pp. 12357–12371, 2014.

[14] C. Pedersen, A. Mihranyan, and M. Strømme, “Surface transition on ice induced by the formation of a grain boundary,” *PLoS One*, vol. 6, no. 9, 2011.

[15] R. F. Egerton, P. Li, and M. Malac, “Radiation damage in the TEM and SEM,” *Micron*, vol. 35, no. 6, pp. 399–409, 2004.

[16] C. P. Royall, B. L. Thiel, and A. M. Donald, “Radiation damage of water in environmental scanning electron microscopy,” *J. Microsc.*, vol. 204, no. January, pp. 185–195, 2001.

[17] R. Henderson, “The potential and limitations of neutrons, electrons and X-rays for atomic resolution microscopy of unstained biological molecu,” *Q. Rev. Biophys.*, vol. 28, no. 2, pp. 171–193, 2009.

[18] R. Henderson, “The potential and limitations of neutrons, electrons and X-rays for atomic resolution microscopy of unstained biological molecu,” *Quarterly Reviews of Biophysics*, vol. 28, no. 2. pp. 171–193, 1995.

[19] U. Mirsaidov, C.-D. Ohl, and P. Matsudaira, “A direct observation of nanometer-size void dynamics in an ultra-thin water film,” *Soft Matter*, vol. 8, no. 27, pp. 7108–7111, 2012.

[20] K. G. Libbrecht and M. E. Rickerby, “Measurements of surface attachment kinetics for faceted ice crystal growth,” *J. Cryst. Growth*, vol. 377, pp. 1–8, 2013.

[21] M. Maruyama, “Roughening transition of prism faces of ice crystals grown from melt under pressure,” *J. Cryst. Growth*, vol. 275, no. 3–4, pp. 598–605, 2005.

[22] T. Gonda and T. Yamazaki, “Morphology of ice droxtals grown from supercooled water droplets,” *J. Cryst. Growth*, vol. 45, no. C, pp. 66–69, 1978.

[23] W. C. Pfalzgraff, R. M. Hulscher, and S. P. Neshyba, “Scanning electron microscopy and molecular dynamics of surfaces of growing and ablating hexagonal ice crystals,” *Atmos. Chem. Phys. Discuss.*, vol. 9, no. 5, pp. 20739–20763, 2009.

[24] K. Thürmer and S. Nie, “Formation of hexagonal and cubic ice during low-temperature growth,” *Proc. Natl. Acad. Sci. U. S. A.*, vol. 110, no. 29, pp. 11757–11762, 2013.

[25] G. Sazaki, H. Asakawa, K. Nagashima, S. Nakatsubo, and Y. Furukawa, “How do quasi-liquid layers emerge from ice crystal surfaces?,” *Cryst. Growth Des.*, vol. 13, no. 4, pp. 1761–1766, 2013.

[26] H. Asakawa, G. Sazaki, K. Nagashima, S. Nakatsubo, and Y. Furukawa, “Prism and Other High-Index Faces of Ice Crystals Exhibit Two Types of Quasi-Liquid Layers,” *Cryst. Growth Des.*, vol. 15, no. 7, pp. 3339–3344, 2015.

[27] S. P. Neshyba, B. Lowen, M. Benning, A. Lawson, and P. M. Rowe, “Roughness metrics of prismatic facets of ice,” *J. Geophys. Res. Atmos.*, vol. 118, no. 8, pp. 3309–3318, 2013.

[28] N. Butterfield, P. M. Rowe, E. Stewart, D. Roesel, and S. Neshyba, “Quantitative three dimensional ice roughness from scanning electron microscopy,” *J. Geophys. Res. Atmos.*122, 2017.

[29] T. Bartels-Rausch *et al.*, “Ice structures, patterns, and processes: A view across the icefields,” *Rev. Mod. Phys.*, vol. 84, no. 2, pp. 885–944, 2012.

[30] T. Bartels-Rausch *et al.*, “A review of air-ice chemical and physical interactions

(AICI): Liquids, quasi-liquids, and solids in snow," *Atmos. Chem. Phys.*, vol. 14, no. 3, pp. 1587–1633, 2014.

[31] J. F. Nye and S. Mae, "The effect of non-hydrostatic stress on intergranular water veins and lenses in ice," *J. Glaciol.*, vol. 11, no. 61, pp. 81–101, 1972.

[32] B. M. E. R. Walford, D. W. Roberts, and I. Hill, "Optical measuremen ts of water lenses in ice," vol. 33, no. 114, pp. 159–161, 1987.

[33] H. M. Mader, "Observations of the water-vein system in polycrystalline ice," *J. Glaciol.*, vol. 38, no. 130, pp. 333–347, 1992.

[34] P. R. F. Barnes, E. W. Wolff, D. C. Mallard, and H. M. Mader, "SEM studies of the morphology and chemistry of polar ice," *Microsc. Res. Tech.*, vol. 62, no. 1, pp. 62–69, 2003.

[35] M. Krzyzak, K. Techmer, S. Faria, G. Genov, and W. Kuhs, "Atomic force microscopy of rearranging ice surfaces," *Phys. Chem. Ice*, vol. 1, p. 347, 2007.

[36] J. D. Cross, "Scanning Electron Microscopy of Evaporating Ice," *Science (80-.).*, vol. 164, pp. 174–175, 1969.

[37] J. D. Cross, "The effect of impurities on the structure of evaporating ice," *J. Glaciol.*, vol. 10, no. 59, 1971.

[38] D. Waller, D. J. Stokes, and A. M. Donald, "Development of Low Temperature ESEM: Exploring Sublimation," *Microsc. Microanal.*, vol. 11, no. S02, pp. 414–415, 2005.

[39] J. Nelson and C. A. Knight, "A new technique for growing crystals from the vapor," *J. Cr*, vol. 169, pp. 795–797, 1996.

[40] I. Baker, D. Cullen, and D. Iliescu, "The microstructural location of impurities in ice," *Can. J. Phys.*, vol. 81, no. 1–2, pp. 1–9, 2003.

[41] W. Rosenthal, J. Saleta, and J. Dozier, "Scanning electron microscopy of impurity structures in snow," *Cold Reg. Sci. Technol.*, vol. 47, no. 1–2 SPEC. ISS., pp. 80–

89, 2007.

[42] R. Mulvaney, E. W. Wolff, and K. Oates, “Sulphuric acid at grain boundaries in Antarctic ice,” *Nature*, vol. 331, no. 6153, pp. 247–249, 1988.

[43] D. Cullen and I. Baker, “Observation of impurities in ice,” *Microsc. Res. Tech.*, vol. 55, no. 3, pp. 198–207, 2001.

[44] S. M. DE MICHELl, “Experimental Study of the Evaporation of Ice in Controlled Conditions of Subsaturation,” *Physics of Snow and Ice : proceedings*, vol. 1, no. 1. pp. 259–266, 1967.

[45] C. S. Hvidberg and H. J. Zwally, “Sublimation of water from the north polar cap on Mars,” Workshop “Mars Atmosphere Modelling and Observations” Granada, Spain, pp. 13–15, 2003.

[46] A. K. Bliss, K. M. Cuffey, and J. L. Kavanaugh, “Sublimation and surface energy budget of Taylor Glacier, Antarctica,” *J. Glaciol.*, vol. 57, no. 204, pp. 684–696, 2011.

[47] J. P. L. Johnson, “Journal of Geophysical Research : Earth Surface,” pp. 1–27, 2014.

[48] E. L. Andreas, “New estimates for the sublimation rate for ice on the Moon,” *Icarus*, vol. 186, no. 1, pp. 24–30, 2007.

[49] D. Nowak, M. Heuberger, M. Zäch, and H. K. Christenson, “Thermodynamic and kinetic supercooling of liquid in a wedge pore,” *J. Chem. Phys.*, vol. 129, no. 15, pp. 1–8, 2008.

Chapter 3:
Imaging and particle tracking analysis of the quasi-liquid layer

3.1. Experimental part

As described in the previous chapter, the investigations were carried out on an *n*-type silicon substrate. Silicon wafers ((111) orientation, thickness 0.27mm, doped with phosphorus, resistivity >1) were cut into 4x4 mm squares with a wafer dicing saw (Disco DAD321) and thoroughly cleaned by sonication in an ultrasonicator (VWR Ultrasonic Cleaner) for 15 minutes in a sequence of three solvents: isopropanol (LC-MS chromasolv®, Sigma-Aldrich), acetone (ACS reagent >99.5%, Sigma-Aldrich), water (18 MOhm cm, <5ppb total organic content, Millipore) solutions.

The nanoparticles were introduced into the system by pipetting 10µl of a commercial gold nanoparticle (150nm diameter) solution (stabilized suspension in citrate buffer, Sigma Aldrich, Missouri, USA) (see figure 3.1).

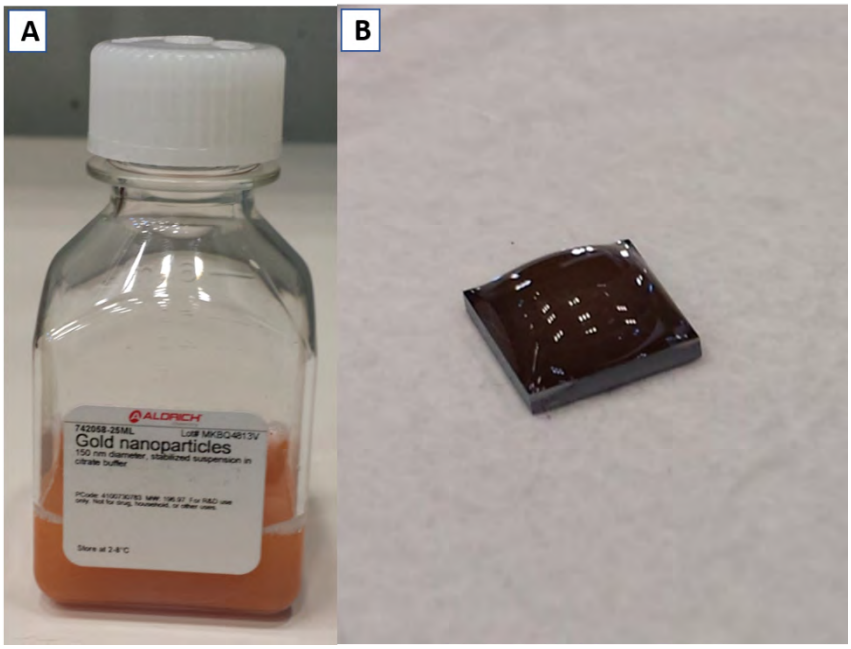

Figure 3.1. A) Gold nanoparticles commercial solution. **B)** 10µl droplet gold nanoparticle solution on silicon wafer.

To ensure that the sample remains fixed throughout the experiments, an indium bonding technique was used, replacing the previously used gallium indium alloy. The bond was made by melting a thin strip of indium (melting point is 156.6°C) with a soldering iron. The indium was then placed between the silicon wafer and the copper stub. Mechanical pressure was exerted until the indium cooled and solidified. The final ensemble consisted of an oxidized silicon wafer placed on a copper stub (see figure 3.2). Once the silicon wafer was firmly fixed to the copper stub, the complete ensemble was introduced in an oxygen plasma cleaner ("Femto", Diener) for approximately 8 min with a 10 sscm gas flow to remove impurities from the surface. In the last step of the sample preparation process, 10µl of a gold nanoparticle solution were pipetted onto the silicon wafer and allowed to dry in air.

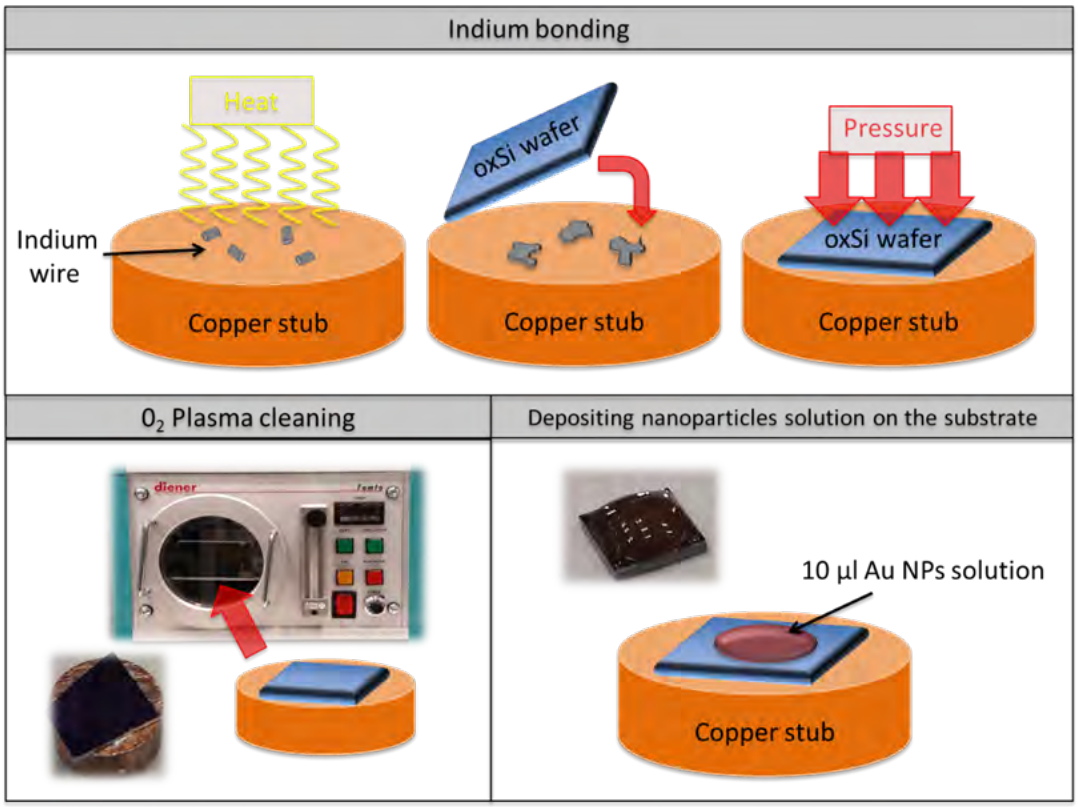

Figure 3.2. Sample preparation process.

As it is illustrated in figure 3.3, the evaporation flux (vertical arrows) is greatest at the edges of the droplet of the nanoparticle solution; this drives the flow of particles towards the edge. The flow becomes stronger radially outwards. It was observed that a ring forms when a dispersion of gold nanoparticles is dried over the silicon substrate.

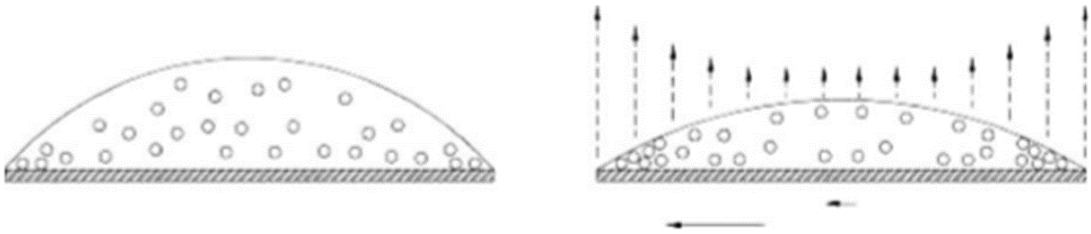

Figure 3.3. Mechanism of coffee ring formation (taken from [1]).

Once the nanoparticles solution is dried, the sample can be introduced into the ESEM (see figure 3.4). The copper stub was fixed in the Peltier stage with aluminium foil, which assures a good thermal contact.

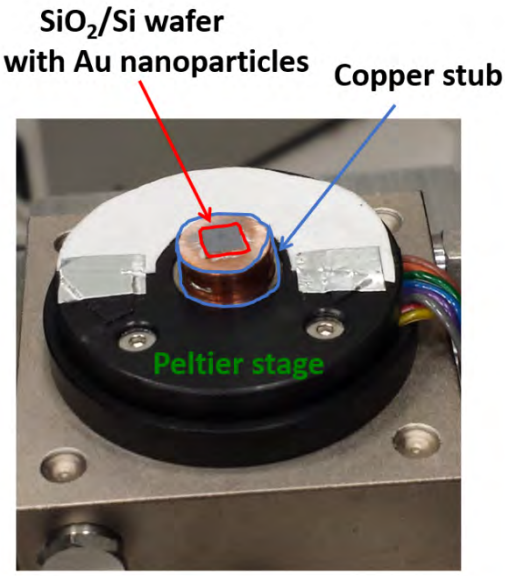

Figure 3.4. Sample mounted in the ESEM Peltier stage.

The sample was evacuated, the chamber was purged with water vapour (see section 2.2 in chapter 2), and then cooled with the Peltier stage. The temperature was kept at around -15°C (for section 3.2 at higher temperatures). At low pressures, all water remains in the gas phase. The pressure was then increased until the sublimation line was crossed (see figure 3.5). At this point ice starts to grow on the sample, at the same time images and movies can be recorded in real time.

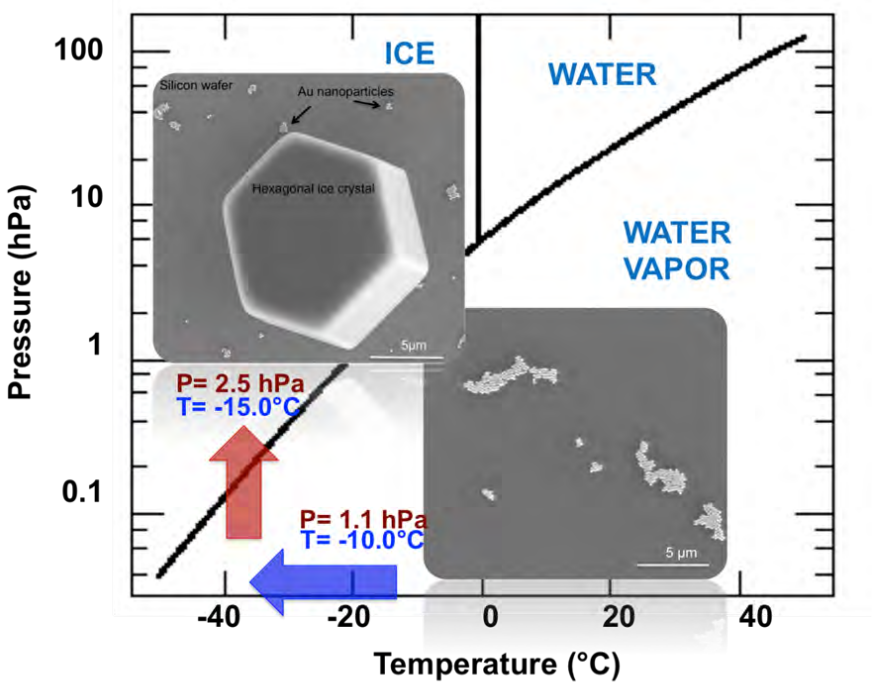

Figure 3.5. Water phase diagram and experimental procedure used in the ESEM.

Most of the gold nanoparticles remained on the wafer (see figure 3.6), but some of them appeared on the ice and nanoparticles movements were detected.

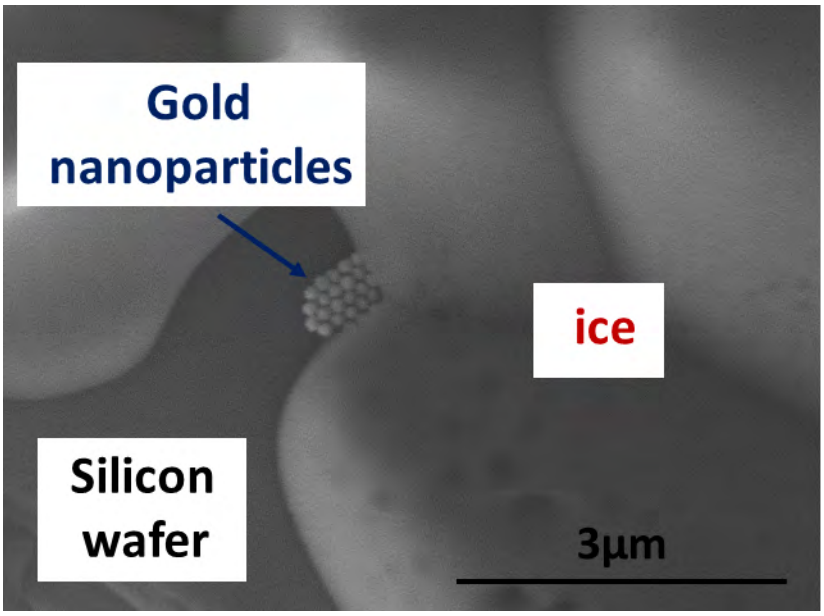

Figure 3.6. ESEM image showing the gold nanoparticles stuck to the wafer and not on top of the ice. The lower left part shows some defects of the wafer, close to its edge.

When a nanoparticle or a cluster of aggregated nanoparticles was detected on top of the grown ice, video capture was initiated, but only after the system had stabilized, once no more ice growth was observed. This procedure was used to ensure that the movement of the nanoparticle was not influenced by abrupt changes in pressure or temperature.

3.2. Preliminary ESEM tests for ice surface dynamics at high T (close to 0ºC)

When the ice samples were heated to just below 0°C, the formation of microdroplets was observed, although the temperature should not allow for melting (see figure 3.7 and phase diagram figure 1.3 in chapter 1). This premelting phenomenon is due to the so-called alpha- and beta-QLLs at temperatures higher than −1.4 to −0.5 °C and −0.8 to −0.3 °C, respectively, as described by *Sazaki et al.* in optical microscopy studies [2]–[4]. Size and shape of the droplets assigned to the alpha phase are similar to the findings in this study, which show that these types of “high temperature” QLLs are accessible by SEM. Various other studies have found very thick premelted layers (10 to 100 nm) in the range 1 K to 0.1 K below melting [5], but not locally (microscopy).

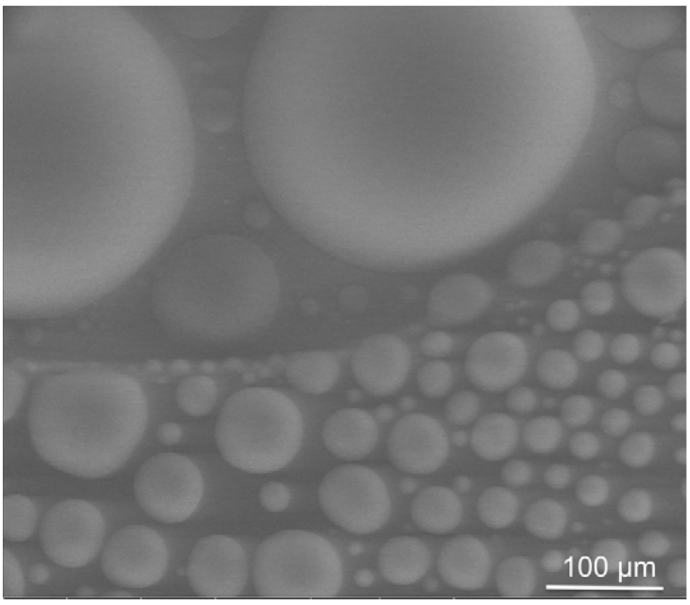

Figure 3.7. Structure of bulk ice observed after heating to a few Kelvin below melting. Imaging conditions: P = 511 Pa, T = -2.3 °C, h = 0.98 after excursion to h > 1.

Premelting and hence QLLs can also occur at much lower temperatures, and in this case the phenomenon should depend very much on the local topography, especially on the crystal surface orientation. SEM was thought to be able to image the QLL on metals[6], though charging effects can easily be misinterpreted. At the temperatures studied here, the QLL or disordered top layers on Ih ice should have a thickness of only a few molecular layers [5].

Contrary to the conventional hypothesis of surface melting, according to which only one QLL phase fully covers the ice surface at the solid−vapour equilibrium. *Asakawa et al.*, using laser confocal microscopy combined with differential interference contrast microscopy, have found that the two types of QLLs are kinetically formed, not by the melting of ice surfaces, but by the deposition of supersaturated (h>1) water vapour on ice surfaces [7]. In this study, it has been found that on the surface of ice grown using ESEM, thin liquid-like layers (β-QLL phases), marked with red arrows in figure 3.8, spontaneously appear at temperatures below the range suggested by *Asakawa et al*. Figure 3.8 shows a somehow complex scenario: A TEM grid, made from copper (cross-like structure), covered by a thin carbon film (invisible) is slowly covered by a thin ice layer. On the copper (red marker at right) and on the carbon film (red marker at left) round objects appear, which coalesce into a larger object. These resemble probably the droplets in figure 3.7.

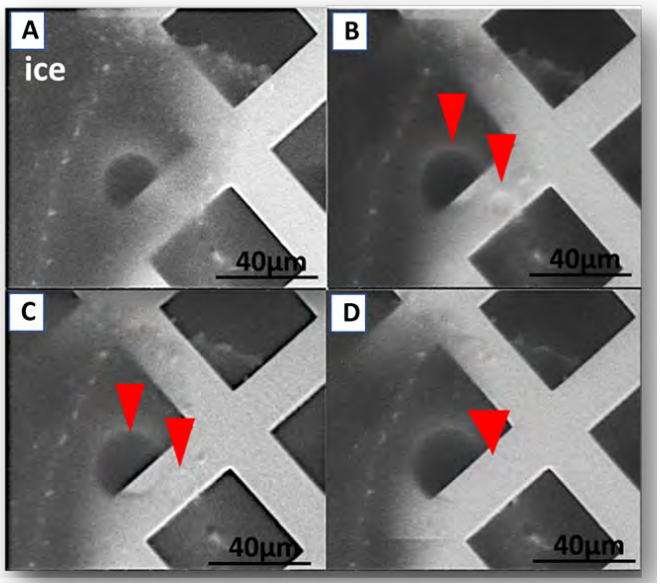

Figure 3.8. Serie of images showing dynamic behaviour of the β-QLLs. Droplets coalesce (red markers), see text. Imaging conditions: P = 257 Pa, T = -10 °C, h = 0.89

The same images are shown in greater detail in figure 3.9.A and figure 3.9.B. The thinly layered objects (marked with a red arrowhead) spontaneously appeared on the ice surface. This β-QLL gradually becomes larger before coalescing with each other, showing significant fluidity. The thinly layered object exhibits a circular disk shape due to its surface tension. These findings provide strong evidence that the thinly layered objects are in the liquid state.

In a recently study[8], the formation of QLLs has been classified into two distinct processes, surface condensation for supersaturation and surface premelting for undersaturation, proving the existence of QLL also in undersaturated conditions, such as in the case shown in figure 3.8 (h = 0.89).

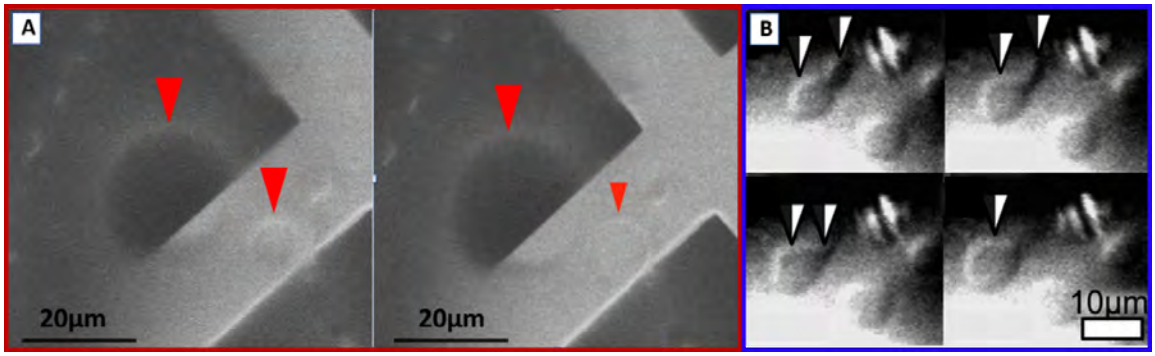

Figure 3.9. A) Features found in the ESEM at T = -10 °C, P = 257 Pa and h = 0.89. **B)** Coalescence of thin liquid-like layers (β-QLLs) observed by laser confocal microscopy combined with differential interference contrast microscopy. T= −0.6 °C [9]

Experimental efforts have been accomplished to reveal the origin of surface melting, including the nature of QLLs themselves but it is still far from completely understood and a matter of active debate. A direct visualization or in situ observation of the quasi liquid layer was rarely achieved; ref. [34] is a notable exception.

3.3. Nanoparticle tracking method

Experiments to date have generally shown a very thin QLL, which continuously grows in thickness up to 45 nm right below the bulk melting point at 0°C. Note that the chemical nature of the QLL is practically identical to solid ice, so that it escapes most experimental

techniques. A proof of the fluid nature of the QLL, and its quantification require two changes in the experimental approach: First, lower temperatures assure that the QLL is so thin that it resembles the standard ice surface, without droplet-like features, and without the complication of beam-induced heating, which might locally melt the solid. In other words, a thick solid ice surface is assured. Second, the mobility of the (presumably ultrathin) QLL requires a local probe, spherical nanoparticles. They could potentially indicate the presence of a quasi-liquid layer since they should be mobile only on the QLL, not on solid ice (see figure 3.10)

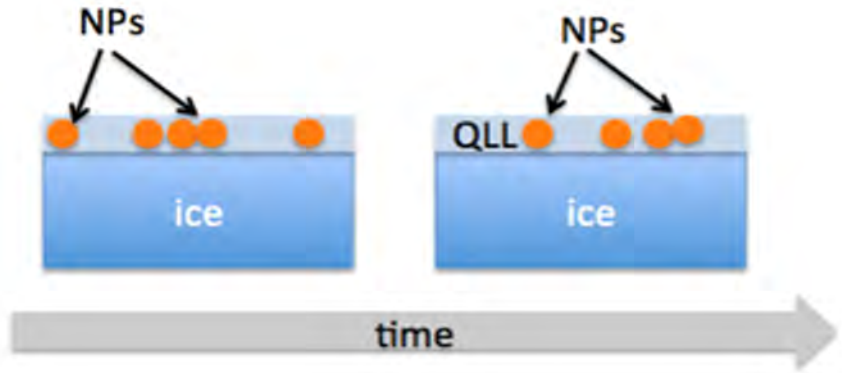

Figure 3.10. Scheme showing a potential movement of the nanoparticles on or in the QLL.

As previously mentioned, for a spherical particle the diffusion in a low-viscosity medium can be predicted by the Stokes-Einstein (SE) equation:

$$D = \frac{k_B T}{6\pi\eta R_H} \qquad (3.1)$$

where k_B is the Boltzmann constant, T is the temperature and R_H the hydrodynamic radius of the particle. In microrheology, a relatively new technique based on microparticle motion, the viscosity η of the medium can be calculated from the diffusion coefficient D, which in turn is extracted from tracking the movements of individual Brownian microparticles. One intuitive question to ask is if a "nanorheology" can be developed, based on diffusion of nanoparticles observed by SEM, and in case of an affirmative answer, which particles of which size would qualify.

There might be a principal barrier: If the SE equation is applicable to the diffusion of nanoparticles, especially at surfaces or interfaces, remains like one unanswered question. For example, it has been reported [10] that cadmium selenide nanoparticles diffuse approximately 200 times faster in a polystyrene melt than the prediction from the SE equation. Using MD simulations, the diffusive behaviour of nanoparticles in pure water and low-viscosity PDMS oil is found to be consistent with the prediction from the Stokes-Einstein equation[11]. In this same study, it has been found that the lateral diffusion of nanoparticles at two different phase interfaces (in this case PDMS oil-water interface) is independent of the position of the nanoparticle at the interface even if it is clear that the nanoparticle immerses more deeply into the water phase with increasing surface charges (see figure 3.11). This could indicate that the even when the position of the nanoparticle along the z axis is unknown, the obtained translational diffusion coefficients can be reliable and constitute a good approximation.

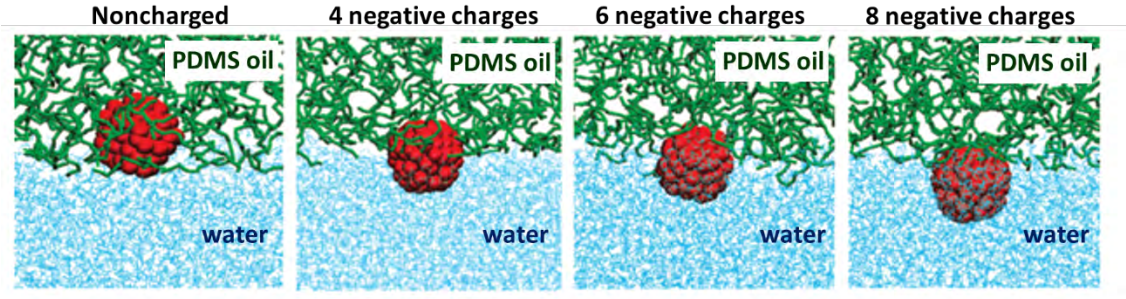

surface charges of nanoparticle	D_{xyz} ($\times 10^{-5}$ cm^2/s)	D_{xy} ($\times 10^{-5}$ cm^2/s)	D_z ($\times 10^{-5}$ cm^2/s)
no charge	0.077 ± 0.004	0.082 ± 0.009	0.043 ± 0.004
4 negative charges	0.059 ± 0.006	0.082 ± 0.007	0.003 ± 0.001
6 negative charges	0.057 ± 0.007	0.081 ± 0.008	0.017 ± 0.002
8 negative charges	0.067 ± 0.004	0.084 ± 0.005	0.019 ± 0.002

Figure 3.11. The immersion of the nanoparticles with different surface charges at the PDMS oil-water interfaces Diffusion constants of nanoparticles at PDMS oil-water interfaces. Inside the red rectangle are shown the lateral diffusion constants (xy plane) of the nanoparticles at the oil-water interfaces, all of them with similar values. Redrawn from [11]

An investigation of diverse types of nanoparticles has been undertaken (see figure 3.12). Here gold, latex and polystyrene nanoparticles of various sizes have been tested. In the absence of ice (at high vacuum) all nanoparticles are easily imaged with an electron microscope, but the experimental procedure used in this study requires not only a good characterization of the nanoparticles but also to distinguish them from the growing ice.

Gold nanoparticles with 15nm diameter were found to be too small for these experiments since high magnification images are needed to detect them. Latex nanoparticles (200 nm diameter) appear to affect the ice nucleation on the silicon wafer, and fewer ice crystals were observed. Most of the ice grows at the edge of the wafer and not on across the entire surface of the substrate. In the case of the 90nm-diameter polystyrene nanoparticles, the ice layer appears between the nanoparticles. However, growth is very slow and single crystals have not been observed.

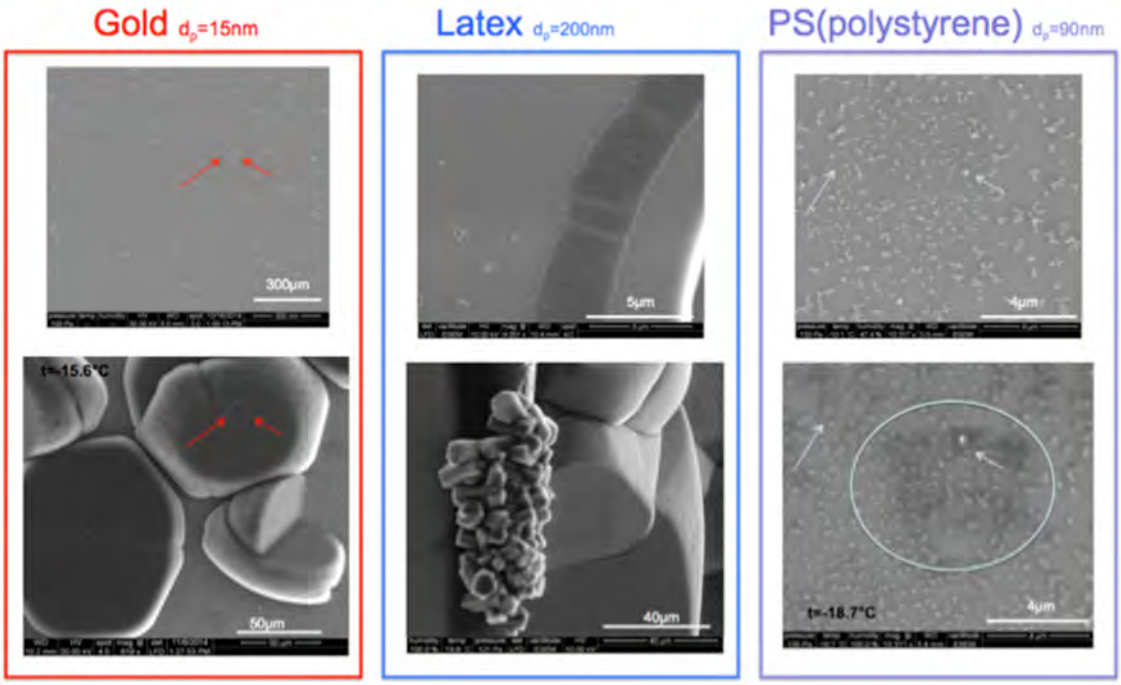

Figure 3.12. Diverse types of nanoparticles tested: 15nm diameter gold nanoparticles, 200nm diameter latex nanoparticles and 90nm polystyrene nanoparticles. Imaging conditions: (Gold NP) P = 135 Pa, T = -18.4 °C, h = 1.12; (Latex NP) P = 121 Pa, T = -19.8 °C, h = 1.15; (PS NP) P = 135 Pa, T = -18.7 °C, h = 1.15.

Figure 3.13 demonstrates the enormous difference in contrast between the gold and the latex nanoparticles, making the gold nanoparticles the most suitable candidate for observation on ice. Different concentrations of nanoparticle solutions have been studied for the purpose of preventing excessive self-assembly or arrangement of the nanoparticles. For developing subsequent tracking experiments, single nanoparticles rather than clusters of nanoparticles should be obtained. It can be observed (figure 3.13) that latex nanoparticles tend to self-assemble, while gold nanoparticles remain as individual entities or form only small clusters, composed of 2-10 nanoparticles.

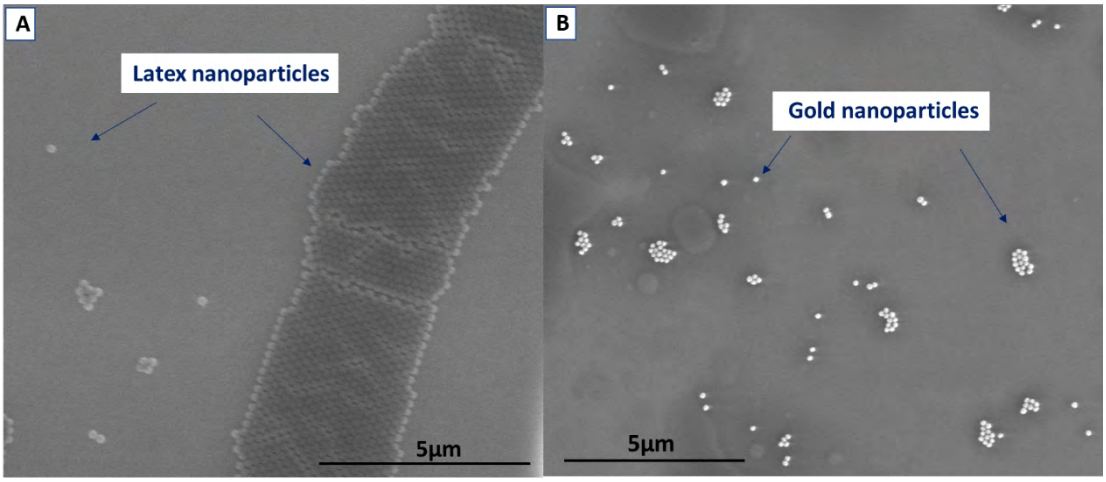

Figure 3.13. SEM images from **A)** 200 nm diameter latex nanoparticles and **B)** 150 nm diameter gold nanoparticles. Imaging conditions: (a) P = 165 Pa, T = -16.6 °C, h = 1.16; (b) P = 200 Pa, T = -15.0 °C, h = 1.20.

After imaging the nanoparticles under high vacuum, the microscope was switched to ESEM mode to initiate the growth of ice from the water vapour inside the microscope chamber (see figure 3.14). Again, it is obvious that the contrast one can achieve is higher with the gold nanoparticles than with the latex ones, making the distinction between ice, substrate and nanoparticles straightforward.

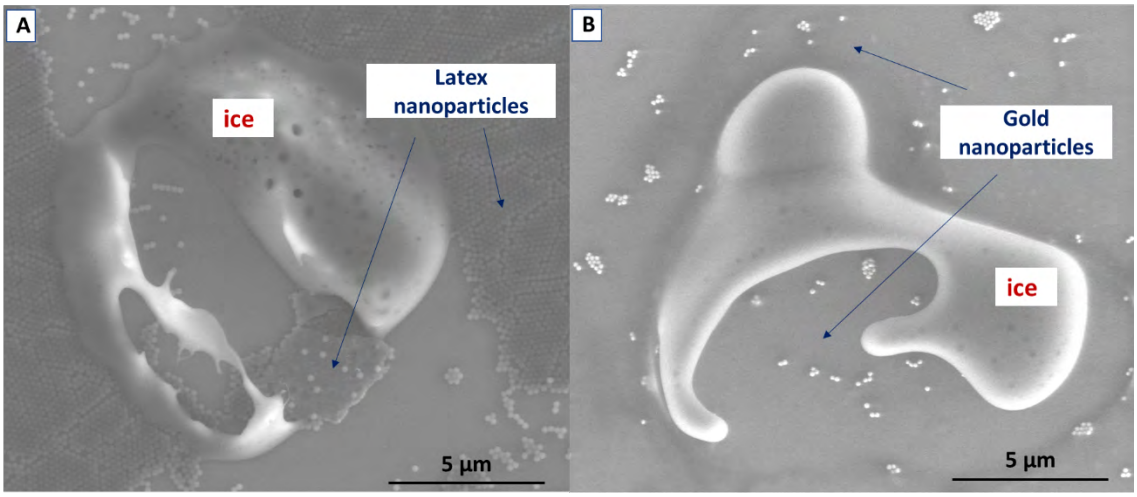

Figure 3.14. ESEM images from ice grown on a silicon substrate with **A)** 200 nm diameter latex nanoparticles and with **B)** 150 nm diameter gold nanoparticles. Imaging conditions: (a) P = 165 Pa, T = -16.6 °C, h = 1.16; (b) P = 170 Pa, T = -16.5 °C, h = 1.19.

After testing several types and sizes, 150 nm diameter gold nanoparticles were selected (see figure 3.15).

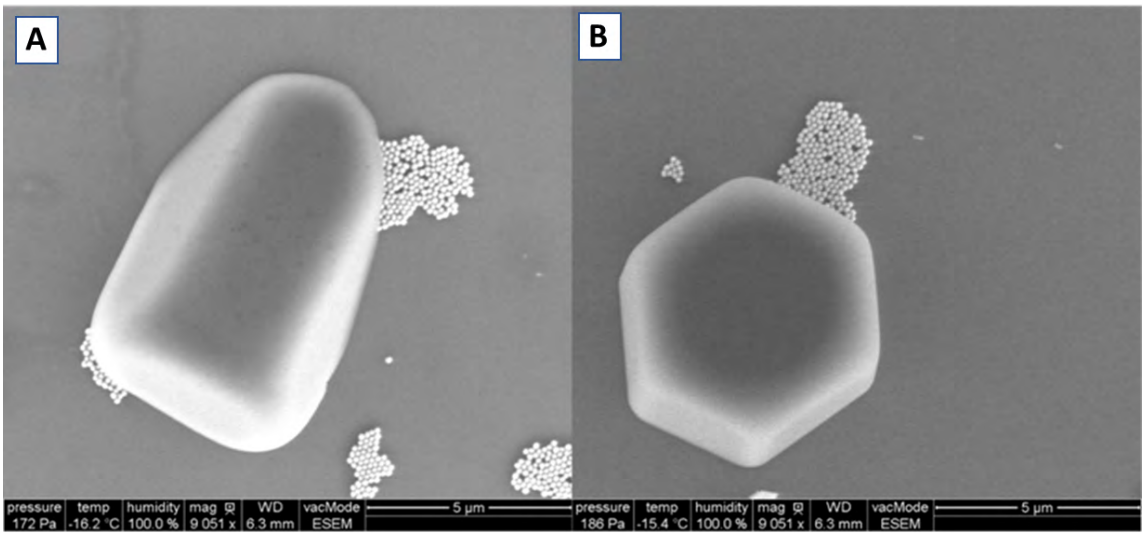

Figure 3.15. 150 nm diameter gold nanoparticles and hexagonal ice crystals growth on a silicon wafer. Imaging conditions: (a) P = 172 Pa, T = -16.2 °C, h = 1.16; (b) P = 186 Pa, T = -15.4 °C, h = 1.17.

3.3.1. Tracking analysis

Using fast ESEM imaging, videos were recorded of nanoparticle movement on the ice surface at a rate of one frame per second. The obtained videos are processed and analysed with different software tools:

- *Ffmpeg* is a free cross-platform software for video processing. This software was used for converting the .mov videos recorded by the microscope software to another more suitable format (.avi). The primary role of *ffmpeg* is to normalize the framerate of these videos. In this analysis videos at one frame per second (1fps) were used.
- *ImageJ* is a public domain Java image and analysis software. It was used to measure distances between two points in an image and set the scale (pixels per micrometre). There are many plugins developed for this software that can be used for extra functionalities, for example the *MTrackJ* plugin.

- *MTrackJ*. This software is developed as a plugin for ImageJ. It gives the possibility of plotting trajectories in videos recorded with the environmental scanning electron microscope.

The tools above mentioned are useful for acquiring data from the videos obtained in this study. Subsequently, *MATLAB* was used to obtain useful parameters for analysis of the nanoparticle movements.

A detailed description of the software tools mentioned above is given in Appendix I.

As mentioned, the *MTrackJ* software is used to carry out the tracking, providing the chance to visualize the trajectories followed by each nanoparticle (see figure 3.16).

Each coloured trajectory represents one nanoparticle movement with time.

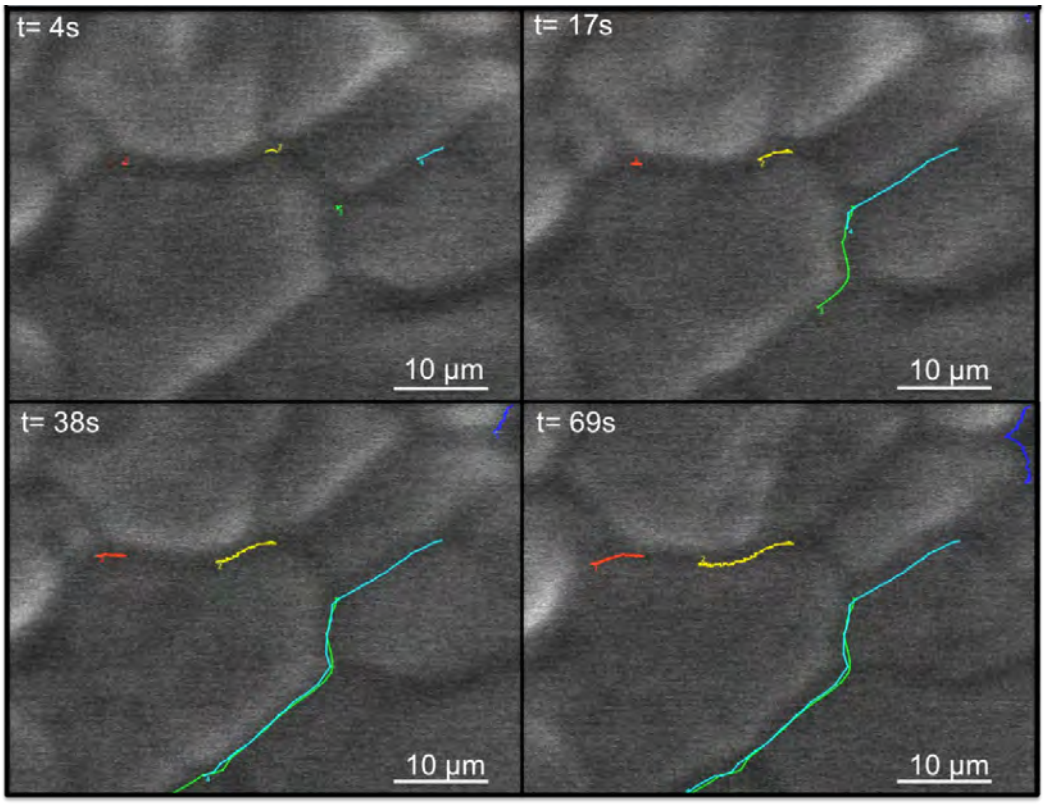

Figure 3.16. Sequence of images showing a tracking example, in which trajectories of five different nanoparticles are determined and drawn. Imaging conditions: (a) P = 448 Pa, T = -5.5 °C, h = 1.16.

3.3.2. MATLAB code

The MATLAB code uses the positions of particles that have been saved in a file after the tracking procedure to compute the mean-squared displacement (MSD) of each particle for time intervals ranging from 1/frame rate, to frame rate/(number of frames −1), at multiples of 1/frame rate. Here, as a frame rate of 1 s^{-1} is used to capture the videos, for a movie clip of 40 frames, the MSD is calculated for time intervals 1−39 s, at one second intervals.

The MATLAB code (for details see appendix I and appendix II) calculates not only the mean square displacement, but also plots the trajectories of the different nanoparticles that appear in each analysed video (see figure 3.17). The mean square displacement is plotted for each individual nanoparticle (see figure 3.18) and in the logarithmic plot of the mean square displacement versus τ (see figure 3.19) automated fits of the MSD curves are included, allowing derivation of the type of motion and its characteristics. Finally, the MATLAB code can plot the velocities of each nanoparticle in x and y separately (see figure 3.20.A) and the speed of each nanoparticle throughout the complete movement (see figure 3.20.B).

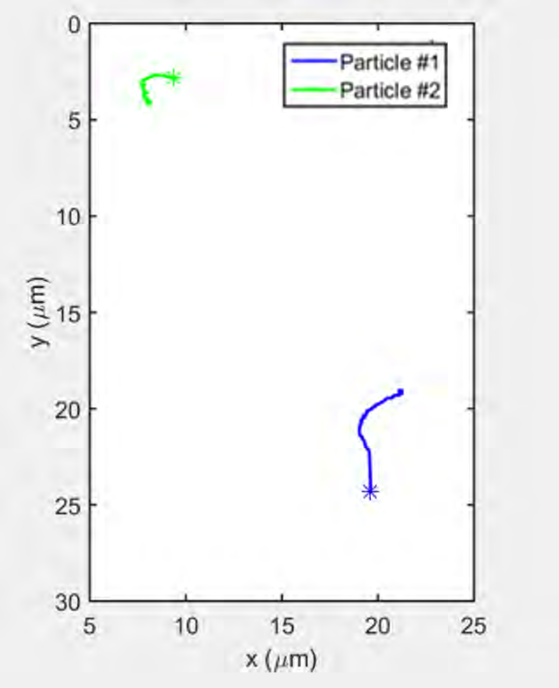

Figure 3.17. Trajectories followed by each nanoparticle in the analysed video. Asterisks mark the start of the trajectories.

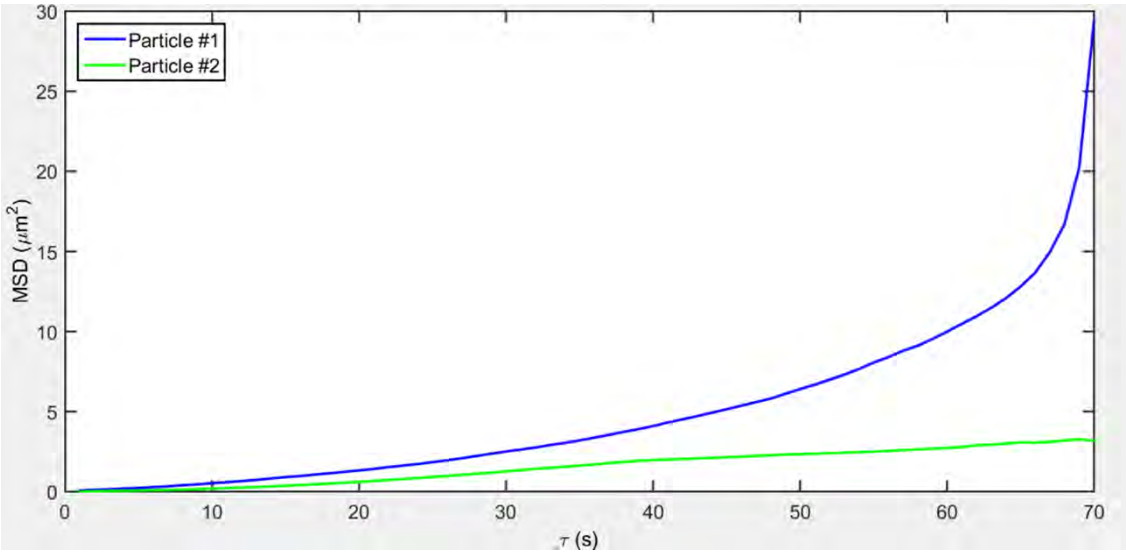

Figure 3.18. Individual MSD curves of each nanoparticle in the analysed video. Curves appear to differ largely due to the spread of experimental data.

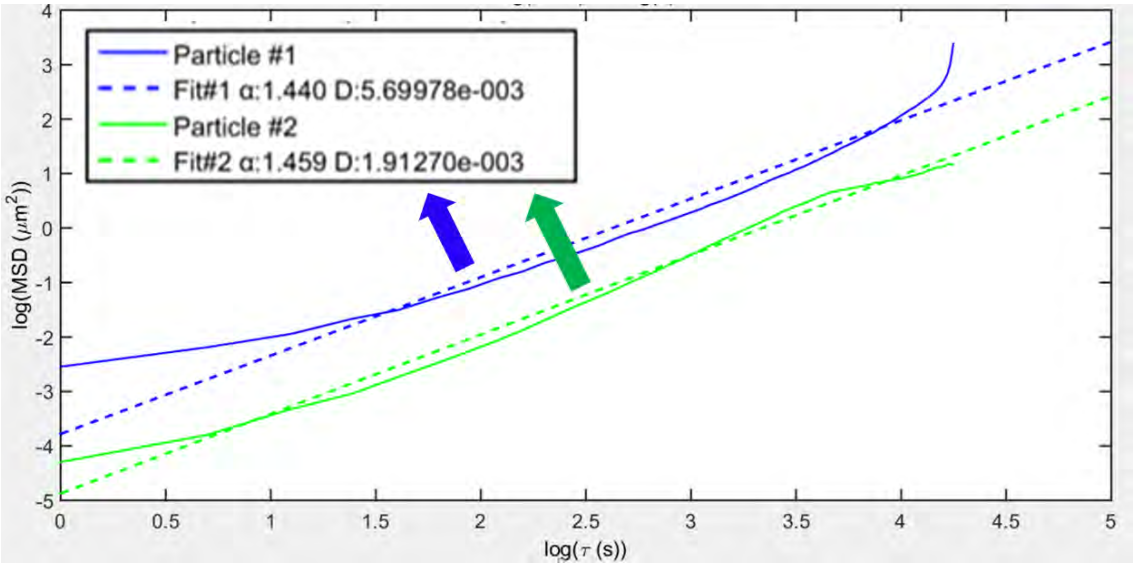

Figure 3.19. Logarithmic plot of the MSD respect to τ (log is the natural logarithm ln). Diffusion coefficient values D (for anomalous diffusion D') and the type of movement α undergone by each nanoparticle can be derived from fitting.

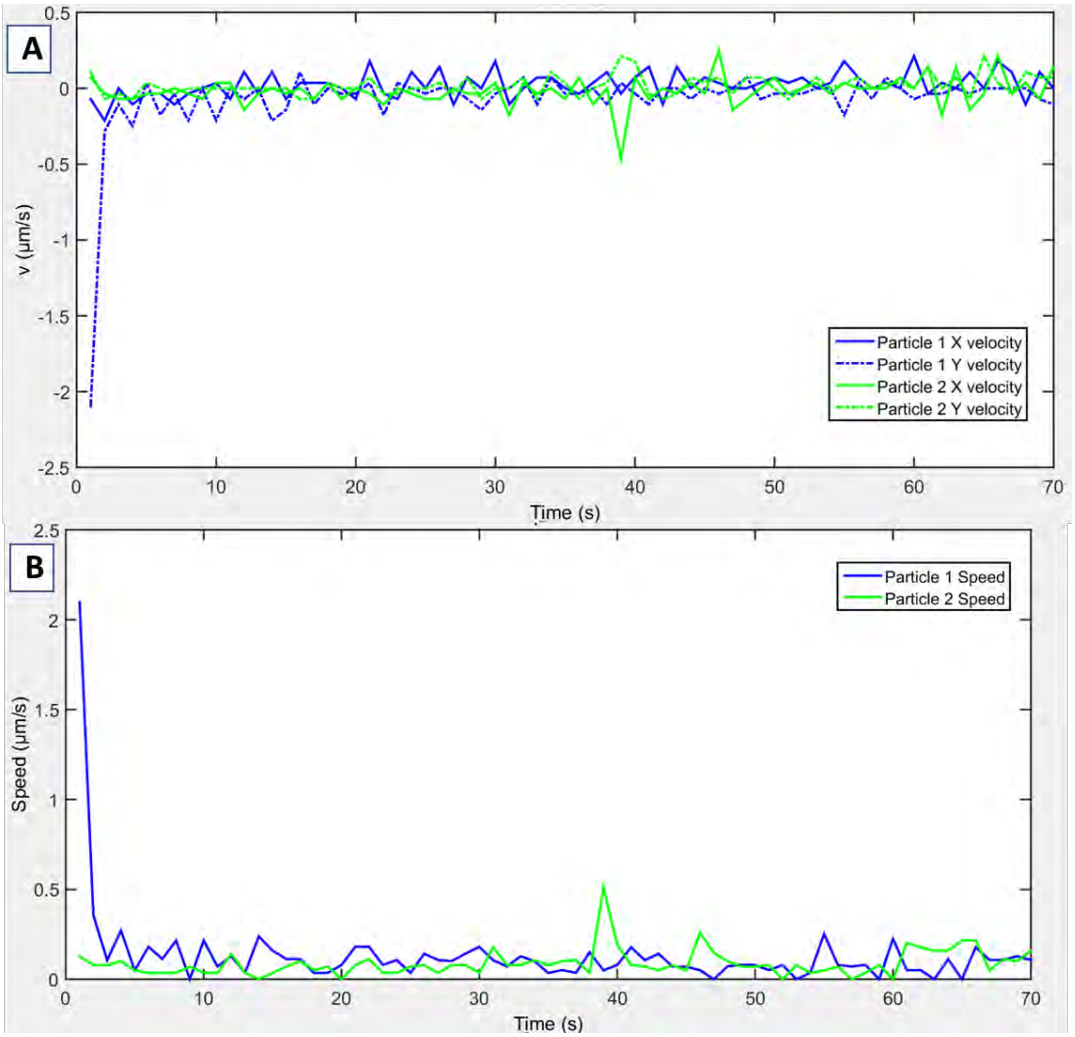

Figure 3.20. A) Velocities in x and y for each nanoparticle. **B)** Speed of each nanoparticle during the analysed movement.

3.4. Nanoparticle tracking results

First and foremost, Au NPs do move at temperatures well below the documented alpha and beta phases, i.e. at temperatures where the "thin layer QLL" should exist. Two possible models explain the nanoparticle movement (see figure 3.21). According to model (I), nanoparticles would be rolling or floating on a thin pure water QLL and, if we are in the environment depicted by model (II), charged counterions could detach from the particles and liquify more ice to create a thick QLL.

Model (I) requires wetting, not only by water, but also by the QLL. Wetting can be traced back to surface chemistry and charge of citrate-covered Au: *Tisserant et al.* shows that Au NPs adhere to SiO_2, but they can rearrange on the surface [12]. This should suffice to support the entrainment on top of the ice. Water is called a "binding agent" between the NPs, and a 2-nm layer is assumed. *Kruglenko et al.* show that a layer of citrate is far less sensitive to water adsorption than a layer of citrate with Au NPs. The NPs are thus drains (or sinks) for water [13].

Turning to model (II), in the view of surface chemistry, Au NPs in water are charged and its counterions (Na^+ was detected) could affect the diffusion[14]. This could be in the spirit of a melting point depression (Raoult's law, equation 1.9, section 1.1.4 in chapter 1). However, experimental proof for such a local and fast temperature change does not appear to exist, although the local Na^+ concentration must be high.

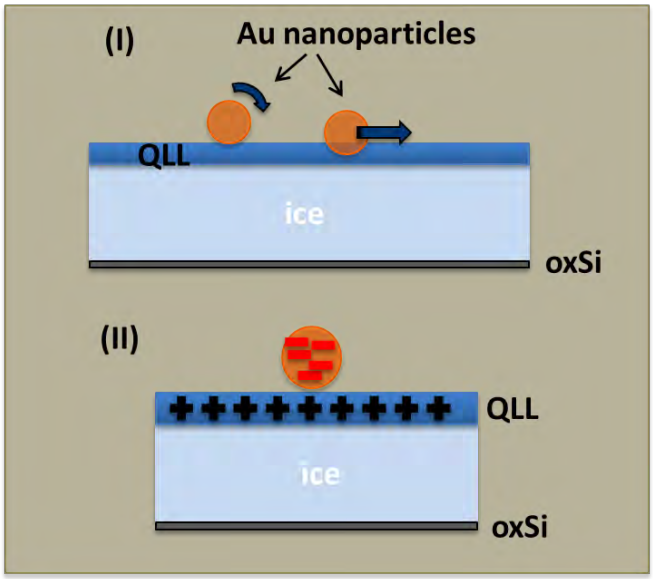

Figure 3.21. Two possible models to explain the observed nanoparticle movements in my tracking videos.

Another theoretical problem might be the large size of the particle, compared to the ultrathin QLL (figure 3.21). Wetting as in model (I) would however involve the whole particle, and also be sufficiently fast.

3.4.1. Movement type I

Concentrating now only on the observed motion of 150 nm diameter gold nanoparticles on the ice surface, single particle tracking has led to the observation of two distinct types of movements, exemplified in this and the following subchapter. The following figures correspond to one of the movies recorded in the ESEM, in which movement of two single nanoparticles has been detected.

The complete video has been recorded under the following conditions: a pressure of 154 Pa and a temperature of -17.2°C. Although the conditions are stable (or at least not huge changes occur, that would have been detected by the microscope software), one could easily notice how ice appears to sublimate slowly.

In the snapshot corresponding to the first frame of the analysed video, two gold nanoparticles (marked with blue and red circles in figure 3.22) appear on top of the surface of a polycrystalline ice structure that has grown on the silicon substrate. At the same time, other gold nanoparticles remain stuck to the silicon substrate, but the focus of the experiment falls on the two nanoparticles observed on top of the ice surface.

Figure 3.22.B depicts the scenario of the last frame of the studied video, after 149 seconds of the beginning of the movie. The two nanoparticles have moved in different directions and at the end of their respective movements both nanoparticles detach the ice surface and fall to the silicon substrate.

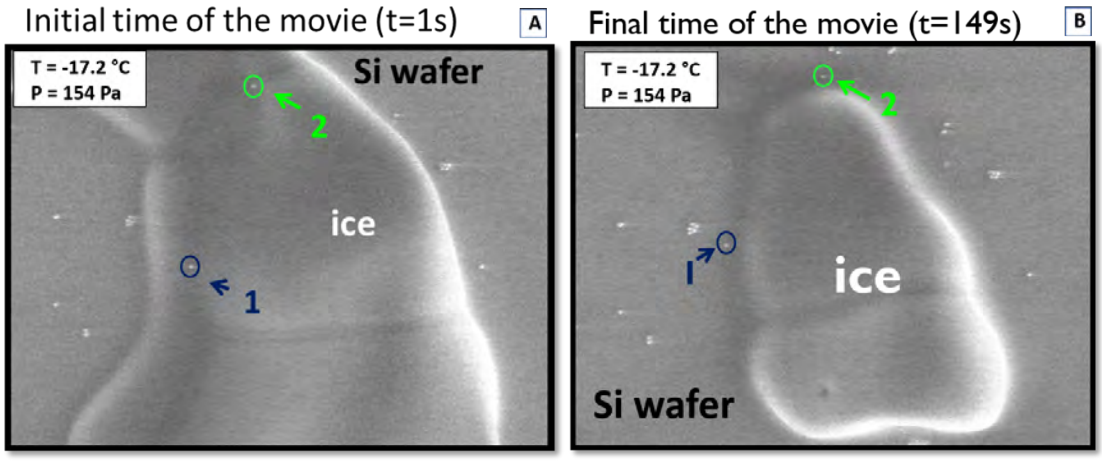

Figure 3.22. Snapshot of the video recorded in the ESEM showing **(A)** the initial time of the movie (t= 1s) and **(B)** the last frame (t=149s) of the movie. Imaging conditions: (a) P = 154 Pa, T = -17.2 °C, h = 1.13.

The purpose of the figure 3.23, with a schematic representation of the scenarios corresponding to the beginning (figure 3.23.A) and the end (figure 3.23.B) of the movie, is to show the random nature of nanoparticle movement with no preferential direction. Also, the influence of the sublimating ice front appears to be rather small.

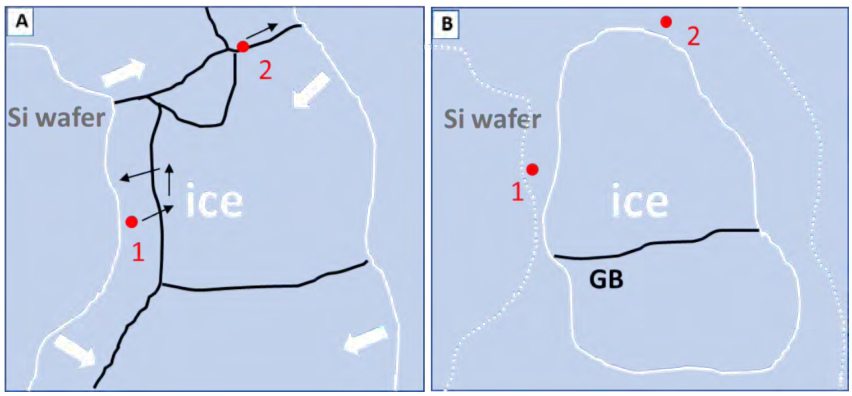

Figure 3.23. Schematic representation of the movement of the two nanoparticles that show up in this movie. **A)** Correspond to the beginning of the movie and of the movement of both nanoparticles. **B)** End of the movie and of the movement of both nanoparticles.

As previously explained (section 3.3.3) the MATLAB code gives the possibility of visualizing the tracked trajectories. In figure 3.24 the trajectories of the two nanoparticles that show movement in the analysed video are shown.

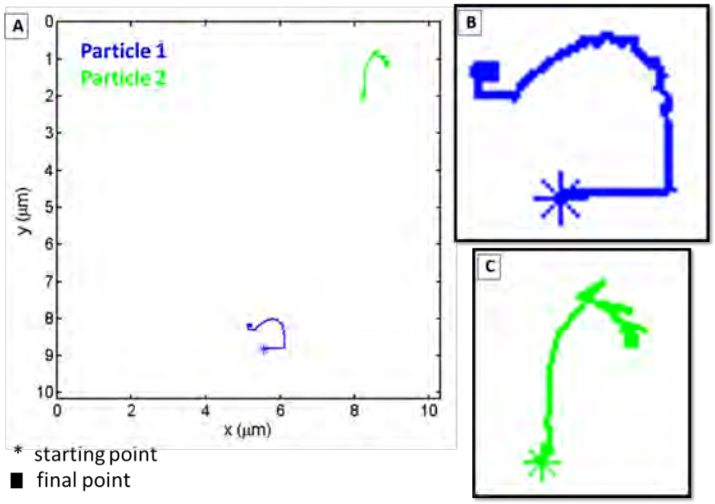

Figure 3.24. A) Trajectories followed by the two nanoparticles on the ice surface. Asterisks indicate the starting point and squares the last point of the trajectories. **B)** Inlet showing a zoom version of particle 1 trajectory. **C)** Inlet showing a zoom version of particle 2 trajectory.

If one has a closer look at the shape of both trajectories (figure 3.24.B. and C), large variations are observed in step lengths at different parts of the given trajectories. These can be attributed to the presence of physical heterogeneities on the ice surface such as grain boundaries or local curvature.

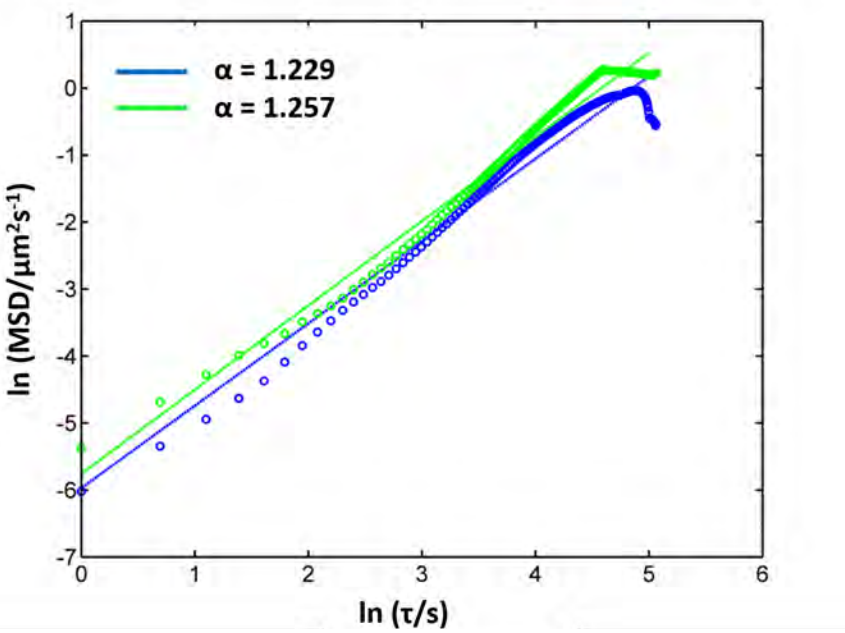

Figure 3.25. MSD(τ) vs τ for the two nanoparticles in the analyzed video. From the slope of each curve, one alpha value is obtained that characterizes the movement.

From the logarithmic plot (see figure 3.25), alpha values of around 1.2 were obtained for both trajectories, which should signify weak superdiffusion. However, given that pure Brownian diffusion (alpha=1) is hard to observe, and that very few experiments indicated alpha<1, despite the experimental error, the movements are classified as Brownian. The 2D diffusion coefficients of the nanoparticles are determined to $6.38 \cdot 10^{-4} \mu m^2/s$ and $7.88 \cdot 10^{-4} \mu m^2/s$. Note that in this case, the error in slope will cause a rather large error in the diffusion coefficient.

As mentioned previously, the speed of the nanoparticles throughout the entire displacement can be measured and is plotted in figure 3.26. It can be appreciated that the speed is not constant and at certain instants of the movement abrupt changes in the speed are produced most likely due to the presence of heterogeneities in the sample.

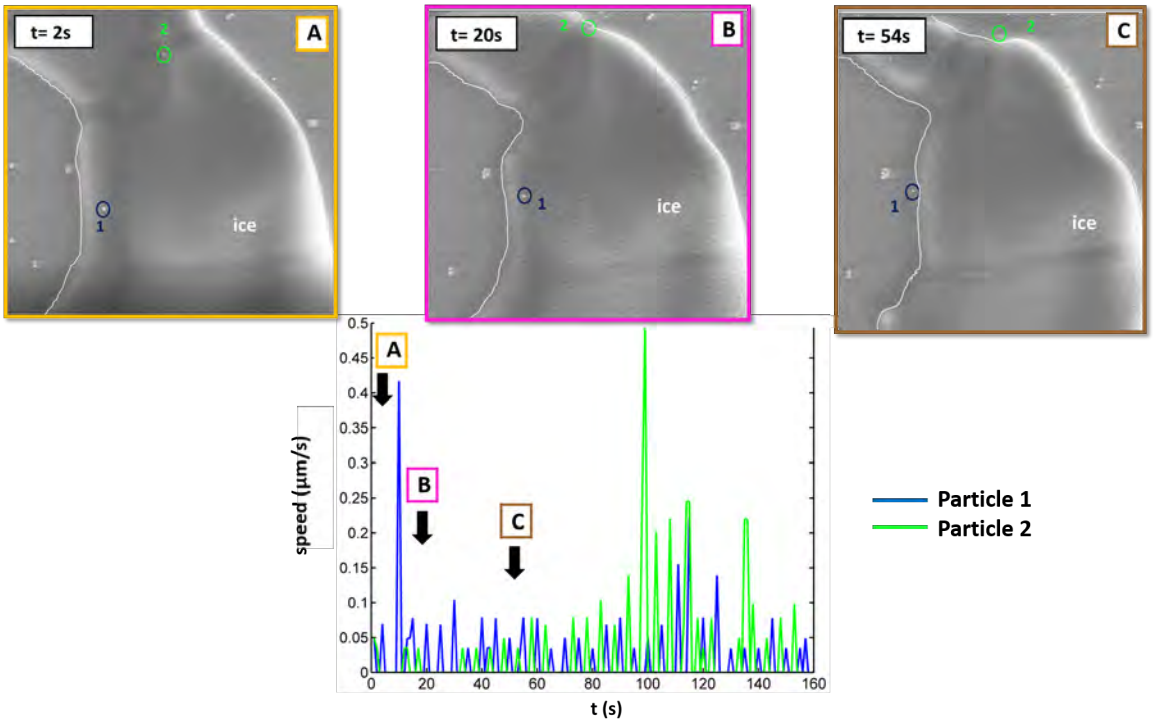

Figure 3.26. Speed analysis of the nanoparticles throughout the complete displacement performed by each nanoparticle. Blue curve corresponds to nanoparticle 1 and the green one to nanoparticle 2.

In figure 3.26 three different instants (insets A, B and C) are shown. By close examination of the graph in figure 3.26 one can detect a huge increase in the speed of particle 1 just between the two first instants shown (A and B). This increase corresponds to a jump performed by nanoparticle that cannot be detected by simple visualization from the images but is noticeable during the examination of the tracking video. Such events are probably to blame for the apparent "superdiffusion". During the first 100 seconds of movement the average speed for both nanoparticles is 0.05µm/s. The ice front moves at maximum 0.2 µm/s.

3.4.2. Movement type II

The following figures correspond to another movie recorded in the ESEM in which movement of three single nanoparticles has been detected and is an example of the movement classified as type II. The complete video has been recorded under the following conditions: A pressure of 448 Pa, a temperature of -5.5°C and humidity h = 1.16.

In the snapshot corresponding to the first frame of the analysed video, three gold nanoparticles (marked with blue, green and red circles in figure 3.27) appear “inside” the channel of a grain boundary of a polycrystalline ice structure that has grown on the silicon substrate.

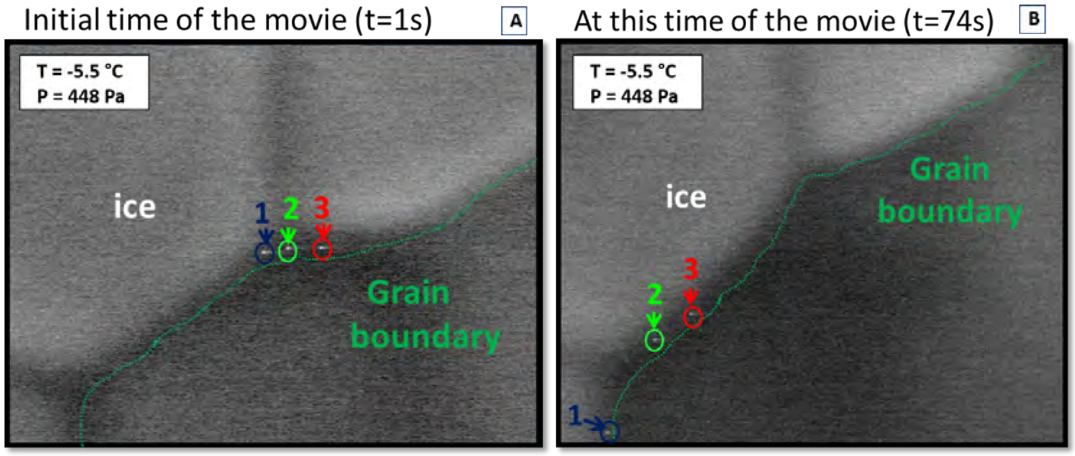

Figure 3.27. Snapshot of the video recorded in the ESEM showing **(A)** the initial time of the movie (t= 1s) and **(B)** one frame (t=74s) of the movie. Imaging conditions: (a) P = 448 Pa, T = -5.5 °C, h = 1.16.

In figure 3.27.B the scenario corresponding to the video frame after 74 seconds of the beginning of the movie is shown. The three nanoparticles are moving along the grain boundary (marked with a dashed green line on figure 3.27). During the first instants of the movie all of three of the nanoparticles move in a similar trend but after a certain amount of time particle 1 experiences an increase in its speed going forward faster than particle 2 and 3.

In figure 3.28 it is shown that, unlike in the previous case, there is a preferred direction followed by all the nanoparticles and that obviously matches the direction of the grain boundary itself. In addition, the complete structure moves or deforms, but at much lower speed.

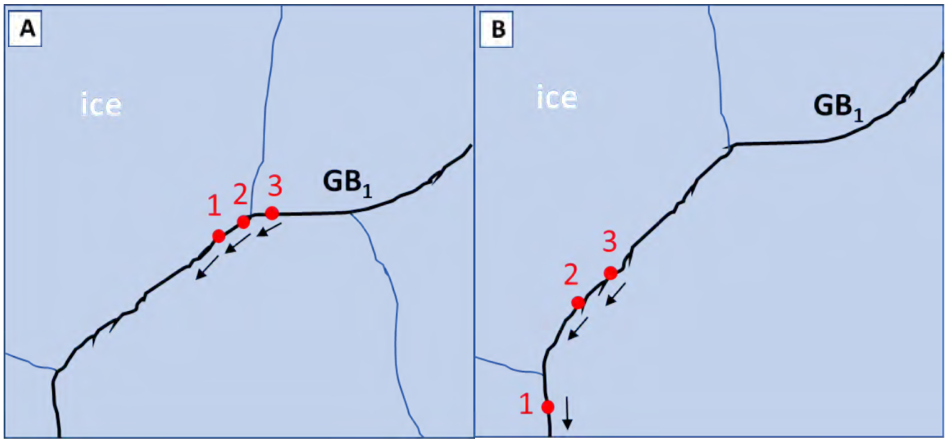

Figure 3.28. Schematic representation of the movement of the three nanoparticles that show up in this movie. **A)** Scenario at the beginning of the movie and of the nanoparticles movement. **B)** Scenario after 74 seconds of the beginning of the nanoparticles movement.

Looking at figure 3.29, in which the trajectories of the three nanoparticles are plotted by means of the MATLAB software, one can easily appreciate how the shape of all three trajectories is almost identical to the shape of the grain boundary, through which nanoparticles are diffusing, and of course that is the reason for the great similarity in the trajectories for the three nanoparticles that are in a way “forced” to diffuse along this "channel".

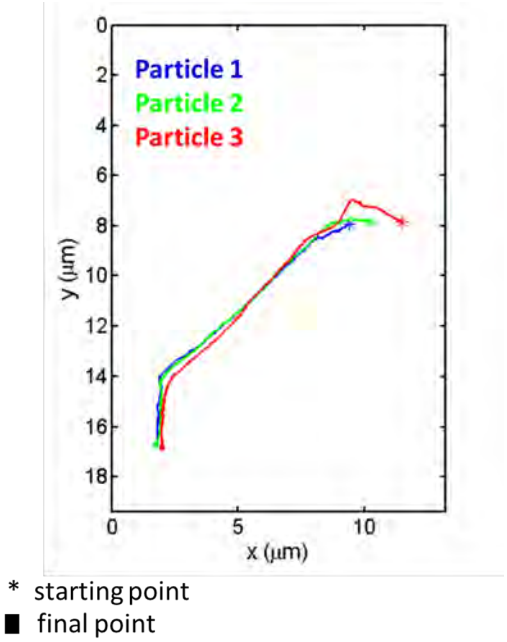

Figure 3.29. Trajectories followed by the three nanoparticles along the grain boundary of the ice. Asterisks indicate the starting point and squares the last point of the trajectories.

As in the previous case (movement type I), the mean square displacement as a function of the lag time τ is plotted for each particle. From the logarithmic plot (figure 3.30) alpha values between 1.7 and 1.8 were obtained, which might purely mathematically suggest a strong superdiffusive behaviour. However, even for extreme cases of linear movement, the slope never reached the ideal value of 2, hence such high values can be taken as signature for linear, directional movement (drag).

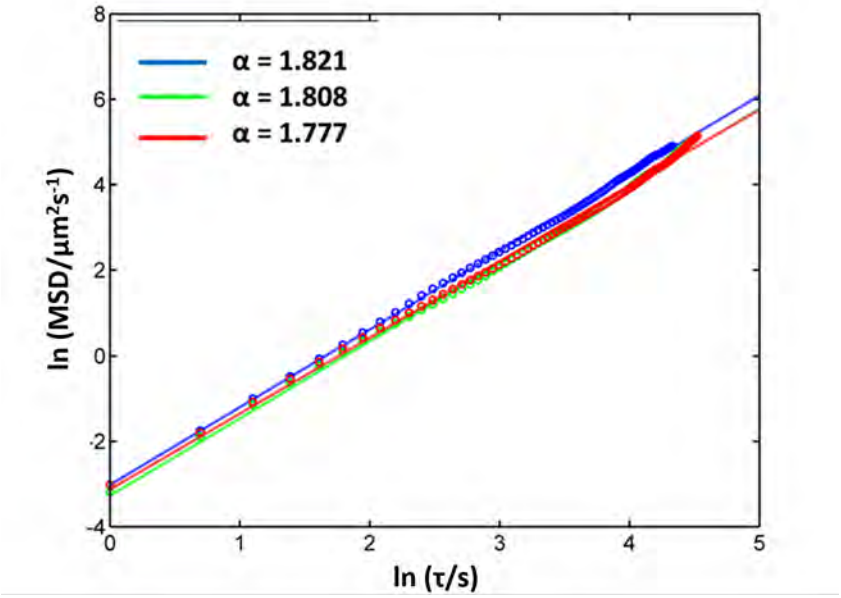

Figure 3.30. MSD(τ) vs τ for the three nanoparticles in the analyzed video. From the slope of each curve, one alpha value is obtained that characterize the movement.

The nanoparticle speed throughout the entire displacement can be measured (figure 3.31). As it has been proved in the other type (better to name that type) of movement, the speed is not constant and at certain instants of the movement abrupt changes in the speed are produced. In this concrete example, during roughly the first twenty seconds (inlet A shows the location of the nanoparticles at time t = 2s) the nanoparticles are placed in the intersection of the grains showing lower speed (averaged speed is 0.07μm/s) than in subsequent instants. Then, at the time corresponding to 29 seconds after the start of the movie and of the nanoparticles movement (inlet B, figure 3.31) the speed of the three nanoparticles increases from 0.1μm/s to 0.55μm/s. This time is just at the moment when the three nanoparticles have left behind the area of the three-grain-junction and are lined up with the straight section of the grain boundary. At the time corresponding to 69

seconds after the start of the movie there is a huge increase in the speed of nanoparticle 1 reaching a value 0.9μm/s. Indeed, inset C in figure 3.31 shows how nanoparticle 1 has started to diffuse faster than the other two nanoparticles and appears separate from the others, while the distance between nanoparticle 2 and 3 remains constant throughout the whole movement.

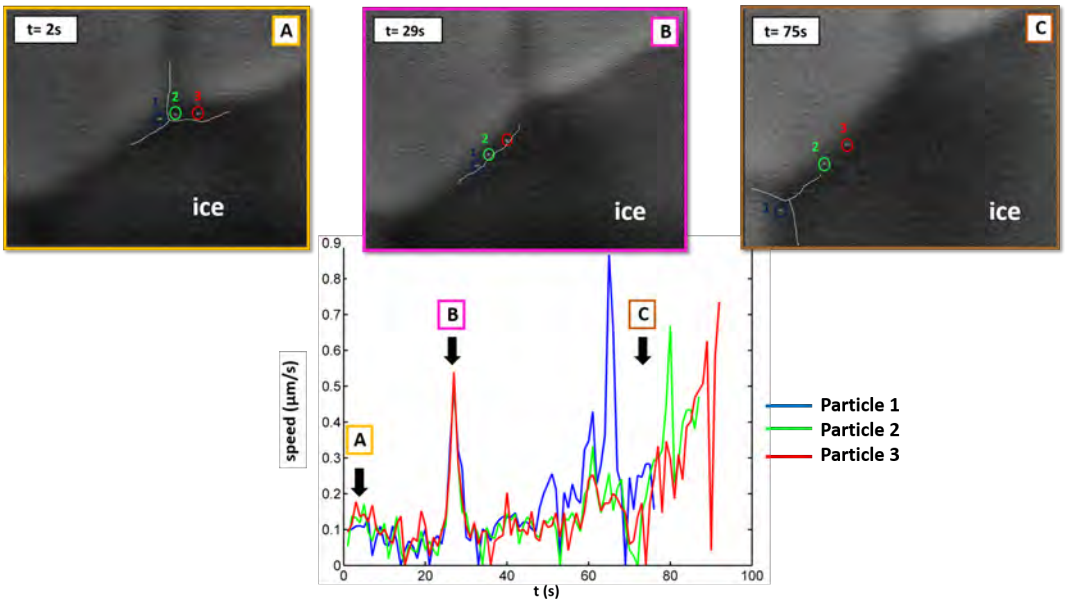

Figure 3.31. Speed analysis of the nanoparticles throughout the complete displacement performed by each nanoparticle. Blue curve corresponds to nanoparticle 1, the green one to nanoparticle 2 and the red to the nanoparticle 3.

In summary, the average speed experienced by the nanoparticles on the ice surface is about 0.05μm/s, whereas along grain boundaries values as high as 0.9μm/s have been reached by the diffusing nanoparticles. These values are quite close to typical values observed for the movement of macroscale ice deposits. A possible explanation for the movement is that the (slow) growth or sublimation of ice pushes or drags the particles. It is intriguing that the particles prefer the grain boundaries, which must offer less resistance and lower viscosity. The grain boundaries are too wide that their curvature would induce melting according to the Gibbs-Thomson equation (eq. 1.7 section 1.1.2 in chapter 1) - this would require curvatures on the nanoscale.

Further evaluation would require a very careful subtraction of the linear movement from the much smaller Brownian movement (the "jiggle" of the trajectories in figure 3.29). In contrast, it has been reported that the water mobility across grain boundaries is two orders of magnitude smaller than the mobility at the ice surface[15].

3.5. Conclusions and future prospects

A droplet-like QLL was detected close to the melting temperature, in agreement with reported results. This is the first ESEM study on this phenomenon.

An in-depth interpretation of the results at lower temperature is not yet possible. It is, however a great success to show local mobility on rather cold ice surfaces, and even finding local differences. In this respect, the rather fast directional motion in grain boundaries deserves an attempt at higher spatiotemporal resolution, and/or with an ensemble of trajectories. [14] However, when analysing single trajectories of particles that exhibit anomalous diffusion, these techniques could be insufficient. In single particle tracking experiments, the location of the tracked particle is known up to a finite accuracy and incorporates some degree of uncertainty. Errors could be corrected by increasing the amount of averaged particle locations performing longer measurements, using faster acquisition rates or tracking more particle trajectories. Furthermore, it would be desirable to eliminate external forces on the macroscale ice deposit, which are possibly causing the movement.

In this study of the QLL, one of the main purposes of MSD analysis is the extraction of the diffusion coefficient value D from the Brownian motions. Since a single diffusion constant is extracted from such an analysis, it is important to realize that if the nanoparticle is subjected to multiple types of diffusion during the observed trajectory, the extracted value will only be an average one. For example, if the nanoparticle undergoes slow diffusion during the first half of the trajectory, followed by faster diffusion during the second half, the measured average diffusion constant will tell nothing about the two hidden and very different diffusion coefficients and will be biased toward the larger value [16]. For this work, the diffusion coefficient is on average $7.13 \cdot 10^{-4}\ \mu m^2/s$. With eq. (3.1), one can estimate the viscosity of the QLL as $\eta \approx 3500$ mPa·s at -17.2ºC, with the average

Brownian diffusion constant and a particle radius of 75nm. This value is far higher than the viscosity of supercooled water (<20 mPa·s even at -25ºC) [17]. This would indeed be expected from a layer of disordered ice, which contains a much larger number of directional hydrogen bonds than liquid water. Although motions inside a grain boundary were mostly found to be linear, it was possible to detect one Brownian motion a few times. From this Brownian diffusion coefficient obtained (D = 4.41·10^{-3} μm^2/s), as previously, the local viscosity of the grain boundary has been estimated as η ≈ 600 mPa·s. As expected the viscosity in the grain boundary has be found to be lower than on the ice surface (QLL), but the statistics are not yet sufficiently good to find this clearly. However, again this value is very much higher than that of water, even of supercooled water. It is obvious (and in terms of physics correct) that both the grain boundaries and the ice surface are covered by highly viscous water layers; from everyday experience, such layers might better be addressed as “mobile ice” or “syrup-like ice”.

As demonstrated, the (nearly) Brownian motions can be analysed easily. However, further evaluation requires great care: When analysing experimental data, one has a limited trajectory length and for the gold nanoparticle trajectories used in this study, it is often shorter than 500 time points. This introduces another fundamental problem in fitting the data $< r^2(\tau)$ according to

$$\log(< \Delta r^2(\tau) >) = \log(D_\alpha) + \alpha \log(\tau), \quad \tau = 1, \ldots\ldots, \tau_M \qquad (3.2)$$

Displacements can be defined for different time intervals between positions. There are therefore many distinct displacements for small time lags and very few for large time lags. As shown in figure 3.32, selecting the optimal τ_M value is not trivial and may lead to erroneous results [18]

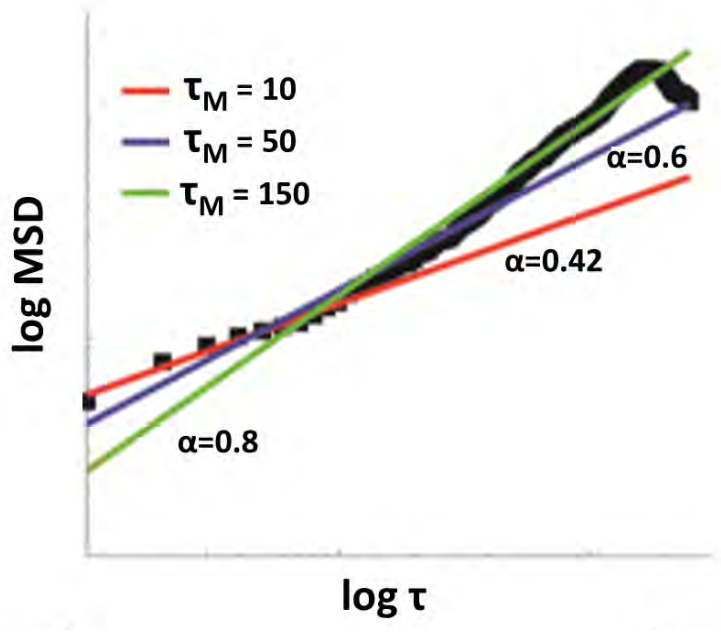

Figure 3.32 Fitting a time averaged MSD with various maximum time lags. Redrawn from [18]. The maximum of the data (black squares) is at τ_M=150.

Stable pressure and temperature conditions in the ESEM are not easily achieved, and thus limits the duration of the tracking experiments, and thereby the possibility of doing longer measurements. The acquisition rate is also limited to the fastest acquisition rate of the microscope software (1 frame each 0.5 seconds). Worse, the heterogeneity of the ice samples (and potentially of the quasi liquid layer) implies that each tracked nanoparticle experience different surroundings, making it impossible to reproduce measurements.

3.6. References

[1] V. Sharma, K. Park, and M. Srinivasarao, “Colloidal dispersion of gold nanorods: Historical background, optical properties, seed-mediated synthesis, shape separation and self-assembly,” *Mater. Sci. Eng. R Reports*, vol. 65, no. 1–3, pp. 1–38, 2009.

[2] G. Sazaki, S. Zepeda, S. Nakatsubo, M. Yokomine, and Y. Furukawa, “Quasi-liquid layers on ice crystal surfaces are made up of two different phases,” *Proc. Natl. Acad. Sci. U. S. A.*, vol. 109, no. 4, pp. 2–5, 2011.

[3] G. Sazaki, H. Asakawa, K. Nagashima, S. Nakatsubo, and Y. Furukawa, “How do quasi-liquid layers emerge from ice crystal surfaces?,” *Cryst. Growth Des.*, vol. 13, no. 4, pp. 1761–1766, 2013.

[4] C. Soong, P. Woo, and D. Hoyle, “Contamination Cleaning of TEM/SEM Samples with the ZONE Cleaner,” *Micros. Today*, vol. 20, no. 6, pp. 44–48, 2012.

[5] J. G. Dash, A. W. Rempel, and J. S. Wettlaufer, “The physics of premelted ice and its geophysical consequences,” *Rev. Mod. Phys.*, vol. 78, no. 3, pp. 695–741, 2006.

[6] A. Pavlovska, D. Dobrev, and E. Bauer, “Orientation dependence of the quasi-liquid layer on tin and indium crystals,” *Surf. Sci.*, vol. 314, no. 3, pp. 341–352, 1994.

[7] H. Asakawa, G. Sazaki, K. Nagashima, S. Nakatsubo, and Y. Furukawa, “Two types of quasi-liquid layers on ice crystals are formed kinetically,” *Proc. Natl. Acad. Sci.*, vol. 113, no. 7, pp. 1749–1753, 2016.

[8] K. Murata, H. Asakawa, K. Nagashima, Y. Furukawa, and G. Sazaki, “Thermodynamic origin of surface melting on ice crystals,” *Proc. Natl. Acad. Sci.*, no. 1608888113, pp. 1–8, 2016.

[9] H. Asakawa, G. Sazaki, K. Nagashima, S. Nakatsubo, and Y. Furukawa, “Prism and Other High-Index Faces of Ice Crystals Exhibit Two Types of Quasi-Liquid Layers,” *Cryst. Growth Des.*, vol. 15, no. 7, pp. 3339–3344, 2015.

[10] C. Jung *et al.*, “Diffusion of oriented single molecules with switchable mobility in

networks of long unidimensional nanochannels," *J. Am. Chem. Soc.*, vol. 130, no. 5, pp. 1638–1648, 2008.

[11] Y. Song, M. Luo, and L. L. Dai, "Understanding nanoparticle diffusion and exploring interfacial nanorheology using molecular dynamics simulations," *Langmuir*, vol. 26, no. 1, pp. 5–9, 2010.

[12] J.-N. Tisserant, P. a. Reissner, H. Beyer, Y. Fedoryshyn, and A. Stemmer, "Water-Mediated Assembly of Gold Nanoparticles into Aligned One-Dimensional Superstructures," *Langmuir*, vol. 31, no. 26, pp. 7220–7227, 2015.

[13] I. Kruglenko, Y. Shirshov, J. Burlachenko, A. Savchenko, O. Kukla, and O. Belyaev, "Sensor for detection of water presence in gaseous mixtures based on gold nanoparticles stabilized by sodium citrate," *Sensors Actuators, B Chem.*, vol. 170, pp. 109–114, 2012.

[14] E. Kepten, I. Bronshtein, and Y. Garini, "Improved estimation of anomalous diffusion exponents in single-particle tracking experiments," *Phys. Rev. E - Stat. Nonlinear, Soft Matter Phys.*, vol. 87, no. 5, pp. 1–10, 2013.

[15] O. B. Nasello, S. Navarro de Juarez, and C. L. Di Prinzio, "Measurement of self-diffusion on ice surface," *Scr. Mater.*, vol. 56, no. 12, pp. 1071–1073, 2007.

[16] X. Michalet, "Mean square displacement analysis of single-particle trajectories with localization error: Brownian motion in an isotropic medium," *Phys. Rev. E*, vol. 82, 2010.

[17] A. Dehaoui, B. Issenmann, and F. Caupin, "Viscosity of deeply supercooled water and its coupling to molecular diffusion," *Proc. Natl. Acad. Sci.*, vol. 112, no. 39, pp. 12020–12025, 2015.

[18] E. Kepten, A. Weron, G. Sikora, K. Burnecki, and Y. Garini, "Guidelines for the fitting of anomalous diffusion mean square displacement graphs from single particle tracking experiments," *PLoS One*, vol. 10, no. 2, pp. 1–10, 2015.

Chapter 4:

Ice nucleation in presence of proteins

4.1. Proteins and virus description

The proteins and virus employed to study their ice nucleation ability were:

1. Albumin from bovine serum, BSA, (Sigma, A0281), lyophilized powder, ≥99% purity.
2. Albumin (Sigma, A5503) from chicken egg white (can be named "ovalbumin") lyophilized powder, ≥98% purity.
3. Casein (Sigma, C7078) from bovine milk, technical grade.
4. Apoferritin (Sigma, A3641) from equine spleen, filtered through 0.2µm pores.
5. Ferritin (Sigma, F4503) from equine spleen, type I saline solution.
6. Hydrophobins (BASF), from a recombinant production process described in [1]. There are two fusion proteins H*Protein A (HP-A) and H*Protein B (HP-B).
7. Ice-binding protein (Le-IBP)
8. Tobacco Mosaic Virus, (so called "wild type") [2]

Hydrophobins were supplied by BASF (Ludwigshafen, Germany) and Le-IBP for KOPRI (Korea Polar Research Institute). The rest of the materials were purchased from Sigma-Aldrich (Madrid, Spain)

Albumin (M_n = 67 kDa, see figure 4.1) is a transport protein that is present in the body fluids of vertebrates [3] with multiple functions such as maintaining colloid osmotic pressure, ligand binding, and transporting [4]. The size of albumin is unusually large (> 300 amino acids), and the shape can depend on the environment, for example on the pH. Albumin architecture is predominately α-helical and consists of three domains with very similar conformations to create an overall heart-like shape.

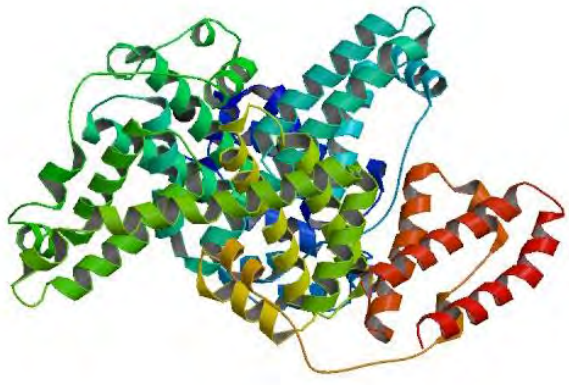

Figure 4.1. Bovine serum albumin (PDB entry: 4F5S).

Ovalbumin (see Figure 4.2) is a protein of unknown function found in large quantities in avian egg-white [5]. Its molecular weight is ~ 44.3 kDa (385 amino acids).

Figure 4.2. Ovalbumin (PDB entry: 1OVA).

Casein (see Figure 4.3) is a protein that gives milk both its white colour and unique "texture" as well as being a carrier of calcium [6]. Whole casein is predominantly made up of four different subunits that range from 19 to 25kDa. In the presence of calcium (milk), casein forms micelles of 50−500 nm, where as in the absence of calcium the micelles disassemble into smaller assemblies (submicelles). Casein subunits are amphiphilic and it has been suggested that casein acts as a stabilizer of protein structure, or even as a chaperone in promoting proper protein folding. Casein, although less ordered in structure and more flexible than the typical globular whey proteins, has significant amounts of secondary and, probably, tertiary structure [7]. Casein (M_n ~24 kDa (~ 209 amino acids)) from bovine milk is used in this work.

Figure 4.3. α-casein subunit (PDB entry: 5M44).

Ferritin and apoferritin

Monomeric ferritin has an approximate molecular weight of 20 kDa and is found in almost all living organisms. Monomers are folded in a characteristic four-helical bundle, formed by four antiparallel helices (A-D), and a shorter helix on the top of them (E) (see figure 4.4). The most variable part of the monomer fold is represented by the loops connecting the helices, in particular the long BC loop, which stretches along the length of the helical bundle (see figure 4.4), and by the short non-helical regions at the N- and C-termini. In the quaternary structure the N-terminus, BC loop, and helices A and C face the external side of the spherical shell, while helices B and D are on the internal side [8]

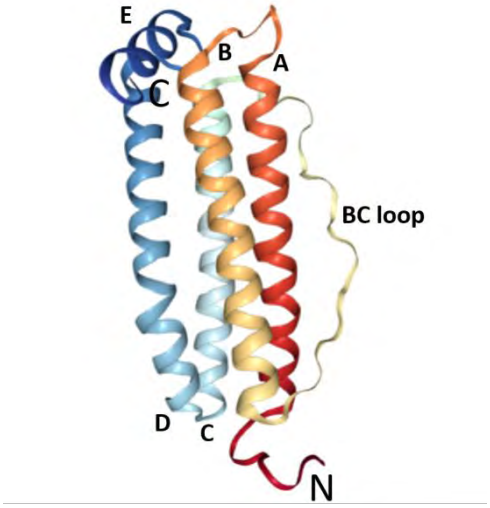

Figure 4.4. Monomeric fold of Human H ferritin (PDB entry: 2CEI). Helices A-D forming the four-helical bundle, the E-helix and the BC loop are indicated.

In bacteria and plants, ferritin complexes are formed by 24 identical subunits assembled into a 432-point symmetric, 12 nm diameter structure with a storage capacity of around 4000 iron atoms [9]. The molecular weight of ferritin (i.e., with all 24 subunits combined) is 474 kDa (see figure 4.5). Free ferritin (not combined with iron) is called apoferritin.

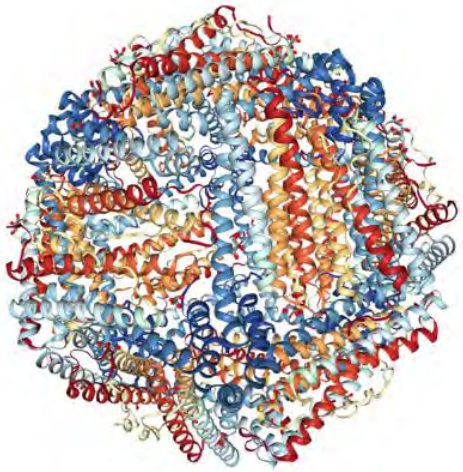

Figure 4.5. Structure of ferritin (PDB entry: 4MJY).

Among the important structural features of ferritin is the presence of channels that occur in the protein wall at the intersection of the subunits. Channels are small holes through which certain ions or molecules can travel. These channels are critical to ferritin's ability to release iron in a controlled fashion. Two types of channels exist in ferritin. Four-fold channels occur at the intersection of four peptide subunits. Three-fold channels occur at the intersection of three peptide subunits. The two types of channels have different chemical properties, and hence perform different functions.

The four-fold channel (see figure 4.6), which is lined with leucine residues, is hydrophobic ("water-fearing," lined with nonpolar side chains).

Figure 4.6. Molecular model of the four-fold channel with the four intersecting subunits. Leucine is the amino-acid residue that lines the four-fold channel. This residue contains two functional groups that are polar; -CO and -NH.

The three-fold channel (see figure 4.7), which is lined with glutamate and aspartate residues, is hydrophilic ("water-loving," lined with polar side chains).

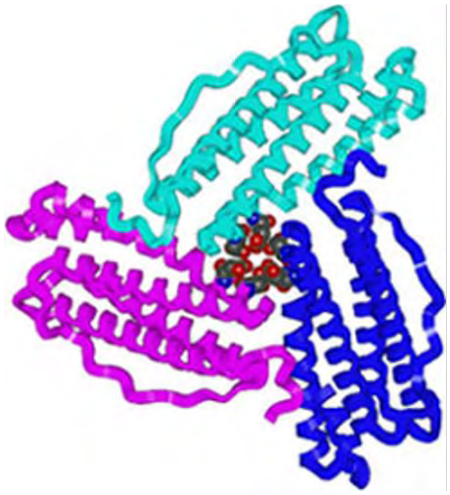

Figure 4.7. Molecular model of the three-fold channel with the three intersecting subunits. Glutamate and aspartate are the amino-acid residues that line the three-fold channel. These residues contain only one functional group that is charged: $-COO^-$.

Calculations to determine the electrostatic potential of the iron storage protein ferritin [10] reveal that the three-fold channels, the putative ferroxidase sites, and the nucleation sites all show negative values of the electrostatic potential. However, the outer entrance to the three-fold channels is surrounded by regions of positive potential, creating an electrostatic field directed toward the interior cavity. This electrostatic gradient provides a guidance mechanism for cations entering the protein cavity, indicating the three-fold channel as the major entrance to the protein.

Hydrophobins (HPs) are small cysteine-rich proteins (M_n ~ 10 kDa) and moderately hydrophobic. HPs are naturally found on fungi, where they determine the very hydrophobic nature of the fungus cap. Hence, this protein is introduced by the name “hydrophobins” [11]. These proteins have several key roles in fungal development, for example 1) acting to allow the emergence of aerial hyphae from the mycelial growth medium and providing a water-repellent coating to spores that are aerally dispersed; 2) allowing fungi to escape their aqueous environment, as well as the hydrophobization of spores facilitating improved dispersal of the conidiospores [1].

HPs are identified into Class I and Class II depending on their hydropathy patterns and solubility characteristics.

Hydrophobin HFBII from *Trichoderma reesei* has a novel, compact single domain structure containing one α-helix (A) and four antiparallel β-strands (B-E) (see figure 4.8) that completely envelop two disulphide bridges. The protein surface is mainly hydrophilic, but two β-hairpin loops contain several conserved aliphatic side chains that form a flat hydrophobic patch that makes the molecule amphiphilic [12] .

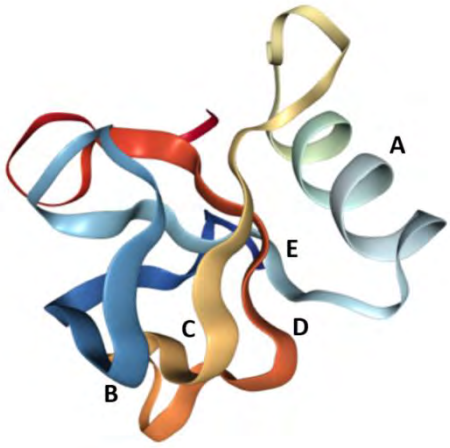

Figure 4.8. Structure of HFBII Hydrophobin (PDB entry: 2B97).

LeIBP. Arctic yeast Leucosporidium sp. produces a "sugar-coated" ice-binding protein (LeIBP) with a molecular mass of approximately 25 kDa, which can lower the freezing point below the melting point once it binds to ice. LeIBP (see figure 4.9) is a member of a large class of ice binding proteins, the general structures of which are unknown.[13] Structural analysis of the LeIBPs revealed a dimeric right handed β-helix fold, which is composed of three parts: a large coiled structural domain, a long helix region (residues 96–115 form a long α-helix that packs along one face of the β-helix) and a C-terminal hydrophobic loop region. LeIBP monomers occur in solution, but the preferred state of the protein is a dimer.

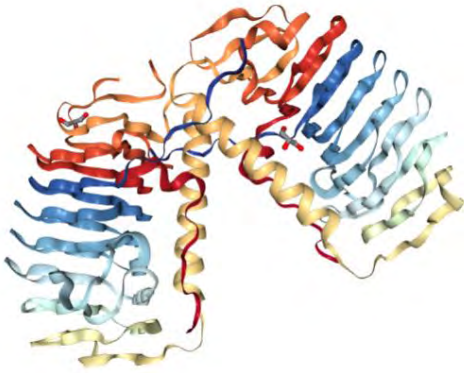

Figure 4.9. Crystal structure of the dimeric structure of LeIBP observed in the asymmetric unit of the crystal (PDB entry: 3UYU)

Tobacco Mosaic Virus (TMV) infects plants of the family of Solanaceae such us tobacco, tomato or pepper. It causes characteristic mosaic-like patterns, especially on tobacco plants, but it is harmless to mammals [14]. It is a tubular hollow particle where the helical symmetry capsid formed by 2130 coat proteins surrounds the single-stranded RNA genome. The virus is 300 nm long, has an external diameter of 18 nm and a 4-nm wide internal channel [15]. TMV is a very versatile and stable virus because of its resilience to extreme conditions at temperature, pH, in solvents, under chemical reactions or pressure.

The secondary structure of the coat proteins in TMV comprises a core of four closely packed α-helices and a small β-sheet, plus two small extra helical segments. Between the β-sheet and the outer viral surface, numerous aromatic and hydrophobic amino acid side chains interact within the coat protein (CP) and across coat protein boundaries to form a continuous hydrophobic ribbon around the axis. The ribonucleic acid (RNA) phosphate backbone is stabilized in the CP structure.

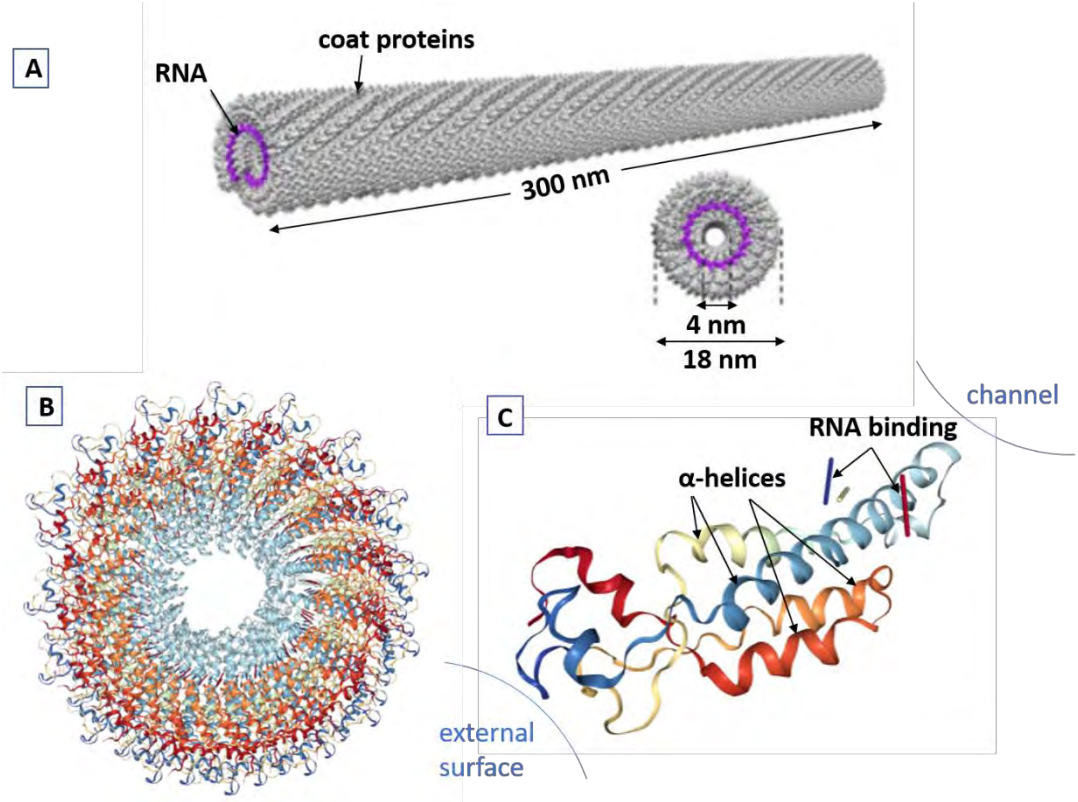

Figure 4.10. A) Overview of the solid three-dimensional TMV model (300 nm x 18 nm) and the lateral view where 4 nm channel is observed. B) 49mer, three turns of the capsid protein (PDB entry: 3J06). C) Ribbon diagram of a single coat protein.

4.2. Experimental techniques

4.2.1 Drop freezing technique

The drop freezing experiment allows studying the heterogeneous ice nucleation in small droplets (normally microliters). Droplet freezing experiments were first reported by *Vali and Stansbury* [16] and have been since used in numerous studies [17],[18],[19].

Setup 1

Eight sterilised pipette tips were mounted onto the eight-channel automatic pipette (VWR Electronic Pipettor). The sample solution was poured into a sterilised dispensing tray. Then 50 µl aliquots were pipetted into a polymerase chain reaction (PCR) microliter-well tray (each well has a maximum capacity of 200 µl), repeating the procedure twelve times (the PCR tray consists of a 12 × 8 array of individual wells) for a total of 96 aliquots (see figure 4.12.A). Wells were sealed with transparent sealable foil to prevent any impurities from settling into the sample. The PCR tray was placed into an ethanol bath taking care that the ethanol only just covers the PCR wells to the liquid level as shown in figure 4.11.

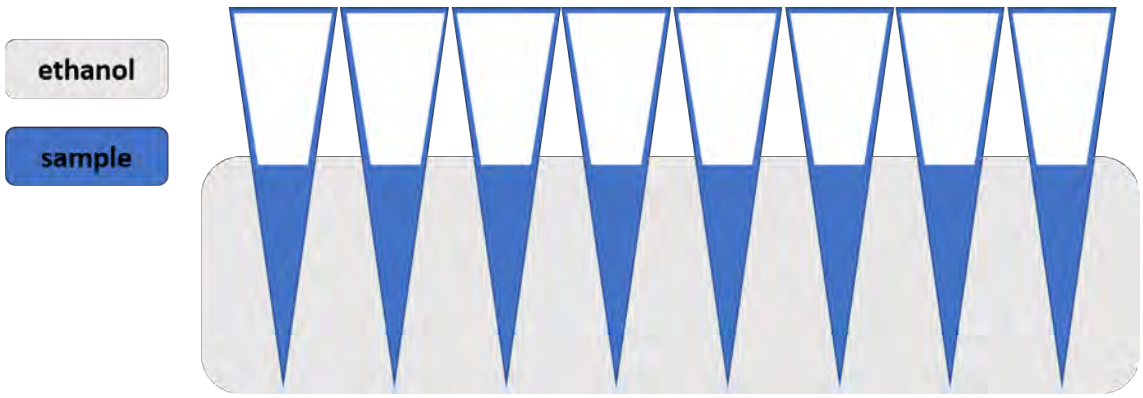

Figure 4.11. Side view of PCR tray with 8 wells submerged into ethanol bath just to the level of the sample in the microliter wells.

Before starting with the experiment, it is necessary to carefully check the tray position. If the ethanol level is too high, the tray holders should be raised so that only the parts that have the liquid sample in it are submerged in the ethanol. Once the tray was placed correctly, the recirculating chiller (LAUDA Proline RP 845 Refrigerating Circulator, see figure 4.12.B) was switched on and the temperature set to 0 °C.

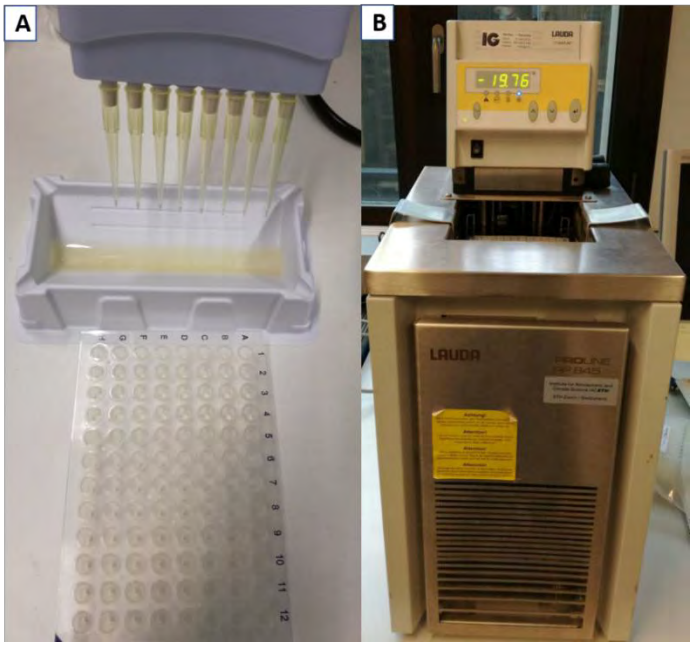

Figure 4.12. A) Pipetting process with automatic pipette. **B)** the recirculating chiller bath filled with ethanol.

Once the chiller reached 0 °C, it was checked out if any of the 96 wells was frozen and the number of frozen wells was written down. A flash light was used to get a clear view (see figure 4.14.A). Afterwards, the chiller temperature was set to -1 °C to check again if some well was frozen. This process was repeated for all temperatures in steps of 1 °C until the 96 wells were frozen. (see scheme figure 4.13).

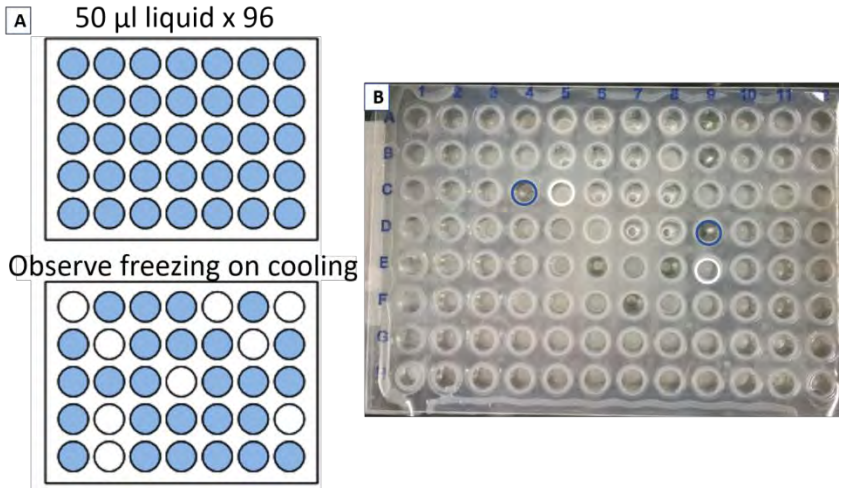

Figure 4.13 A) Example of samples in a tray that are unfrozen (blue circles) followed by freezing (white circles) upon cooling. **B)** Real example with a protein solution sample.

Setup 2

This setup is similar to setup 1 but automatized. The experimental setup consists of four main parts: (i) the LED light including an USB camera to observe the freezing experiment, (ii) the recirculating chiller bath filled with ethanol to cool down the sample, (iii) the PCR tray with 96 wells containing each 50 µL of liquid sample and (iv) a computer to control sample temperature and cooling rate as well as to record and evaluate pictures of the freezing wells.

The USB Camera mounted is placed above the chiller and directed toward the PCR plate, which is illuminated from below (see figure 4.14.B). The camera is connected to the computer and the images are recorded every fifteen seconds through a MATLAB code (see appendix I)

The temperature ramp is adjusted via the control software (LabVIEW). The freezing images are evaluated automatically by MATLAB (*well_compare* code). During the freezing process the wells turn dark, because ice shows a light scattering behaviour that differs from liquid water.

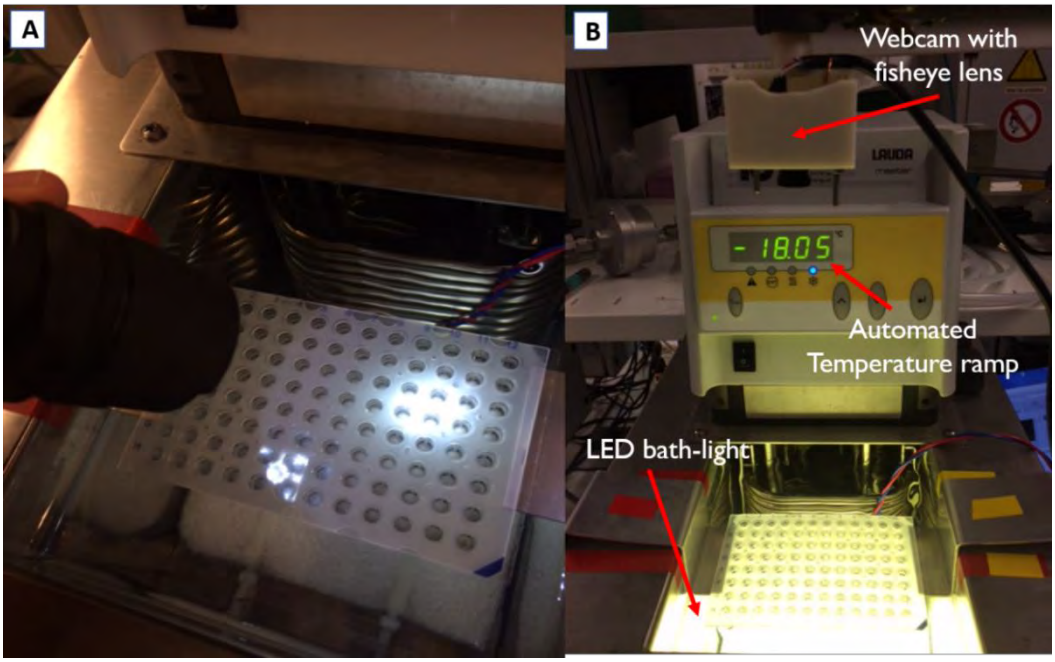

Figure 4.14. A) Setup 1. The freezing process is detected visually with the help of a flash light. **B) Setup 2.**

This system provides in general good detection of freezing events without loss of reliability even at temperatures close to 0 ˚C, where visual detection is very difficult.

Two types of failures were detected in relatively small percentage of the analysed samples.

1. The first one is due to an incorrect identification of the PCR plate when the *well_compare* code was run (see figure 4.15.B). In this case, the experiments should be redone. In the future, this problem will be overcome easily by placing the plate in a fixed position.

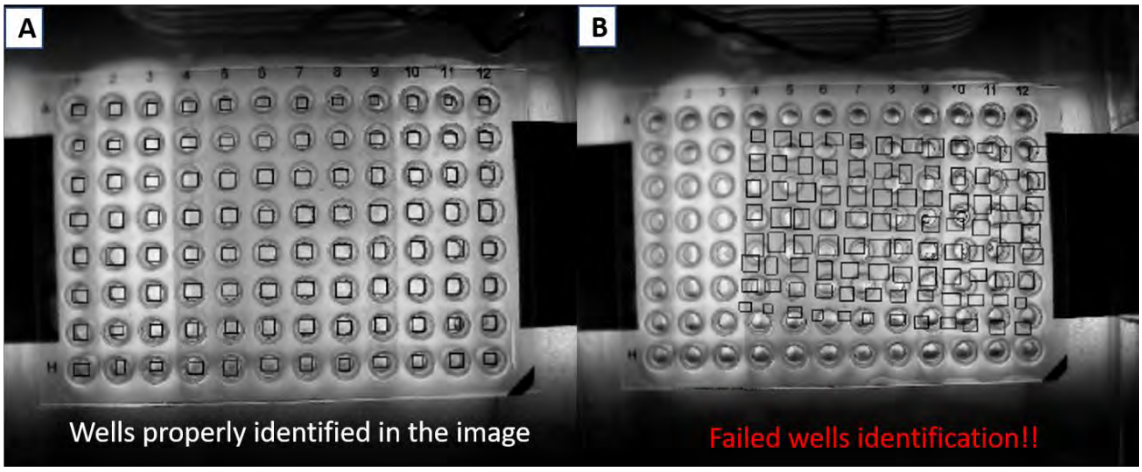

Figure 4.15. A) PCR plate with properly identified wells. **B)** The code has failed to identify the wells in the PCR plate.

2. The second type of deficiency is related to the image processing when abrupt changes in the LED light intensity are produced during the experiment (see figure 4.16). This type of failure could be solved by adjusting the threshold for removing camera lighting changes in the code.

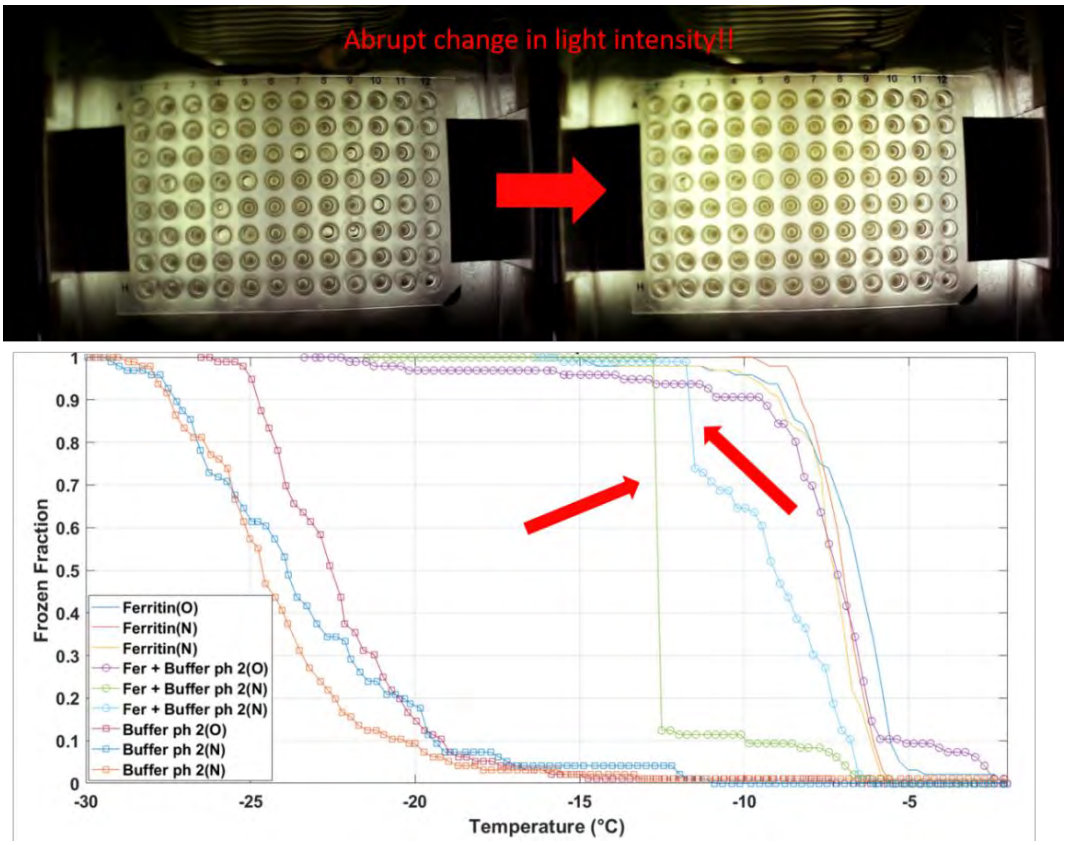

Figure 4.16. An abrupt change in the illumination system generates errors in the subsequent data plots.

4.2.2 Differential scanning calorimetry (DSC)

Differential scanning calorimetry (DSC) measures temperatures and heat flows associated with thermal transitions in a material.

DSC is a thermo-analytical technique in which the difference of required heat to increase or decrease the temperature of a sample and a reference is measured as a function of time or temperature [20]. The sample and reference pans are both kept during the experiment at approximately the same temperature. The cell with the sample and the reference are heated or cooled at constant rate. Therefore, while no chemical or physical reaction happens (i.e. the two pans are in a thermodynamic equilibrium) the measured heat flow difference is zero. When a melting process occurs in the sample, the heat flow to the sample must be increased to keep the same temperature as in the reference sample. Thus, by observing this difference in heat flow as a function of time or temperature, the total

amount of absorbed or released energy during such a transition can be measured. Further the phase transition temperature (e.g. melting or freezing point of ice) can be determined.

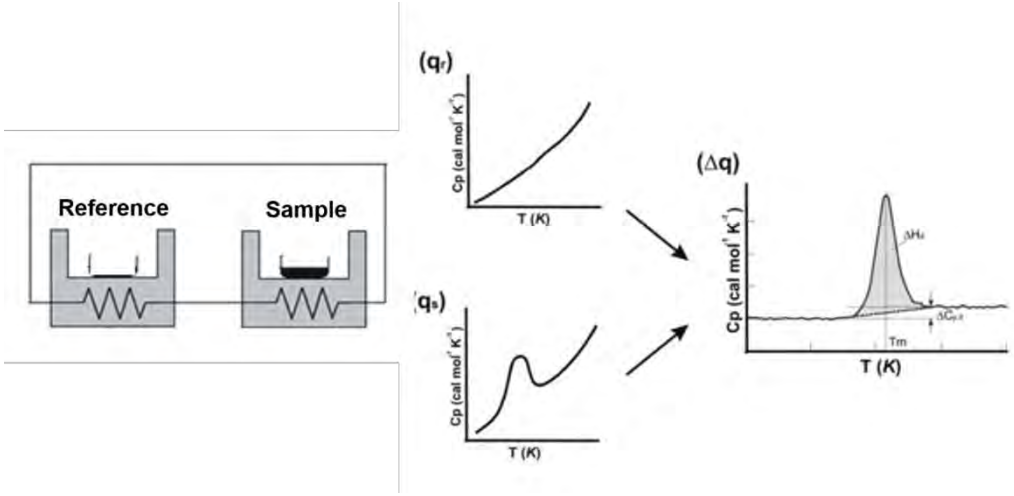

Figure 4.17. Experimental setup for a DSC experiment. The amount of heat required to increase the temperature by the same increment (ΔT) of a sample cell (q_s) is higher than that required for the reference cell (q_r) by the excess heat absorbed by the molecules in the sample (Δq). (Taken from [20]).

The main application of DSC is the study of phase transitions because they involve energy changes or heat capacity changes that can be detected by this technique. In our case, the principal objective of using this technique is the easy and fast determination of the crystallization temperature of protein solutions. The most common type of thermal transitions observed in a DSC experiment is illustrated in figure 4.18.

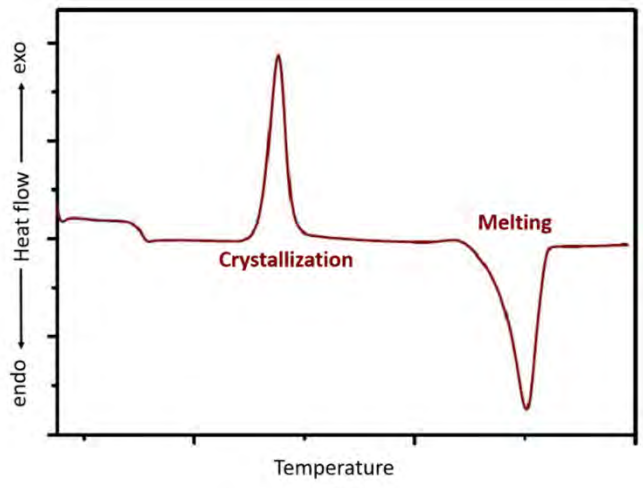

Figure 4.18. Some thermal transitions observed in DSC curves; crystallization as an exothermic transition which releases energy (heat) and melting process as an endothermic transition which absorbs energy.

In this thesis, a differential scanning calorimeter of TA Instrument Q2000 (see figure 4.19) was used to determine the thermal events on the samples. Samples of about 2 to 10 mg were sealed in aluminum hermetic pans and cooled down to – 50 °C to ensure complete freezing and subsequently warmed up at a rate of 1 K/min under nitrogen flow. From the heat flow - temperature curves, the crystallization and melting temperatures of the different samples can be determined.

Figure 4.19. DSC Q2000 from TA Instruments.

4.3 Ice nucleation of proteins

4.3.1. Sample preparation

Different types of proteins in powder (see subchapter 4.2) and one virus in solution were used to test the ability of proteins as ice nucleating particles (INPs). Solutions at the desired concentration were prepared dissolving the specified amount of the commercial samples (see table I) with ultrapure water (Aldrich Chemical Co. Inc.).

Sample	Solute mass [mg]	Water [ml]	Concentration [g/ml]
BSA	50	50	$1{\cdot}10^{-3}$
Ovoc1	50	50	$1{\cdot}10^{-3}$
Ovoc2	250	25	$1{\cdot}10^{-2}$
HPA*	50	50	$1{\cdot}10^{-3}$
HPB*	50	50	$1{\cdot}10^{-3}$
IBPc1	50	50	$1{\cdot}10^{-3}$
IBPc2	250	25	$1{\cdot}10^{-2}$
Casc1	50	50	$1{\cdot}10^{-3}$
Casc2	500	50	$1{\cdot}10^{-2}$
TMV	5µl*	25	$2{\cdot}10^{-6}$

Table I: Biological solutions used in this thesis. (* TMV sample is expressed in µl as the original sample was liquid).

4.3.2. Results

Freezing experiments with the solutions in table I were performed with the setup 2 using a cooling ramp of 1 K/min from 273 to 233 K. The fraction of frozen droplets was recorded as a function of temperature at 0.1 K of resolution. Plots of the measured temperature dependence of the frozen fraction of droplets for the different solutions are shown in appendix II.

In figure 4.20 the frozen fraction for the different biological solutions are shown to compare the ice nucleation efficiency of the studied proteins and virus. The results of ultrapure water are also included for comparison. At this cooling rate, water starts to freeze at ≈ -20 °C.

From figure 4.20 it is possible to observe two different types of behaviours. In the case of ovalbumin, BSA and HPB* solutions the onset of crystallization is in the temperature range of -8 ºC to -11 ºC. This temperature range is much higher than that observed for water. By contrast, casein, IBP, HPA* and TMV start to freeze at relative lower temperature (-14 ºC and -18 ºC). In addition, the shape of the curve is also different. Casein, IBP, HPA* and TMV show steeper freezing curves compared to BSA, HPB* and ovalbumin. Specially the casein solution which shows a relatively small freezing range (the freezing onset is at -13 ºC and the complete freezing happens at -19 ºC).

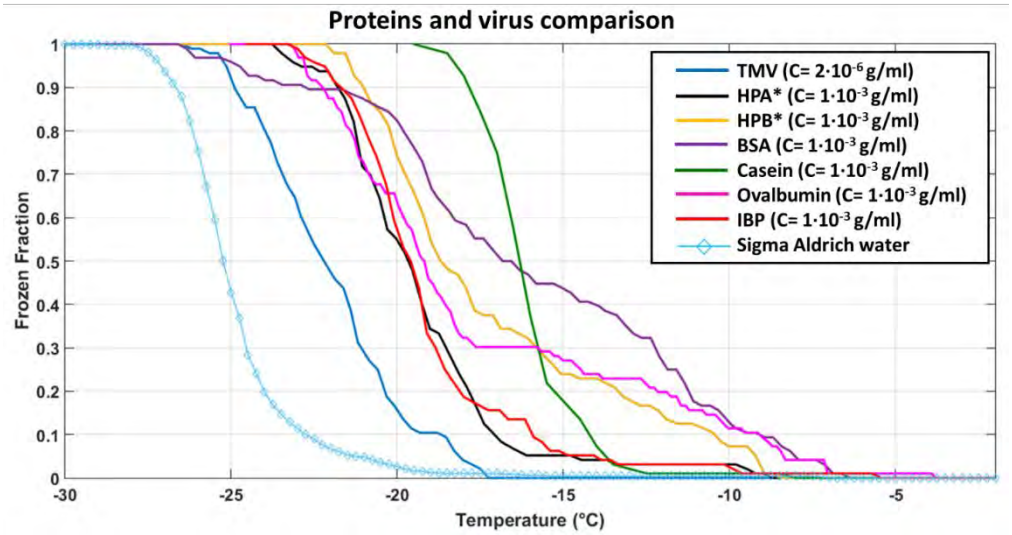

Figure 4.20. Fraction of droplets frozen as function of temperature for different biological solutions and for pure water.

It can be concluded that these proteins or virus solutions freeze above the homogeneous freezing limit of pure water and all these materials have the ability to act as INP. The sample with less capacity to let the ice grows is TMV, although it corresponds to the most diluted sample (c_{TMV} = 2·10^{-6}g/ml). Casein shows a strong freezing activity in a narrow temperature range. Both, BSA and ovalbumin, show the highest freezing onset temperature (around -7 ^{o}C) and therefore classified as good INPs.

Figures 4.21 and 4.22 represent the number of freezing events at a certain temperature for the different biological samples studied (the results are shown in two independent plots to avoid an overcrowded representation).

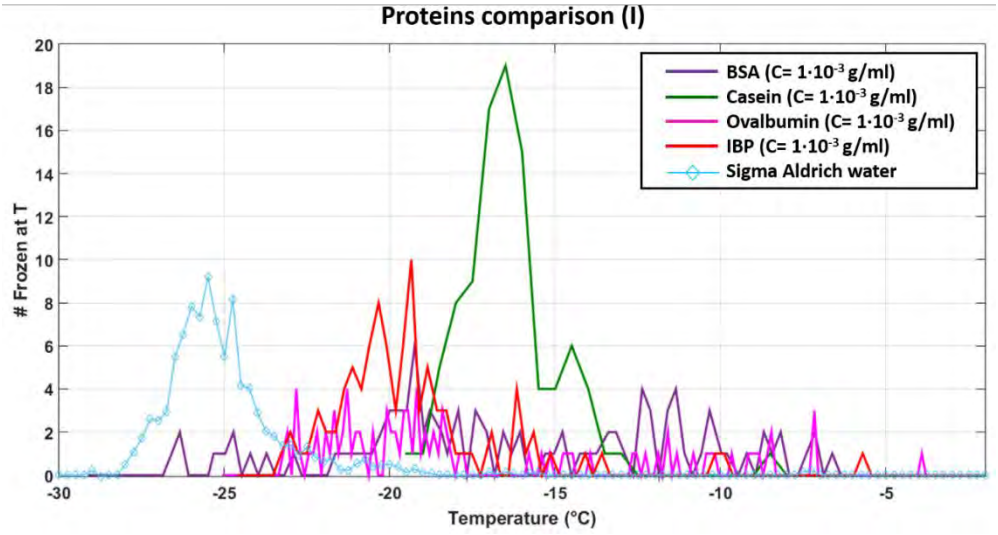

Figure 4.21. Number of freezing events as function of temperature for BSA, casein, ovalbumin, IBP and pure water.

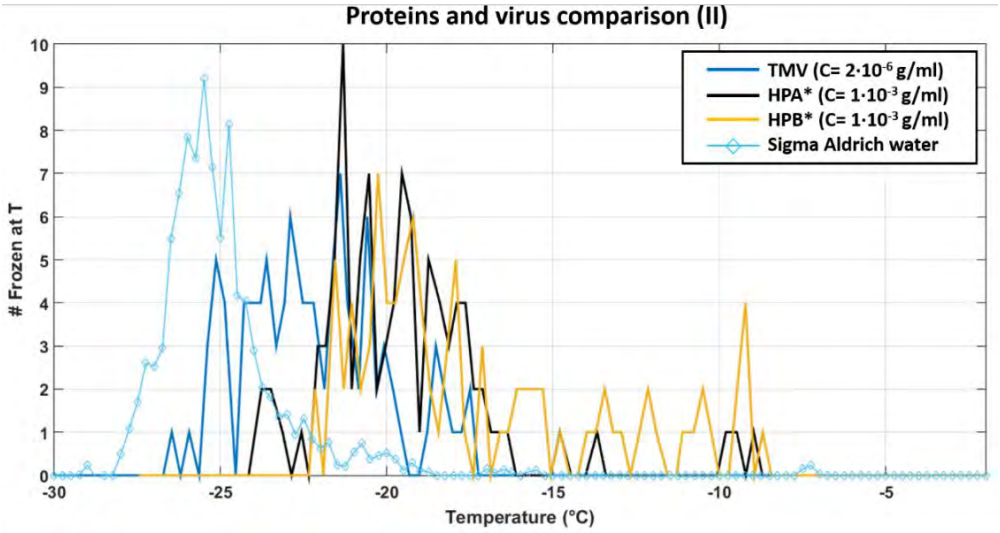

Figure 4.22. Number of freezing events as function of temperature for TMV, HPA*, HPB* and pure water.

From figures 4.21 and 4.22 one can confirm that ovalbumin, BSA and HPB* do not show a huge number of freezing events at any temperature and the freezing is more uniform within the studied temperature interval. However, for the rest of biological solutions analysed, some temperatures show more than 10 freezing events: IBP and HPA* show 10 freezing events between -19 ºC and -21.5 ºC. This effect is more pronounced in the case of casein which shows 19 freezing events at -16.5 ºC.

Figure 4.23 shows the concentration effect on the onset of the freezing temperature. Two different concentrations for ovalbumin and IBP were prepared as shown in figure 4.23 (frozen fractions are shown in Appendix VII). In the case of ovalbumin solutions, increasing the protein concentration increases the onset of the freezing. This behaviour represents the "normal" behaviour for most of the proteins. However, for the IBP solutions the opposite behaviour was found. Increasing the protein concentration, decreases the onset of the freezing.

Although the slope of the freezing curve is similar for the four samples irrespective of solution concentration, there is a significant difference in freezing temperatures for $1{\cdot}10^{-3}$ g/ml and $1{\cdot}10^{-2}$ g/ml samples**.** The median freezing temperature (T_{50}, which indicates the fraction 50% of all droplets are frozen) increases from -19.2 ºC to -10 ºC increasing the concentration from $1{\cdot}10^{-3}$ g/ml to $1{\cdot}10^{-2}$ g/ml for the ovalbumin. However, for the IBP solutions increasing the concentration from $1{\cdot}10^{-3}$ g/ml to $1{\cdot}10^{-2}$g/ml, causes a diminution of about 5 ºC in the median freezing temperature, T_{50}, from -19.7 ºC to -24.5 ºC.

The median freezing temperatures of all the biological samples tested are shown in table II.

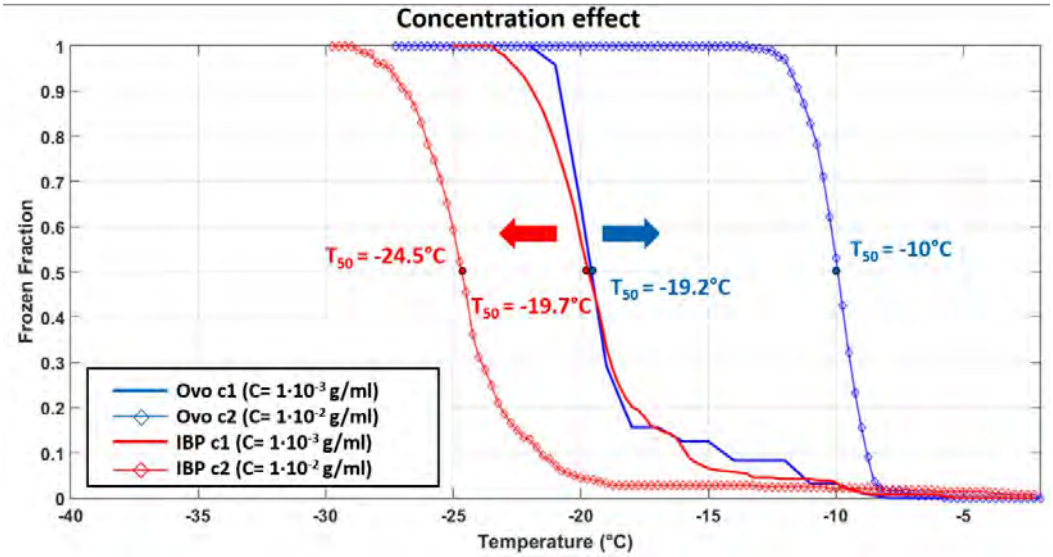

Figure 4.23. Dependence of freezing temperatures of ovalbumin and IBP on concentration.

Sample	T_{50} [°C]
BSA	-16.8
Ovoc1/Ovoc2	-19.2/-10.0
HPA*	-19.4
HPB*	-18.2
IBPc1/IBPc2	-19.7/-24.5
Casc1/Casc2	-16.3/-13.0
TMV	-22.5

Table II. Median freezing temperatures for the different biological solutions.

As a conclusion, this is the first report of ice nucleation activity in the selected proteins and virus. No one of them was found to be a good INA (ice nucleation active) protein compared to other proteins analysed in the literature (see chapter 1.3.3).

In addition, two more proteins have been tested: apoferritin and ferritin (see subchapter 4.2). Due to the high ice nucleation activity found out in both proteins, the experiments performed and the obtained results are presented independently in the next subchapter.

4.4. Ice nucleation of apoferritin and ferritin

4.4.1. Sample preparation

Apoferritin from equine spleen (0.2 µm filtered, Sigma Aldrich, Missouri, USA) and ferritin from equine spleen (saline solution, Sigma Aldrich, Missouri, USA) were used to prepare solutions at different water concentration (Aldrich Chemical Co. Inc.). The concentration of the commercial solutions was determined by UV-vis spectroscopy measurements, obtaining values of $33.2 \cdot 10^{-3}$ g/ml and $49.7 \cdot 10^{-3}$ g/ml for the apoferritin and the ferritin, respectively. All the materials were used without any further purification.

Different hydration levels were obtained by mixing a desired quantity of the protein solution with water as shown in Table III. Apoferritin solutions are colourless (see figure 4.24.A) whereas ferritin solutions show a yellow/orange colour due to the iron presence (see figure 4.24.B).

Sample	Pipetted commercial solution volume [µl]	Water [ml]	Concentration [g/ml]
Apo c1	54	50	$3.6 \cdot 10^{-5}$
Apo c2	540	50	$3.4 \cdot 10^{-4}$
Fer c1	40	50	$4 \cdot 10^{-5}$
Fer c2	400	50	$3.9 \cdot 10^{-4}$

Table III: Concentrations used for apoferritin and ferritin solutions.

Figure 4.24. High concentration apoferritin (A) and ferritin (B) solutions.

4.4.2. Results in water

Freezing experiments using apoferritin and ferritin solutions have been performed with the setup 2 using a cooling ramp of 1 K/min from 273 to 233 K. The fraction of frozen droplets was recorded as a function of temperature at 0.1 K of resolution. Plots of the temperature dependence of the frozen fraction of droplets for the two solutions at different concentrations are shown in Figures 4.25 to 4.28. The result of ultrapure water is also included for comparison.

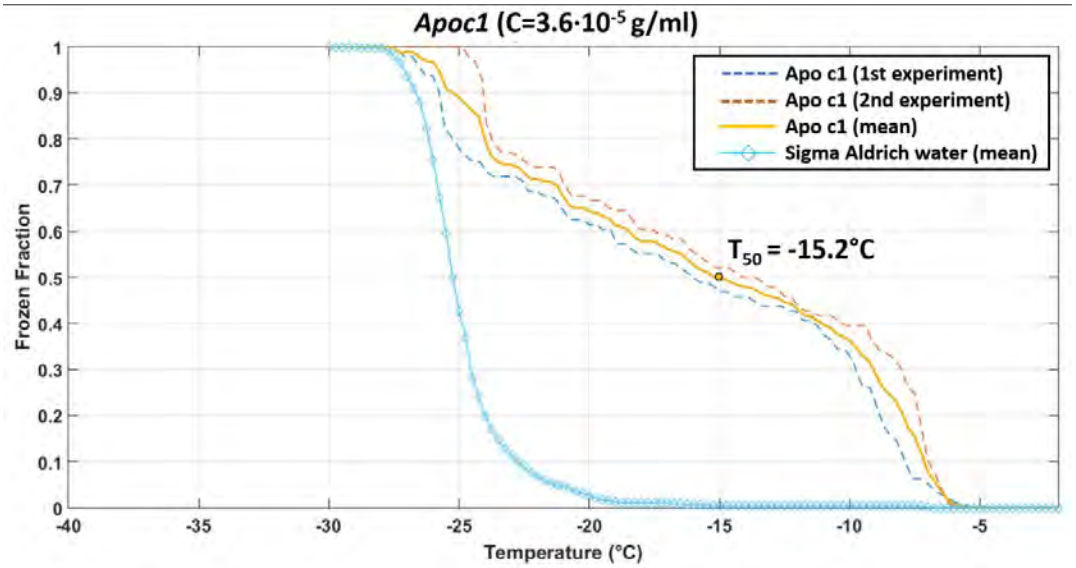

Figure 4.25. Fraction of droplets frozen as function of temperature for well diluted apoferritin (*Apoc1*) solution. T_{50} indicates the fraction at which 50% of all droplets are frozen (median freezing temperatures).

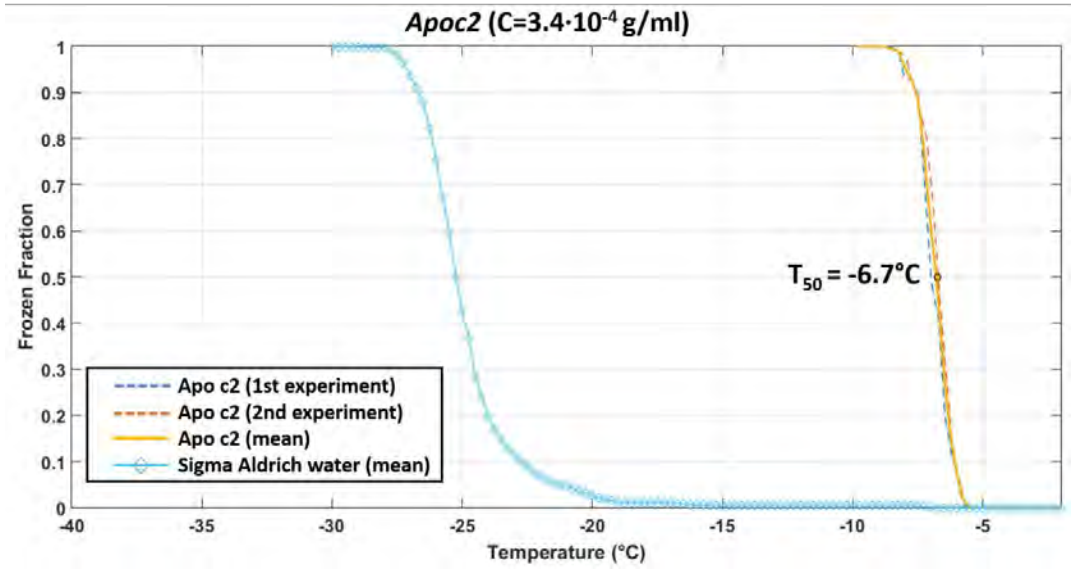

Figure 4.26. Fraction of droplets frozen as function of temperature for concentrated apoferritin (*Apoc2*) solution. T_{50} indicates the fraction at which 50% of all droplets are frozen (median freezing temperatures).

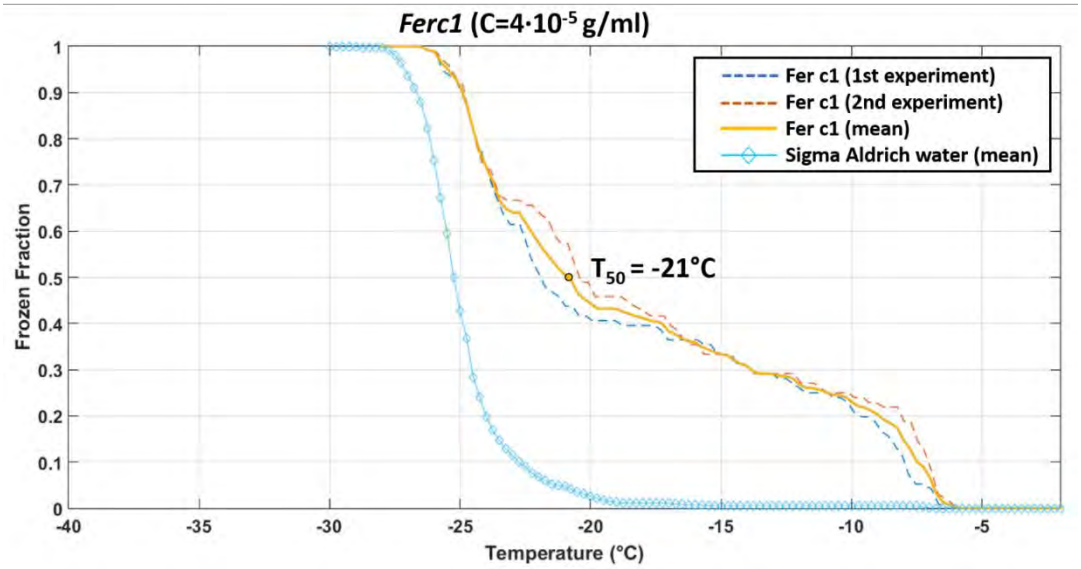

Figure 4.27. Fraction of droplets frozen as function of temperature for well diluted ferritin (*Ferc1*) solution. T_{50} indicates the fraction 50% at which of all droplets are frozen (median freezing temperatures).

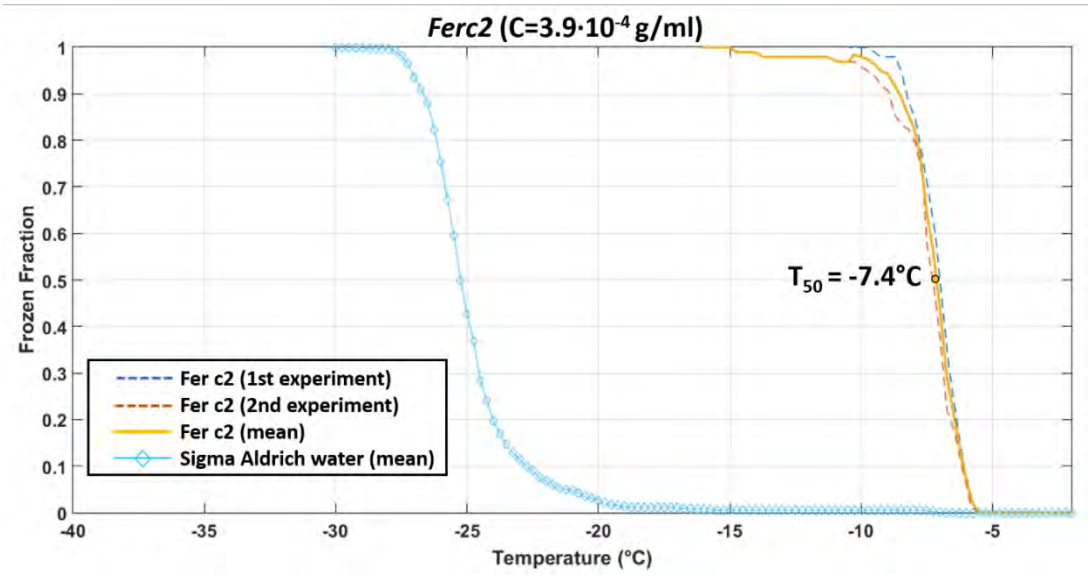

Figure 4.28. Fraction of droplets frozen as function of temperature for concentrated ferritin (*Ferc2*) solution. T_{50} indicates the fraction 50% at which of all droplets are frozen (median freezing temperatures).

Firstly, the results of pure water are discussed. Five independent experiments (see figure 4.29) with water (Aldrich Chemical Co. Inc.) were performed at a cooling rate of 1 °C/min. For pure water, freezing was observed to occur between -17 and -29.2 °C. The median freezing temperature was found to -25.2 °C (mean value).

Experiments with smaller droplets (volume of 5 µl) were performed with the same cooling rate (1 °C/min) and onset freezing temperature was found in the temperature range from −30 °C to −28 °C [19]. In contrast, for 50 µl volume droplets used in the drop freezing experiments, the onset of the freezing temperature is at −20 °C (see figure 4.29)

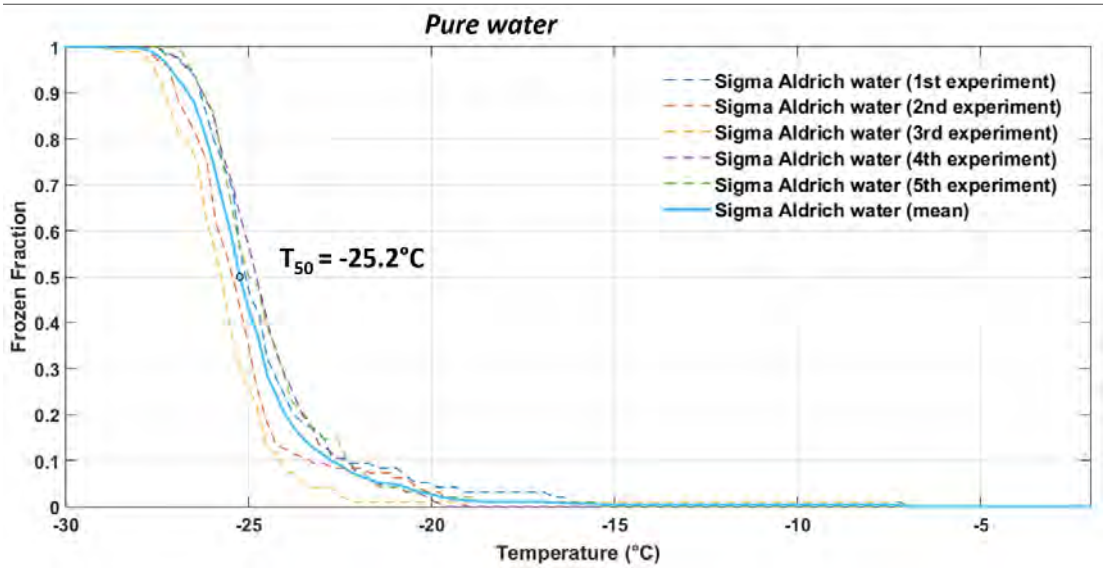

Figure 4.29. Fraction of droplets frozen as function of temperature for pure water (Aldrich Chemical Co. Inc.) T_{50} indicates the fraction 50% at which of all droplets are frozen (median freezing temperatures)

When some apoferritin and ferritin was added to water, the behaviour dramatically changes. For the well-diluted solutions (concentration c_1) the starting of crystallization occurs at much higher temperatures (about -7 ^{o}C). In addition, the shape of the curve is different compared to pure water being more extended to cover a broader temperature range. In this case, freezing took place in the temperature range between -7 and -27 ^{o}C. By contrast, for the more concentrated solutions (concentration c_2), both solutions freeze well above the homogeneous freezing limit of pure water. For apoferritin T_{50} = -6.7 ^{o}C whereas for ferritin is T_{50} = -7.4 ^{o}C. This indicates that apoferritin and ferritin at this concentration acts as INP for water. The frozen fraction sharply increases with decreasing

temperature and the shape of the curve is more similar to that of pure water. In this case, the freezing was observed to occur between -7 and -10 ^{o}C.

From these results, it can be concluded that the ability to nucleate ice increases with increasing the protein concentration, showing the same behaviour as for the other proteins analysed with exception of IBP (see Figure 4.23).

The different samples are compared using the median freezing temperature (T_{50}, the temperature at which 50% of the droplets are frozen) which is shown in each plot. Whereas the onset of the freezing temperature (the temperature where the first droplet freezes) is less reproducible for the different experiments, the median freezing temperature is more reliable[21]. The different median freezing temperatures of apoferritin and ferritin solutions are shown in Table IV.

Sample	T_{50} [°C]
Apo c1	-15.2
Apo c2	-6.70
Fer c1	-21.0
Fer c2	-7.40

Table IV. Median freezing temperatures from the drop freezing measurements for the different concentrations apoferritin and ferritin samples.

In figures 4.30 and 4.31 these results are compared to that obtained for the other proteins and the TMV (section 4.3).

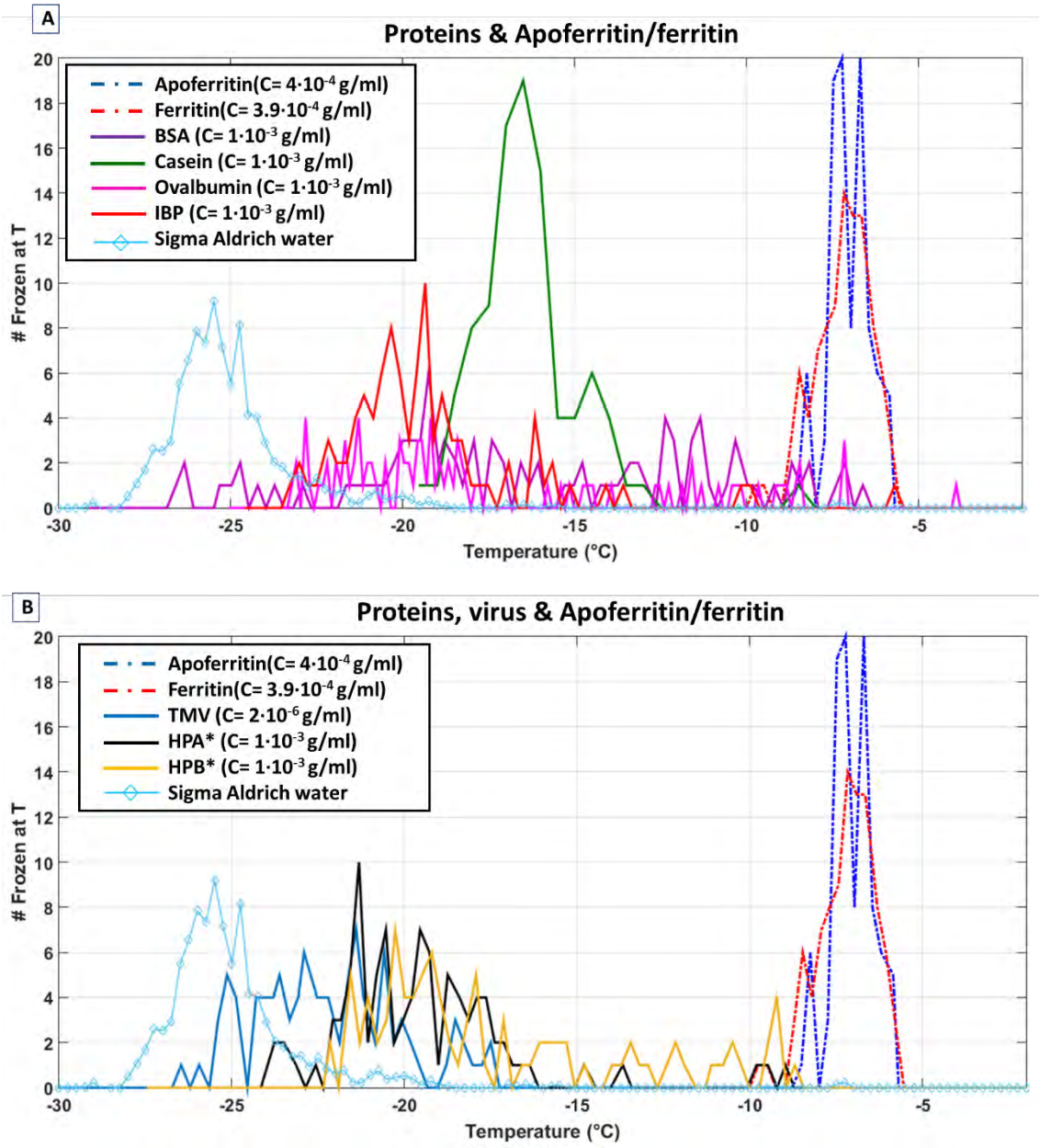

Figure 4.30.A) Number of freezing events as function of temperature for BSA, casein, ovalbumin and IBP and for **B)** TMV, HPA*, HPB*, pure water compared to apoferritin and ferritin.

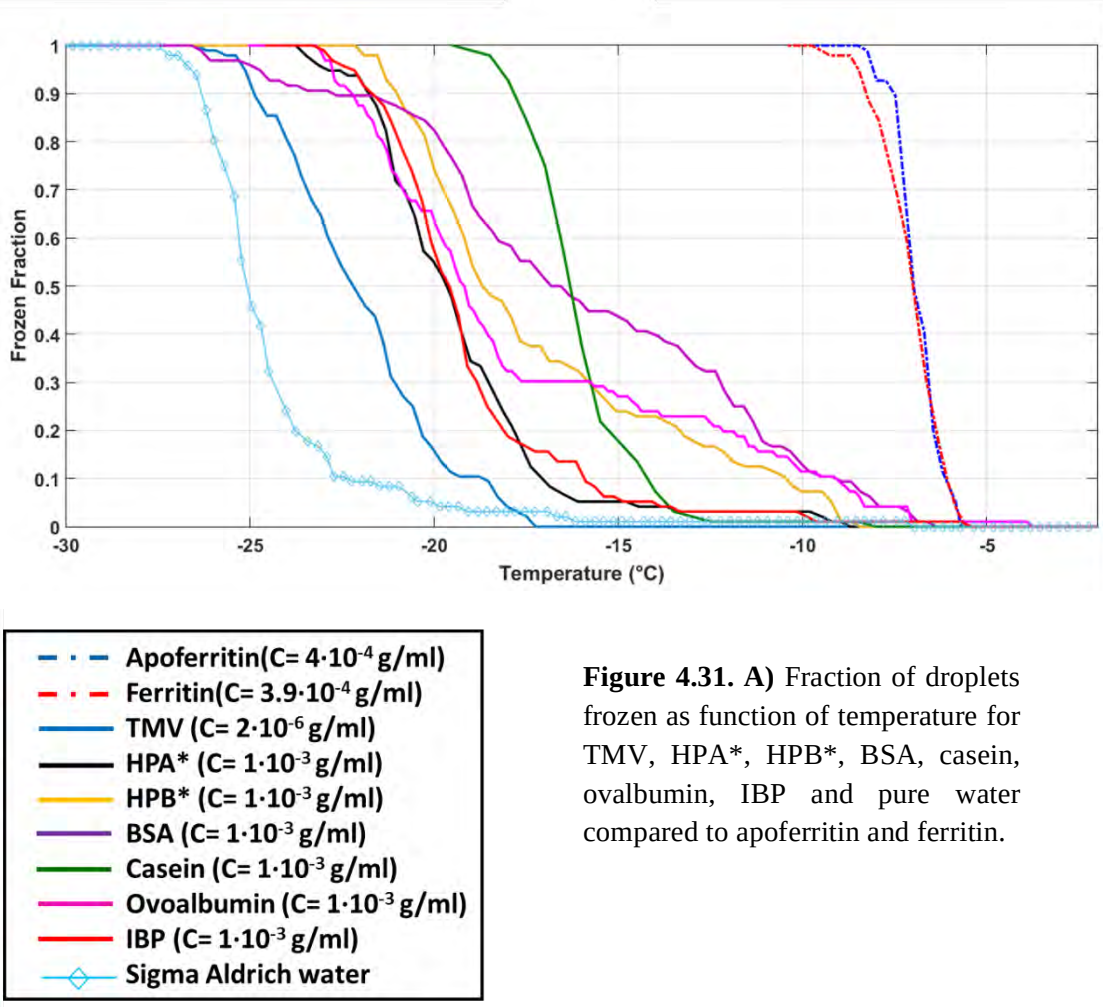

Figure 4.31. A) Fraction of droplets frozen as function of temperature for TMV, HPA*, HPB*, BSA, casein, ovalbumin, IBP and pure water compared to apoferritin and ferritin.

Aggregation of proteins in solution

The effect of protein aggregation has been previously studied in the literature for other INP, like soot [22] or hematite particles[23]. In those cases, it was shown that aggregation of particles in the solutions has an influence on the ability for ice nucleation. Therefore, in the following the formation of aggregates in the apoferritin and ferritin solutions is explored.

The interaction and aggregation of apoferritin molecules in solution have been studied using chromatographic, static and dynamic light scattering techniques, and atomic force microscopy [24]. In this study, fractions of monomers, dimers, trimers, and higher oligomers have been found in the commercial apoferritin solutions using size-exclusion fast protein liquid chromatography (see figure 4.32.A)

Petsev et al. have postulated two options for apoferritin dimerization (see figure 4.32B). Monomers can either stick maintaining their separate spherical shapes, or coalesce into a single sphere with a double volume. The second option would require a substantial change in the arrangement of the molecular subunits.

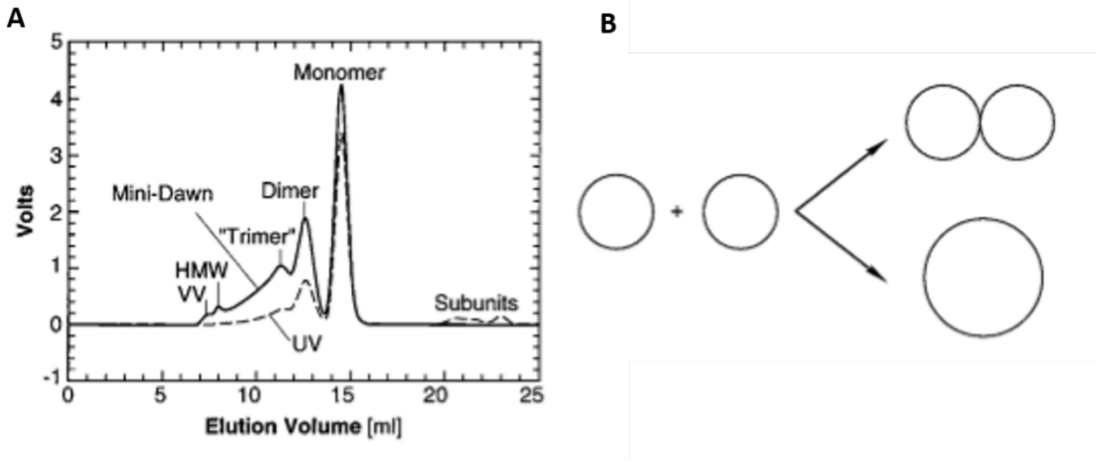

Figure 4.32. A) Size-exclusion FPLC analysis of commercial apoferritin solution.
B) Two options for apoferritin dimerization. (Taken from [24])

Petsev et al. based on AFM observations have concluded that the first option is more likely showing AFM images where clusters are apoferritin dimers shaped as two bound monomer spheres.

Another interesting point included in this study is the analysis of the effects of added electrolytes in the apoferritin solution. Since both commercial solutions of apoferritin and ferritin (Sigma Aldrich) used in the experiments incorporate sodium chloride at 0.150 M, similar arguments could be used to postulate a hypothesis about the influence of the salt presence in the aggregation or no aggregation process inside the protein solutions.

Petsev et al. also showed that the overall interactions between the monomer apoferritin molecules in sodium acetate are repulsive with a minimum around [Na^+] of 0.10-0.15M (see figure 4.33).

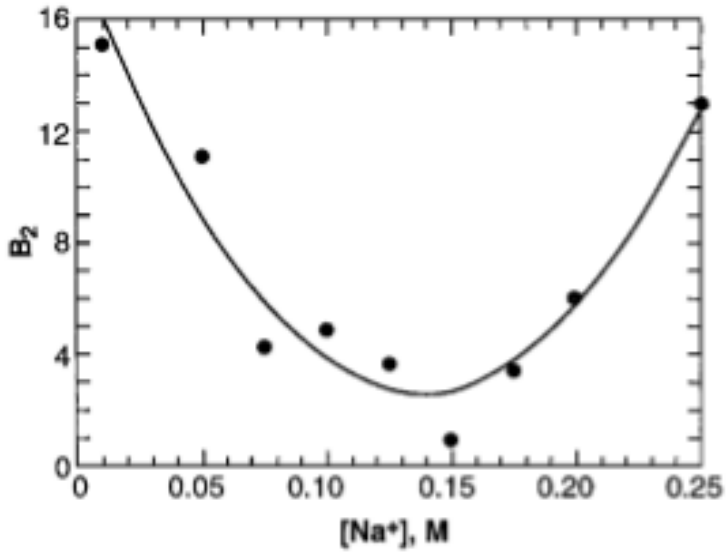

Figure 4.33. Dimensionless second osmotic virial coefficient B2 for the apoferritin monomer as a function of the sodium cation concentration [Na^+]. (Taken from [24]).

On the other hand, positive second osmotic virial coefficient values indicate net repulsive forces between solute molecules. This means that the monomers in apoferritin and ferritin solutions would feel repulsion between monomers. To explain the presence of dimers and higher aggregates in the commercial product *Petsev et al*. have speculated that this type of oligomerization may be induced by partial denaturation of the apoferritin monomers that expose hydrophobic parts of the molecule to the water environment and make oligomerization a favoured option. Sedimentation velocity and circular dichroism experiments [25] also provide evidence that dimers represent the basic building block for shell assembly and indicate that assembly of the apoferritin shell proceeds from dimers through tetramers and octamers.

Based on these studies, one can expect some aggregation of ferritin and apoferritin in the solutions. The presence of monomers and dimers could make difficult to discriminate the effect of each one of this entity in the ice activity of the apoferritin and ferritin.

In the following, the effect of aggregation and the variation of the chemical environment on the high efficient of apoferritin and ferritin solutions to produce ice will be analysed.

4.4.3 pH variations

The objective of the chemical treatment experiments is to test the effect of pH changes in the ice nucleation ability of ferritin and apoferritin which are the most ice active proteins studied in this thesis. Besides, in clouds, there are particular environmental conditions such as light intensity that could affect the ice nucleation activity. For non-biological ice nucleation particles, several data are available in the literature about the influence of environmental conditions on their activity [26] but not many studies were done with biological material. Therefore, in the following the effect of the pH on cloud water using the apoferritin and ferritin as INP will be evaluated.

Literature review

The pH-dependent structures of the ferritin shell (apoferritin, 24-mer) and the ferrihydrite core have been investigated by small-angle X-ray scattering (SAXS) [27]. The intact hollow spherical apoferritin is stable over a wide pH range, 3.40-10.0, and the ferrihydrite core is stable over the pH range 2.10-10.0. The apoferritin subunits undergo aggregation below pH = 0.80, whereas the ferrihydrite cores aggregate below pH = 2.10 because of the disassembly of the ferritin shell under the strongly acidic conditions. As the pH decreases from 3.40 to 0.80, apoferritin undergoes stepwise disassembly by first forming a hollow sphere with two holes, then a headset-shaped structure, and, finally, rod like oligomers.

The effect of low pH on protein structure is related to the electrostatic forces that originate from the changes in net charge and charge distribution attendant with the addition of protons. In monomeric proteins, the progressive protonation of amino acid residues on decreasing the pH gives rise to repulsive interactions that lead to loss of secondary and tertiary structure. Typically, a nearly fully unfolded conformation is attained near pH 2 because stabilizing salt-bridges are removed and buried side chains become protonated. Several proteins do not unfold completely, however, and adopt relatively compact, soluble conformational states that differ from the native structure as indicated by their spectroscopic properties. In oligomeric proteins, the acid denaturation is not limited to the destruction of secondary and tertiary structure of each subunit, but entails the perturbation of intersubunit interactions. In oligomeric proteins, therefore, the

structural changes induced by low pH provide additional information on the forces involved in subunit recognition and association, and on the intermediates that may be formed during the assembly/disassembly processes[28].

Ferritin is remarkably stable and robust, and can resist wide pH variations. Its isoelectric point is ca. 4.5, so that at pH values below 4.5 it becomes positively charged, while at larger pH values the ferritin is negatively charged (see figure 4.34).

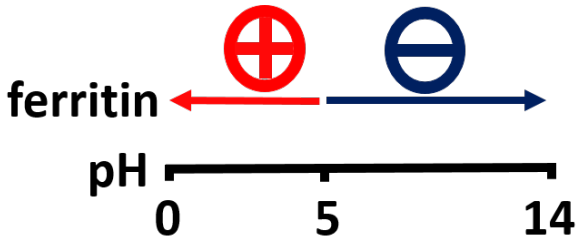

Figure 4.34. Effective surface charge polarization as a function of the pH.

Based on this property, an efficient method to deposit ferritin biomolecules over large areas has been reported [29]. The selective deposition is driven by the electrostatic interactions existing between the proteins and the nanopatterned surface. The sign of the interaction is controlled by changing the pH of the solution. A remarkable fact is that this patterning method does not alter the morphology of the ferritin deposited molecules. Similar conclusions can be obtained from the subsequently presented results which show how in the same pH range ($3 < pH < 9$) apoferritin solutions show similar frozen fraction meaning that the differences in pH values do not affect the ice nucleation efficiency of the apoferritin.

The influence of extreme pH was studied by *Chrichton et al*.,[30] in horse spleen apoferritin claiming that "the oligomer is stable in the range pH 2.8-10.6. Between pH 2.8 and 1.6 and 10.6 and 13.0 both oligomer and subunits can be detected. At pH values between 1.6 and 1.0 the subunit is the only species observed, although below pH 1.0 aggregation of the subunits to a particle sedimenting much faster than the oligomer occurs". *Chrichton et al*. also explain the changes in conformation that occur on dissociation of apoferritin by extremes of pH suggesting that "at low pH values, the first transition to occur involves the transfer of one tryptophan residue/subunit from the

interior of the protein to the solvent; accompanying this transition one or more carboxyl groups of pK 3.29 is protonated. Subunit dissociation involves the transfer of four to five tyrosine residues/subunit to a more hydrophilic environment, most likely to the solvent, accompanied by protonation of at least two carboxyl groups of pK 2.16 (which might be in salt linkage with lysine or arginine residues)".

In studies which combine heating and pH treatments [31], even at pH 5 and after a heat treatment of 40 min, the globular structure of apoferritin is barely observed since the fibrillation process goes on.

Based on the referenced studies, both apoferritin and ferritin are quite stable against changes in pH, but the objective here is to test possible changes in the ice nucleation efficiency of these proteins.

Sample preparation

Six different buffers with pH values between 0 and 9.5 were prepared.

The buffer at pH = 0 was prepared with 85.8 mM HCl (Hydrochloric acid fuming 37%, Merck KGaA, Darmstadt). The buffer at pH = 2 was prepared with 50mM KCl (Potassium chloride >99.5%, Sigma Aldrich, Missouri, USA) and 10.6mM HCl (Hydrochloric acid fuming 37%, Merck KGaA, Darmstadt). The pH = 3.5 buffer was prepared taking 71.5 mM $C_6H_8O_7$ (Citric acid 99%, Sigma Aldrich, Missouri, USA) and 57 mM $Na_2HPO_4 \cdot 7H_2O$ (Sodium phosphate dibasic heptahydrate, Sigma Aldrich, Missouri, USA). The same chemicals were used for preparing the pH = 5: 48.5 mM $C_6H_8O_7$ (Citric acid 99%, Sigma Aldrich, Missouri, USA) and 103mM $Na_2HPO_4 \cdot 7H_2O$ (Sodium phosphate dibasic heptahydrate, Sigma Aldrich, Missouri, USA). The buffer at pH = 7 was prepared with 0.5mM $C_8H_{18}N_2O_4S$ (HEPES, >99.5%, Sigma Aldrich, Missouri, USA) adjusted with some microliters of 5 M NaOH (Sodium hydroxide, >98%, Sigma Aldrich, Missouri, USA). The last buffer (pH = 9.5) was prepared with 12.5 mM $Na_2B_4O_7 \cdot 10H_2O$ (Sodium tetraborate decahydrate, Merck KGaA, Darmstadt) and 3.6 mM NaOH (Sodium hydroxide, >98%, Sigma Aldrich, Missouri, USA).

Results

Once the buffers have been prepared, their ice nucleation efficiency was tested performing drop freezing experiments. The fraction of frozen droplets was recorded as a function of temperature at 0.1 K of resolution. Three independent experiments (see figure 4.35, for the buffer with pH = 5) were performed for each buffer using a cooling rate of 1 °C/min. The mean of the frozen fraction was calculated from the average of these three measurements. The reproducibility of the experiments ensures the high accuracy of the setup and its reliability.

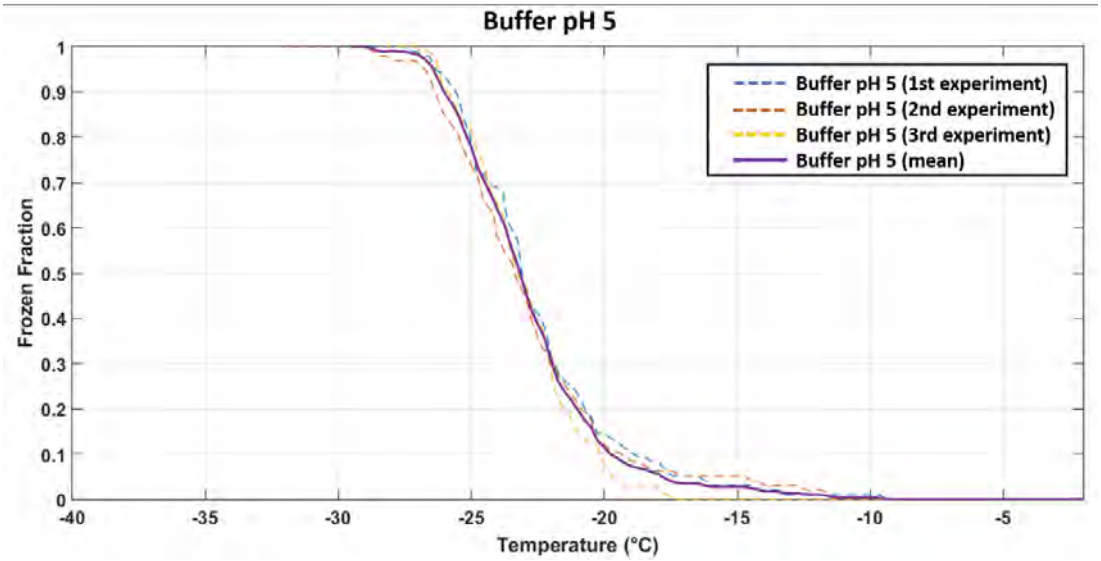

Figure 4.35. Fraction of droplets frozen as function of temperature for the independent experiments with pH 5 buffer solution (dashed curves) and the mean of the fraction frozen is shown (solid purple line)

Figure 4.36 shows the temperature dependence of the frozen fraction of droplets and the median freezing temperature (T_{50}) for all the buffer solutions. These temperatures are also shown in table V. Figure 4.36 shows the differences of the ice nucleation activity between the different buffers, where it can be seen how the most efficient INP results to be the buffer with pH = 3.5 and the worst INP, the buffer with pH = 0.

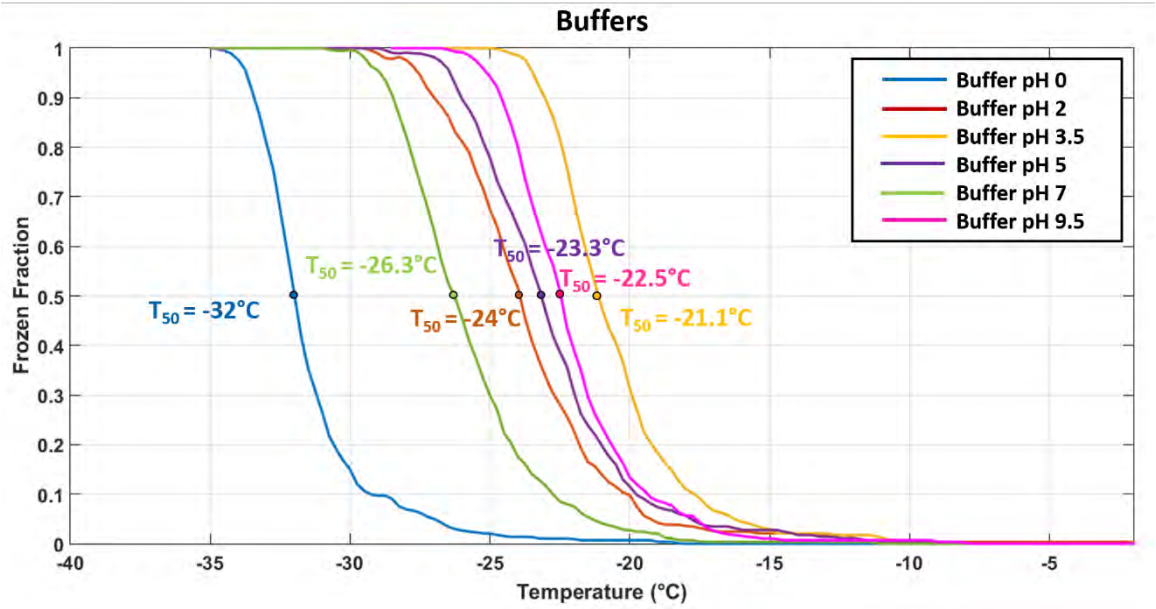

Figure 4.36. Fraction of droplets frozen as function of temperature for the six different pH buffer solutions prepared. T_{50} indicates the fraction 50% of all droplets are frozen (median freezing temperatures)

Sample	T_{50} (°C)
Buffer pH 0	-32.0
Buffer pH 2	-24.0
Buffer pH 3.5	-21.1
Buffer pH 5	-23.3
Buffer pH 7	-26.3
Buffer pH 9.5	-22.5
Sigma Aldrich water	-25.2

Table V. Median freezing temperatures for the different pH buffers and pure water (Aldrich Chemical Co. Inc.)

Comparing the median freezing temperatures of the different buffers with that of pure water, (see table V and figure 4.37), one could easily associate the differences in the ice nucleation activity to the presence of different counterions in the solution. A considerable difference shows up between pure water and the pH = 0 buffer (up to 8 °C).

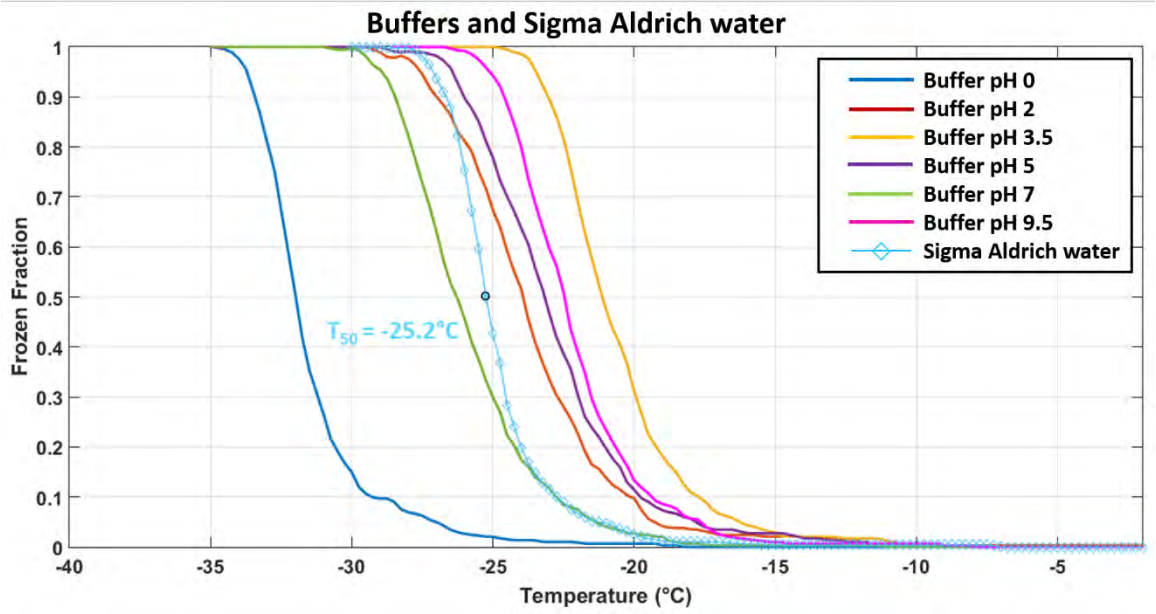

Figure 4.37. Fraction of droplets frozen as function of temperature for the six different pH buffer solutions prepared compared to pure water (T_{50} for water is shown in the plot)

Once the ice nucleation efficiency of the buffers was tested, they were used to change the pH of apoferritin and ferritin solutions. Two different concentrations of apoferritin (*Apoc1*, *Apoc2*) and ferritin (*Ferc1*, *Ferc2*) solutions were prepared following the same procedure previously mentioned (see section 4.4.1). The pH of apoferritin and ferritin solutions in water were measured using a pH-meter (691 pH Meter, Metrohm, Swiss) and all the measurements are shown in table VI.

Sample	pH
Apo c1	7.00
Apo c2	6.97
Fer c1	7.60
Fer c2	7.27

Table VI. pH values of the samples used in chemical

Buffers were added to ferritin and apoferritin solutions to assess the effect of the chemical treatment on the IN activity. Samples were kept in these buffers overnight. Depending on pH value, ferritin solutions have different colours (see appendix VIII). By contrast for apoferritin solutions, no appreciable difference was observed for the different

pH values (the solutions are always transparent). However, it is interesting to note that at pH = 3.5 and after an incubation time, the solutions lose transparency and become hazy (see appendix VIII). This observation indicates that a possible aggregation takes place at this pH value.

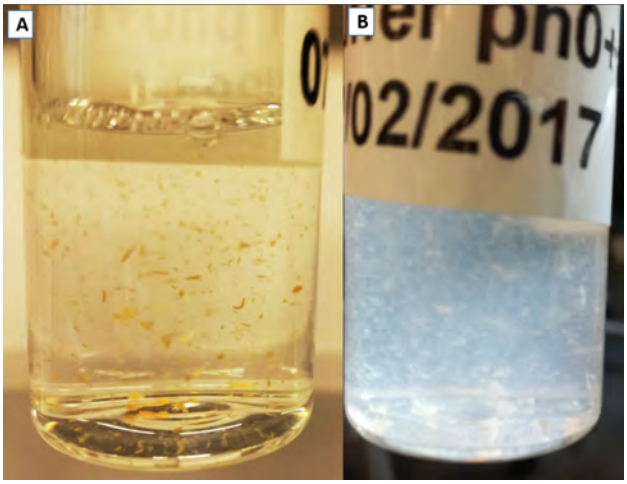

Figure 4.38. A) Well diluted (*Ferc1*) ferritin in pH 0 buffer solution. Once the ferritin is added, some precipitates are formed immediately and remain floating in the buffer solution. **B)** High concentration apoferritin (*Apoc2*) in pH 0 buffer solution. A huge amount of precipitate is formed and remains floating in the buffer solution.

In all the different pH analysed solutions, apoferritin and ferritin are perfectly dissolved with the exception of solutions with pH = 0 where flocculation was observed immediately (see figure 4.38).

The pH of the different solutions was measured before the drop freezing experiments to be sure the pH does not change with time. These measurements are shown in table VI.

Sample	Buffer	pH
Apo c1	85.8 mM HCl	0.27
	50 mM KCl + 10.6 mM HCl	2.08
	71.5 mM $C_6H_8O_7$ + 57 mM $Na_2HPO_4 \cdot 7H_2O$	3.52
	48.5 mM $C_6H_8O_7$ + 103 mM $Na_2HPO_4 \cdot 7H_2O$	5.27
	0.5 mM $C_8H_{18}N_2O_4S$ (adjusted with 5M NaOH)	7.06
	12.5 mM $Na_2B_4O_7 \cdot 10H_2O$ + 3.6mM NaOH	9.50
Apo c2	85.8 mM HCl	0.16
	50 mM KCl + 10.6 mM HCl	2.07
	71.5 mM $C_6H_8O_7$ + 57 mM $Na_2HPO_4 \cdot 7H_2O$	3.47
	48.5 mM $C_6H_8O_7$ + 103 mM $Na_2HPO_4 \cdot 7H_2O$	5.07
	0.5 mM $C_8H_{18}N_2O_4S$ (adjusted with 5M NaOH)	7.11
	12.5 mM $Na_2B_4O_7 \cdot 10H_2O$ + 3.6mM NaOH	9.51
Fer c1	85.8 mM HCl	0.02
	50 mM KCl + 10.6 mM HCl	2.08
	71.5 mM $C_6H_8O_7$ + 57 mM $Na_2HPO_4 \cdot 7H_2O$	3.67
	48.5 mM $C_6H_8O_7$ + 103 mM $Na_2HPO_4 \cdot 7H_2O$	5.14
	0.5 mM $C_8H_{18}N_2O_4S$ (adjusted with 5M NaOH)	7.07
	12.5 mM $Na_2B_4O_7 \cdot 10H_2O$ + 3.6mM NaOH	9.49
Fer c2	85.8 mM HCl	0.07
	50 mM KCl + 10.6 mM HCl	2.06
	71.5 mM $C_6H_8O_7$ + 57 mM $Na_2HPO_4 \cdot 7H_2O$	3.46
	48.5 mM $C_6H_8O_7$ + 103 mM $Na_2HPO_4 \cdot 7H_2O$	5.06
	0.5 mM $C_8H_{18}N_2O_4S$ (adjusted with 5M NaOH)	7.12
	12.5 mM $Na_2B_4O_7 \cdot 10H_2O$ + 3.6mM NaOH	9.48

Table VI. pH values of the samples used in chemical treatment experiments

The ice activity of the different pH samples was tested, included the pH = 0, although the aggregation process that takes place at this pH might produce non-reliable data.

Figures 4.39 and 4.40 show the temperature dependence of the frozen fraction for two different concentrations of apoferritin (*Apoc1*, *Apoc2*) at different pH. The median

freezing temperatures for the different pH values and the different concentrations are summarized in table VII.

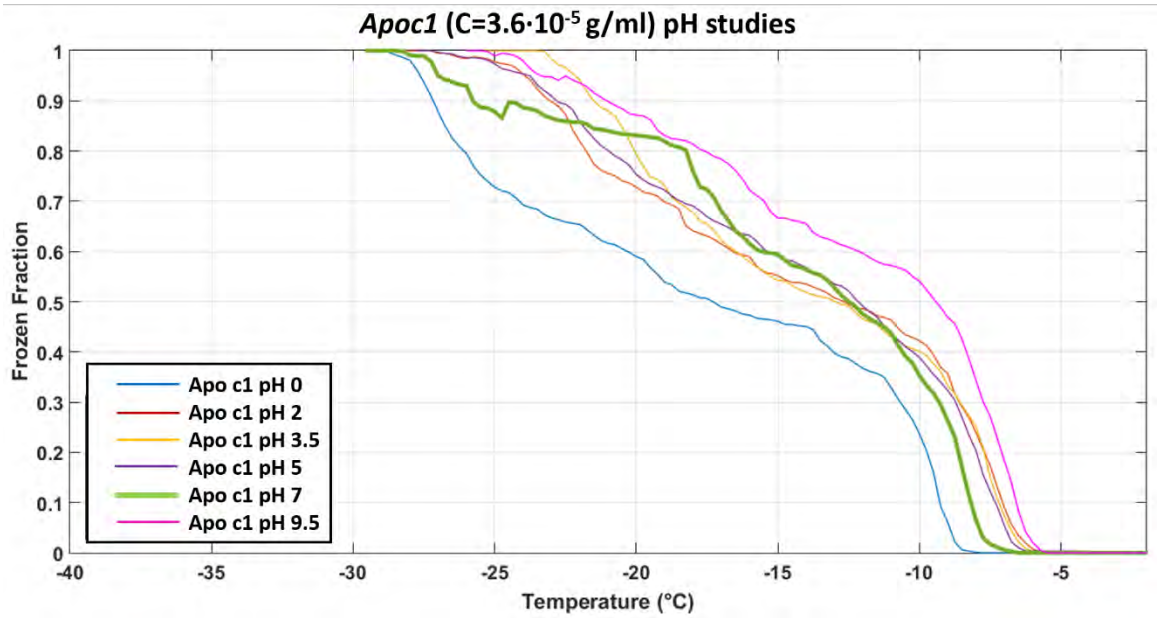

Figure 4.39. Fraction of droplets frozen as function of temperature for well diluted apoferritin in six different pH buffer solutions. pH 7 (that correspond to the value of the apoferritin in water) is marked with a thicker line.

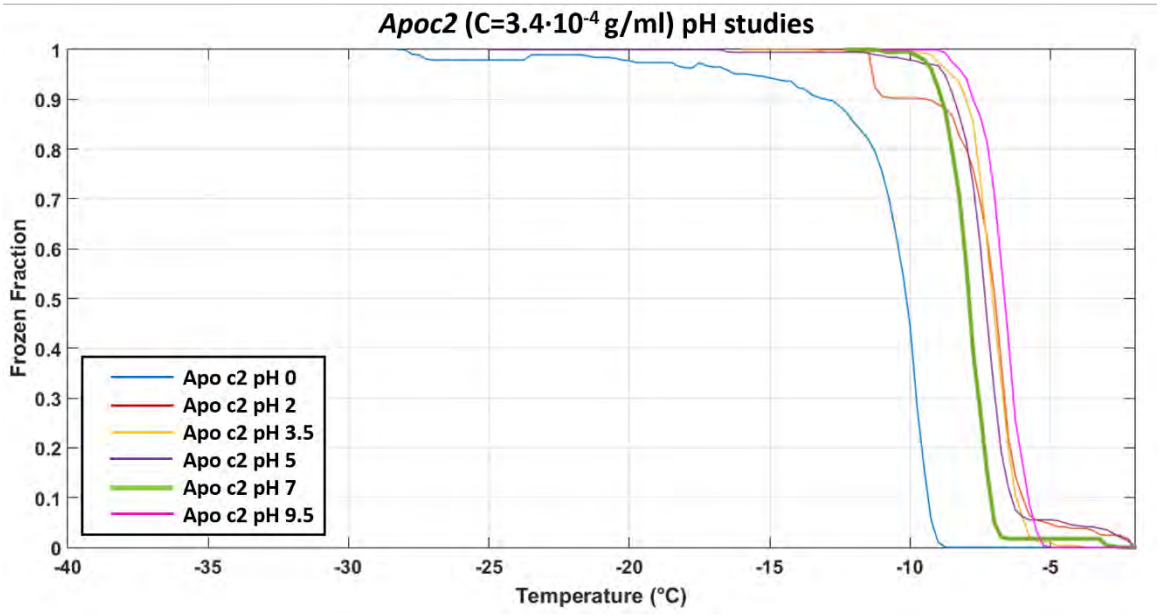

Figure 4.40. Fraction of droplets frozen as function of temperature for concentrated apoferritin in six different pH buffer solutions. pH 7 (that correspond to the value of the apoferritin in water) is marked with a thicker line.

The samples with pH = 0 and pH = 9.5 are the only that show an appreciable difference in the ice nucleation ability whereas for well diluted apoferritin solutions with pH in the range from 2 to 7 appear to show similar frozen fraction curves.

As in the case of the less concentrated apoferritin solution, differences appear to be significant mostly for pH = 0 and pH = 9.5, although the concentrated apoferritin solutions with pH = 2, 3.5 and 5, shows a slight increase in the ice nucleation efficiency compared to the solution at pH = 7 and the curves are shifted to higher temperatures.

Sample	T_{50} (°C)
Apo c1 pH 0	-17.30
Apo c1 pH 2	-12.70
Apo c1 pH 3.5	-13.00
Apo c1 pH 5	-12.25
Apo c1 pH 7	-12.50
Apo c1 pH 9.5	-9.50
Apo c2 pH 0	-10.10
Apo c2 pH 2	-6.90
Apo c2 pH 3.5	-7.10
Apo c2 pH 5	-7.30
Apo c2 pH 7	-7.80
Apo c2 pH 9.5	-6.60

Table VII. Median freezing temperatures for different pH and concentration apoferritin solutions.

In the same way, the frozen fractions for the two different concentration ferritin solutions (*Ferc1*, *Ferc2*) at the different pH solutions are shown in figure 4.41 and 4.42 and the median freezing temperatures for each different pH and concentration sample solutions are summarized in table VIII.

Ferritin shows a similar behaviour as the apoferritin respect to the pH changes. Again, there is significant difference in the ice nucleation activity for buffer at pH = 0 and pH =

9.5 and a slight increase in the ice nucleation compared to the pH = 7 (the “normal” pH of ferritin in water without chemical treatment).

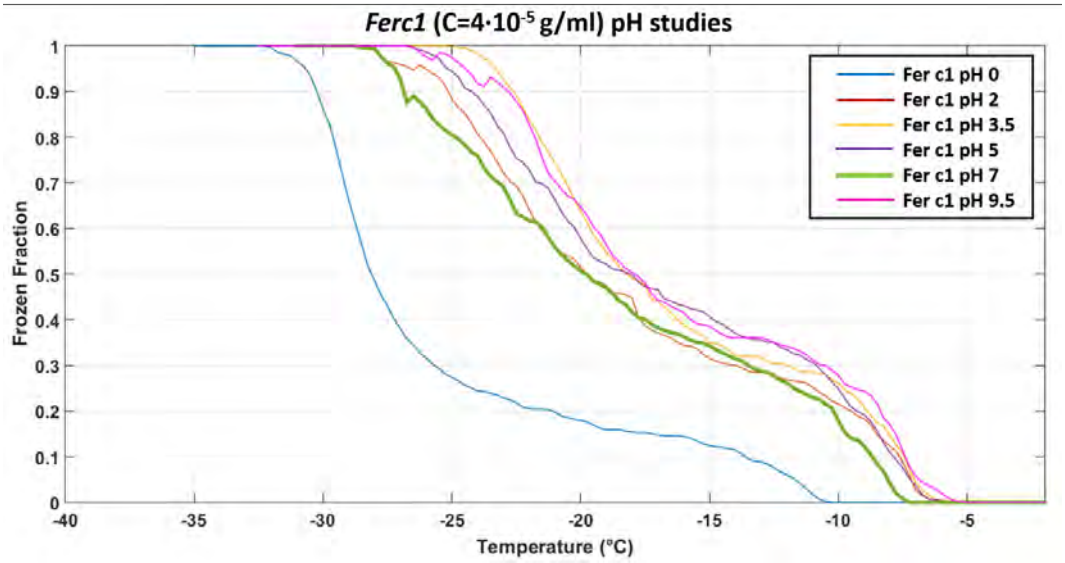

Figure 4.41. Fraction of droplets frozen as function of temperature for well diluted ferritin in six different pH buffer solutions. pH 7 (that correspond to the value of the apoferritin in water) is marked with a thicker line.

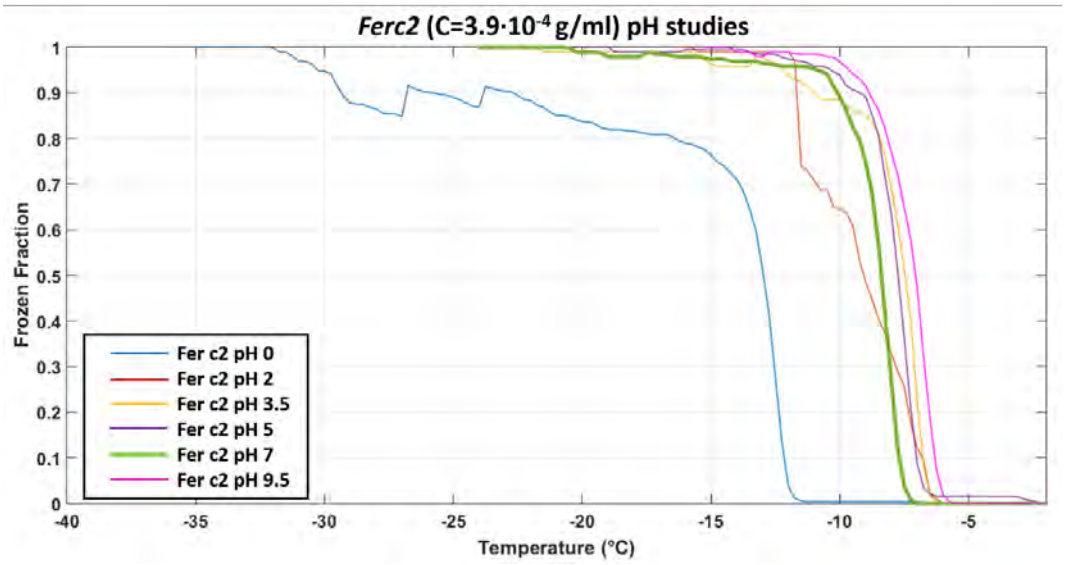

Figure 4.42. Fraction of droplets frozen as function of temperature for concentrated ferritin in six different pH buffer solutions. pH 7 (that correspond to the value of the apoferritin in water) is marked with a thicker line.

Sample	T_{50} (°C)
Fer c1 pH 0	-28.2
Fer c1 pH 2	-20.2
Fer c1 pH 3.5	-18.7
Fer c1 pH 5	-18.8
Fer c1 pH 7	-20.0
Fer c1 pH 9.5	-18.5
Fer c2 pH 0	-13.0
Fer c2 pH 2	-9.0
Fer c2 pH 3.5	-7.50
Fer c2 pH 5	-7.8
Fer c2 pH 7	-8.3
Fer c2 pH 9.5	-7.1

Table VIII. Median freezing temperatures for different pH and concentration ferritin solutions.

In the pH range 2 - 9.5, uniform solutions are obtained when apoferritin or ferritin are incorporated to the different pH buffers, but for the lower pH (pH = 0) an unstable suspension is formed (see figure 4.43) and sedimentation takes place after some time.

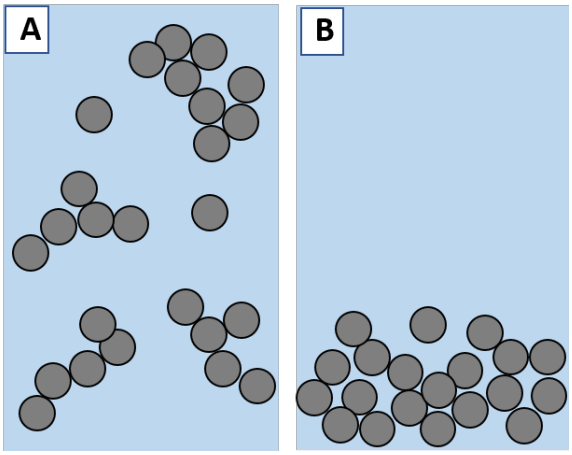

Figure 4.43. A) Unstable suspension: particles stick to each other and form larger and larger aggregates. **B)** Sedimentation: As these aggregates grow larger, they sediment, and the suspension clarifies.

The influence of having an unstable suspension at pH = 0 for both type of proteins (apoferritin and ferritin) displayed in figure 4.44 where the frozen fraction of two independent experiments (red dash and red solid curves) with low concentration ferritin (*Ferc1*) at pH = 0 are different depending on the fraction of sample that has been pipetted.

The red dash curve corresponds to supernatant solution, i.e., the solution has been let sitting down for two hours and only the supernatant solution (containing basically buffer solution) has been pipetted. On the other hand, red solid frozen fraction curve has been obtained shaking the solution before pipetting and it is obvious that the INP concentration is higher for this latter case.

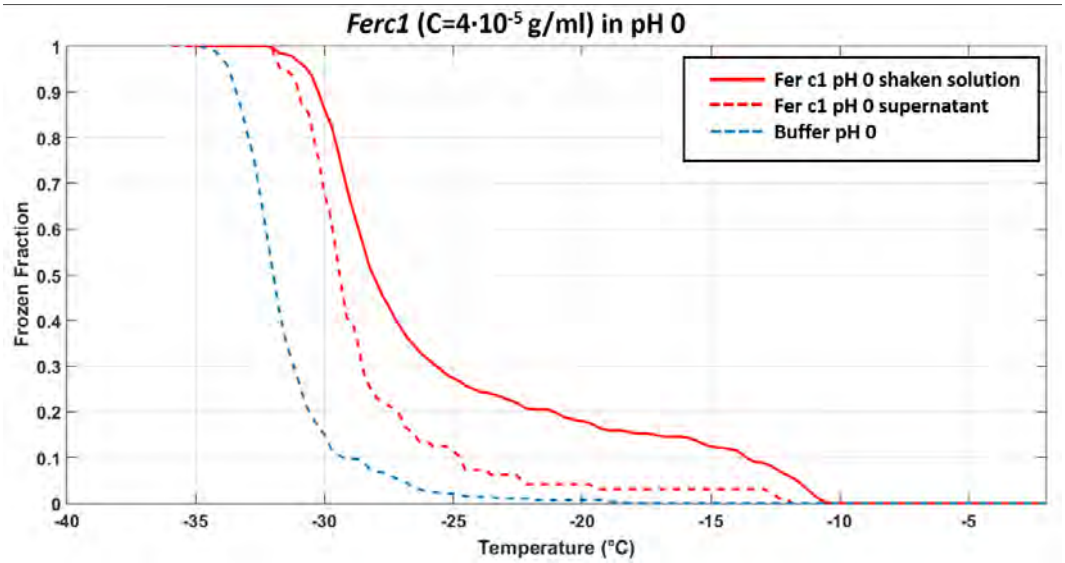

Figure 4.44. Fraction of droplets frozen as function of temperature for well diluted ferritin solution in pH 0 showing the influence of the pipetting style. The frozen fraction of the blank (buffer pH 0, blue dash lined) is shown just for comparison.

To perform the drop freezing experiments a uniform solution is needed because the concentration should be the same in all the wells. Otherwise the data evaluation turns out difficult and results slightly reliable.

Apoferritin and ferritin suspensions at pH = 0 were submitted to different heat treatments to reduce the presence of large aggregates suspended in the solutions. First, samples were heated in the oven during three hours at 70 °C without completely achieved the dissapearance of the aggregates. A stronger heat treatment was applied to the apoferritin

and ferritin samples heating them during 5 hours at 110 °C. After this treatment aggregates dissapeared completely and solutions became clearer (see appendix VIII).

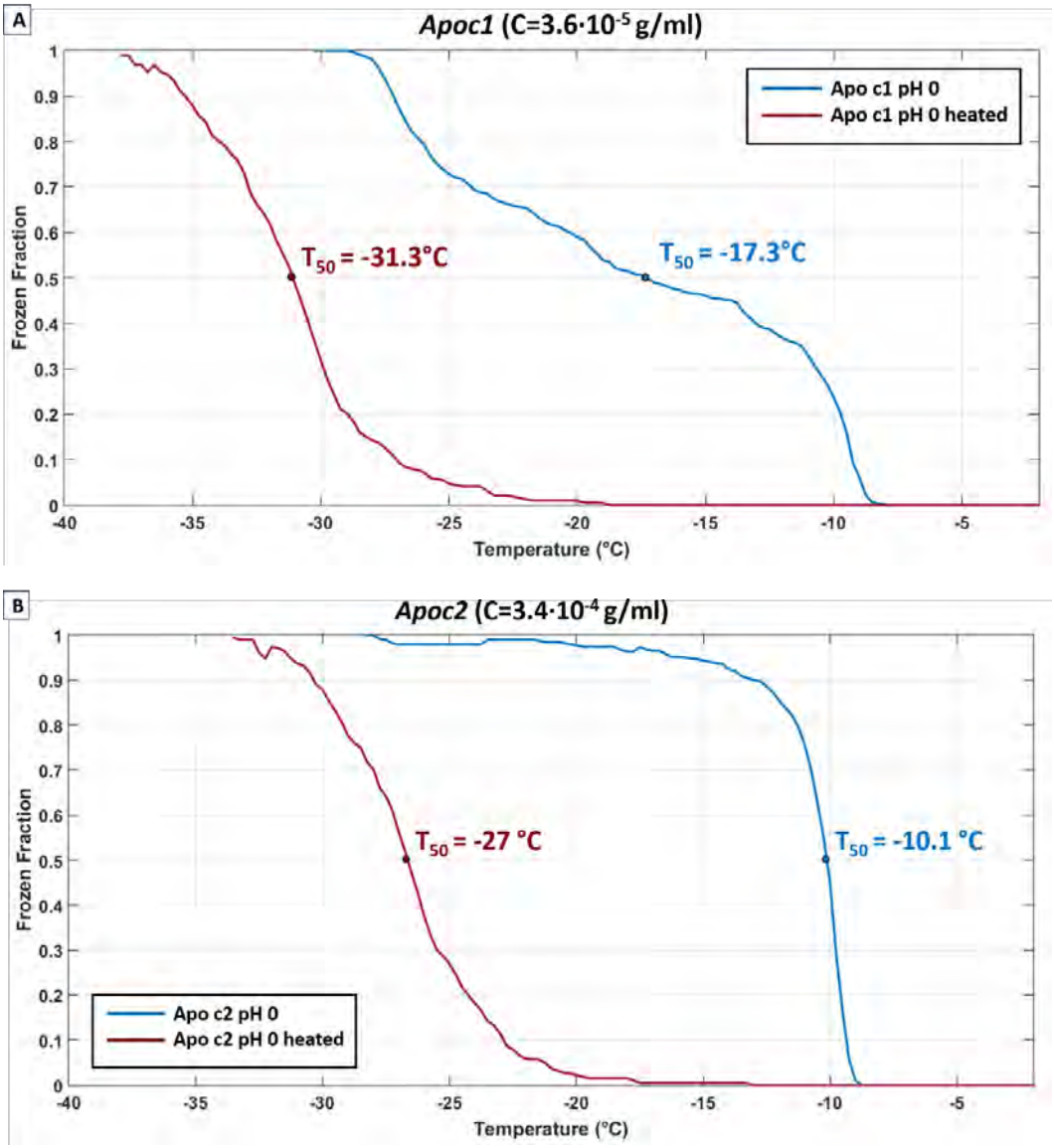

Figure 4.45. A) Fraction of droplets frozen as function of temperature for well diluted apoferritin (*Apoc1*) solution in pH 0 (light blue curve) and the same solution after heat treatment at 110 °C (purple curve) **B)** Fraction of droplets frozen as function of temperature for concentrated apoferritin (*Apoc2*) solution in pH 0 (light blue curve) and the same solution after heat treatment at 110 °C (purple curve). Median freezing temperatures ,T_{50} , are shown in the plots.

The results of the drop freezing experiments of this two steps treatment (pH = 0 plus heating) are shown in terms of frozen fraction (figures 4.45 and 4.46) and suggest that while at pH = 0 the frozen fraction curves are similar to other pH frozen fraction curves, with a shift of the ice nucleation activity to lower temperatures, the heating at pH = 0 destroys the ice nucleation activity almost completely.

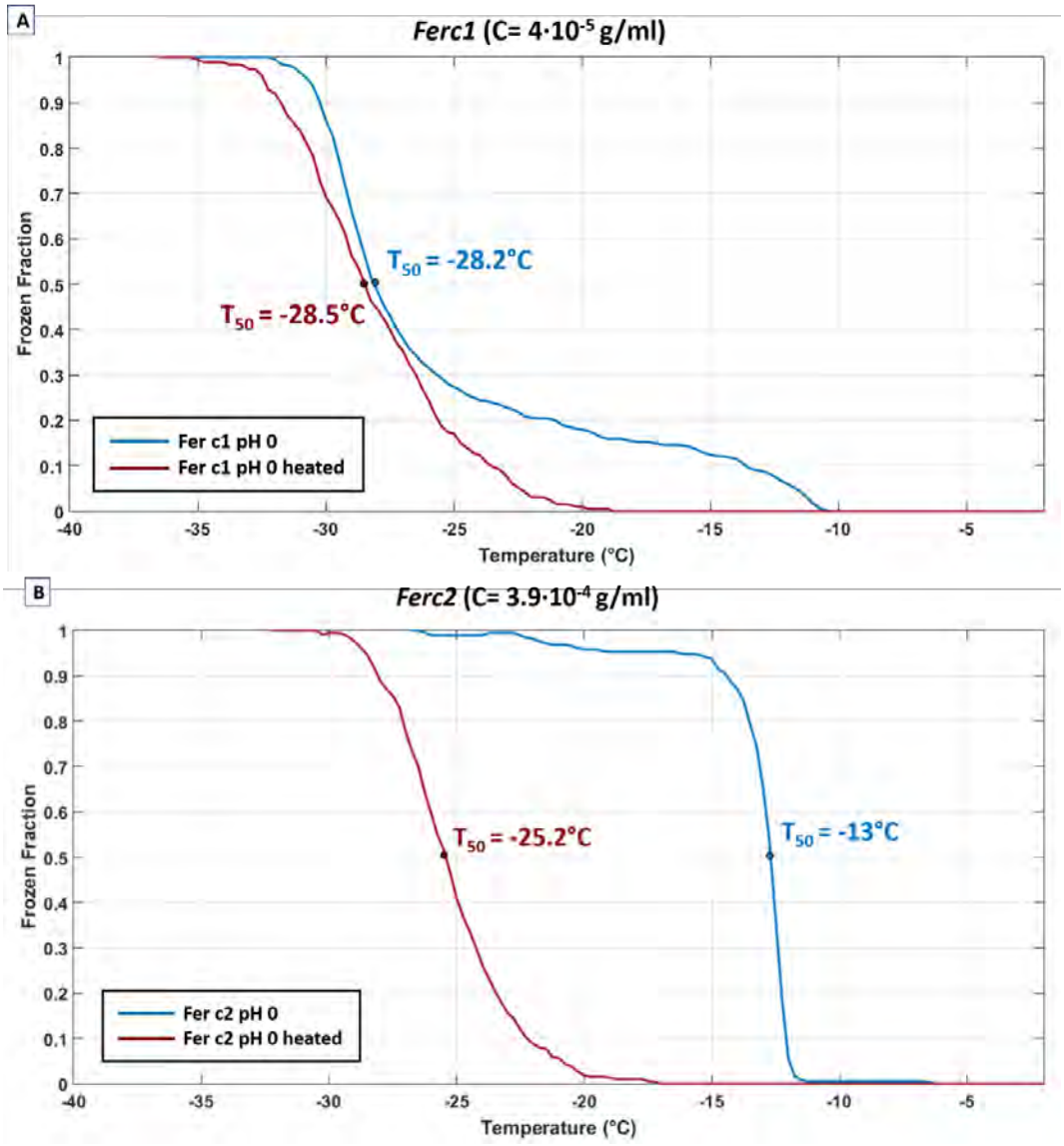

Figure 4.46. A) Fraction of droplets frozen as function of temperature for well diluted ferritin (*Ferc1*) solution in pH 0 (light blue curve) and the same solution after heat treatment at 110 °C (purple curve) **B)** Fraction of droplets frozen as function of temperature for concentrated ferritin (*Ferc2*) solution in pH 0 (light blue curve) and the same solution after heat treatment at 110 °C (purple curve). Median freezing temperatures ,T_{50} , are shown in the plots.

Sample	T_{50} (°C)	Sample	T_{50} (°C)
Apo c1 pH 0	-17.3	Apo c1 pH 0 heated	-31.3
Apo c2 pH 0	-10.1	Apo c2 pH 0 heated	-27
Fer c1 pH 0	-28.5	Fer c1 pH 0 heated	-28.2
Fer c2 pH 0	-13	Fer c2 pH 0 heated	-25.2

Table IX. Median freezing temperatures for pH = 0 and pH = 0 heated apoferritin and ferritin solutions.

4.4.4 Heating experiments

With the heating experiments, it will be attempted to show a relationship between the denaturation of the protein and the reduction of it ice nucleation properties.

Literature review

The thermostability of horse spleen apoferritin has been tested and its unfolding at 70 ºC was observed [32]. The heating of apoferritin above 36 degrees resulted in the conformational changes of the apoferritin subunits and total denaturation at 68 ºC is observed; nevertheless, the substantial reversibility of horse spleen apoferritin denaturation is observed up to a few degrees below denaturation temperature.

The unfolding and denaturation of apoferritin have been also examined using gel electrophoresis. Smears corresponding to the release of apoferritin subunits are observed in case of samples heated above 65 ºC but it seems to have reached a higher intensity at 70 ºC. Taking together data from UV absorption and gel electrophoresis, *J. Kudr et al.* have concluded that the spherical structure of apoferritin degrades in temperature above 65 ºC.

The thermal stability of horse spleen apoferritin has been studied by differential scanning calorimetry and the denaturation temperature, T_d, at pH 7 has been found to be >93ºC [33] .The DSC measurements confirm not only the high stability of horse spleen apoferritin, but also demonstrate that the stabilization of the polymeric structure is governed by subunit interactions at the three- and fourfold symmetry axes.

The denaturation process displays significant reversibility after heating to temperatures only a few degrees lower than the T_d value, but in the same study [33], 80ºC is defined as the temperature which should not be exceeded to avoid irreversible denaturation for horse spleen apoferritin.

According to this assessment, the heat treatment that will be performed to the samples should cause the irreversible denaturation of the protein.

It has been suggested that the thermal denaturation does not lead to the complete unfolding of the molecule. The presence of substantial amounts of secondary structure at high temperatures is often observed in the case of multi subunit proteins which do not undergo dissociation upon heating.

Sample preparation

Two different concentrations of apoferritin (*Apoc1, Apoc2*) and ferritin (*Ferc1, Ferc2*) solutions were prepared following the same procedure previously mentioned (see section 4.4.1).

The four prepared solutions were kept at 110 ºC during 5 hours. The solutions were completely uniform, but after the heating treatment the aspect of the samples completely changed (see figure 4.47 and appendix VIII).

In figure 4.47.A it can be observed how the heat treatment changes completely the appearance of the ferritin solution. A huge number of aggregates are sitting at the bottom of the bottle after the heating and the solution has lost it yellow-orange appearance and appears transparent.

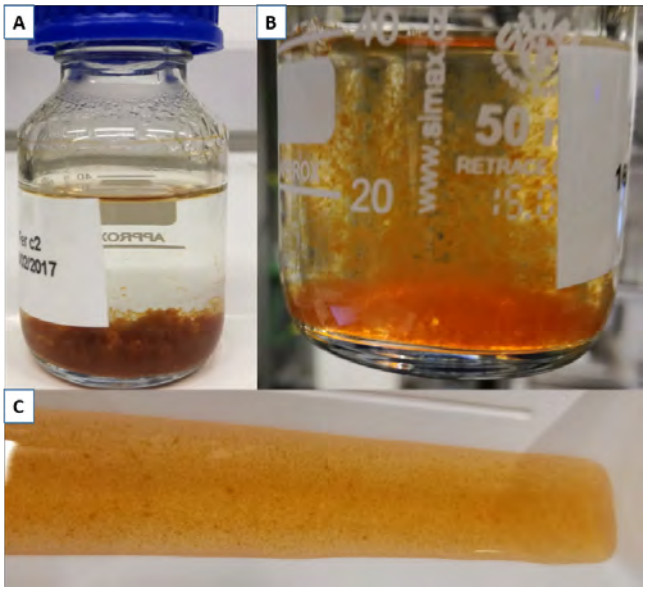

Figure 4.47. High concentrated (*Fer c2)* ferritin solution after being heated at 110 °C during 5 hours. **A)** Glass bottle with heated ferritin solution just after being taken from the oven. A huge amount of precipitate has been formed and settled to the bottom of the glass bottle. **B)** Appearance of the solution just after shaking. **C)** *Fer c2* solution in the dispersion tray just before being pipetted.

Due to the inhomogeneity of the heated solutions, two different experimental procedures were used to test the ice nucleation in the drop freezing setup. For the first type of measurements, aliquots of 50 μL of the supernatant apoferritin and ferritin heated solutions were transferred to the 96-well PCR-tray. Due to the heating, a phase separation happened (see figure 4.47.A) and based on the colour of upper part of the solution, the supernatant was mainly composed of water. In this kind of measurements, it can be tested the ice nucleation of the water, which has been in contact with apoferritin or ferritin for some hours and check if it adopts the ice nucleation properties from the apoferritin and ferritin.

In the second method, the suspensions were shaken (see figure 4.47.B) and poured into the sterilised dispensing tray. Aliquots of 50 μL of this poured solution which has an orange colour and an enormous number of particles in it (see figure 4.47.C) were transferred to the 96-well PCR-tray to perform the drop freezing experiments.

The obtained frozen fraction for the first method is shown in figure 4.48 whereas the results obtained for the second method are shown in figure 4.49.

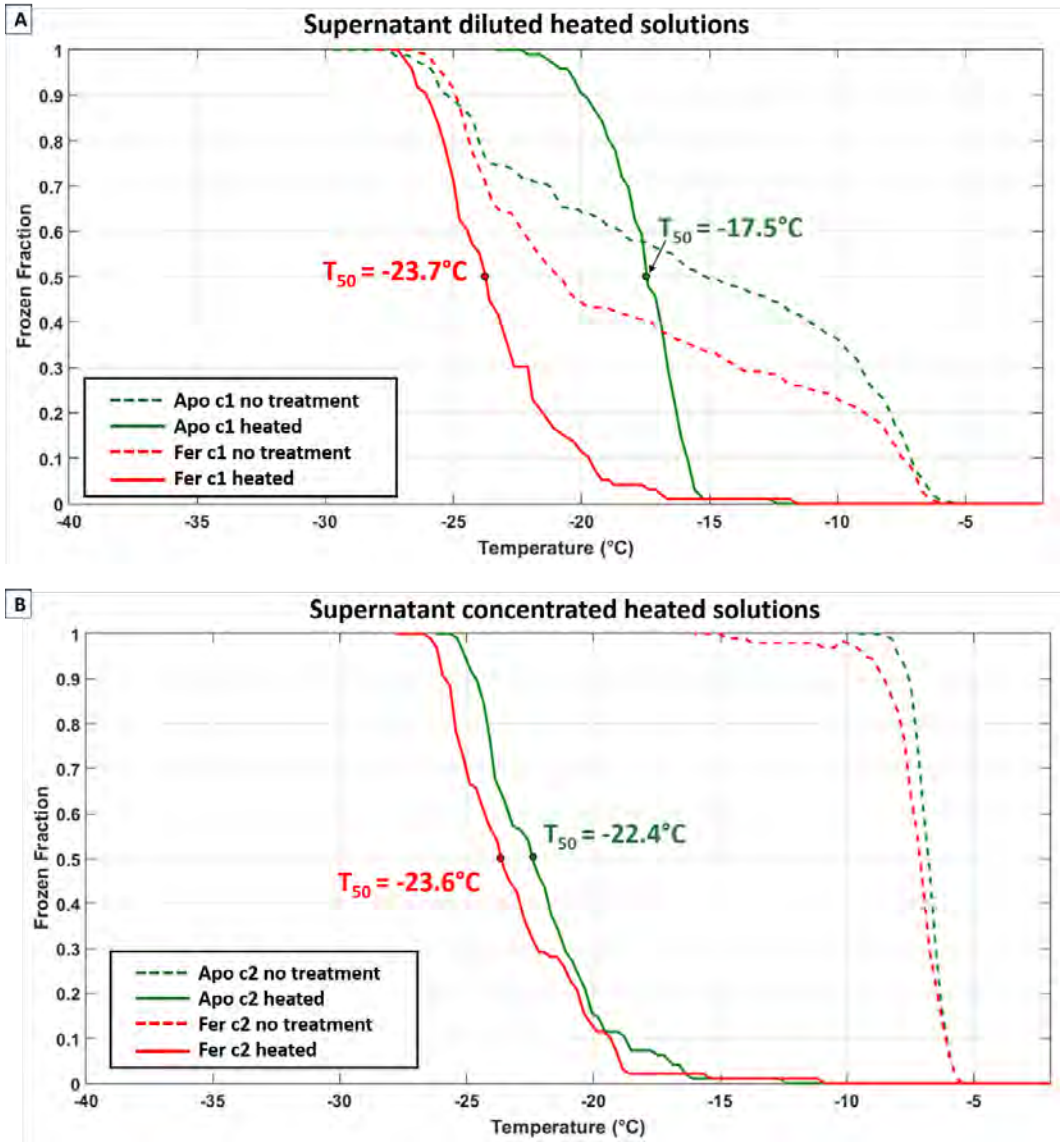

Figure 4.48. A) Fraction of droplets frozen as function of temperature for supernatant samples of well diluted apoferritin (*Apoc1*) and ferritin (*Ferc1*) heated solutions compared to apoferritin and ferritin solutions without treatment. **B)** Fraction of droplets frozen as function of temperature for supernatant samples of concentrated apoferritin (*Apoc1*) and ferritin (*Ferc1*) heated solutions compared to apoferritin and ferritin solutions without treatment. Median freezing temperatures ,T_{50} , are shown in the plots.

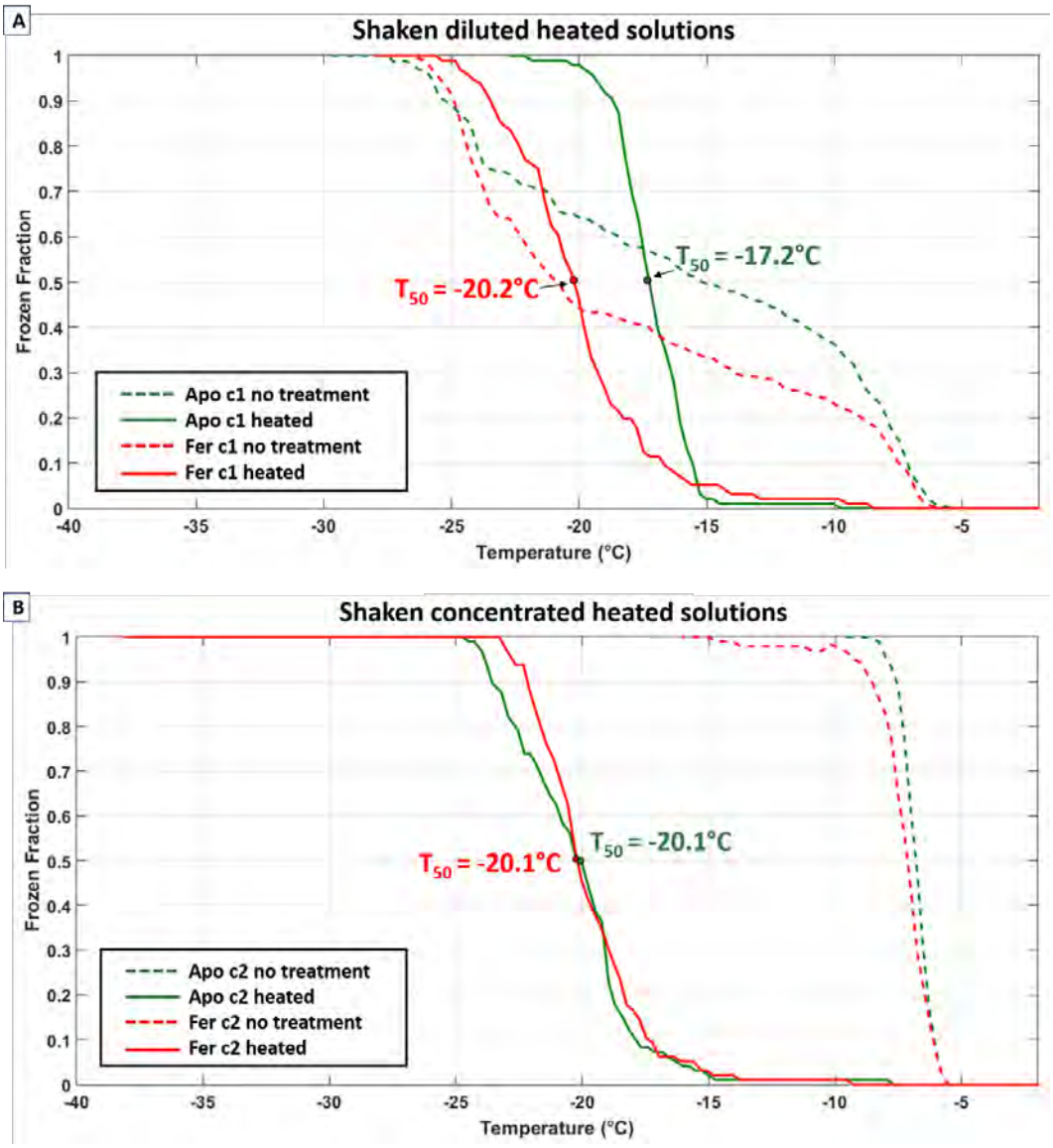

Figure 4.49. A) Fraction of droplets frozen as function of temperature for shaken samples of well diluted apoferritin (*Apoc1*) and ferritin (*Ferc1*) heated solutions compared to apoferritin and ferritin solutions without treatment. **B)** Fraction of droplets frozen as function of temperature for shaken samples of concentrated apoferritin (*Apoc1*) and ferritin (*Ferc1*) heated solutions compared to apoferritin and ferritin solutions without treatment. Median freezing temperatures ,T_{50} , are shown in the plots.

The differences between the two methods can be explained in terms of the concentration differences. For the high concentration, *Apo c2*, the choice on how the solution was pipetted, supernatant vs. shaking the solution, makes a big difference. For ferritin solution, at both concentrations low (*Fer c1*) and high (*Fer c2*), the supernatant has

significantly less ice active than the sample prepared after having shaken the solution. Overall this suggests having more solids in the wells increases the ice activity.

To conclude a summary of the results obtained with the apoferritin and ferritin is presented to have a general perspective.

The results of the different measurements are shown in figure 4.50 and 4.51 for *Apoc1* and *Apoc2* respectively. Tables X and XI summarise the onset nucleation temperature for *Apoc1* and *Apoc2*.

In terms of the onset temperature of ice formation, there is not much difference between *Apoc1* and *Apoc2* for all samples and treatments (water, heating, pH 0 and heated-pH0), see tables X and XI.

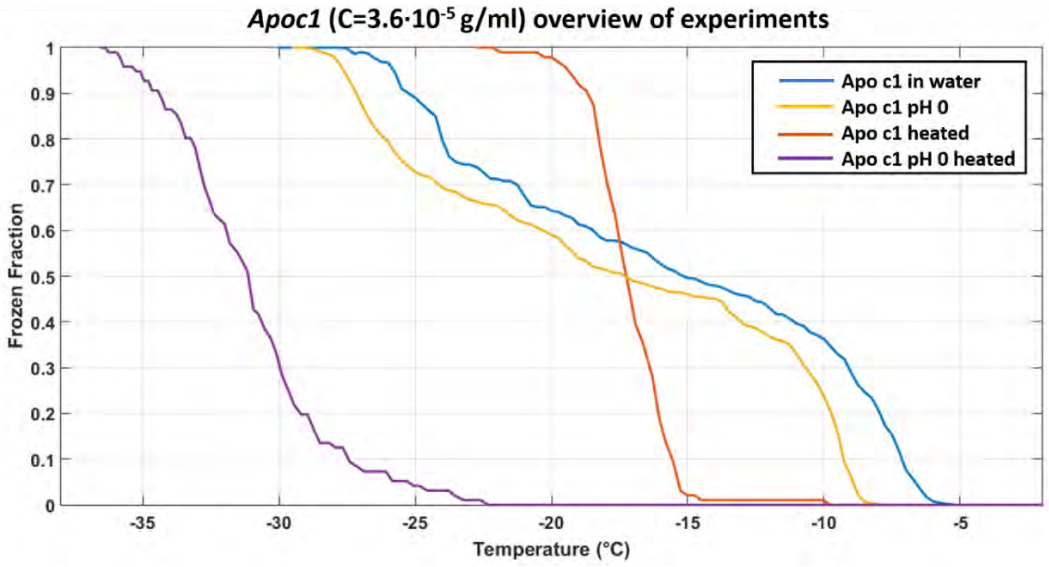

Figure 4.50. Fraction of droplets frozen as function of temperature for well diluted (*Apoc1*) apoferritin for the different treatments.

Sample type	T_{onset} [°C]
Apoc1 in water	-6.5
Apoc1 in pH 0	-8.5
Apoc1 heated in water	-15
Apoc1 heated in pH 0	-22.5

Table X. The onset temperatures () for well diluted (*Apoc1*) apoferritin in the different experiments.

From the overview plot shown in figure 4.50 it can be concluded that for the well diluted apoferritin (*Apoc1*), the addition of the buffer to produce pH = 0 only causes a decreasing of 2 °C in the ice nucleation. However, the combination of the pH = 0 buffer and heating, completely destroys the ice nucleation ability of the apoferritin solution since the temperature decreases so strongly down to -22.5 C. From these facts, it is clear that the change of the charge on apoferritin does not modify the ice nucleation ability. However, the addition of heating and therefore the probably denaturation of the protein or even the change in conformation has an impact on the IN ability. The heating effect for this sample (red curve in figure 4.59) is unusual and the shape of the frozen fraction of the curve makes suspicious that a possible source of contamination may have affected the results and bring the need of repeating this kind of treatment for this well diluted apoferritin solution.

Figure 4.51 gives the same information than figure 4.50 but referred to the high concentrated apoferritin solution (*Apoc2*). Again, the change of pH and the heating do not eliminate completely the ice nucleation ability, but both treatments decrease the median freezing temperature (T_{50}) in 3 °C and 12 °C, respectively. The buffer pH = 0 combined with heating, as in the case of the well diluted apoferritin, completely destroys the ice nucleation of the apoferritin solution.

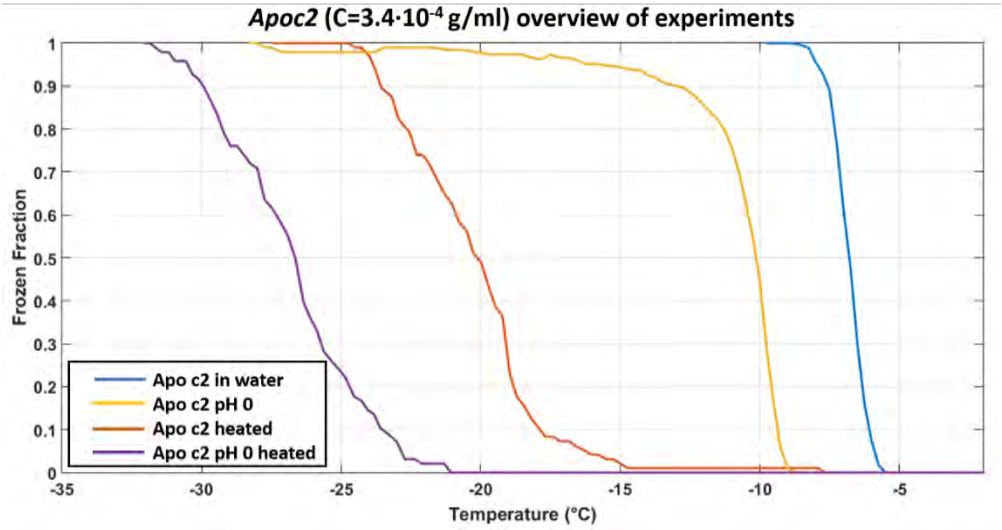

Figure 4.51. Frozen fraction of high concentration (C_2=3.4·10^{-4}g/ml) apoferritin for different treatments.

Sample type	T_{onset} [°C]
Apoc2 in water	-6
Apoc2 in pH 0	-9
Apoc2 heated in water	-15
Apoc2 heated in pH 0	-21

Table XI. The onset temperatures for high concentrated (*Apoc2*) apoferritin in the different experiments.

The results of different measurements performed are shown in figure 4.52 for *Ferc1* and figure 4.53 for *Ferc2* show an overview of the different experiments performed with these samples. Tables XII and XIII summarise the onset nucleation temperature for *Ferc1* and *Ferc2*, respectively. Again, in terms of the onset temperature of ice formation there is not much difference between *Ferc1* and *Ferc2* for all samples and treatments (water, heating, pH 0 and heated-pH0), see tables XII and XIII.

From the overview plot shown in figure 4.52 it can be concluded that the change to pH = 0, causes a higher decrease in the well diluted ferritin (*Ferc1*) than in the apoferritin. The onset temperature for *Ferc1* at pH = 0 decreases in 3 °C, but this reduction continues

increasing and the difference in T_{50} between *Ferc1* in the pH 0 buffer and in pure water goes up to 7 °C. The heating causes a decrease of 8 °C in the onset temperature, but the ferritin solution does not lose its ice nucleation activity. However, as previously found in the case of the apoferritin, the combination of the pH 0 buffer together with heating completely destroys the ice nucleation ability of the ferritin solution.

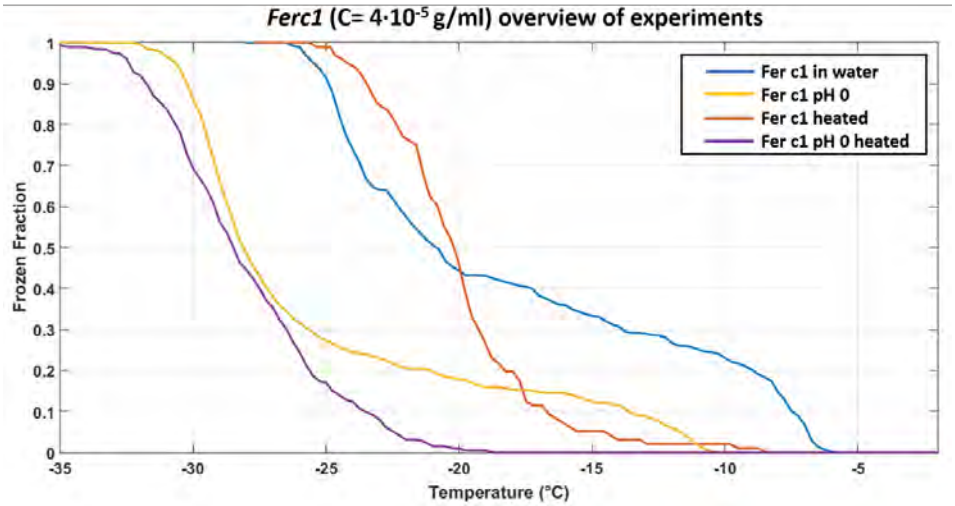

Figure 4.52. Frozen fraction of low concentration (C_1=4·10^{-5}g/ml) ferritin for different treatments.

Sample type	T_{onset} [°C]
Ferc1 in water	-7
Ferc1 in pH 0	-11
Ferc1 heated in water	-15
Ferc1 heated in pH 0	-20

Table XII. The onset temperatures for well diluted (*Ferc1*) ferritin in the different experiments.

Figure 4.53 summarizes the results obtained for the high concentrated ferritin solution (*Ferc2*). Again, the pH buffer and the heating do not eliminate completely the ice nucleation of the sample, but both treatments decrease the median freezing temperature (T_{50}) in 6 °C and 12 °C, respectively. The buffer pH 0 combined with heating, as in all the previous cases, completely destroys the ice nucleation of the apoferritin solution.

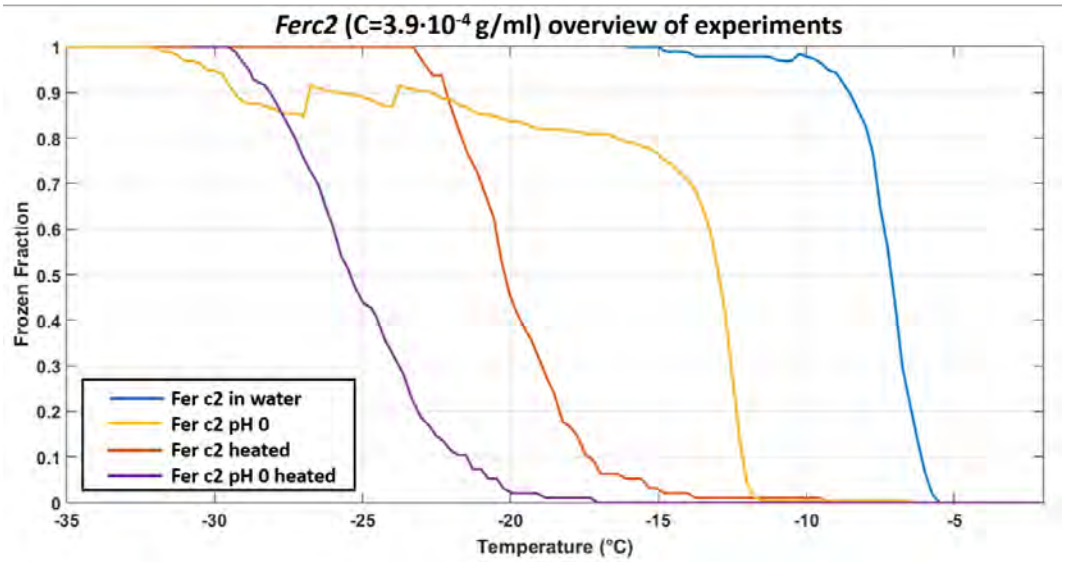

Figure 4.53. Frozen fraction of high concentration (C_2=3.9·10^{-4}g/ml) ferritin for different treatments

Sample type	T_{onset} [°C]
Ferc2 in water	-6
Ferc2 in pH 0	-12
Ferc2 heated in water	-15
Ferc2 heated in pH 0	-20

Table XIII. The onset temperatures for high concentrated (*Ferc2*) ferritin in the different experiments.

4.5. DSC measurements

In this section, experimental results of crystallization and melting using a differential scanning calorimeter (DSC) will be described mainly on a qualitative point of view. This test was done on the same protein solutions as previously studied in the section 4.2 and 4.4. The main difference between these experiments and those using the drop freezing technique is the size of the sample. In a DSC experiment the size of the sample is about 1-10 mg whereas in the drop freezing technique approximately 50 mg were used.

4.5.1 DSC results on pure water

Figure 4.54.A shows the raw data for cooling and heating runs of pure water. The size of the drop was 2.1 mg. The sample was cooled at 1 K/min and a very large exothermic peak appears at about -24.56 ^{o}C which is assigned to water crystallization. In figure 4.54.B an amplification of this plot is also shown. In the case of pure water (or even for samples very diluted as those studied here), the heat flow as a function of the temperature shows a strong saturation (see figure 4.54.A) due to the rapid transformation from liquid water to solid ice. In such a case, these data can be represented as a function of the time instead of the temperature without any loss of information. The onset of the freezing temperatures ($T_{onset,c}$) in all the cases was determined as the temperature when the heat flow starts to increase.

Homogeneous freezing temperatures of -40.15 °C (233K) have been reported for droplets with a diameter of 1 μm and -35.15 °C (238K) for 100 μm droplets[34]. However, in this experiment water freezes at higher temperature (-24.56 °C). Therefore, in these experiments (and also in the case of the drop freezing experiments) the homogeneous ice nucleation is not being observed. Instead these experiments detect the heterogeneous nucleation of water likely because some ice nucleus is formed on the interface between water and aluminum (container) or some impurity is already present in the sample.

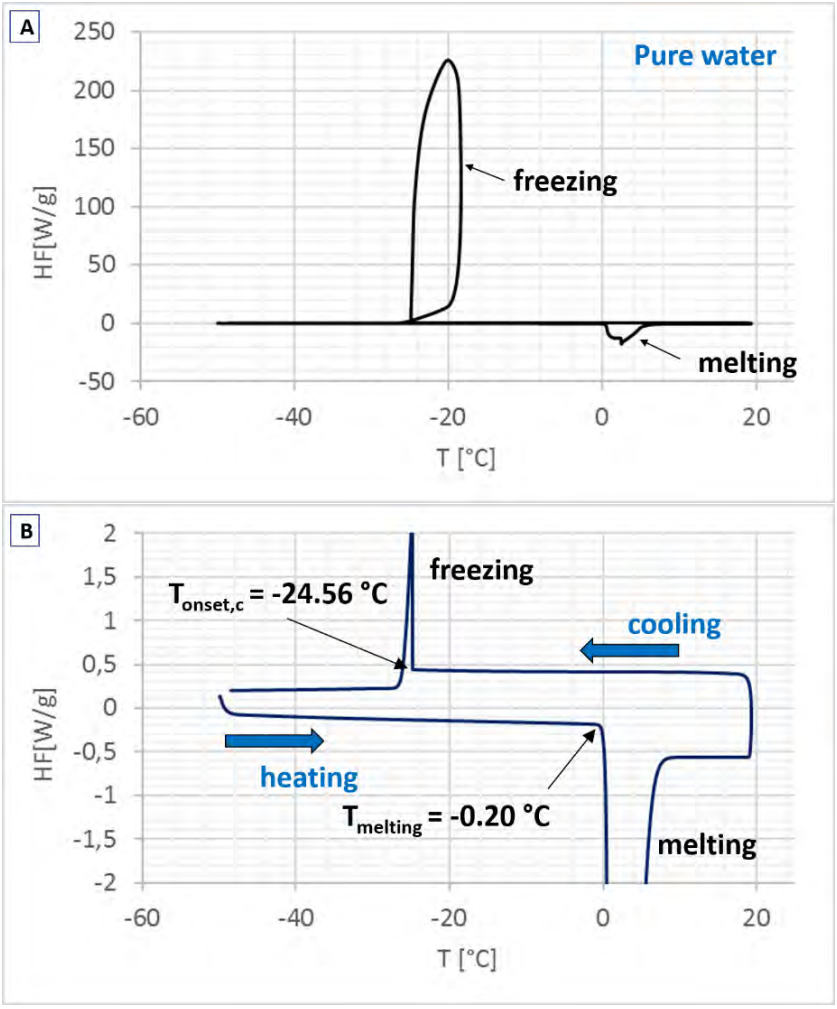

Figure 4.54.A) Heat flow as a function of the temperature of pure water at a cooling rate of 1 K/min. **B)** Magnification of A).

The heat flow of pure water is shown as a function of the temperature in figure 4.55.A and in a function of the time in figure 4.55.B. Three cooling rates were used (20, 10 and 1 K/min) from + 20 ^{o}C down to -80 ^{o}C and the measured sample mass was 2.1 mg. The heating rate in the three cases was 10 K/min. These figures show that at a cooling rate of 20 K/min, the onset of water crystallization is $T_{onset,c}$ = -25.2 ^{o}C whereas at 1 K/min water crystallizes at -24.6 ^{o}C. Therefore, for the highest cooling rate the crystallization of water occurs at lower temperature as expected.

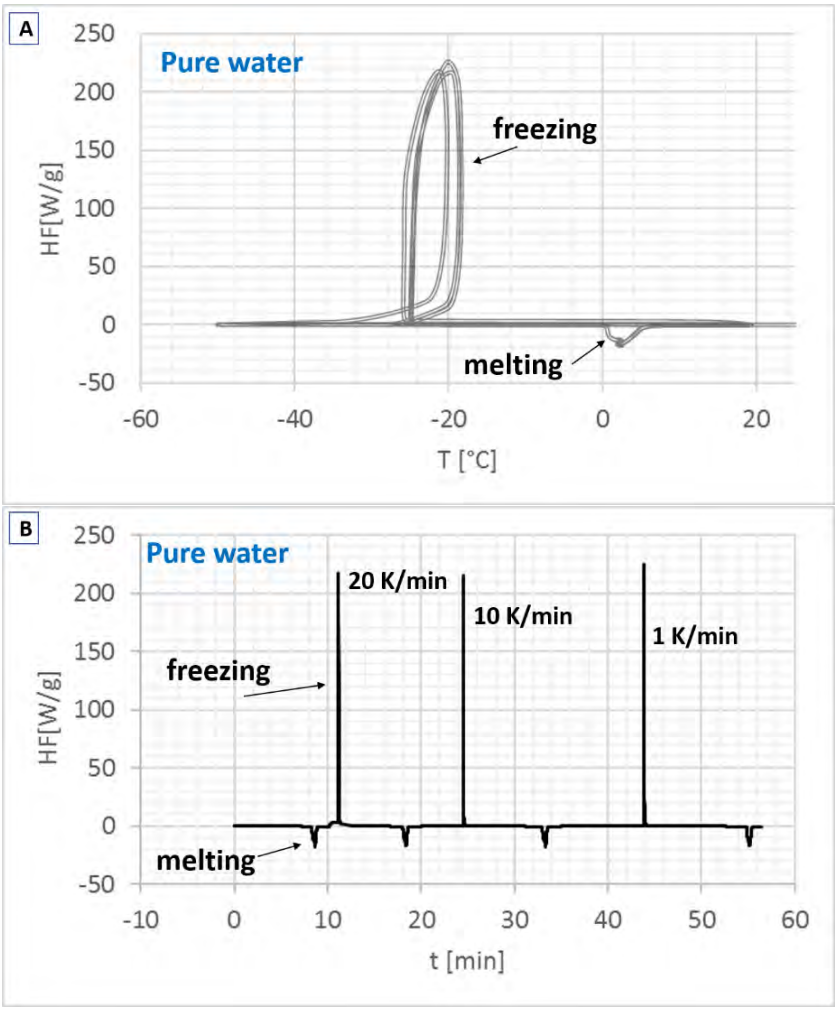

Figure 4.55.A) Heat flow as a function of the temperature of pure water at different cooling rates (20, 10 and 1 K/min). **B)** Heat flow as a function of the time of pure water at different cooling rates (20, 10 and 1 K/min). In both cases, the heating rate was 10 K/min.

Finally, three different cooling runs of pure water for three different samples were prepared in different conditions. Two of the samples were prepared inside the Glovebox (in Argon atmosphere) whereas the third one was prepared directly on the laboratory without using a free-air technique. The result of the sample prepared in the laboratory is shown in figure 4.56. In addition, in the same figure it is shown how the onset and the final temperatures are determined using the heat flow derivate.

Sample	$T_{onset,c}$[°C]	$T_{final,c}$ [°C]	ΔT[°C]
Clean water	-24.56	-26.15	1.59
Clean water	-23.62	-23.27	0.35
Non-clean water	-11.75	-14.55	2.80

Table XIV. The onset ($T_{onset,c}$) and the final ($T_{final,c}$) temperatures of crystallization for three different samples prepared in different conditions.

Table XIV shows the onset and final temperatures for these three samples where can be observed the importance of the sample preparation. In the case of the sample, which was not prepared using a free-air technique (Glovebox), the onset of the crystallization temperature is -11.75 °C which is much higher than that observed in figure 4.54 (-24.56 °C) since some contamination particle can act as INP. In addition, it is possible to observe that, for all the cases the crystallization of water shows a single peak and the broadness can be determined as the different between $T_{onset,c}$ and $T_{final,c}$ (see Table XIV). From the table, the broadness of crystallization seems to be bigger in the contaminated sample.

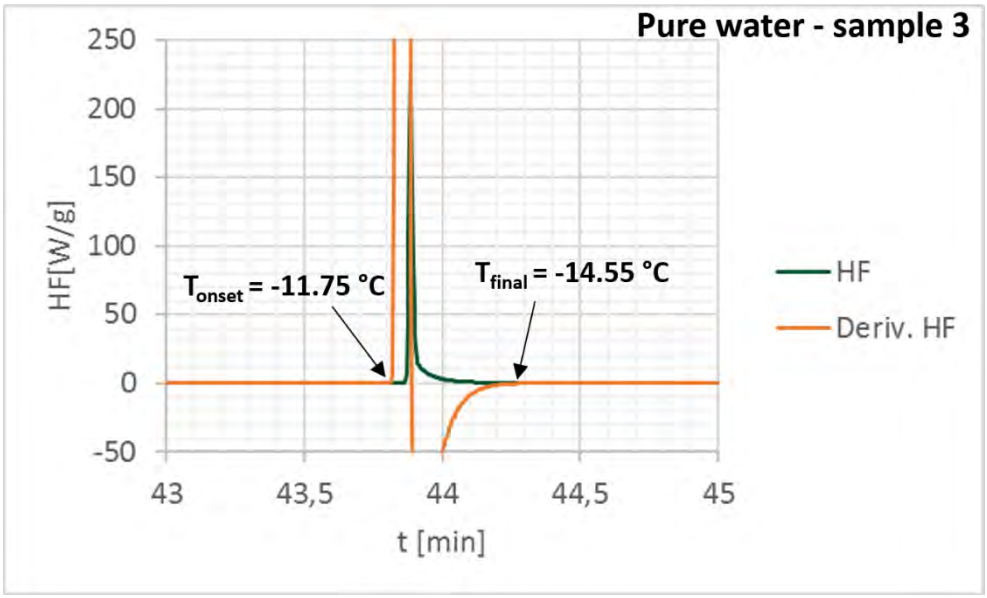

Figure 4.56. Heat flow (HF) and derivate of heat flow (Deriv. HF) as a function of the time of non-clean pure water at a cooling rate of 1 K/min.

4.5.2 DSC results on protein solutions

Figure 4.57 shows the results of *Apoc1*. In this case, the crystallization temperatures are higher than those of pure water as previously detected using the drop freezing technique. At 20 K/min, $T_{onset,c}$ = -7.80 ^{o}C whereas at 1 K/min water in *Apoc1* crystallizes at -5.80 ^{o}C. Similar to pure water (see figures 4.54 and 4.55), for the fastest cooling rate, $T_{onset,c}$ is the lowest.

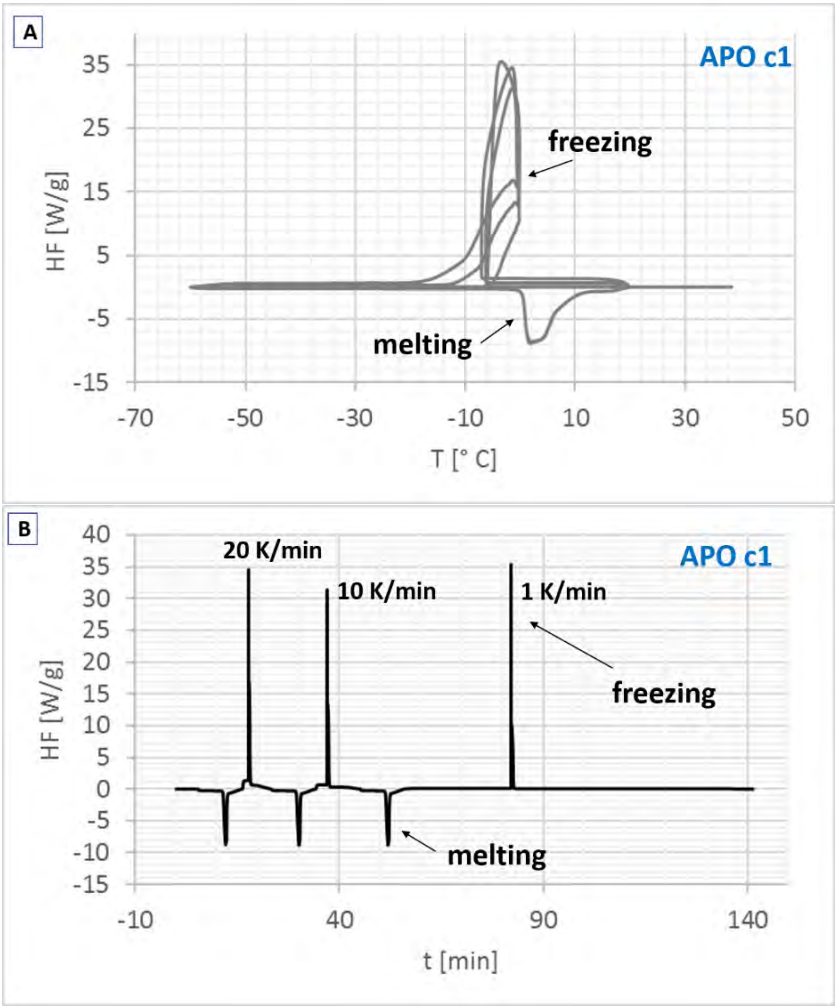

Figure 4.57.A) Heat flow as a function of the temperature of *Apoc1* at different cooling rates (20, 10 and 1 K/min). **B)** Heat flow as a function of the time of *Apoc1* at different cooling rates (20, 10 and 1 K/min). In both cases, the heating rate was 10 K/min

In the following only the results at a cooling rate of 1 K/min will be shown, since this is the cooling ratio used in the drop freezing experiments.

Table XV shows a summary of the results for some of the protein solutions showed in Table I and Table III. In addition, two more concentrated solutions of apoferritin and ferritin (called "as received") and a sample with ubiquitin were analysed by DSC.

Sample	Concentration [g/ml]	$T_{onset,c}$ [°C]
Apo c1	$3.6 \cdot 10^{-5}$	-5.40
Apo c2	$3.4 \cdot 10^{-4}$	-5.10
Apo as rec.	$33.2 \cdot 10^{-3}$	-4.90
Fer c1	$4 \cdot 10^{-5}$	-19.80
Fer c2	$3.9 \cdot 10^{-4}$	-6.50
Fer as rec.	$49.7 \cdot 10^{-3}$	-5.00
Ubiquitin	$6.25 \cdot 10^{-4}$	-20.6
IBP	0.01	-16.6
Water	0	-23.7

Table XV. The onset temperatures ($T_{onset,c}$) of crystallization from a single DSC measurements cooling rate 1 K/min) for different protein solutions at different concentrations.

As previously observed in the drop freezing experiments, both apoferritin and ferritin show a great ability to nucleate ice. In fact, the $T_{onset,c}$ for apoferritin and ferritin are -4.9 and -5.0 ^{o}C respectively for the most concentrated solutions. As previously observed in the drop freezing technique, the more concentrated the solution the higher crystallization temperature, i.e., decreasing the concentration, the crystallization temperature decreases.

As previously proved by means the drop freezing technique, IBP and ubiquitin are bad INPs compared to apoferritin and ferritin, since the $T_{onset,c}$ for both IBP and ubiquitin are much lower (-16.6 and -20.6 ^{o}C, respectively) than that of the apoferritin and ferritin freezing temperatures.

Figure 4.58 shows a magnification of the heat flow during cooling of *Ferc1*, *Ferc2*, *Fer as rec.* and water at 1 K/min. For water (figure 4.58.B) the crystallization peak is very sharp (i.e. spread over less than one degree). A similar behaviour was observed for *Ferc1* (the more diluted sample): a sharp peak with an onset of crystallization at -19.8 ^{o}C. This

means that, for this run and for this concentration, ferritin is not acting as a good INP. By contrast, the more concentrated ferritin solutions (*Ferc2* and *Fer as rec.*) show a relative broader crystallization peak than water. In fact, for these two samples, the crystallization peak is composed by two freezing peaks: one very sharp at the onset of crystallization and the other soft and more spread. The observation of two crystallization peaks could indicate the formation of different hydrates in the sample. The first peak of crystallization is due to water (or water with a low presence of the protein) and the second one could represent the crystallization of a more concentrated solution because part of the water turned into ice. As a conclusion, this behaviour could indicate a wide size distribution of water and ferritin/water domains in the sample (larger domains freeze at warmer temperatures whereas smaller domains freeze at cooler temperatures).

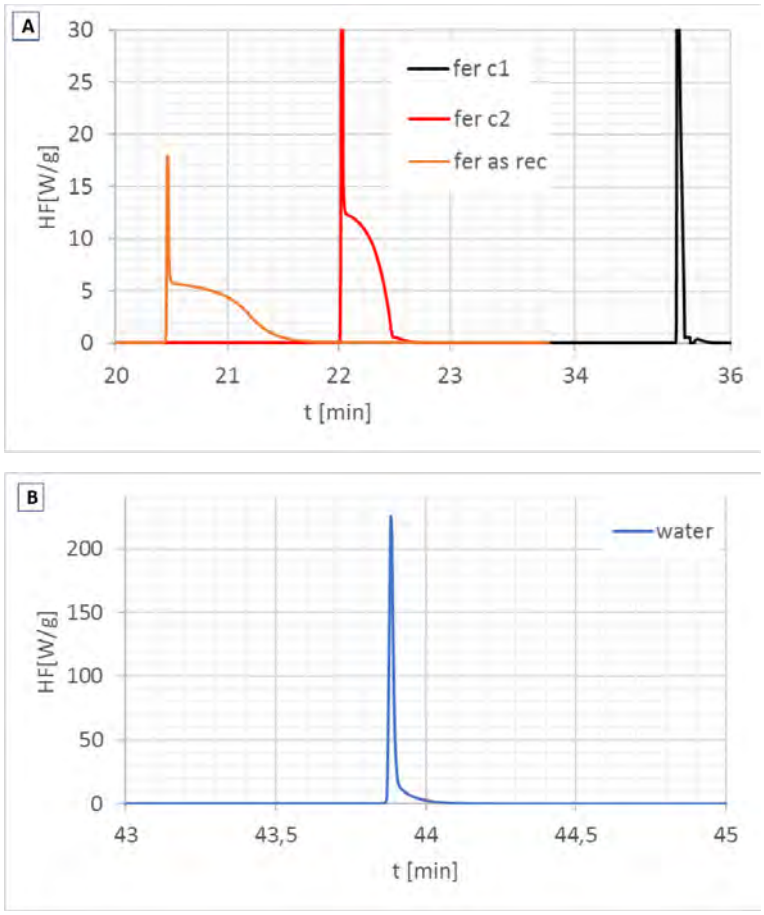

Figure 4.58. A) Heat flow as a function of the time during cooling of *Ferc1*, *Ferc2*, *Fer as rec*. and **B)** water at 1 K/min.

Figure 4.59 also shows a magnification of the heat flow during cooling of *Apoc1*, *Apoc2*, *Apo as rec.* and water at 1 K/min. The results are very similar to that observed for ferritin

solutions but in this case even for the most diluted sample the response shows a relative broader crystallization peak than water. For *Apoc1* three crystallization peaks were observed and two peaks were detected for *Apoc2* and *Apo as rec* similar to that observed for ferritin solutions. For a second time, these results can be rationalized as a wide size distribution of water and apoferritin/water domains in the sample. This behaviour is also partially observed in the melting peak of these three samples (see figure 4.60) where a broader peak is observed increasing the concentration of apoferritin in the samples.

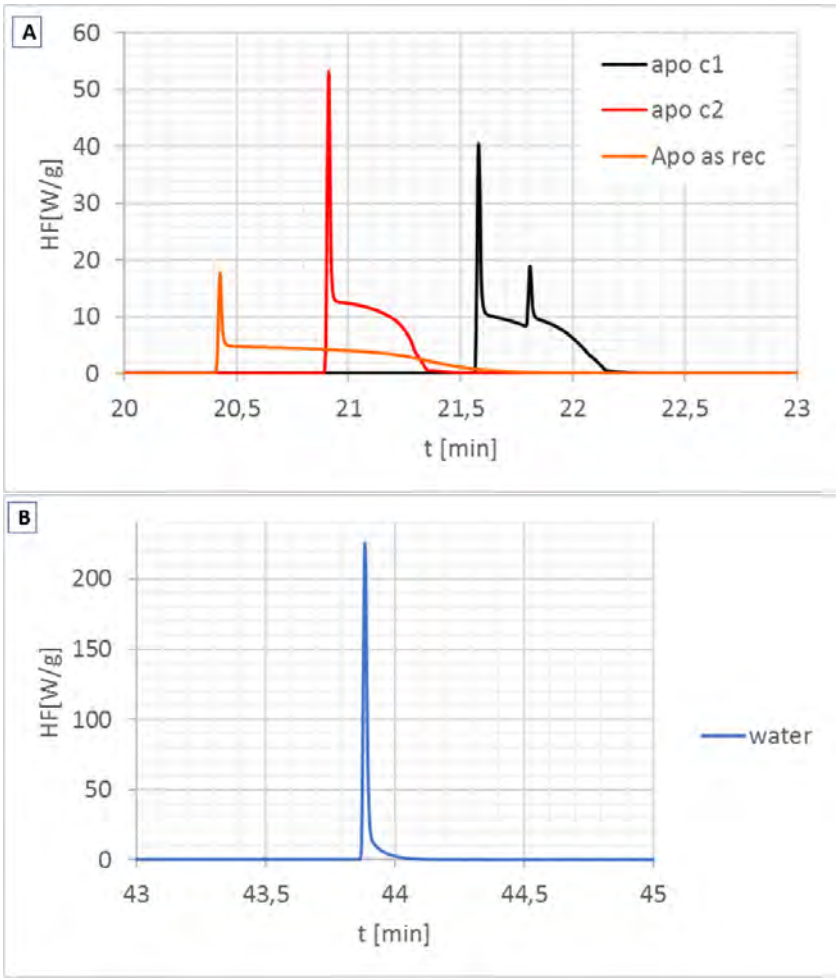

Figure 4.59. A) Heat flow as a function of the time during cooling of *Apoc1*, *Apoc2*, *Apo as rec.* and **B)** water at 1 K/min.

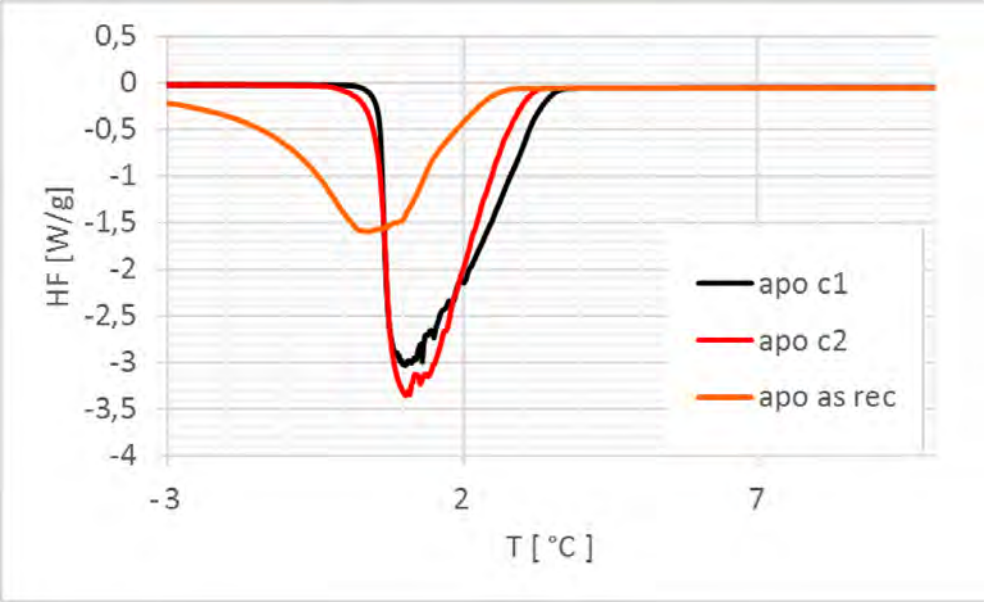

Figure 4.60. Melting of *Apoc1*, *Apoc2*, *Apo as rec.* at 1 K/min. Peak are broad and extended.

It is well known that ice nucleation is random or stochastic process. Therefore, in the following the stochastic origin of nucleation by refreezing experiments on the same drop of liquid will be analysed. Due to the random (stochastic) character of the crystallization of the supercooled liquids, freezing occur in a wide temperature range as previously observed in the drop freezing technique. To probe this, 35 DSC runs on *Apoc1* (using the same sample) were measured and the $T_{onset,c}$ is shown in figure 4.61.A. In the case of *Apoc1* the onset of the freezing temperatures varies between -18.44 and -16.7 °C. Therefore, for this particular drop, water crystallization extends on two degrees. Note that this experiment cannot be compared with the drop freezing technique because in that case different samples are analysed.

The refreezing experiments on *Apoc2* were also done. In this case three different samples were refreezing during 10 times. The result is shown in figure 4.61.B. For each sample the $T_{onset,c}$ is very similar and averaged values are -7.4, -5.3, -4.7 °C respectively. In this case, the variation of the onset of crystallization is 2.7 °C.

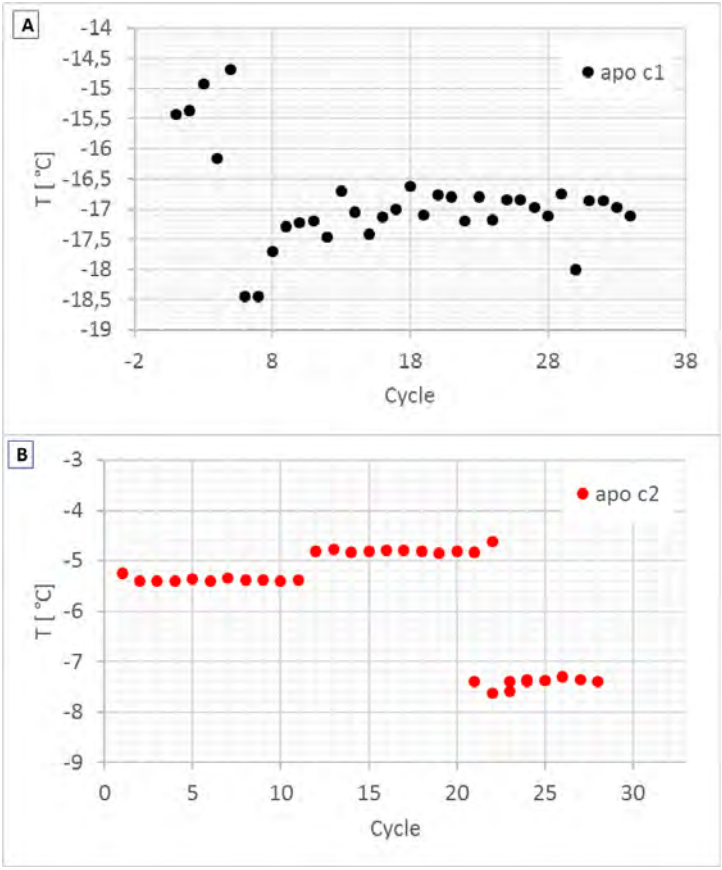

Figure 4.61. Onset of crystallization temperatures for different cycles at 1K/min.

A similar result was obtained using the drop freezing technique for *Apoc2* (see figure 4.62).

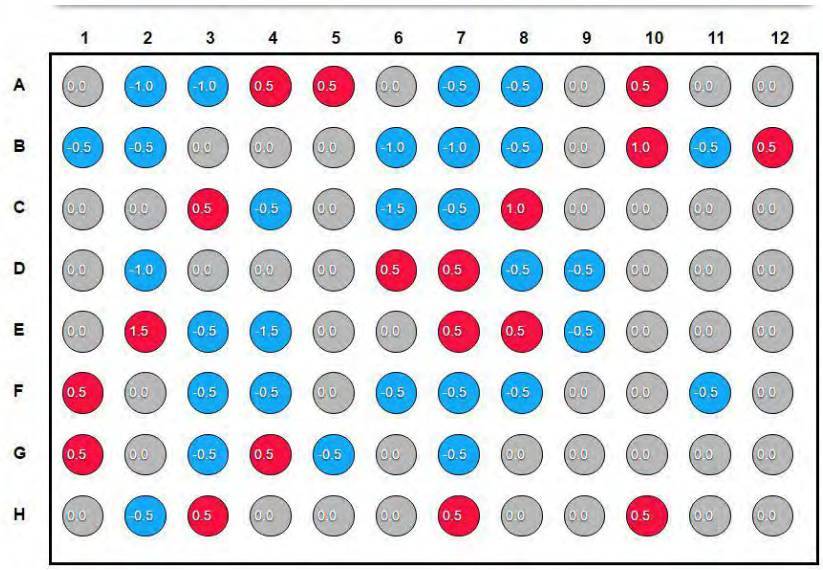

Figure 4.62. Refreezing experiment for *Apoc2* in the drop freezing setup 1.

4.6 Conclusions and future prospects

Despite the importance of heterogeneous ice nucleation to a variety of fields, from cloud science to microbiology, there are major gaps in the complete understanding of this ubiquitous process and no satisfactory answer has been found yet. Besides, the apparent contradiction between the low ratio of biological to inorganic IN and the importance of bio-aerosols in atmospheric processes has not been determined, and the role of biological IN in precipitation is still elusive.

In the last decades, a huge number of experiments, based on cloud chamber-like setups, and on individual drop isolation techniques, have measured ice nucleation temperatures or rates, allowing the discrimination between materials which can effectively promote heterogeneous ice nucleation and others that do not favour this process. Thus, far the mechanism through which molecular biology influences the ability of biological IN to initiate the freezing at higher temperatures in the laboratory has not been elucidated, since experiments do not provide information on the molecular details of individual ice nucleation events. There are still open questions in the literature such as what makes a material a good ice nucleating agent? what are the most important factors to promote ice nucleation: hydrophobicity, morphology of the surface, size, charge….?

In a recent review about ice-binding proteins [35], it has been proposed that “the ice-binding sites are extensive, relatively flat, and hydrophobic, largely devoid of charged residues, and often have some repeating motifs and structural analysis shows that these binding sites share features of flatness, regularity, extensiveness, rigidity, and hydrophobicity that are consistent with the ability to organize ice-like water on one face/area of the IBP. This suggests a common mechanism for binding to ice, which might be expressed in ice nucleation proteins as the ability to form ice”. Similar arguments (the flatness of apoferritin) could be used for explaining the better ice nucleation activity of the apoferritin compared to other tested proteins. Both apoferritin and ferritin have larger molecular weight than the rest of the proteins analysed (except for TMV, which however shows worse ice nucleation activity) and, compared to single protein molecules, they are indeed “flat” (i.e. they have a small curvature). This interpretation also fits with the aggregate casein; however, it should be taken as a first idea because more work should be done to elucidate such origin.

The results obtained with the proteins, except for apoferritin and ferritin, show in all cases at least some ice nucleation ability. However; the effect is so small (<10 K above pure water) that the respective proteins should not be able to offer a concurrence to even smallest amounts of mineral dust. For this reason, they have not been investigated in full detail. Casein might be a good candidate for more experiments, but its aggregation status is probably crucial, and a special preparation of casein might be required.

The conclusions will thus be centred on the "successful" cases of apoferritin and ferritin. Supercooled water droplets containing apoferritin and ferritin freeze well above the homogeneous freezing limit (which was found to be -27 °C for 50 µm droplets; see figure 4.29) were analysed. The concentrated solutions (*Apoc2* and *Ferc2*) have shown steeper freezing curves as compared to the well diluted solutions. The onset and T_{50} temperatures were found to be very similar for the concentrated solutions (*Apoc2* and *Ferc2*), suggesting no difference in ice nucleating abilities. However for the well diluted solutions (*Apoc1* and *Ferc1*), the onset temperatures were found to be similar (0.5 K difference), but T_{50} was considerably different (6 K), with apoferritin centred at higher temperatures than ferritin.

Regarding the pH = 0, apoferritin solutions shows the onset of crystallization at higher temperatures than ferritin solutions for both concentrations, as well as higher T_{50} values. No explanation was found for this behaviour, but this fact suggests that the products added to the solution to reach the pH = 0, which might be protein aggregates, produce more IN active species for the apoferritin than the ferritin.

For the samples heated, the onset of the nucleation temperature was ~-15 °C for both apoferritin and ferritin. This suggests that the heat treatment equally reduces the IN activity of both proteins, compared to the pure water case. The heat treatment is supposed to cause denaturation, presumably followed by aggregation.

For the treatment performed combining the buffer pH = 0 and heating, the onset of the nucleation temperature of apoferritin is reported to be about 2 degrees colder than that of ferritin. This suggests that in the case of apoferritin the products added after this treatment yielded less IN active material. The median freezing temperature, $T_{50,}$ gives the same information for the onset. Both apoferritin and ferritin lose completely their IN activity with this treatment probably because they are decomposed into small molecules.

The proteins are to a large extent hydrolysed, i.e. decomposed into amino acids, which have very small ice nucleation abilities.

Based on the pH variation studies, the surface charge of the ferritin or the apoferritin does not appear to have an influence in the ice nucleation activity of those proteins, since the effective surface charge of ferritin changes substantially with the pH (see figure 4.34). Ferritin in buffers at pH = 0, 2 and 3.5 are positively charged, and for the rest of the tested pH buffers (pH = 5, 7 and 9.5) it is negatively charged. However, no appreciable effects on the ice nucleation activity were observed related with the different surface charge in ferritin solutions.

This is surprising, and contradicts some theories [35] that predict a direct influence of the protein surface chemistry on it. For all experimental conditions (except heating at pH = 0) the secondary structure of the apoferritin subunit is still present [30]. However at low pH, the acidic groups become protonated. This has no influence on ice nucleation activity at pH = 2, where the 24-mer apoferritin cage is dissociated and dimers prevail, but shifts the ice nucleation activity to lower temperatures at pH = 0.

Apoferritin was found to be highly resistant to chemical and physical denaturants because for example, horse spleen apoferritin was denatured only when heated above 80 °C for 10 min or at extreme pH values (pH < 1.0 or > 13.0). These studies did not provide any direct structural insight into denaturation and the denatured state [27]. “Denatured state” in this context does not appear to imply that the secondary structure of the dimer needs to be destroyed. At pH = 0 and for heating to 110 °C, the subunits of apoferritin form aggregates, but their secondary structure seems to be at least partly preserved. During heating at pH = 0, the amino acid chain is broken up and it has been shown that the heating at pH = 0 destroyed the ice nucleation activity. This enforces that at least the protein structure is responsible for the ice nucleation activity and not just a random impurity.

According to the literature (see section 4.4.4), heating the apoferritin and the ferritin above 80 °C should lead to irreversible denaturation. From the experiments here performed (heating for 5 hours at 110 °C), proteins are denatured and in agreement with literature, the denaturation causes the reduction in the ice nucleating activity (INA). However, it is proved that not totally eliminates the ice nucleation ability. This reduction

of the INA with heating has been also reported for mineral dust, and it has been speculated that it is due to the effect on the organic material on the dust particles. Apoferritin might well be a good demonstration of this effect.

Considering that some monomeric or dimeric apoferritin subunits might be the entities that nucleate ice, it would be very good in the future conduct experiments using a dilution series, to analyse whether the ice nucleation activity remains or disappears by dilution.

Almost all the studies regarding biological aerosols in the literature used frozen droplet fractions and/or onset temperatures of freezing for quantifying the ice nucleation behaviour, as here. This implies that the reported results are dependent on the specific experiment and their conclusion could not be general [36].
Therefore, for further analysis the results reported in this chapter, another approach could be used for quantifying the protein's ice nucleation behaviour.

Apoferritin and ferritin seem to have a quite uniform ice-nucleating site, because, heterogeneous freezing occurs in a narrow temperature range. For the more concentrated solutions, all wells freeze above the freezing range of the blank (water or buffer). For this concentration, it cannot be determined whether 10, 100 or 1000 active sites present in one well are responsible for the freezing. However, if the concentration is so low (much diluted samples) only part of the wells freezes above the blank and therefore it is likely that these contain only 1 or a few sites. Only those concentration and temperature ranges where only a fraction of the wells is frozen should be evaluated. The results should be consistent, independent of concentration.

Some refreezing experiments were done with the high concentrated (*Apoc2*) apoferritin solution (see figure 4.58). It has been found that 50% of the wells freeze exactly at the same temperature and the other 50% within 0.5 and 1.5 K, when the initial measurement is compared to the refreezing experiment. To a further interpretation and to characterize the stability and reproducibility of the INPs, new refreezing experiments with the highly diluted apoferritin (*Apoc1)* could be done in the future to evaluate what percentage of wells froze twice (or always) above a threshold temperature of e.g.-12 °C, and what percentage froze only once above -12 °C. By doing a set of refreezing experiments it may be possible to evaluate also what percentage of wells froze within 2 K and 1 K when one compares the first and the following freezing. This experiment would give interesting

information about the stability of the ice nucleating sites. When all the wells that freeze at high temperatures in the first cycle also freeze at high temperatures in the second (i.e. due to the apoferritin/ferritin), then the ice nucleating sites are quite stable. If the same well freezes high in the first cycle and low in the second one or vice versa, the sites would be not very stable.

With regards to the calorimetric measurements, it is concluded that the preparation of the pans must be done on a very controlled way in order to avoid the presence of undesired particles that can act as potential INP which would radically change the temperature of crystallization. In addition, probabilistic studies are necessary (tens or hundreds of measurements) due to the fact that the crystallization of water has a stochastic component. Finally, the freezing temperature could depend on the size of the sample, and this should be also considered when comparing results of different experiments.

With regards to apoferritin and ferritin solutions, it was found that crystallization occurs in two different stages. This behaviour was not observed in pure water as well as in other proteins like IBP or ferritin at pH = 0, which has lost the IN property. This behaviour should be explored in the future.

4.7. References

[1] W. Wohlleben *et al.*, "Recombinantly produced hydrophobins from fungal analogues as highly surface-active performance proteins," *Eur. Biophys. J.*, vol. 39, no. 3, pp. 457–468, 2010.

[2] S. Balci *et al.*, "Self-assembly of metal-virus nanodumbbells," *Angew. Chemie - Int. Ed.*, vol. 46, no. 17, pp. 3149–3151, 2007.

[3] A. Bujacz, "Structures of bovine, equine and leporine serum albumin," *Acta Crystallogr. Sect. D Biol. Crystallogr.*, vol. 68, no. 10, pp. 1278–1289, 2012.

[4] S. Klammt *et al.*, "Albumin-binding function is reduced in patients with decompensated cirrhosis and correlates inversely with severity of liver disease assessed by model for end-stage liver disease.," *Eur. J. Gastroenterol Hepatol*, vol. 19, no. 3, pp. 257–63, 2007.

[5] J. A. Huntington, "Structure and properties of ovalbumin," *J. Chromatogr. B*, vol. 756, pp. 189–198, 2001.

[6] T. Ozeki *et al.*, "Surface-bound casein modulates the adsorption and activity of kinesin on SiO2 surfaces," *Biophys. J.*, vol. 96, no. 8, pp. 3305–3318, 2009.

[7] H. E. Swaisgood, "Review and update of casein chemistry.," *J. Dairy Sci.*, vol. 76, no. 10, pp. 3054–3061, 1993.

[8] P. Ceci, V. Morea, M. Fornara, and G. Bellapadrona, "Biomimetic Materials Synthesis from Ferritin-Related, Cage-Shaped Proteins," *Cdn.Intechweb.Org*, no. 432, 2002.

[9] K. Zeth, E. Hoiczyk, and M. Okuda, "Ferroxidase-Mediated Iron Oxide Biomineralization: Novel Pathways to Multifunctional Nanoparticles," *Trends Biochem. Sci.*, vol. 41, no. 2, pp. 190–203, 2016.

[10] T. Douglas and D. R. Ripoll, "Calculated electrostatic gradients in recombinant human H-chain ferritin.," *Protein Sci.*, vol. 7, no. 5, pp. 1083–1091, 1998.

[11] J. G. H. Wessels, “Fungal hydrophobins: proteins that function at an interface,” *Trends Plant Sci.*, vol. 1, no. 1, pp. 9–15, 1996.

[12] J. Hakanpää *et al.*, “Atomic Resolution Structure of the HFBII Hydrophobin, a Self-assembling Amphiphile,” *J. Biol. Chem.*, vol. 279, no. 1, pp. 534–539, 2004.

[13] J. H. Lee *et al.*, “Structural basis for antifreeze activity of ice-binding protein from arctic yeast,” *J. Biol. Chem.*, vol. 287, no. 14, pp. 11460–11468, 2012.

[14] A. Eleta-Lopez and A. Calò, “Key factors of scanning a plant virus with AFM in air and aqueous solution,” *Microsc. Res. Tech.*, vol. 80, no. 1,pp. 18–29, 2017.

[15] J. M. Alonso, M. L. Górzny, and A. M. Bittner, “The physics of tobacco mosaic virus and virus-based devices in biotechnology,” *Trends Biotechnol.*, vol. 31, no. 9, pp. 530–538, 2013.

[16] G. Vali and E. J. Stansbury, “Time-Dependent Characteristics of the Heterogeneous Nucleation of Ice,” *Can. J. Phys.*, vol. 44, no. 3, pp. 477–502, 1966.

[17] N. Hiranuma *et al.*, “A comprehensive laboratory study on the immersion freezing behavior of illite NX particles: A comparison of 17 ice nucleation measurement techniques,” *Atmos. Chem. Phys.*, vol. 15, no. 5, pp. 2489–2518, 2015.

[18] C. Budke and T. Koop, “BINARY: An optical freezing array for assessing temperature and time dependence of heterogeneous ice nucleation,” *Atmos. Meas. Tech.*, vol. 8, no. 2, pp. 689–703, 2015.

[19] Y. Tobo, “An improved approach for measuring immersion freezing in large droplets over a wide temperature range,” *Sci Rep*, vol. 6, no. August, p. 32930, 2016.

[20] P. Gill, T. T. Moghadam, and B. Ranjbar, “Differential Scanning Calorimetry Techniques: Applications in Biology and Nanoscience,” *J. Biomol. Tech.*, vol. 21, no. 4, pp. 167–193, 2010.

[21] B. G. Pummer, H. Bauer, J. Bernardi, S. Bleicher, and H. Grothe, “Suspendable macromolecules are responsible for ice nucleation activity of birch and conifer pollen,” *Atmos. Chem. Phys.*, vol. 12, no. 5, pp. 2541–2550, 2012.

[22] O. Popovicheva *et al.*, “Effect of soot on immersion freezing of water and possible atmospheric implications,” *Atmos. Res.*, vol. 90, no. 2–4, pp. 326–337, 2008.

[23] N. Hiranuma *et al.*, “Influence of surface morphology on the immersion mode ice nucleation efficiency of hematite particles,” *Atmos. Chem. Phys.*, vol. 14, no. 5, pp. 2315–2324, 2014.

[24] D. N. Petsev, B. R. Thomas, S.-T. Yau, and P. G. Vekilov, “Interactions and Aggregation of Apoferritin Molecules in Solution: Effects of Added Electrolytes,” *Biophys. J.*, vol. 78, no. 4, pp. 2060–2069, 2000.

[25] S. Stefanini, P. Vecchini, and E. Chiancone, “On the mechanism of horse spleen apoferritin assembly: a sedimentation velocity and circular dichroism study,” *Biochemistry*, vol. 26, no. 7, pp. 1831–1837, 1987.

[26] E. Attard *et al.*, “Effects of atmospheric conditions on ice nucleation activity of Pseudomonas,” *Atmos. Chem. Phys.*, vol. 12, no. 22, pp. 10667–10677, 2012.

[27] M. Kim *et al.*, “PH-dependent structures of ferritin and apoferritin in solution: Disassembly and reassembly,” *Biomacromolecules*, vol. 12, no. 5, pp. 1629–1640, 2011.

[28] R. Chiaraluce, V. Consalvi, S. Cavallo, A. Ilari, S. Stefanini, and E. Chiancone, “The unusual dodecameric ferritin from Listeria innocua dissociates below pH 2.0,” *Eur. J. Biochem.*, vol. 267, no. 18, pp. 5733–5741, 2000.

[29] R. V. Martínez *et al.*, “Large-scale nanopatterning of single proteins used as carriers of magnetic nanoparticles,” *Adv. Mater.*, vol. 22, no. 5, pp. 588–591, 2010.

[30] R. R. Crichton and C. F. Bryce, “Subunit interactions in horse spleen apoferritin. Dissociation by extremes of pH.,” *Biochem. J.*, vol. 133, no. 2, pp. 289–299, 1973.

[31] R. Jurado *et al.*, "Apoferritin Fibers: a New Template for 1D Fluorescent Hybrid Nanostructures," *Nanoscale*, pp. 9648–9656, 2016.

[32] J. Kudr *et al.*, "Use of nucleic acids anchor system to reveal apoferritin modification by cadmium telluride nanoparticles," *J. Mater. Chem. B*, vol. 3, no. 10, pp. 2109–2118, 2015.

[33] S. Stefanini *et al.*, "Thermal stability of horse spleen apoferritin and human recombinant H apoferritin.," *Arch. Biochem. Biophys.*, vol. 325, no. 1, pp. 58–64, 1996.

[34] J. M. Wallace and P. Hobbs, *Atmospheric Science: an introductory survey*. 2006.

[35] P. L. Davies, "Ice-binding proteins: A remarkable diversity of structures for stopping and starting ice growth," *Trends Biochem. Sci.*, vol. 39, no. 11, pp. 548–555, 2014.

[36] S. Hartmann *et al.*, "Immersion freezing of ice nucleation active protein complexes," *Atmos. Chem. Phys.*, vol. 13, no. 11, pp. 5751–5766, 2013.

Appendices

Appendix I

Signal detection in the environmental scanning electron microscope (ESEM)

Table I shows several types of detectors compatible with the ESEM or low vacuum (LV) imaging.

Since the Large Field Detector (LFD) and the Gaseous Secondary Electron Detector (GSED) are the two principal detectors used for developing the experiments, this appendix will focus the attention on these two types of detectors.

Detector Name	UI Tag	Vacuum Mode	Detected Signal	Max. Pressure [Pa]
Backscattered Electron	BSED	**HiVac**, LoVac	BSE	200
Large Field	LFD	**LoVac**, ESEM	SE + BSE	200
Gaseous Secondary Electron	GSED	LoVac, **ESEM**	SE	1000 µm aperture: 750 500 µm aperture: 2600
CCD camera	CCD	any	light, infra-red light	any
External	EXT	detector-dependent	detector-dependent	detector-dependent
Gaseous Backscattered Electron	GBSD	LoVac, **ESEM**	SE, BSE	10 (500 optimal) - 2600
Scanning Transmitted Electron Microscopy	STEM I	**HiVac**, LoVac, ESEM	TE	any
Wet STEM	STEM I	HiVac, LoVac, **ESEM**	TE	any
Wet STEM	STEM I	HiVac, LoVac, **ESEM**	TE	any

Table I. Types of detectors compatible with the ESEM or low vacuum imaging. Taken from [1]

The pressure range can be related to either the useful limits of the detectors (LFD and GSED) or the artificial "mode" of the microscope (LV and ESEM). Low vacuum is considered to be between 10 and 200 Pa, and both detectors (LFD and GSED) can be used in this range. The range of ESEM is 200 to 2600 Pa, and, again, both detectors can be used in this range. For the LFD, FEI recommends a range from 70 to 130 Pa; if the low kV cone is present, a range of 70 to 200 Pa is recommended. For the GSED, FEI recommends a range from 10 to 2600 Pa (300 Pa optimum).

The electron signal used in ESEM is represented by electrons that have interacted with the sample and re-exited through the surface. Depending on the energy, these electrons retain with the sample after interaction. These electrons are divided into two classes. The first class is the backscattered electrons BSEs, which are electrons with high energy that have interacted elastically with the nucleus of specimen atoms and have not lost energy. They are detected above the specimen for this reason by a back scattered electron detector BSED, which is placed directly above the specimen.

The second class is the secondary electrons SEs, which result from inelastic interaction with the electrons of the specimen atoms. The low energy secondary electrons that escape the surface and contribute to the SE image typically have energies below 50 eV [2]. The SE detector is placed to the side of the sample stage and not directly above the specimen. As a result, surfaces facing the detector appear brighter than the ones that do not since electrons escaping surfaces that face away from the detector might get re-absorbed into these surfaces.

Secondary electrons provide the highest resolution images. Unfortunately, the Everhart-Thornley detector (ETD) used in the conventional SEM cannot function in the gaseous environment of the ESEM. In its place one has to use the following detectors:

LARGE FIELD DETECTOR (LFD)

This detector is used with the standard insert. The field of view is unrestricted, and the magnification range is identical to that of high vacuum mode.

The signal from the LFD contains more BSE information than the GSED signal. The detector is ideal for general imaging; it is also the only gaseous SE detector that can be used simultaneously with a BSED Detector.

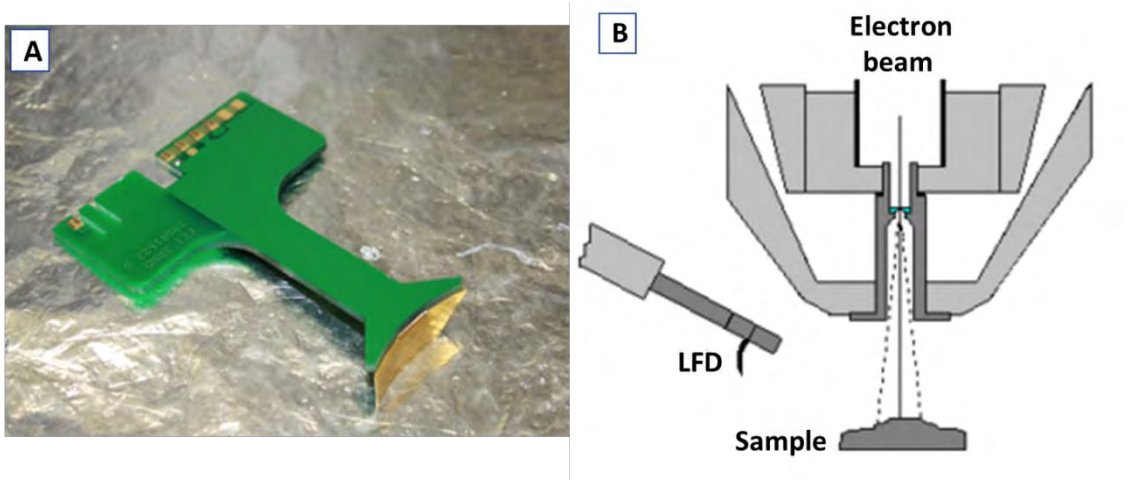

Figure A.I.1. A) Image showing the large field detector (LFD) and **B)** its location inside the microscope (redrawn from [1])

GASEOUS SECONDARY ELECTRON DETECTOR (GSED)

The gaseous secondary electron detector (GSED) consists of a 3-mm diameter positively biased metallic ring (with a voltage, V_{GSED} = +30 to +550 volts) placed above the sample stage and concentrically around the optical axis of the microscope. It accelerates low energy SEs generated at the sample surface by the PE beam through the gas.

The GSED is integrated into a flexible printed circuit board and plugs into the signal connector behind the conical lens. It is used for general wet imaging and for high pressure imaging with auxiliary gases.

The overall image consists of a very pure SE signal with very little BSE signal component, due to the detector design and chamber geometry. This pure SE signal makes this detector best suited for resolution imaging. The field of view is less than the LFD at the lowest magnification. The lower magnification range is about 240x at 7 mm WD.

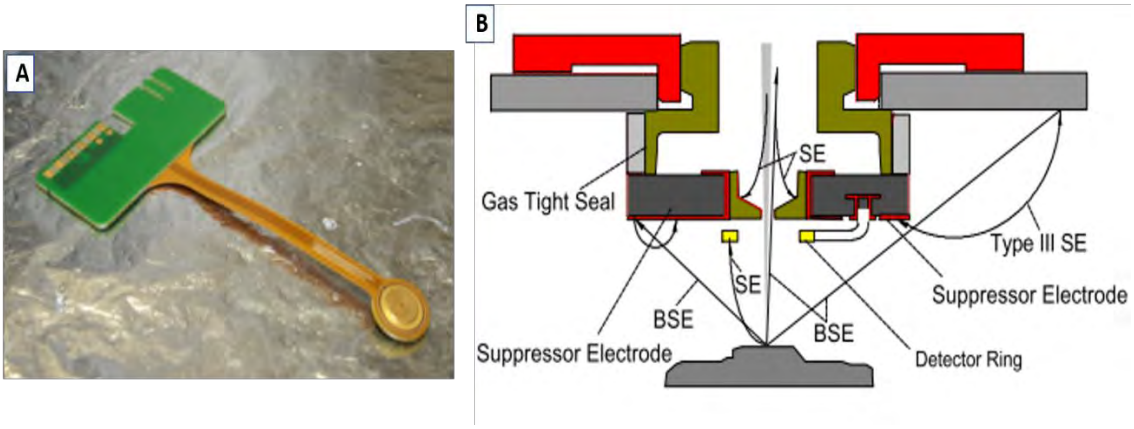

Figure A.I.2. A) Image showing the gaseous secondary electron detector (GSED) and **B)** its location inside the microscope and the various signals used to generate GSED (from [3])

Appendix II

Optimization of the ESEM setup

A good temperature control is needed for the experiments, as well as accuracy in the temperature measurements. For this reason, it was investigated an improvement the thermal contact between the cupper cup in the Peltier element and the stub used for my ice growth experiments (see figure AII.1)

To improve the thermal insulation between the cupper cup and the ceramic part of the Peltier element, different insulating materials were tested.

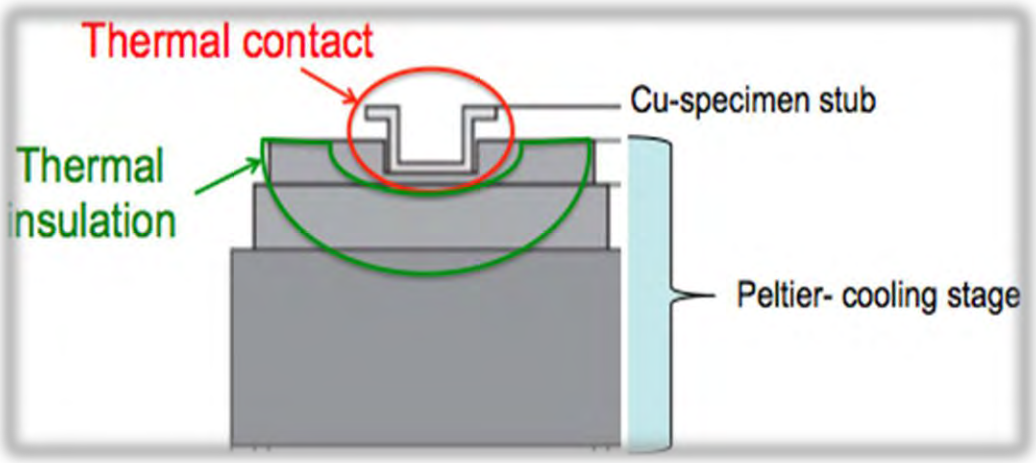

Figure AII.1. The Peltier stage setup (adapted from Zimmermann et al., 2007)

Various improvements to the thermal coupling between the stub and the Peltier stage are investigated: gallium indium (see figure AII.2. A)) and aluminum foil (see figure AII.3. A)) are used as thermal contacts.

The thermal connection between the Peltier element and the copper stub is made using gallium indium and by manually applying the pressure until the gallium indium sets.

As expected with gallium-indium, it is found that more ice can be produced (in air), and faster nucleation and growth are observed (at low pressure) (see figure AII.2. B)).

Ice grows on the surface and sides of the stub, but not on the Peltier base or lower surface.

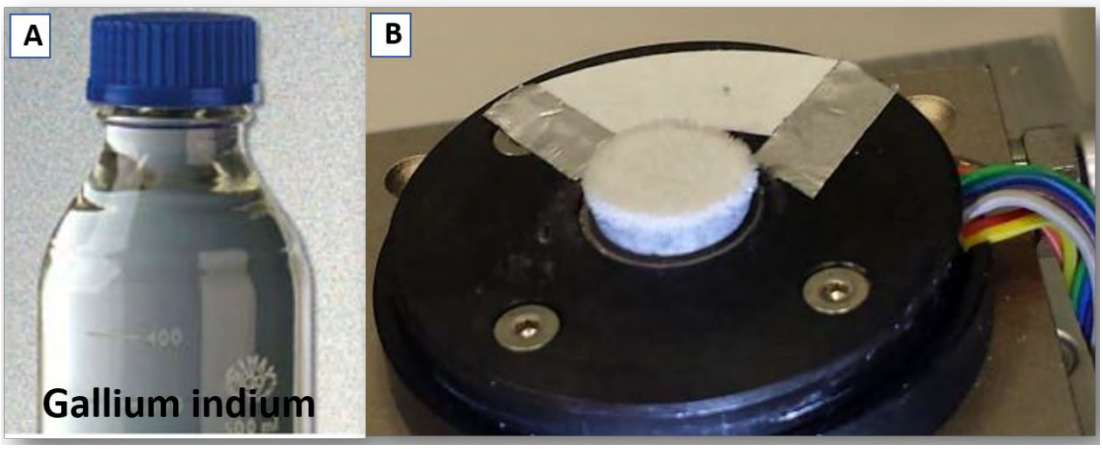

Figure AII.2. A) Gallium indium. **B)** Growth of ice on the cooled Peltier stage in ambient air after 10 mins using gallium indium as thermal contact.

Under the same growth conditions, ice takes longer to grow with aluminum foil.

Ice grows almost exclusively on the upper surface of the stub but mostly from the edge (see figure AII.3. B)). The aluminum probably produces only very small patches of good thermal contact.

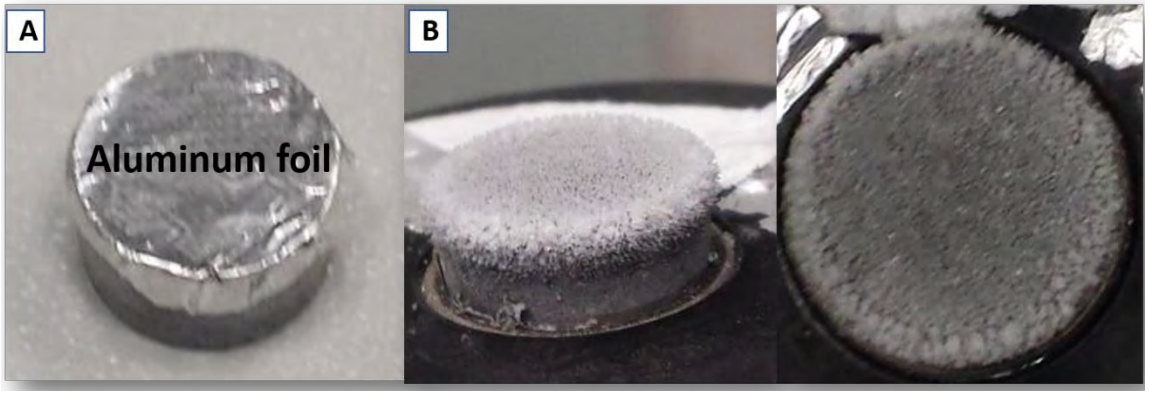

Figure AII.3. A) Aluminum foil. **B)** Growth of ice on the cooled Peltier stage in ambient air after 10 mins using aluminum foil as thermal contact.

To improve the thermal insulation the Peltier stage and area around the stub were covered with insulating material (paraffin or PTFE) of low thermal conductivity (see table AII.1)

Besides, a PVC piece was built up for the same purpose to be attached to the stub. Both methods were found to be ineffective (see figure AII.4).

Appendix II

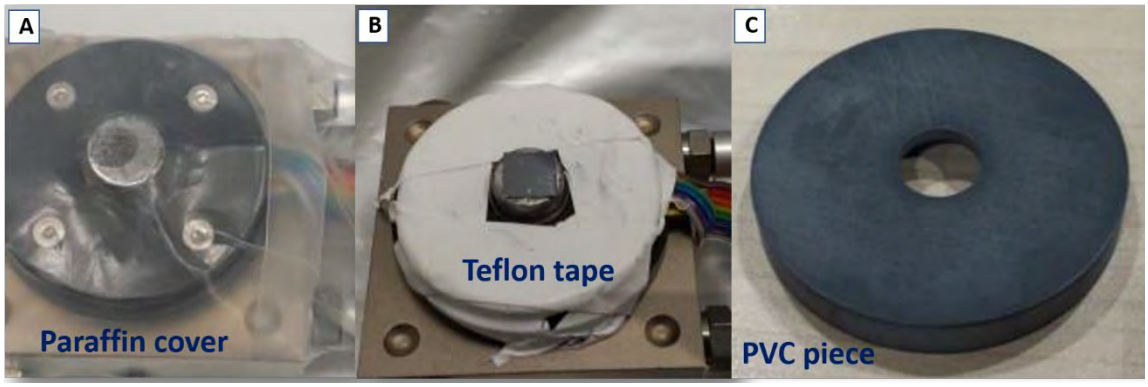

Figure AII.4. Materials tested to improve the thermal insulation in the Peltier stage: **A)** Paraffin cover. **B)** Teflon tape. **C)** PVC piece

Material	Thermal conductivity (W/(m·K))
Paraffin	0.25
Polyvinylchloride, PVC	0.19
Teflon, PTFE	0.25
Copper	401
Gallium indium	28.65[1]
Aluminum	205
Ice	2.18
Air	0.024

Table AII.1. Thermal conductivities table of materials tested

[1] M. J. Duggin, "The thermal conductivity of liquid gallium," *Phys. Lett. A*, vol. 29, no. 8, pp. 7–8, 1969.

Appendix III

Software tools for video processing

***Ffmpeg*:**

This tool is used for the process of normalizing a video file. This software is available at https://ffmpeg.org/.

Original videos need to be converted to a suitable format to subsequently handle them with *ImageJ* and set them to 1 frame per second. *Ffmpeg* is a command line tool. The instructions to implement this operation are the following:

ffmpeg -i "Movie (Channel 2) 025 (Converted).mov" -q:v 3 -vcodec mjpeg 025.avi,

where *"Movie (Channel 2) 025 (Converted).mov"* is the original video recorded, *025.avi* is the output video (which will be analyzed). The parameter *-vcodec mjpeg* sets the video with a codec that works with *ImageJ*, minimizing the quality loss with *-q:v 3* parameter.

After executing this process, a normalized video is obtained.

ImageJ:

It is a processing and analysis software written in Java and available at https://imagej.nih.gov/ij/download.html.

Once a video is normalized, the proper measures for a subsequent nanoparticle tracking are set, which means the process of tracing the path for each nanoparticle detected.

The following steps are needed:

1º) Load the normalized video file:

Selecting *File > Open* the normalized video is opened (see figure A.III.1). Then the frame range for analysis will be asked (usually all the frames are analyzed). *Convert to Grayscale* option is recommended to save memory. Otherwise the amount of data in memory could be excessive. Besides, color data are not useful since movies are recorded in grayscale.

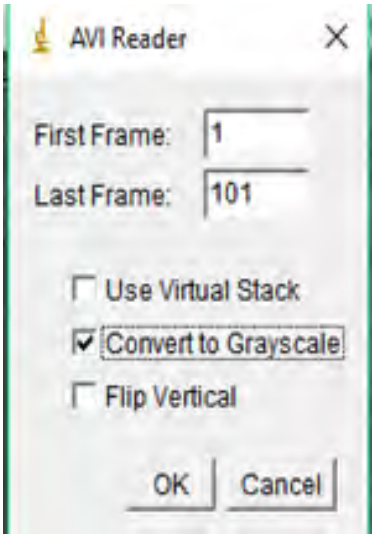

Figure A.III.1. Frame range and grayscale selection in *ImageJ*.

2º) Set scale:

Once the video is loaded, the measures for this video, i.e. the number of pixels per micrometer, need to be stablished. The scale bar is used as a length reference (it is important to note that videos should have the same scale bar during the whole acquisition). A line (see figure A.III.2.) is drawn on the scale bar. Since drawing this line is a manual process, it is important to check its angle to assure the proper drawing. The angle parameter while drawing must be 0.00 degrees.

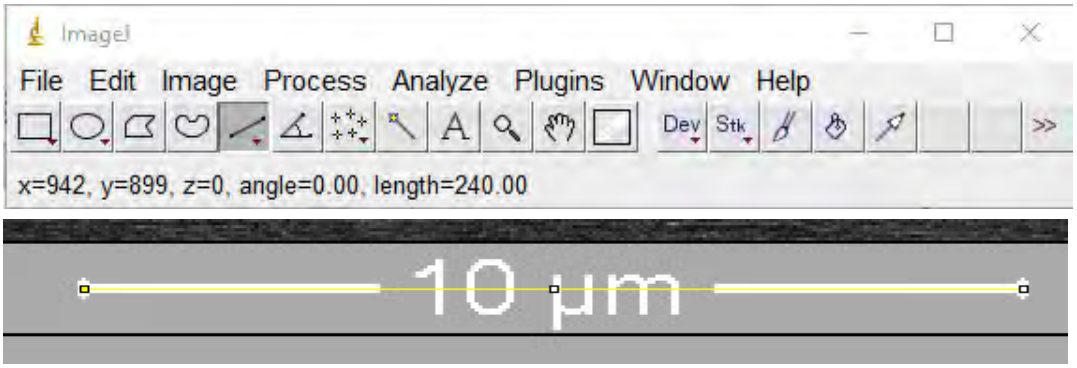

Figure A.III.2. Scale bar is used as a length reference in *ImageJ*.

At this point, *Analyze* > *Set Scale* is chosen and the data (see figure A.III.3) introduced in the dialog box that appears on the screen. In the shown example, the "Known distance"

parameter is 10 (scale bar length) and *um* (micrometers) should be introduced as "Unit of length".

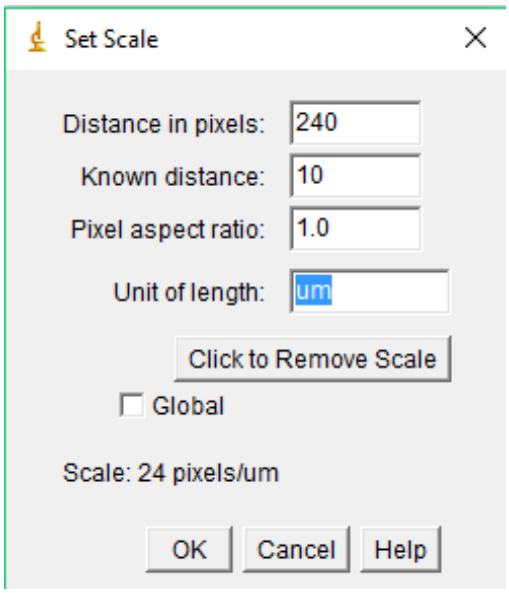

Figure A.III.3. Set scale dialog box in *ImageJ*.

3º) Set frame interval:

It is possible to set the time between frames selecting *Image* > *Properties* (see figure A.III.4). In my case, since all the frames need to be analyzed, 0 seconds are always chosen as the frame interval.

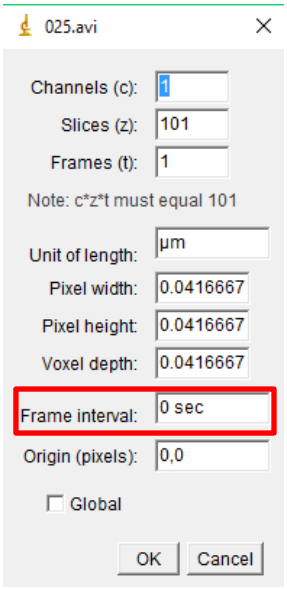

Figure A.III.4. Set frame interval dialog box in *ImageJ*.

Once this process is finished the correct configuration for tracking particles with the plugin *MtrackJ* is achieved.

MtrackJ:

This *ImageJ* plugin is basically used for drawing the nanoparticle paths. To run *MtrackJ*, I select *Plugins* > *MtrackJ*.

Some configurations can be selected to make easier the task of tracking nanoparticle movement in each frame (see figure A.III.5). It is recommended to apply local cursor snapping during tracking to improve the precision or accuracy of the tracking process. The snap feature criterium is maximum intensity; however, a snap range considered suitable for acquiring nanoparticle position by the user can be chosen.

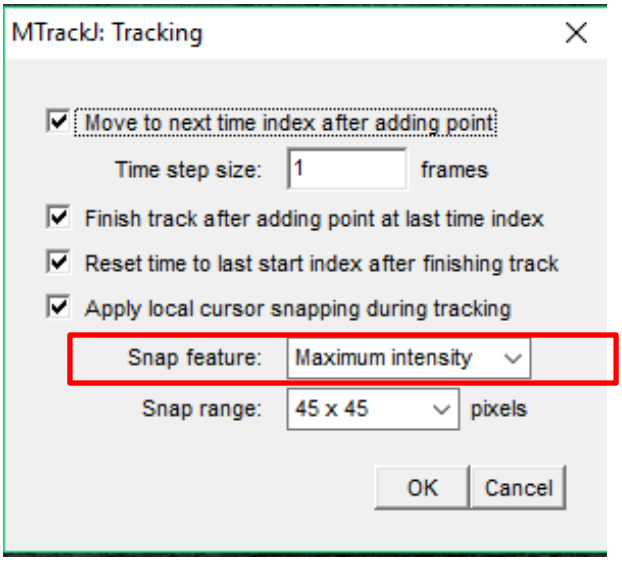

Figure A.III.5. Configurations for the tracking in *MTrackJ*

Clicking on "add", the operation of drawing the path of a chosen nanoparticle starts. Tracking is a manual process. The chosen configuration explained above will minimize errors with data acquiring since the tracking point at each frame will be selected following the same criterion (maximum intensity, in this case).

After the tracking of the first nanoparticle is finished, one can continue with another path. The software assigns a different color to each trajectory (see figure A.III.6).

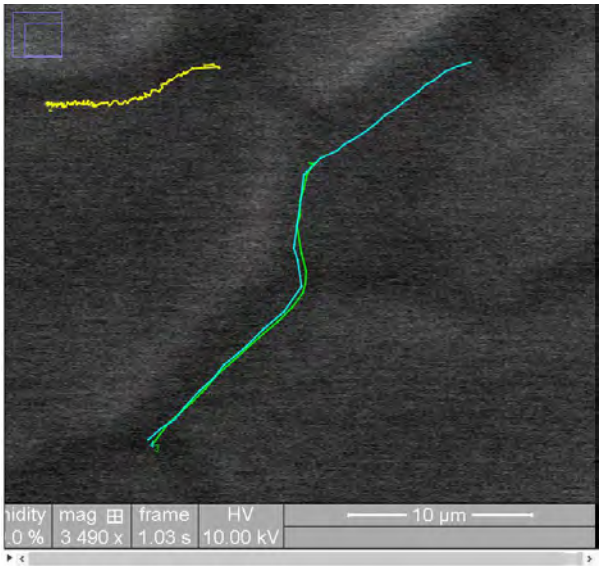

Figure A.III.6. Drawn trajectories. Each path (different color) corresponds to a different nanoparticle.

Once all nanoparticles have been tracked, the tracking data are saved into a file clicking on Save (the file will be saved with .mdf extension). Additionally, the measurement files are generated clicking on "Measure". This way the x and y values for the nanoparticles with time are obtained (see figure A.III.7).

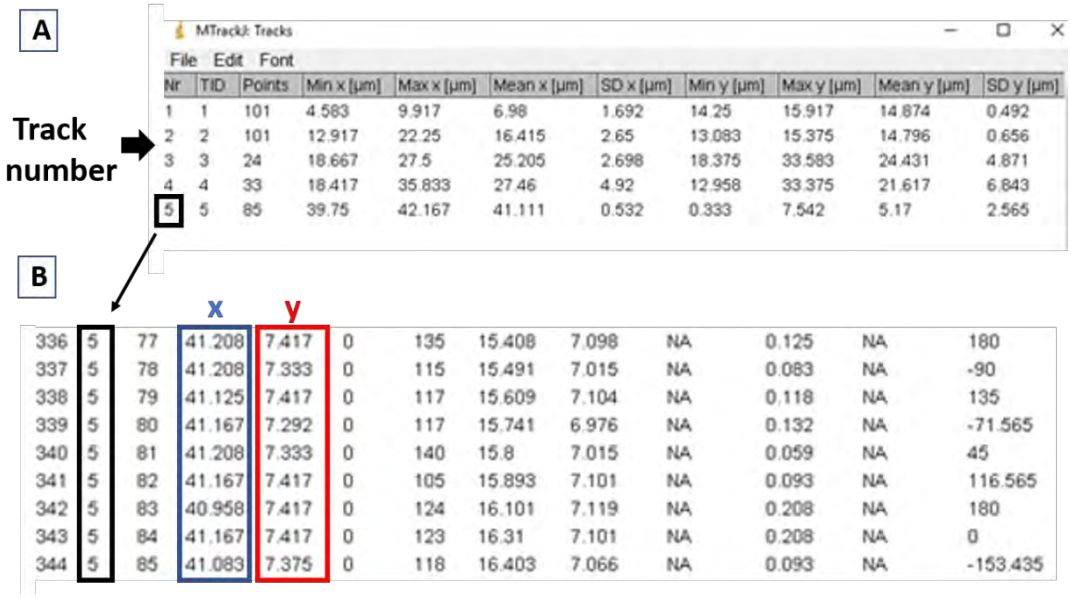

Nr	TID	Points	Min x [µm]	Max x [µm]	Mean x [µm]	SD x [µm]	Min y [µm]	Max y [µm]	Mean y [µm]	SD y [µm]
1	1	101	4.583	9.917	6.98	1.692	14.25	15.917	14.874	0.492
2	2	101	12.917	22.25	16.415	2.65	13.083	15.375	14.796	0.656
3	3	24	18.667	27.5	25.205	2.698	18.375	33.583	24.431	4.871
4	4	33	18.417	35.833	27.46	4.92	12.958	33.375	21.617	6.843
5	5	85	39.75	42.167	41.111	0.532	0.333	7.542	5.17	2.565

336	5	77	41.208	7.417	0	135	15.408	7.098	NA	0.125	NA	180
337	5	78	41.208	7.333	0	115	15.491	7.015	NA	0.083	NA	-90
338	5	79	41.125	7.417	0	117	15.609	7.104	NA	0.118	NA	135
339	5	80	41.167	7.292	0	117	15.741	6.976	NA	0.132	NA	-71.565
340	5	81	41.208	7.333	0	140	15.8	7.015	NA	0.059	NA	45
341	5	82	41.167	7.417	0	105	15.893	7.101	NA	0.093	NA	116.565
342	5	83	40.958	7.417	0	124	16.101	7.119	NA	0.208	NA	180
343	5	84	41.167	7.417	0	123	16.31	7.101	NA	0.208	NA	0
344	5	85	41.083	7.375	0	118	16.403	7.066	NA	0.093	NA	-153.435

Figure A.III.7. A) Five different tracked trajectories. Each number represents the trajectory of a different nanoparticle. **B)** Some points followed by the nanoparticle in trajectory number five. X values are shown inside the blue rectangle and y values inside the red one.

These files are saved for a subsequent analysis using *MATLAB*. Inherently, *MtrackJ* generates CSV files (comma separated values). These files can be loaded with Microsoft Excel and converted into Excel files, with the corresponding .xls extension, since the scripts in *MATLAB* require this type of file to be executed.

MATLAB:

At this point, using the above-mentioned software tools, a file with a collection of points that represents the path of each nanoparticle at each frame has been generated, and each frame corresponds to the position of each second of the whole detected movement.

A *MATLAB* code to determine useful parameters, e.g. the mean square displacement (MSD) or the average speed, for a subsequent analysis has been developed. Different plots could also be generated using this code.

Appendix III

MATLAB code: ***tracking_MAIN***

This code is composed of five different functions (**open_data**, **trajectories**, **MSD_compute**, **FitMSD** and speed), each of which carries out a concrete task when the code is executed.

```
clc;
clear;
dataset = 'MSDlinlar50random450';
output_folder = ['Output/',dataset,'_results'];

if ~exist(output_folder,'dir')
   mkdir(output_folder);
end

fname = [dataset,'/MTrackJ_Points.xlsx'];
[dataM,npts,npart,nframes] = open_data(fname);
```

The **open_data** function finds the number of particles and the number of frames for each different particle:

```
function [dataMAT,n_pts,n_part,n_frames] = open_data(filename)

    fname = filename;
    A = xlsread(fname);
   s = size(A);
    n_pts = s(1);
    dataMAT = A(:,1:7);
    n_part = A(n_pts,2);
    n_frames = zeros(n_part,1);
    current_particle = 1;
    asigned_frames = 0;
    particle_column = 2;

  for current_row = 1:n_pts

        if (current_particle == n_part)
        n_frames(current_particle) = n_pts- asigned_frames;
        break;
      end

      if A(current_row,particle_column) ~= current_particle;
        n_frames(current_particle) = current_row - 1 - asigned_frames;
        asigned_frames = current_row - 1;
        current_particle = current_particle+1;
      end
  end
end
```

Afterwards the ***tracking_MAIN*** code plots the trajectory of each nanoparticle detected using the **trajectories** function:

```
trajectories(dataM,npart,nframes,output_folder)

function trajectories(dataM,npart,nframes,output_folder)
```

```
  color_codes = [0,0,1; 0,1,0; 1,0,0; 1,1,0; ...
      1,0,1; 0,1,1; 0,0,0; 0.5,0.5,0.5];
  figure1 = figure;
  axes1 = axes ('Parent', figure1,...'LineWidth',1.5,...'FontSize',15);
  box(axes1,'on');
  hold(axes1,'all');
  xlabel('x (\mum)','FontSize',16);
  ylabel('y (\mum)','FontSize',16);
  set(gca,'Ydir','reverse');
  axis equal;
  xlim([0 max(dataM(:,4))*1.15]);
  ylim([0 max(dataM(:,5))*1.15]);
  hold on;

  for i = 1:npart

      j1 = 1+sum(nframes(1:i-1));
      j2 = sum(nframes(1:i));

  dataP = [dataM(j1:j2,4:5),dataM(j1:j2,7)];
  plotname = ['Particle #',num2str(i)];
  plot(dataP(:,1),dataP(:,2),'Parent',axes1,'LineWidth',2,...
        'Color',color_codes(i,:),'DisplayName',plotname);

  plot(dataP(1,1),dataP(1,2),'*','Parent',axes1,'MarkerSize',10,...
        'MarkerEdgeColor', color_codes(i,:), ...
        'MarkerFaceColor',color_codes(i,:),...
        'DisplayName',plotname);

  plot(dataP(nframes(i),1),dataP(nframes(i),2),'s','Parent',axes1,...
        'MarkerSize',4,...
        'MarkerEdgeColor', color_codes(i,:), ...
        'MarkerFaceColor',color_codes(i,:),...
        'DisplayName',plotname);
  end

  fig_fname  = [output_folder,'/trajec.fig'];
 fig_fname2 = [output_folder,'/trajec.png'];
 saveas(figure1,fig_fname);
 print('-dpng','-r0',fig_fname2);
 close;
end
```

The next step is to calculate the mean square displacement using the **MSD_compute** function:

```
MSD_matrix = MSD_compute(dataM,npart,nframes,output_folder);

    function [MSD_matrix] = MSD_compute(dataM,npart,nframes,output_folder)

   MSD_matrix = [];

   color_codes = [0,0,1; 0,1,0; 1,0,0; 1,1,0; ...
      1,0,1; 0,1,1; 0,0,0; 0.5,0.5,0.5];
   figure1 = figure;
```

Appendix III

```
axes1 = axes('Parent',figure1,...
    'LineWidth',1.5,...
    'FontSize',15);
box(axes1,'on');
hold(axes1,'all');
xlabel('\tau (sec)','FontSize',16);
ylabel('MSD (\mum^2)','FontSize',16);
title('MSD vs. \tau','FontSize',16);
figure2 = figure;
axes2 = axes('Parent',figure2,...
    'LineWidth',1.5,...
    'XScale','log','YScale','log',...
    'FontSize',15);
box(axes2,'on');
hold(axes2,'all');

xlabel('\tau (sec)','FontSize',16);
ylabel('MSD (\mum^2)','FontSize',16);
title('log(MSD) vs. log(\tau)','FontSize',16);


for i = 1:npart
    j1 = 1+sum(nframes(1:i-1));
    j2 = sum(nframes(1:i));
    dataP = [dataM(j1:j2,4:5),dataM(j1:j2,7)];
    MSD_vector = zeros(nframes(i)-1,1);

   for tau = 1:nframes(i)-1
       MSD = 0;
       for k = 1:nframes(i)-tau
         MSD = MSD + (dataP(k+tau,1)-dataP(k,1))^2 +...
             (dataP(k+tau,2)-dataP(k,2))^2;
        end
      MSD_vector(tau) = MSD/(nframes(i)-tau);

    end
    tau_vector = (1:nframes(i)-1)';
    MSD_matrix = [MSD_matrix; zeros(tau,1)+i,tau_vector,MSD_vector];
    plotname = ['Particle #',num2str(i)];
    plot(tau_vector,MSD_vector,'Parent',axes1,'LineWidth',2,...
        'Color',color_codes(i,:),'DisplayName',plotname);
    plot(tau_vector,MSD_vector,'Parent',axes2,'LineWidth',2,...
        'Color',color_codes(i,:),'DisplayName',plotname);

end
legend1 = legend(axes1,'show');
set(legend1, 'Location','northwest','LineWidth',1.5);
legend2 = legend(axes2,'show');
set(legend2, 'Location','northwest','LineWidth',1.5);
figname1 = [output_folder,'/MSDvsTAU.fig'];
figname2 = [output_folder,'/LogMSDvsTAU.fig'];
figname1png = [output_folder,'/MSDvsTAU.png'];
figname2png = [output_folder,'/MSDvsTAU_log.png'];
saveas(figure1,figname1);
saveas(figure2,figname2);
print(figure1,'-dpng','-r600',figname1png);
print(figure2,'-dpng','-r600',figname2png);
close;
close;
```

```
end
```

Then the code is asked for fitting the calculated MSD and extracting the alpha value. For this purpose the **Fit_MSD** function is required:

```
fitted = FitMSD(MSD_matrix,npart,nframes,output_folder);

 function [logtau,logMSD]= FitMSD(MSD_matrix,npart,nframes,output_folder)

   color_codes = [0,0,1; 0,1,0; 1,0,0; 1,1,0; ...
       1,0,1; 0,1,1; 0,0,0; 0.5,0.5,0.5];

  figure2 = figure;
  axes2 = axes('Parent',figure2,...
      'LineWidth',1.5,...
      'XScale','linear','YScale','linear',...
      'FontSize',15);
   box(axes2,'on');
   hold(axes2,'all');

   xlabel('log(\tau (sec))','FontSize',16);
   ylabel('log(MSD (\mum^2))','FontSize',16);
   title('log(MSD) vs. log(\tau)','FontSize',16);

   nframes = nframes -1;

   for i = 1:npart

      j1 = 1+sum(nframes(1:i-1));
      j2 = sum(nframes(1:i));

      tau = MSD_matrix(j1:j2,2);
      MSD = MSD_matrix(j1:j2,3);

      logtau = log(tau);
      logMSD = log(MSD);

      plotname = ['Particle #',num2str(i)];
      plot(logtau,logMSD,'Parent',axes2,'LineWidth',2,...
          'Color',color_codes(i,:),'DisplayName',plotname);

      p = polyfit(logtau,logMSD,1);
      x = 0:0.1:5;
      y = p(1)*x+p(2);
      plotname = ['Fit#',sprintf('%s m:%.3f
                D:%0.5e',num2str(i),p(1),((exp(1)^p(2))/4))];
      plot(x,y,'k--','Parent',axes2,'LineWidth',2,...
          'Color',color_codes(i,:),'DisplayName',plotname);

   end
   legend2 = legend(axes2,'show');
   set(legend2, 'Location','northwest','LineWidth',1.5,'FontSize',10);
   figname1 = [output_folder,'/FitMSD.fig'];
   figname1png = [output_folder,'/FitMSD.png'];
   saveas(figure2,figname1);
   print(figure2,'-dpng','-r600',figname1png);
   fitted = 0;
```

```
    close;

end
```

The last step is to calculate the speed of each particle and plot the values. This job is done by means of the **Speed** function:

```
velocities = Speed (dataM,npart,nframes,output_folder);

  function [ Speed ] = Speed(dataM,npart,nframes,output_folder)
    Speed = [];
    max_x = 0;
    max_y = 0;

    for i = 1:npart
      j1 = 1+sum(nframes(1:i-1));
      j2 = sum(nframes(1:i));
      for j=j1+1:j2
        max_x = max(max_x, abs(dataM(j,4) - dataM(j-1,4)));
        max_y = max(max_y, abs(dataM(j,5) - dataM(j-1,5)));
      end
    end
    max_x = max_x * 1.25;
    max_y = max_y * 1.25;
    color_codes = [0,0,1; 0,1,0; 1,0,0; 1,1,0; ...
                   1,0,1; 0,1,1; 0,0,0; 0.5,0.5,0.5];
```

The code creates a plot for the speed in the x-axis:

```
    figure1 = figure;
    axes1 = axes('Parent',figure1,...'LineWidth',0.1,...
          'XScale','linear','YScale','linear',...'FontSize',10);
    box(axes1,'on');
    hold(axes1,'all');
    xlabel('Time (s)','FontSize',12);
    ylabel('Speed (µm/s)','FontSize',12);
    title('Speed X','FontSize',12);
    axis([0,max(nframes),0,max_x]);
```

Plots for the speed in the y-axis and the absolute speed are generated by the following command sequence:

```
figure2 = figure;
axes2 = axes('Parent',figure2,...'LineWidth',1,...
                'XScale','linear','YScale','linear',...'FontSize',15);
box(axes2,'on');
hold(axes2,'all');
xlabel('Time (s)','FontSize',16);
ylabel('Speed (µm/s)','FontSize',16);
title('Speed Y','FontSize',16);
axis([0,max(nframes),0,max_y]);

figure3 = figure;
axes3 = axes('Parent',figure3,...'LineWidth',1,...
       'XScale','linear','YScale','linear',...'FontSize',15);
box(axes3,'on');
hold(axes3,'all');
```

```
xlabel('Time (s)','FontSize',16);
ylabel('Speed (µm/s)','FontSize',16);
title('Speed','FontSize',16);
axis([0,max(nframes),0,sqrt(max_x^2+max_y^2)]);
```

The average speed in the x-axis, in the y-axis and the absolute speed average are calculated:

```
averageSpeedX = zeros(npart);
averageSpeedY = zeros(npart);
averageSpeed = zeros(npart);

   for i = 1:npart
     j1 = 1+sum(nframes(1:i-1));
     j2 = sum(nframes(1:i));
     time = zeros(j2-j1,1);
     partSpeedX = zeros(j2-j1,1);
     partSpeedY = zeros(j2-j1,1);
     partSpeed = zeros(j2-j1,1);
     idx = 1;
     for j=j1+1:j2
       partSpeedX(idx) = abs(dataM(j,4) - dataM(j-1,4));
       partSpeedY(idx) = abs(dataM(j,5) - dataM(j-1,5));
       partSpeed(idx) = sqrt(partSpeedX(idx)^2+partSpeedY(idx)^2);
       time(idx) = idx;
       idx = idx+1;
     end

 averageSpeedX(i) = sum(partSpeedX)/idx;
 averageSpeedY(i) = sum(partSpeedY)/idx;
 averageSpeed(i) = sum(partSpeed)/idx;

  plotname = sprintf('Particle %d X speed (average X speed:
              %.6f)',...i, averageSpeedX(i));
plot(time,partSpeedX,'Parent',axes1,'LineWidth',1,...
         'Color',color_codes(i,:),'DisplayName',plotname);

plotname = sprintf('Particle %d Y speed (average Y speed: %.6f)',...
               i, averageSpeedY(i));

     plot(time,partSpeedY,'Parent',axes2,'LineWidth',1,...
         'Color',color_codes(i,:),'DisplayName',plotname);
     plotname = sprintf('Particle %d speed (average speed: %.6f)',...
                    i, averageSpeed(i));

     plot(time,partSpeed,'Parent',axes3,'LineWidth',1,...
         'Color',color_codes(i,:),'DisplayName',plotname);

   end

   legend1 = legend(axes1,'show');
   set(legend1, 'Location','northwest','LineWidth',1.5,'FontSize',10);
   figname1 = [output_folder,'/SpeedX.fig'];
   figname1png = [output_folder,'/SpeedX.png'];
   saveas(figure1,figname1);
   print(figure1,'-dpng','-r600',figname1png);
```

```
    legend2 = legend(axes2,'show');
    set(legend2, 'Location','northwest','LineWidth',1.5,'FontSize',10);
    figname2 = [output_folder,'/SpeedY.fig'];
    figname2png = [output_folder,'/SpeedY.png'];
    saveas(figure2,figname2);
    print(figure2,'-dpng','-r600',figname2png);

    legend3 = legend(axes3,'show');
    set(legend3, 'Location','northwest','LineWidth',1.5,'FontSize',10);
    figname3 = [output_folder,'/Speed.fig'];
    figname3png = [output_folder,'/Speed.png'];
    saveas(figure3,figname3);
    print(figure3,'-dpng','-r600',figname3png);

    close;
    close;
    close;
end
```

Whenever the ***tracking_MAIN*** code is run, all these steps are executed. The user interface will ask for the file of interest, and the generated results will be automatically saved into a folder called "*_results*".

Appendix IV

Random walk tests

Different random walks have been generated with EXCEL to test the efficiency of the MATLAB code to calculate the mean square displacement of this type of movements.

Example 1:

A 22-point random walk is generated with EXCEL (see figure A.IV.1.), and the MATLAB code is run to obtain the trajectory and the mean square displacement (MSD) of this movement. The slope of the log MSD-log τ plot enables to characterize the type of movement. For a random walk this value is expected to be around 1.

MSDrandom22_step1

0	0
-0.76920403	-0.63900325
-1.71873041	-0.95269044
-1.40151802	-1.90104496
-0.46528176	-2.25241609
-0.63076993	-3.23862786
-0.26688253	-2.30718492
-1.00271058	-1.63001648
-1.83853281	-2.17901665
-1.58465423	-1.21178056
-1.96658928	-0.28759139
-2.93145567	-0.02485035
-2.76121783	-1.01025336
-2.06015701	-0.29715188
-2.92559363	0.20386655
-3.8037662	-0.27447739
-3.06431007	-0.94768214
-3.39889503	-0.00531655
-3.6196308	-0.9806502
-4.51029969	-0.52599767
-4.69176822	0.45739909
-5.06042089	-0.47216813

Figure A.IV.1. Random walk generated with EXCEL

The resulting plots from the MATLAB code for this movement are shown in figure A.IV.2. The slope obtained is equal to 1.028, which shows a good performance of the code.

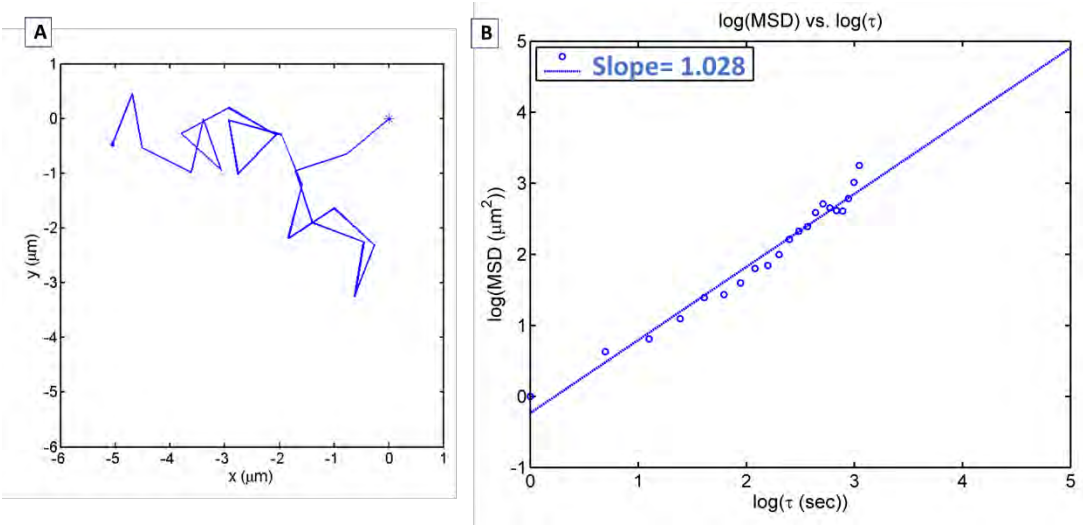

Figure A.IV.2. Plots generated with the MATLAB code. **A)** Trajectory of the random walk. **B)** Mean square displacement (MSD) as function of lag time (τ) in logarithmic scale.

Example 2:

A 10000-point random walk is generated with EXCEL (see figure A.IV.3.), and the MATLAB code is run to obtain the trajectory and the mean square displacement (MSD) of this movement.

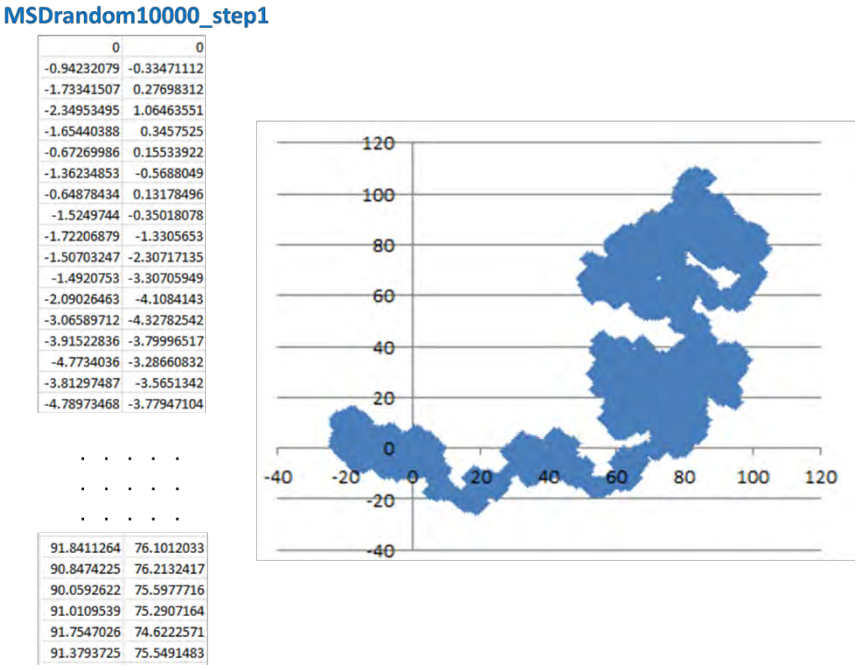

MSDrandom10000_step1

0	0
-0.94232079	-0.33471112
-1.73341507	0.27698312
-2.34953495	1.06463551
-1.65440388	0.3457525
-0.67269986	0.15533922
-1.36234853	-0.5688049
-0.64878434	0.13178496
-1.5249744	-0.35018078
-1.72206879	-1.3305653
-1.50703247	-2.30717135
-1.4920753	-3.30705949
-2.09026463	-4.1084143
-3.06589712	-4.32782542
-3.91522836	-3.79996517
-4.7734036	-3.28660832
-3.81297487	-3.5651342
-4.78973468	-3.77947104
. . . . .	
. . . . .	
. . . . .	
91.8411264	76.1012033
90.8474225	76.2132417
90.0592622	75.5977716
91.0109539	75.2907164
91.7547026	74.6222571
91.3793725	75.5491483

Figure A.IV.3. Random walk generated with EXCEL

The resulting plots from the MATLAB code for this movement are shown in figure A.IV.4. The slope obtained for this example is equal to 1.069, which again shows a good performance of the code.

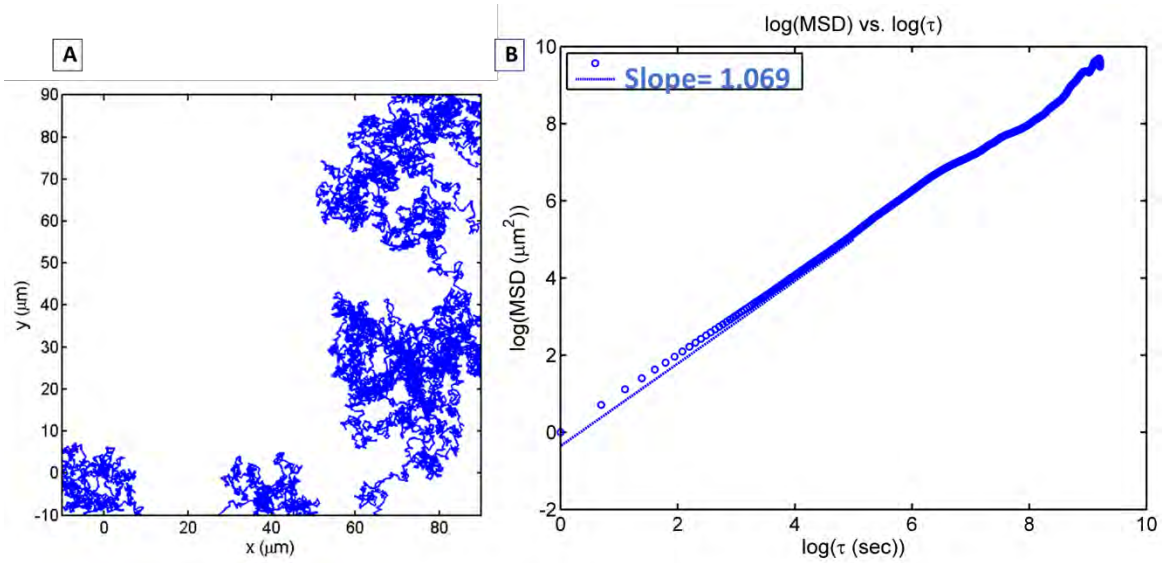

Figure A.IV.4. Plots generated with the MATLAB code. **A)** Trajectory of the random walk. **B)** Mean square displacement (MSD) as function of lag time (τ) in logarithmic scale.

Appendix V

List of analysed videos with nanoparticle movement detection

Movie 25:

The conditions in which this movie have been recorded are the following: a temperature of -5.5 °C and a pressure of 448 Pa. Five different nanoparticles are tracked (see figure A.V.1)

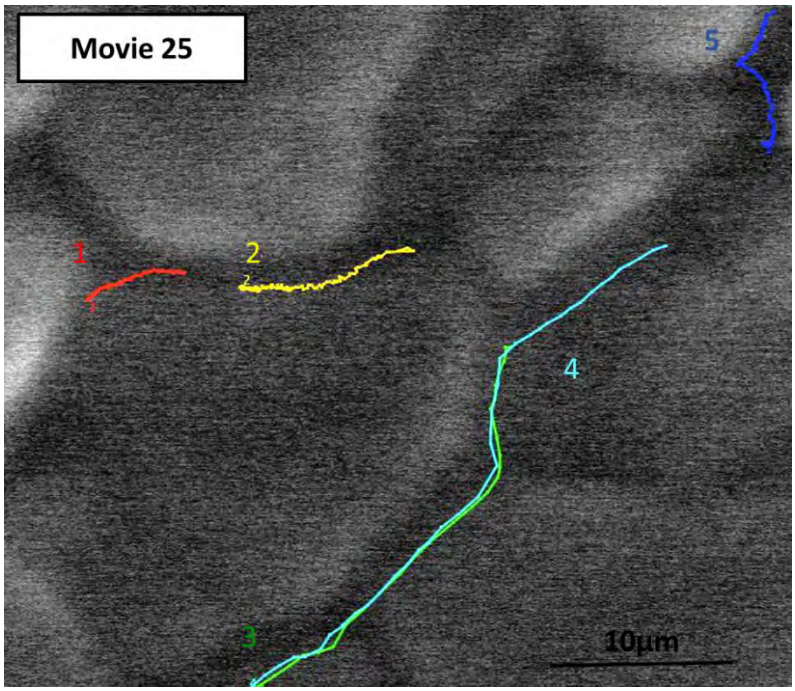

Figure A.V.1. Snapshot of the tracking video showing movement of five independent nanoparticles.

A schematic representation of the movement of the five nanoparticles is shown in Figure A.V.2. Nanoparticles labeled as 1 and 2 appear to move along the grain boundary named GB_1, while nanoparticles 3, 4 and 5 travel through the grain boundary marked as GB_2.

The speed of the nanoparticles moving along the grain boundary GB_1 is lower than the one of the nanoparticles along the grain boundary GB_2. The speed of the nanoparticles is calculated by the MATLAB code and plotted as a function of time (see Figure A.V.3).

The average speed along grain boundary GB_1 is 0.1µm/s for nanoparticle 1 and 0.2µm/s for nanoparticle 2, since along grain boundary GB_2 in the interval of time (15s-30s), nanoparticles 3 and 4 reach an average speed of 1.4µm/s.

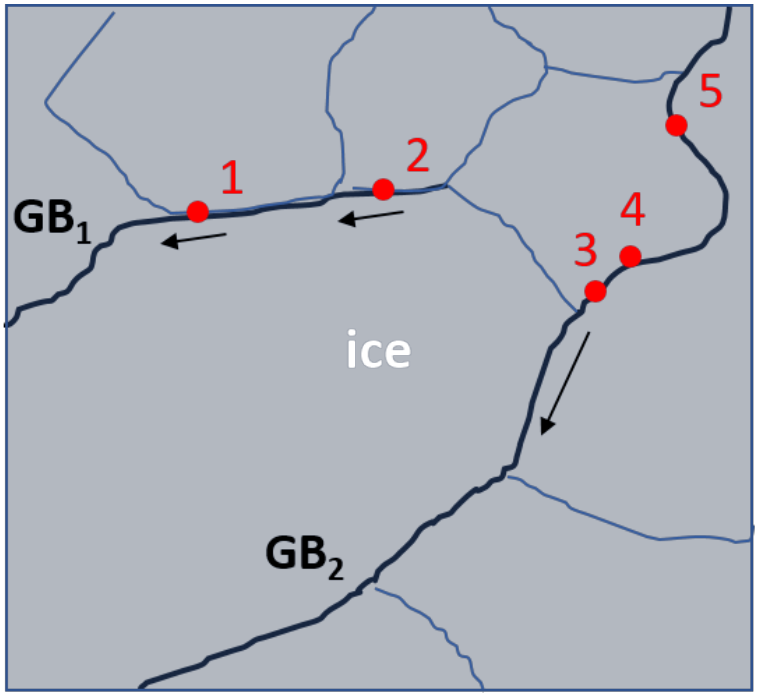

Figure A.V.2. Schematic representation of the movement of the nanoparticles on a polycrystalline ice surface. Nanoparticles labeled as 1 and 2 move along grain boundary 1 (GB_1) and nanoparticles 3,4 and 5 move along grain boundary 2 (GB_2).

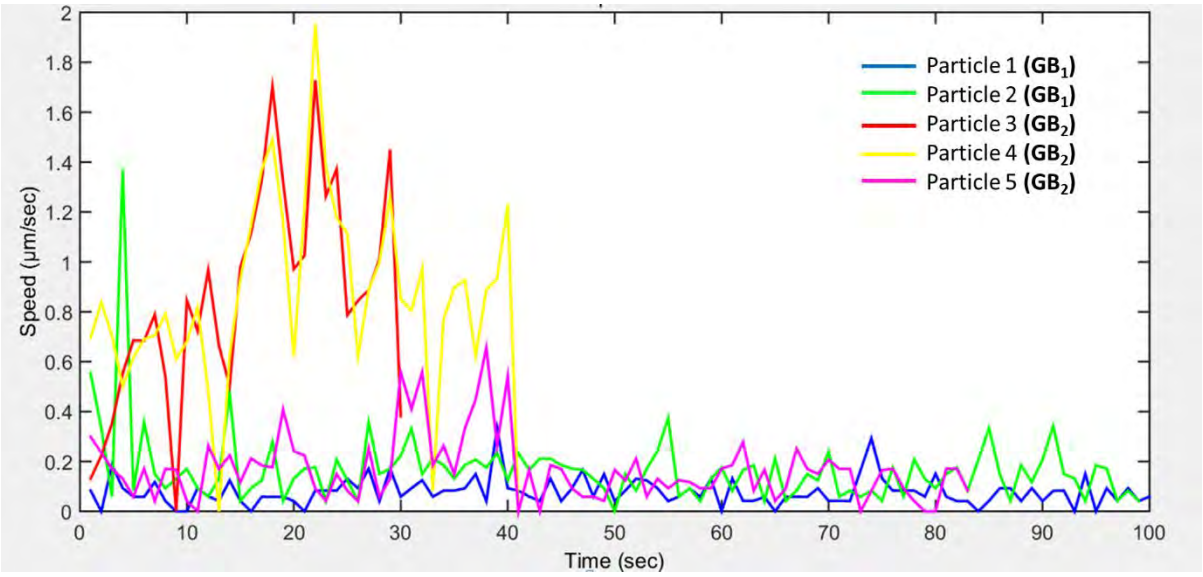

Figure A.V.3. Speed of the different nanoparticles during the recorded movie.

In the next figure (Figure A.V.4) the trajectories and the mean square displacements (MSD) for the five nanoparticles are plotted. As explained in chapter 3, the slope of the curve of the MSD versus the observation time or lag time(τ), provides the alpha value, α, and the type of movement can be interpolated from this alpha value. In this case, all nanoparticles show an anomalous diffusive behavior since all the alpha values are higher than unity. With the exception of nanoparticle 5, the others have alpha values really close to 2 (ballistic regime)

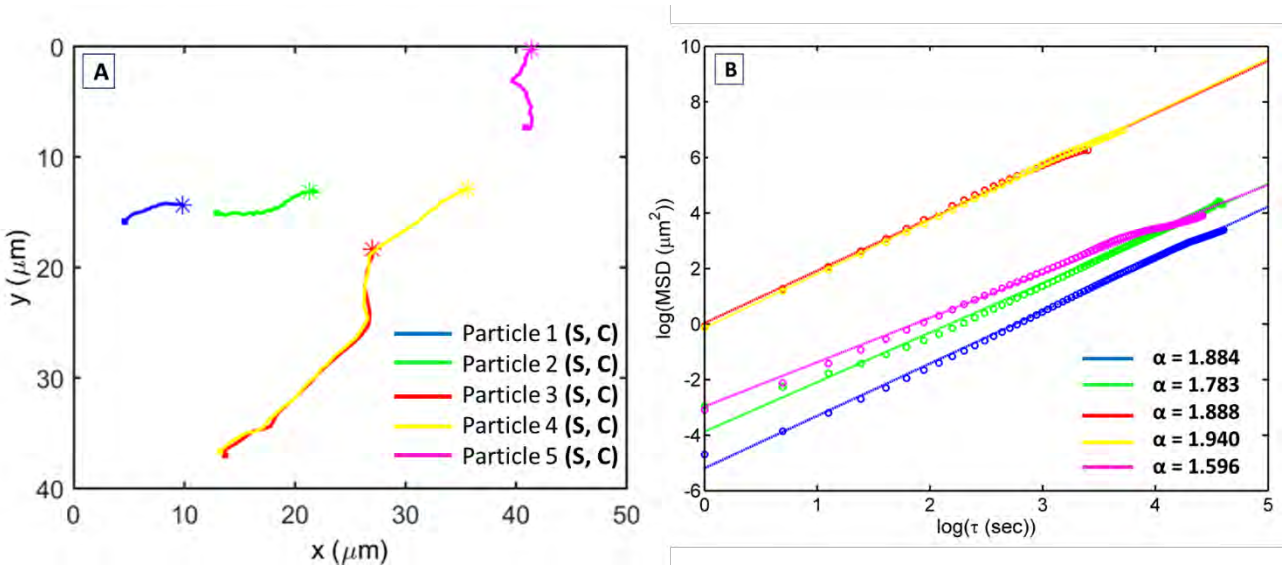

Figure A.V.4. A) Trajectories followed by five different single(S) nanoparticles along the channel(C) or grain boundary. **B)** Log-log plots of mean square displacements as a function of lag time τ.

Movie 90:

The conditions in which this movie has been recorded are the following: a temperature of -7.5 °C and a pressure of 367 Pa. Movement of five particles (three of them correspond to single nanoparticles, since the other two are clusters composed of more than two nanoparticles) is detected and tracked (see Figure A.V.5). In contrast to the previous example (movie 25), nanoparticles are moving not along the channel of a grain boundary but on the surface of the ice grown on the substrate. In fact, particle 5 is moving on the ice surface and its movement ends by the nanoparticles entering the grain boundary. As shown in the schematic representation of the movement performed by the nanoparticles (figure A.V.6), each nanoparticle has a different movement direction. The fact of not

finding a predominant direction in the nanoparticles movement is important and sufficient of an argument to exclude the movement due to a presumed tilting of the substrate.

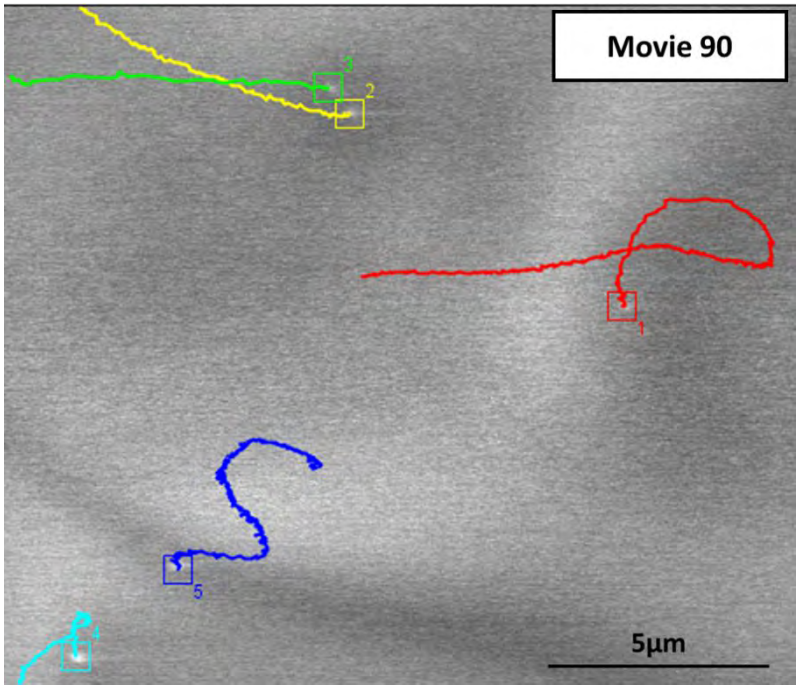

Figure A.V.5. Snapshot of the tracking video showing movement of five independent nanoparticles.

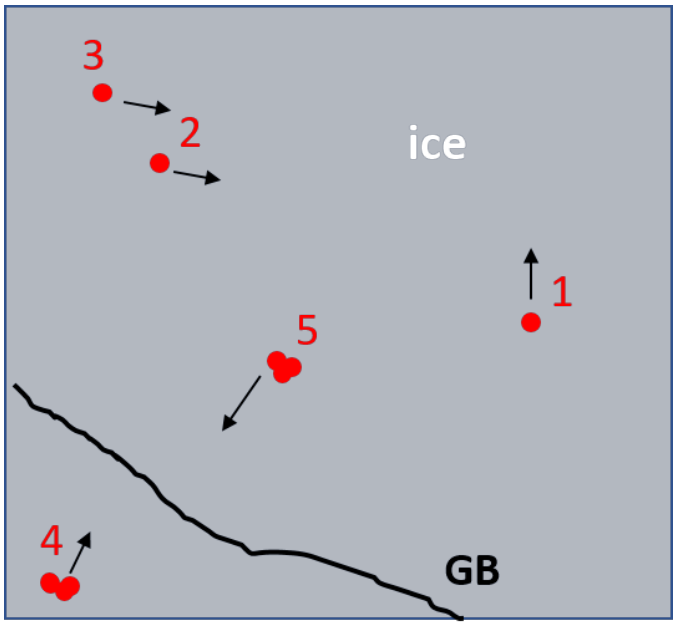

Figure A.V.6. Schematic representation of the movement of the nanoparticles on a polycrystalline ice surface. Each nanoparticle follows a different direction in their movement.

In the next figure (figure A.V.7) the trajectories and the mean square displacements (MSD) for the five nanoparticles are plotted and the alpha value, α, calculated.

Having a simultaneous look to the trajectories and MSD plots it is noticeable to highlight that nanoparticles moving in a straight line (particles 2 and 3) exhibit alpha values close to 2 (α=1.948 and α=1.951), since more twisting trajectories (like the followed by particles 1, 4 and 5) correspond to lower alpha values (α=1.401, α=1.263, α=1.415). In any case, all of them do not correspond to a Brownian diffusive regime.

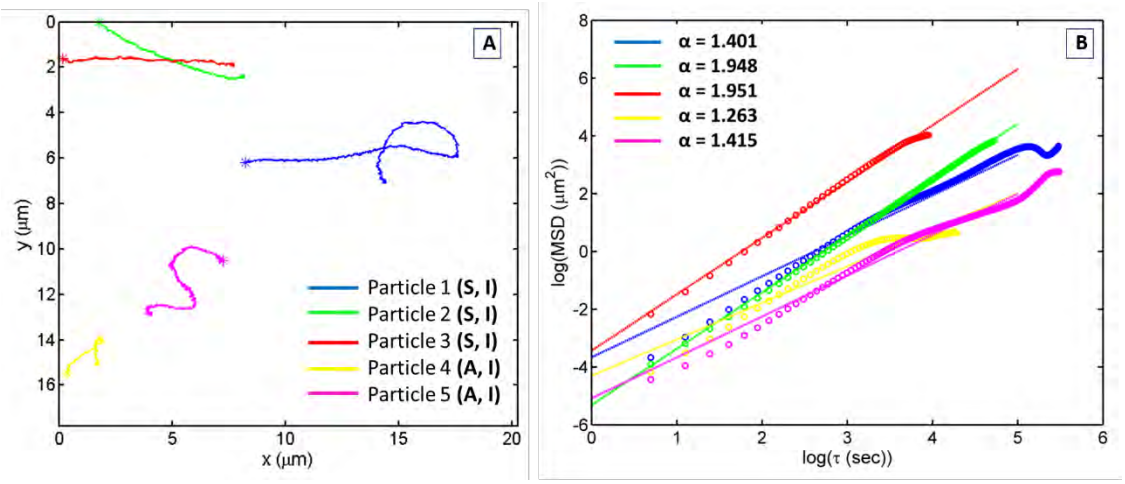

Figure A.V.7. A) Trajectories followed by three different single(S) nanoparticles and two different clusters of aggregated(A) nanoparticles on the ice(I) surface. **B)** Log-log plots of mean square displacements as a function of lag time τ.

Movie 91:

The conditions in which this movie have been recorded are the following: a temperature of -7.6 °C and a pressure of 367 Pa. Movement of five single nanoparticles is detected and tracked (see figure A.V.8). This video shows many similarities to the previous one (movie 90). Again, the nanoparticles are moving on the ice surface and, only in the case of nanoparticle labeled as 5, half of the movement is on the ice and the second part of the movement developed by this particle takes place along a grain boundary. Figure A.V.9 shows how not all the nanoparticles follow the same direction in their movement. Trajectories and mean square displacements (MSD) are plotted in figure A.V.10.

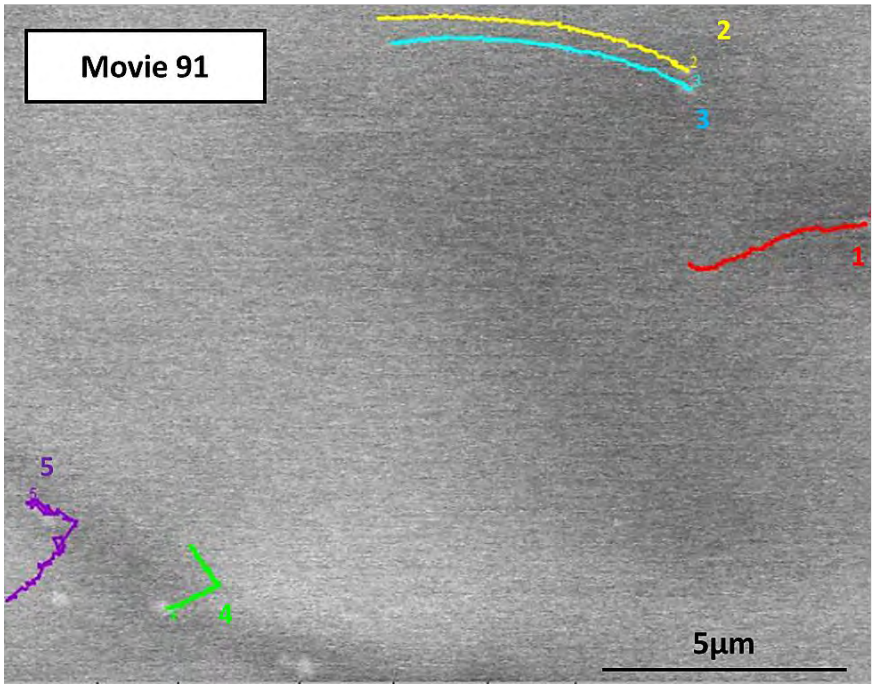

Figure A.V.8. Snapshot of the tracking video showing movement of five independent nanoparticles.

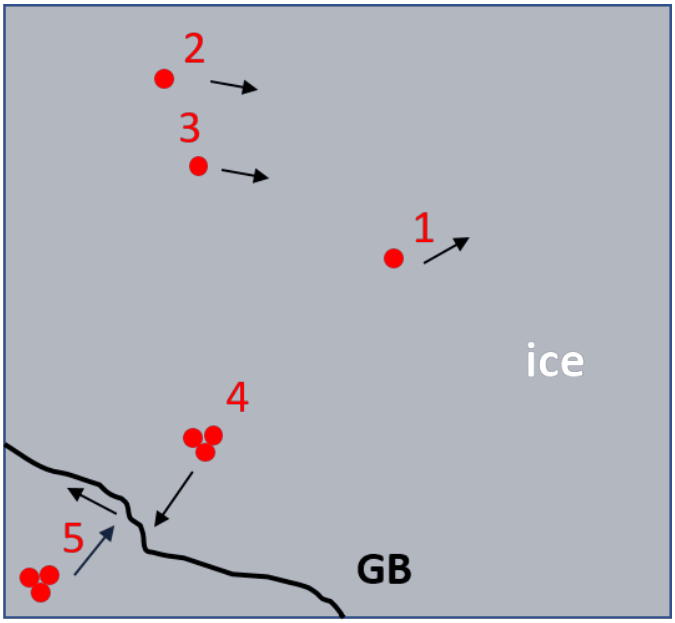

Figure A.V.9. Schematic representation of the movement of the nanoparticles on a polycrystalline ice surface. Each nanoparticle follows a different direction in their movement

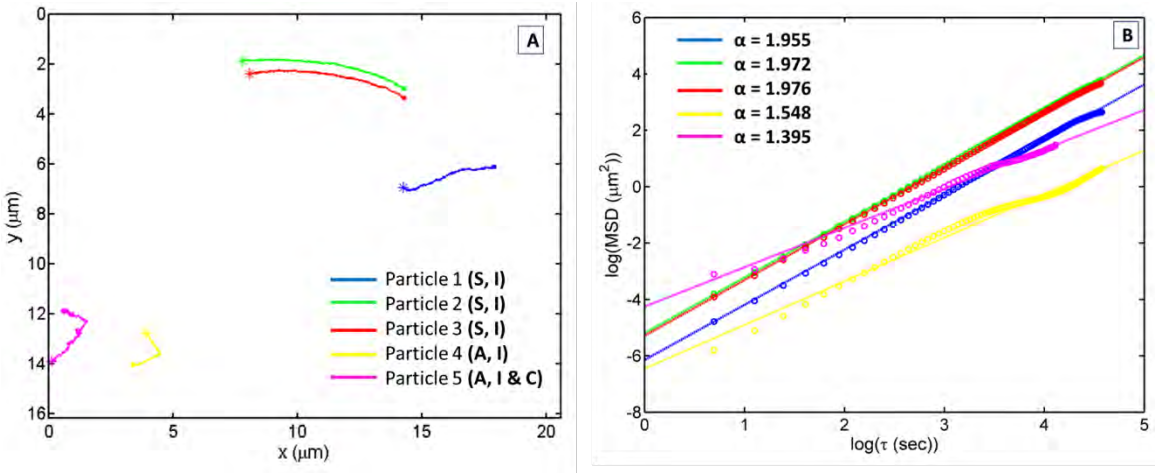

Figure A.V.10. A) Trajectories followed by three different single(S) nanoparticles and two different clusters of aggregated(A) nanoparticles on the ice(I) surface. Nanoparticles cluster named as particle 5 travels on the ice(I) and along the channel(C) or grain boundary. **B)** Log-log plots of mean square displacements as a function of lag time τ.

Movie 93:

The conditions in which this movie has been recorded are the following: a temperature of -7.7 °C and a pressure of 367 Pa. Movement of two single nanoparticles is detected and tracked (see figure A.V.11)

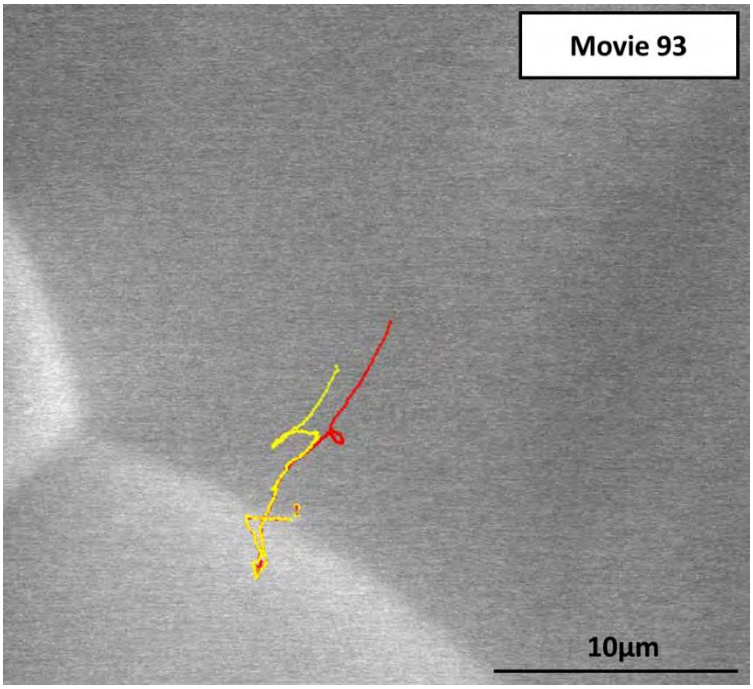

Figure A.V.11. Snapshot of the tracking video showing movement of two independent nanoparticles.

In figure A.V.11 the complete movement and tracked trajectories are shown; however, in order to analyze correctly this video two parts should be considered. The first one is where both nanoparticles are moving freely towards the south (figure A.V.12. A). At the same time from the bottom of the image it can be seen how an ice front is growing in the opposite direction (to the north). The second part will correspond to the sequence of images in which nanoparticles are moving being pushed by the ice front (figure A.V.12. B).

It is important to note that although ice seems to keep growing at certain parts of the substrate, the video has been recorded under the same conditions of pressure and temperature.

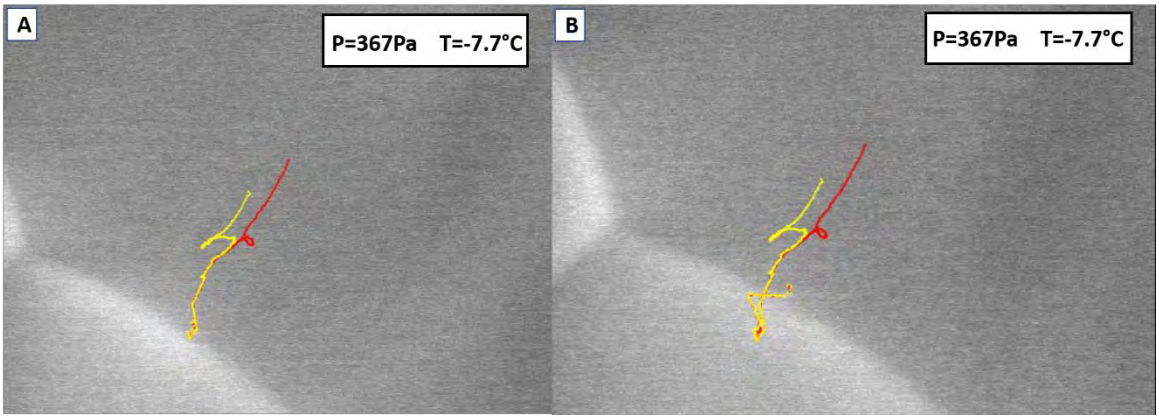

Figure A.V.12. Snapshots of the tracking video: **A)** Correspond to the end of the first part of video. **B)** End of the second part of the video.

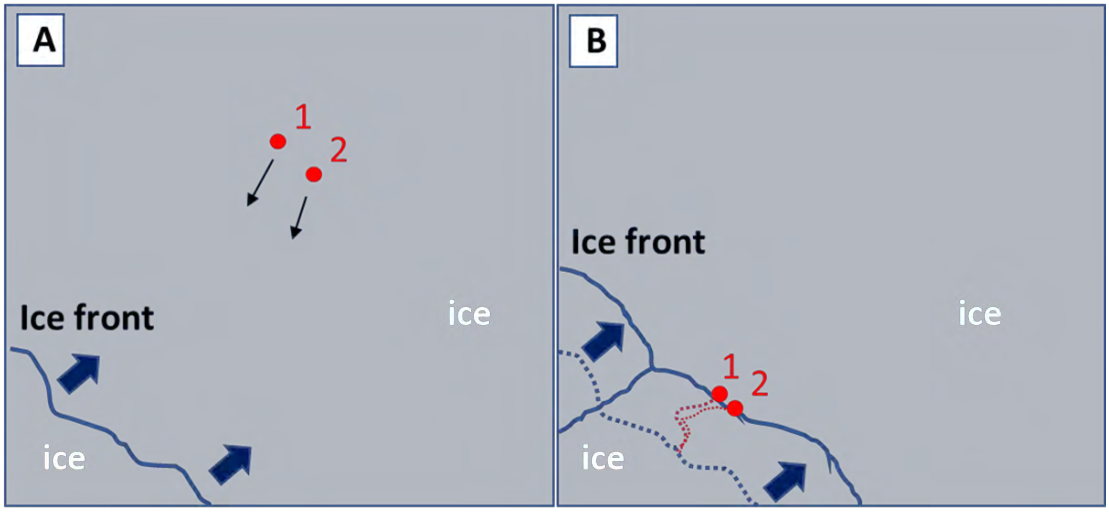

Figure A.V.13. Schematic representation of the movement of the nanoparticles in video 93.**A)** In this part of the video both nanoparticles are moving freely on the ice surface and at the same time ice appears to grow at the bottom of the image. B) Second part of the movement. Both

nanoparticles start to be pushed by the growing ice front and to move in the opposite direction. Trajectories and mean square displacements (MSD) are plotted in figure A.V.14.

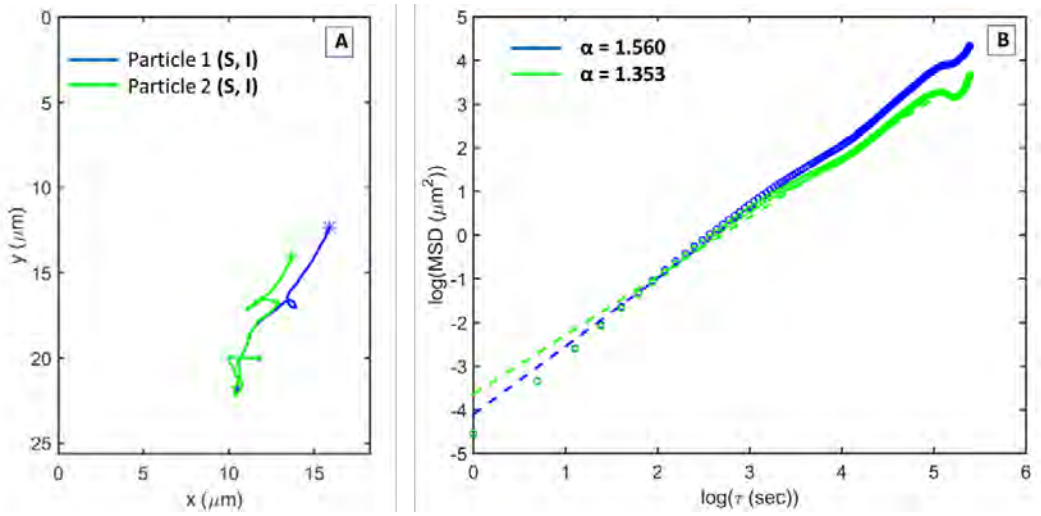

Figure A.V.14. A) Trajectories followed by two different single(S) nanoparticles on the ice(I) surface. **B)** Log-log plots of mean square displacements as a function of lag time τ.

Movie 95:

The conditions in which this movie have been recorded are the following: a temperature of -10°C and a pressure of 260Pa. Two single nanoparticles appear in this video.

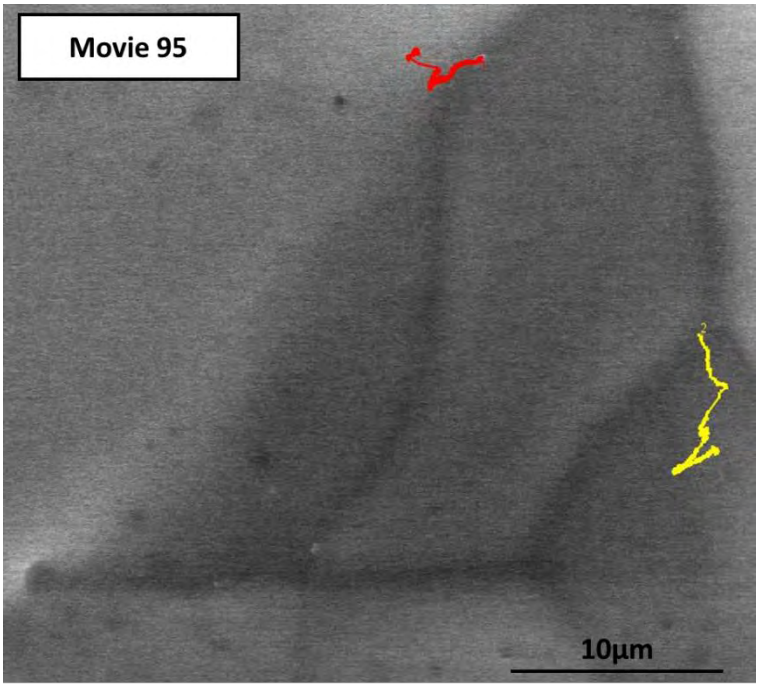

Figure A.V.15. Snapshot of the tracking video showing movement of two independent nanoparticles.

In the next figure (figure A.V.16) the trajectories and the mean square displacements (MSD) for the two nanoparticles are plotted. Both nanoparticles show similar alpha values, close to 1, meaning that in both cases the behavior is similar to a pure diffusive regime.

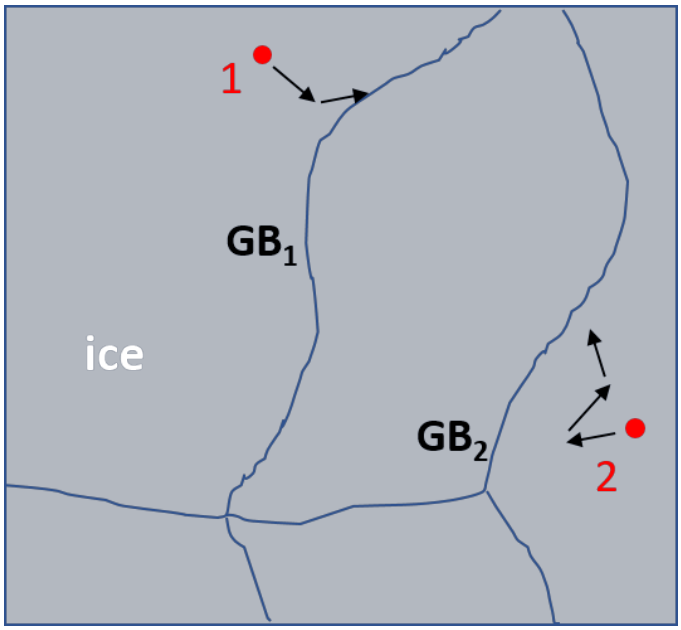

Figure A.V.16. Schematic representation of the movement of the nanoparticles on a polycrystalline ice surface. Each nanoparticle follows a different direction in their movement

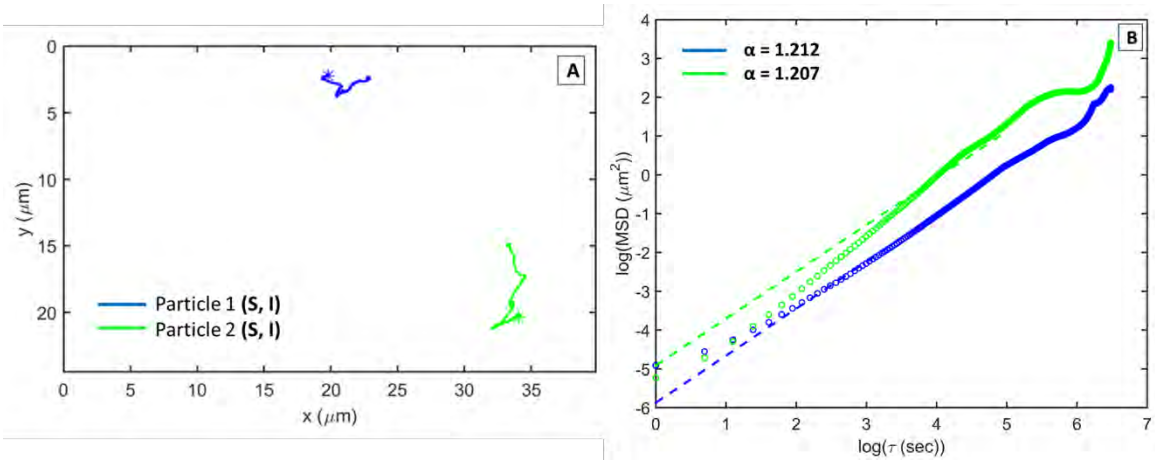

Figure A.V.17. A) Trajectories followed by two different single(S) nanoparticles on the ice(I) surface. **B)** Log-log plots of mean square displacements as a function of lag time τ.

Movie 305:

The conditions in which this movie have been recorded are the following: a temperature of -15.1°C and a pressure of 192Pa.

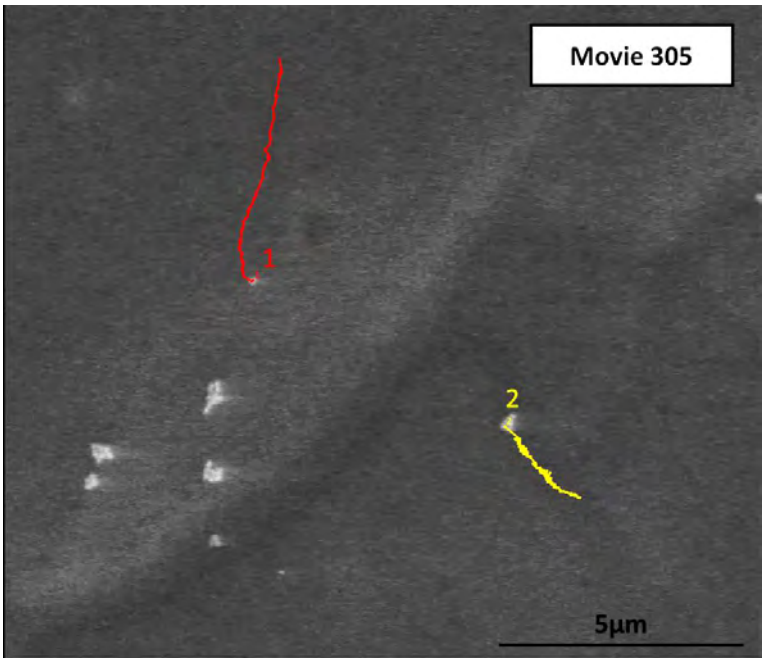

Figure A.V.18. Snapshot of the tracking video showing movement of two independent nanoparticles.

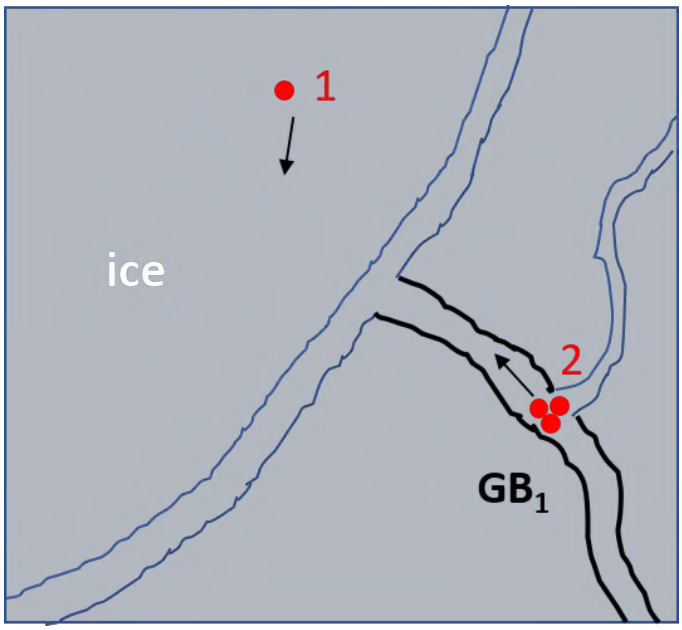

Figure A.V.19. Schematic representation of the movement of the nanoparticles on a polycrystalline ice surface. Each nanoparticle follows a different direction in their movement

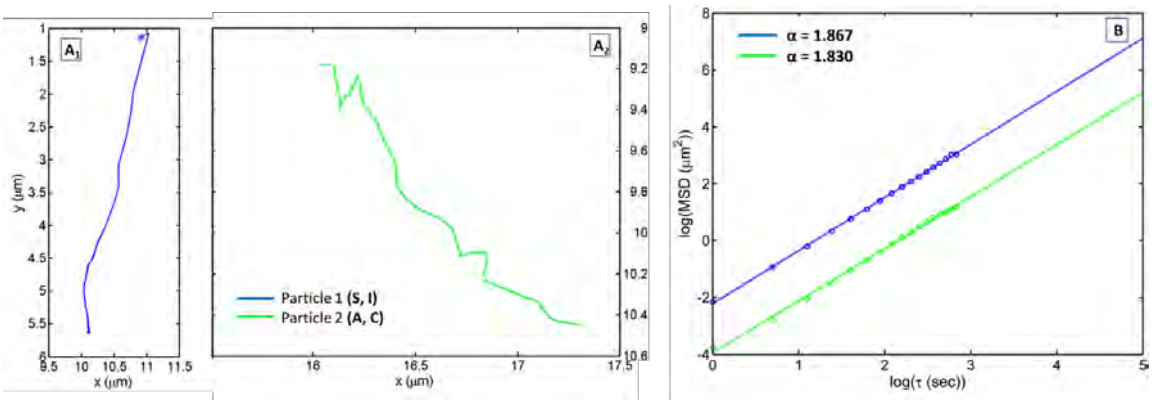

Figure A.V.20. A_1) Trajectory followed by one single(S) nanoparticle on the ice(I) surface. **A_2)** Trajectory followed by one cluster of five agglomerated(A) nanoparticles along a channel(C). **B)** Log-log plots of mean square displacements as a function of lag time τ.

More examples are shown below:

Movie 408:

The conditions in which this movie have been recorded are the following: a temperature of -12.1°C and a pressure of 250 Pa.

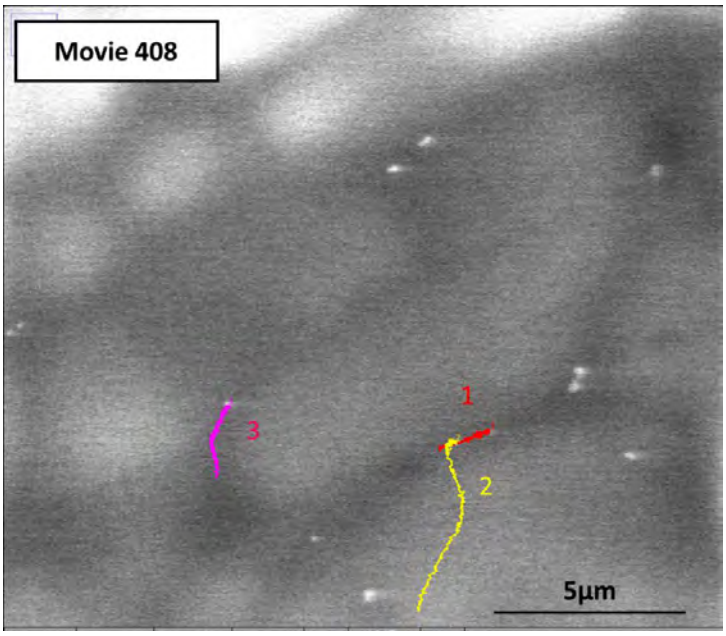

Figure A.V.21. Snapshot of the tracking video showing movement of three independent nanoparticles.

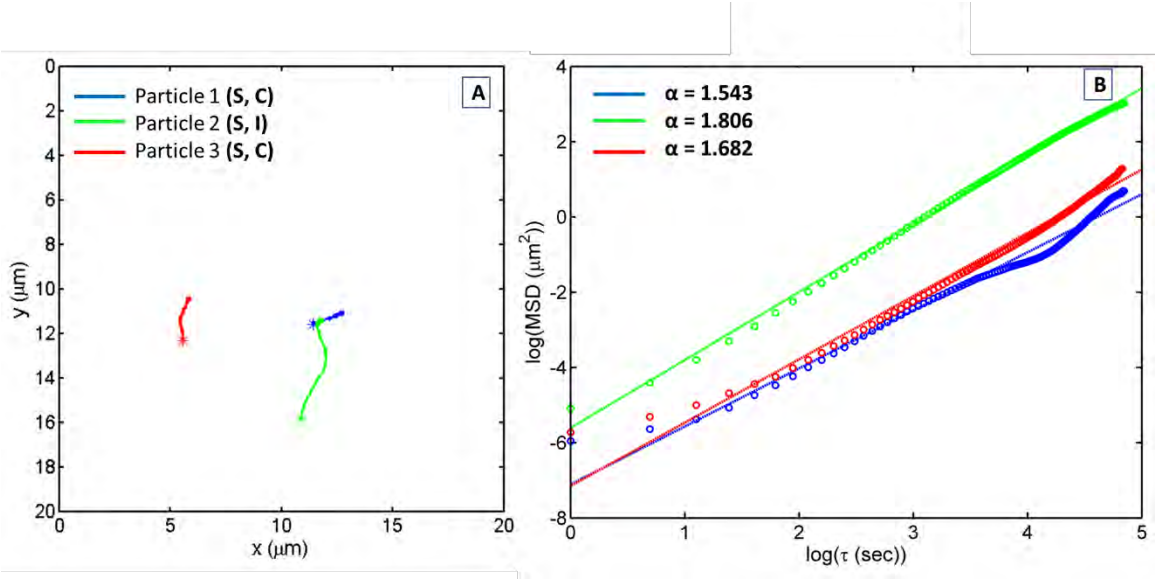

Figure A.V.12. A) Trajectories followed by three different single(S) nanoparticles: two of them along a channel(C) and the third one on the ice(I) surface. **B)** Log-log plots of mean square displacements as a function of lag time τ.

Movie 440:

The conditions in which this movie have been recorded are the following: a temperature of -14.5°C and a pressure of 209 Pa.

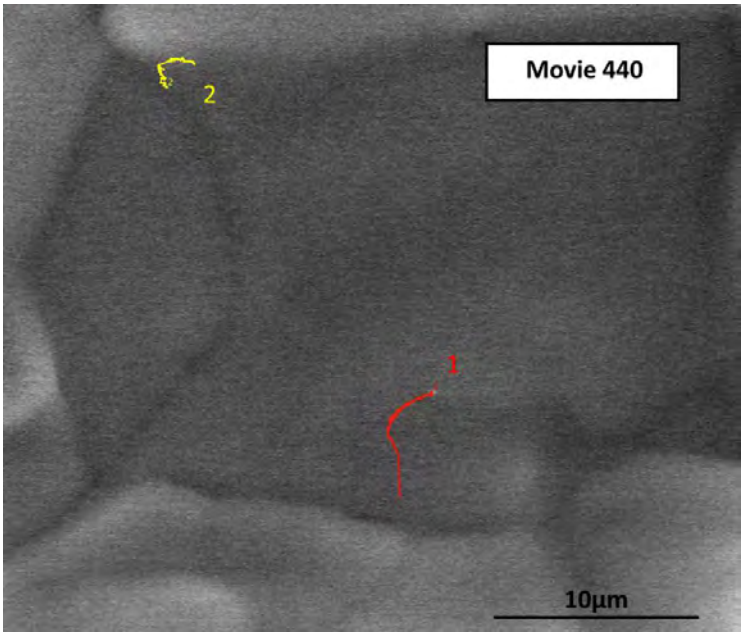

Figure A.V.13. Snapshot of the tracking video showing movement of two independent nanoparticles.

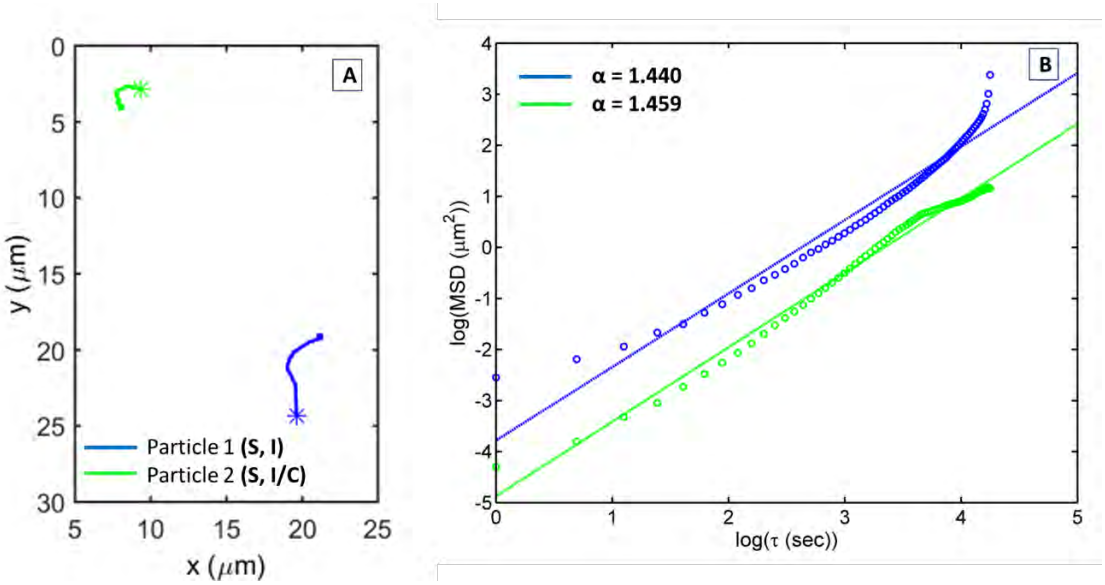

Figure A.V.14. A) Trajectories followed by two different single(S) nanoparticles. Particle 1 moves on the ice(I) surface, while particle 2 is moving on the ice during the first part of the movement and along a channel in the last part of its movement. **B)** Log-log plots of mean square displacements as a function of lag time τ.

Movie 452:

The conditions in which this movie have been recorded are the following: a temperature of -7.6 °C and a pressure of 343 Pa.

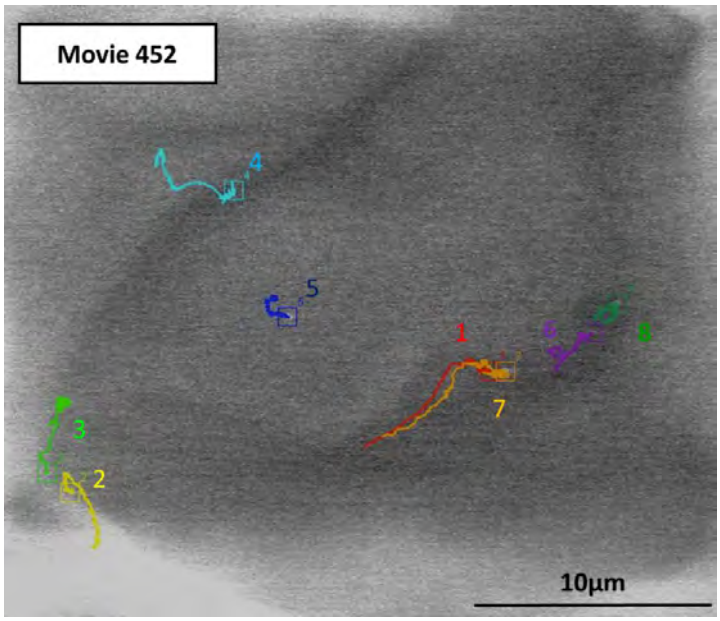

Figure A.V.15. Snapshot of the tracking video showing movement of eight independent nanoparticles.

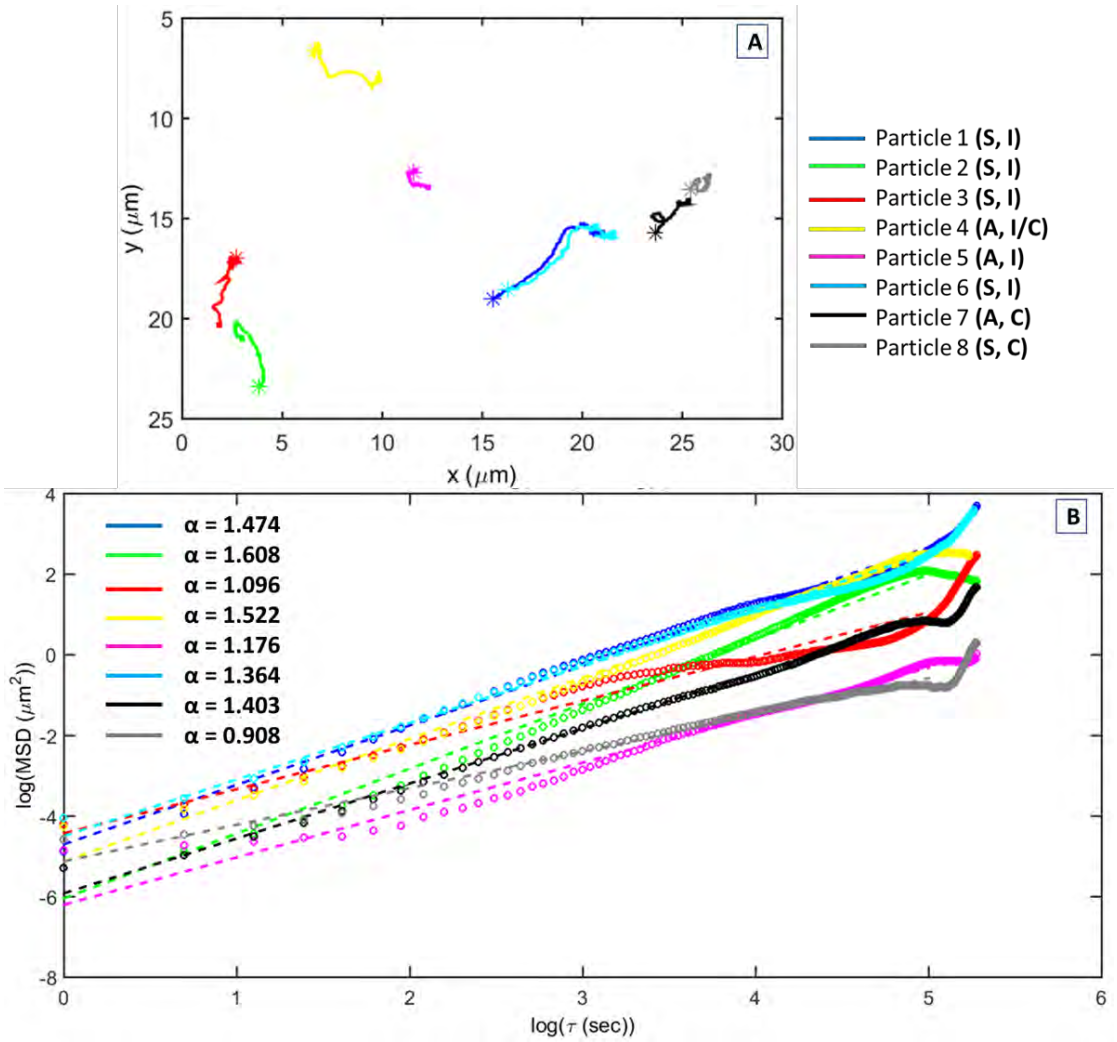

Figure A.V.16. A) Trajectories followed by five different single(S) nanoparticles on the ice(I) surface and three different clusters of aggregated(A) nanoparticles along channels(C) or grain boundaries present on the ice surface. Cluster of nanoparticle numbered as 4 is moving on the ice during the first part of the movement and along a channel in the last part of its movement. **B)** Log-log plots of mean square displacements as a function of lag time τ.

Movie 454:

The conditions in which this movie have been recorded are the following: a temperature of -10.6 °C and a pressure of 260 Pa.

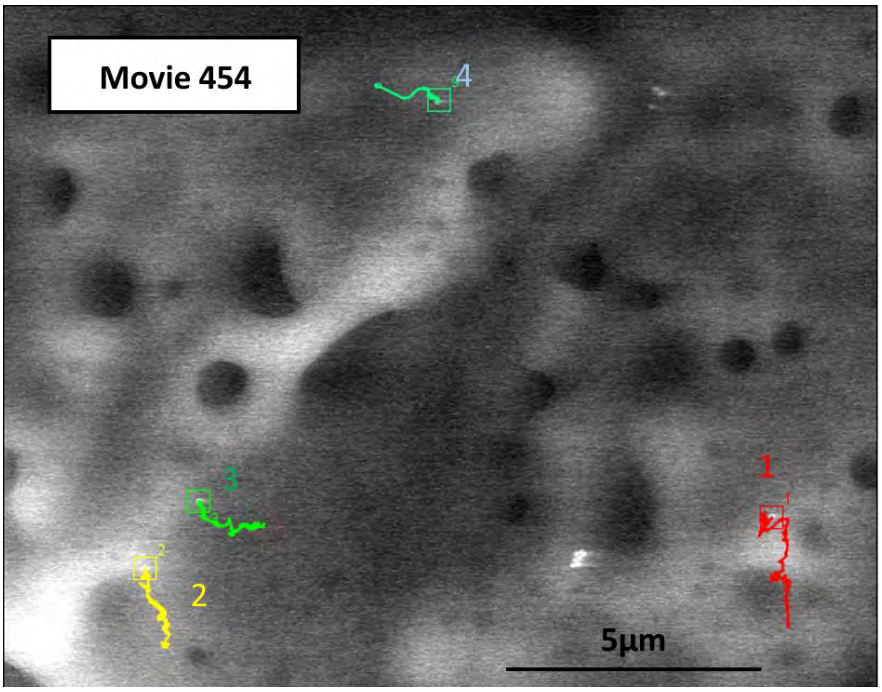

Figure A.V.17. Snapshot of the tracking video showing movement of four independent nanoparticles.

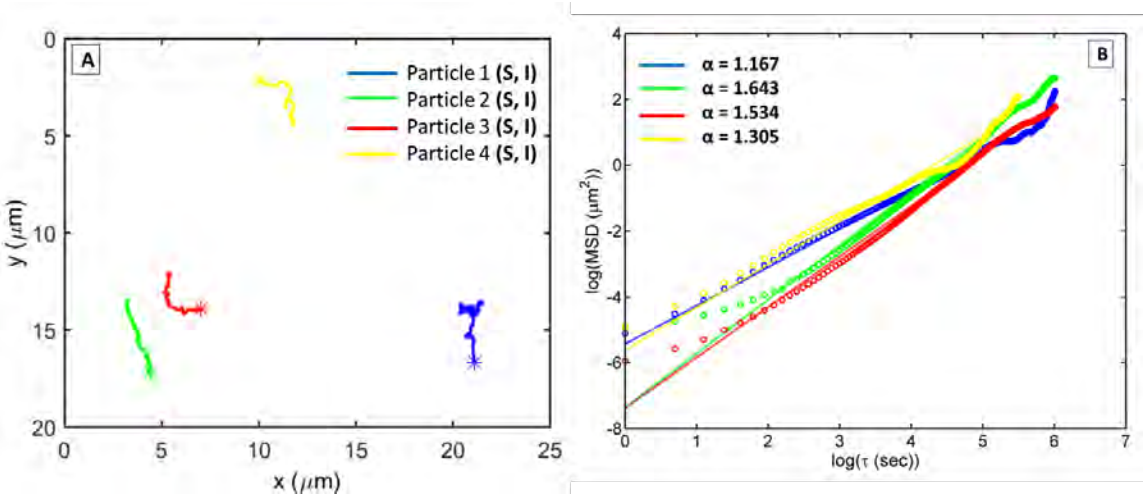

Figure A.V.18. A) Trajectories followed by four different single(S) nanoparticles on the ice(I) surface. **B)** Log-log plots of mean square displacements as a function of lag time τ.

Appendix VI

MATLAB codes for drop freezing image processing

The ***camera_pic*** MATLAB code allows to take pictures with the webcam. The freezing process can be monitored on the computer screen and is recorded and saved as a sequence of image files automatically. All recorded images include a time stamp.

```
    tic
while true
   while (toc<15)
      disp('Waiting...');
      pause(1.0);
   end
   tic
   refImg=snapshot(cam);
   pause(1.5);
   imshow(refImg);
   imageTitle=[datestr(now,'HH_MM_SS') '.jpg'];
   imwrite(refImg,imageTitle);
   fprintf('Image taken and saved, name:%s\n',imageTitle);
   pause(1.0);
   close
end
disp('Over')
return
```

The first step for evaluating the images is to manually identify wells in a reference image. The ***well_refmaker*** code created by Robert O. David (ETH Zürich) is used for this purpose. This function is used to produce a reference image (see figure A.VI.1.B). Wells location is stored relative to the reference image, which will be used to identify wells in other images.

```
function [wells,ref_img]=well_refmaker(input_imgname,savingname)
pic=rgb2gray(imread(input_imgname));
sPath='C:\Users\Maria\Desktop\Code v2';
disp('Please select the PCR tray periferie for reference');
figure
ref_img=imcrop(pic);
disp('Please select each individual well for reference (Note: double click once the box is complete
to move on to the next well)');
for iWell=1:96
   [~,wells{iWell}]=imcrop(ref_img);
```

```
end
cd(sPath)
wells=cell2mat(wells');
imwrite(ref_img,['webcam_PCR_',savingname,'.jpg']);
save(['webcam_wells_',savingname,'.mat'],'wells');
```

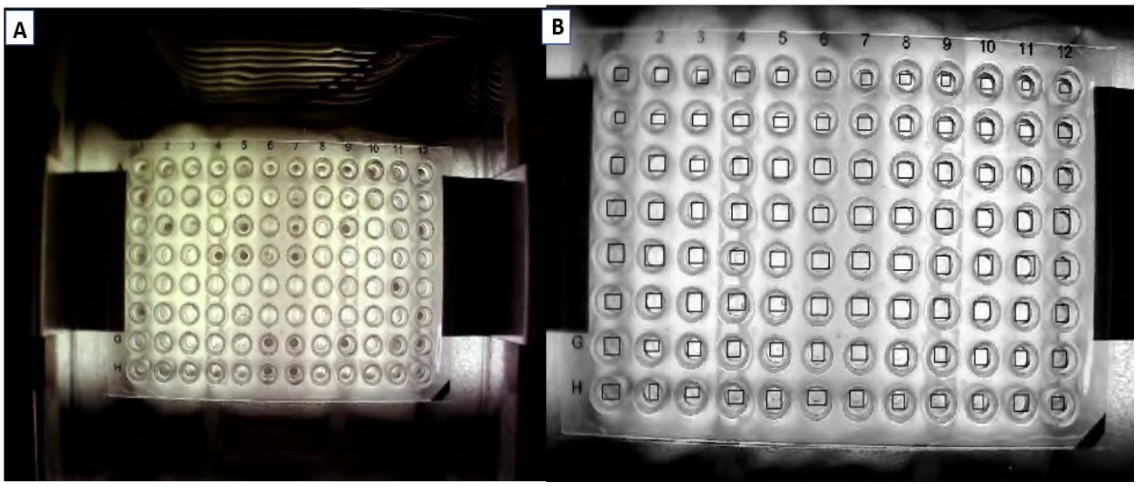

Figure A.VI.1 A) Raw image from the camera (Current image). **B)** Reference image with identified wells used to identify wells in other images

Once the reference image has been created, a new code ***well_locator*** is needed to identify the transformation required to match up the current tray location in a given image to a reference tray (see figure A.VI.1.B).

```
function
[loc_wells,outputView,tform]=well_locator(pcrimgname,reftrayname,well_location)
```

Input:

- *reftrayname:* "name of the reference tray of interest"
- *refwells:* "a MATLAB file with location and dimension of each well corresponding to the reference tray".
- *pcrimgname*: "name of the reference image for the freezing cycle of interest. This should be the first image of a freezing ramp".

Output:

- *wells*: "location of the wells that should be compared to the rest of the freezing cycle of interest".
- *outputView*: "view required to adjust all subsequent images in the freezing cycle to match the reference".
- *tform*: "transformation required for all subsequent images in the freezing cycle".

As a starting point, the code loads the reference tray and well location for comparison:

```
if nargin<=2
reftrayname='C:\Users\maria\Desktop\Code v2\webcam_PCR_ref_fixedsetup.jpg';
refimg=imread(reftrayname);
load('C:\Users\maria\Desktop\Code v2\webcam_wells_ref_fixedsetup.mat');
else
   refimg=imread(reftrayname);
   load(well_location)
end
```

Afterwards the script reads in the first image in the freezing ramp and begins the transformation:

```
pcrimg=rgb2gray(imread(pcrimgname));
ptsPCR  = detectSURFFeatures(pcrimg);
ptsRef = detectSURFFeatures(refimg);
[featuresPCR,   validPtsPCR]  = extractFeatures(pcrimg,  ptsPCR);
[featuresRef, validPtsRef]  = extractFeatures(refimg, ptsRef);
indexPairs = matchFeatures(featuresPCR, featuresRef);
matchedPCR  = validPtsPCR(indexPairs(:,1));
matchedRef = validPtsRef(indexPairs(:,2));
```

The number of points that match (see figure A.VI.2.A) and the points used for the transformation (see figure A.VI.2.B) are plotted:

```
figure;
showMatchedFeatures(pcrimg,refimg,matchedPCR,matchedRef);
title('Putatively matched points (including outliers)');
[tform, inlierRef, inlierPCR] = estimateGeometricTransform(...
   matchedRef, matchedPCR, 'similarity');
figure;
showMatchedFeatures(pcrimg,refimg, inlierPCR, inlierRef);
title('Matching points (inliers only)');
legend('ptsOriginal','ptsDistorted');
```

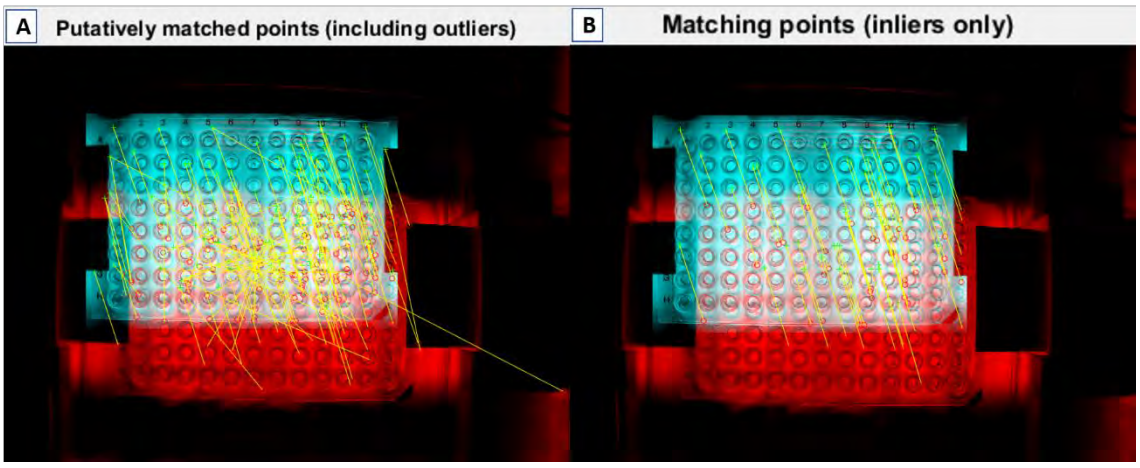

Figure A.VI.2. Transformation process to identify the current plate position.

The last part of the code assigns the inverse transform, finds the scale adjustment factor and the rotation offset, plots the comparison between the original and the recovered image and finds the well location for all subsequent images in the freezing cycle:

```
Tinv  = tform.invert.T;
ss = Tinv(2,1);
sc = Tinv(1,1);
scale_recovered = sqrt(ss*ss + sc*sc);
theta_recovered = atan2(ss,sc)*180/pi;
outputView = imref2d(size(pcrimg));
recovered  = imwarp(refimg,tform,'OutputView',outputView);
figure, imshowpair(pcrimg,recovered,'montage')
[loc_wells(:,1),loc_wells(:,2)]=transformPointsForward(tform,wells(:,1),wells(:,2));
loc_wells(:,3)=scale_recovered.*wells(:,3);
loc_wells(:,4)=scale_recovered.*wells(:,4);
```

Once the transformation is applied, the well location is identified based on the reference tray used for comparison. The well locations are saved and then passed to a subsequent code (*well_compare*) which applies the required transformation and then compares each well with itself to identify when it freezes.

The ***well_compare*** code created by Robert O. David (ETH Zurich) grabs the images in a folder and loops through to find when the wells are frozen. All wells must freeze for this code to work correctly, and the reference wells and the image must be set correctly in the *well_locator* MATLAB function.

```
function
[FF,T,Frz_T,Frz_Index,Frz_Rank,Frz_name,tdiff]=well_compare(foldernm,struct_name,
Ref_PCR_Tray_Path,Ref_wells_location_Path)
```

Input

- *Foldernm*: “Folder name for analysis, must be a string.”
- *struct_name*: “Saving name of the structure one wants the data to be saved as.”
- *Ref_PCR_Tray_Path*: “name of the reference PCR tray, the path must be included.”
- *Ref_wells_location_Path:* “name of the reference wells that correspond to the reference tray, the path must be included.”

Output

- *FF*: “Frozen Fraction at each image time. Output is the number frozen referring to each image in the folder.”

- *T*: “Temperature when the image is taken (corresponds to *FF*)”
- *Frz_T*: “Temperature at which each well froze”
- *Frz_Index:* “The picture number in the folder when each well froze”
- *Frz_name:* “The picture name when each well froze. This corresponds to the time the picture was taken”
- *tdiff :* “The difference between the set and bath temperature in the chiller”

First, the code defines thresholds for processing and identifying the freezing time and then starts looping through images in the folder:

```
peak_thresh=0.6;

if strcmp(pwd,['C:\Users\maria\Desktop\Code v2\',foldernm])==0
   cd(['C:\Users\maria\Desktop\Code v2\',foldernm])
end

pcrnm=ls('*.jpg');
wells=nan(length(pcrnm),96);
for i=1:length(pcrnm)
   if i==1
      if nargin<=3
         [wells_loc]=well_locator(pcrnm(i,:));
         figure
         imshow(rgb2gray(imread(pcrnm(i,:))))
         hold on
         for p=1:length(wells_loc)
            rectangle('position',wells_loc(p,:))
         end
      else
         [wells_loc]=well_locator(pcrnm(i,:),Ref_PCR_Tray_Path,Ref_wells_location_Path);
         figure
         imshow(rgb2gray(imread(pcrnm(i,:))))
         hold on
         for p=1:length(wells_loc)
            rectangle('position',wells_loc(p,:))
         end
      end
   end

   pcrimg=rgb2gray(imread(pcrnm(i,:)));
   for j=1:96
      wells(i,j)=mean(mean(imcrop(pcrimg,wells_loc(j,:))));
   end
   disp(i)
end
```

Afterwards, the code plots the well changes for selection (see figure A.VI.3):

```
figure
for iFrz=1:96
   subplot(8,12,iFrz)
   plot(abs(diff((medfilt1(wells(:,iFrz))-
mean(wells(:,iFrz)))./std(wells(:,iFrz)))))./max(abs(diff((medfilt1(wells(:,iFrz))-
mean(wells(:,iFrz)))./std(wells(:,iFrz))))),'linewidth',2);
   xlim([1 length(pcrnm)])
   grid on
end
```

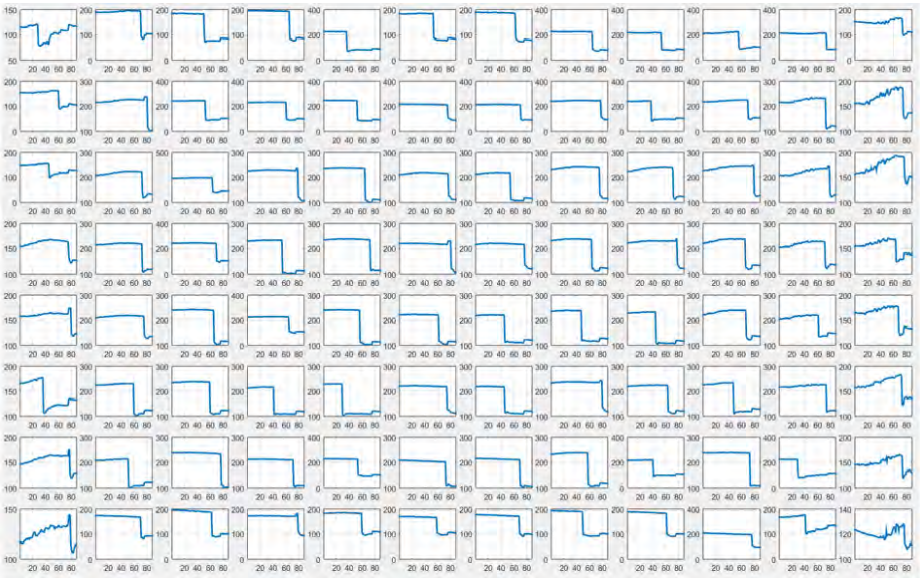

Figure A.VI.3. The graph shows the pixel value versus the picture number for each well.

Looking closer at figure A.VI.4, it is easily seen that while one can detect a clear signal at the centre of the tray (see figure A.VI.4.B), noisy signal appears at tray edges (see figure A.VI.4.A)):

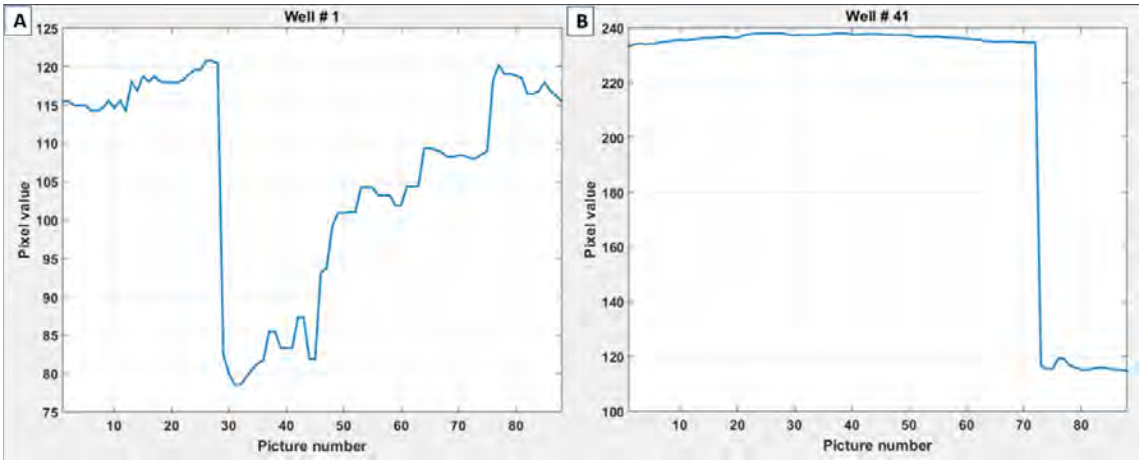

Figure A.I.4. A) Pixel value versus the picture number for well number 1. An example of aoisy signal. **B)** Pixel value versus the picture number for well number 1. An example of alear signal.

To resolve this issue, the code normalizes the well change and looks for the first change where the value is at least 50% (or the value assigned to the *peak_thresh* variable) of the maximum change of the well:

```
Frz_Index=nan(1,96);
for iFrz=1:96
      Frz_Index(1,iFrz)=find(abs(diff((medfilt1(wells(:,iFrz))-
mean(wells(:,iFrz)))./std(wells(:,iFrz)))))./max(abs(diff((medfilt1(wells(:,iFrz))-
mean(wells(:,iFrz)))./std(wells(:,iFrz)))))>=peak_thresh,1,'first')+1;
end

[~,Frz_Rank]=sort(Frz_Index);
Frz_name=pcrnm(Frz_Index,:);
Frz_time=Frz_name(:,1:end-4);
Scan_time=pcrnm(:,1:end-4);
```

This process could be summarized in three steps:

1º) Standardize the well signal (Z-Score): $Z_i = \frac{x_i - \mu}{\sigma}$

2º) Take the absolute value of the time derivative of the Z-Score: $Z_i' = \left|\frac{dZ_i}{dt}\right|$

3º) Normalize by the maximum derivative of the Z-Score: $\widetilde{Z_i'} = \frac{Z_i'}{max\, Z_i'}$

The well signal now is given by the normalized Z-Score value and as one can visualize in figure A.VI.5., there is a clear freezing signal in all of the wells.

Figure A.VI.5. The graph shows the normalized Z-Score value versus the picture number for each well.

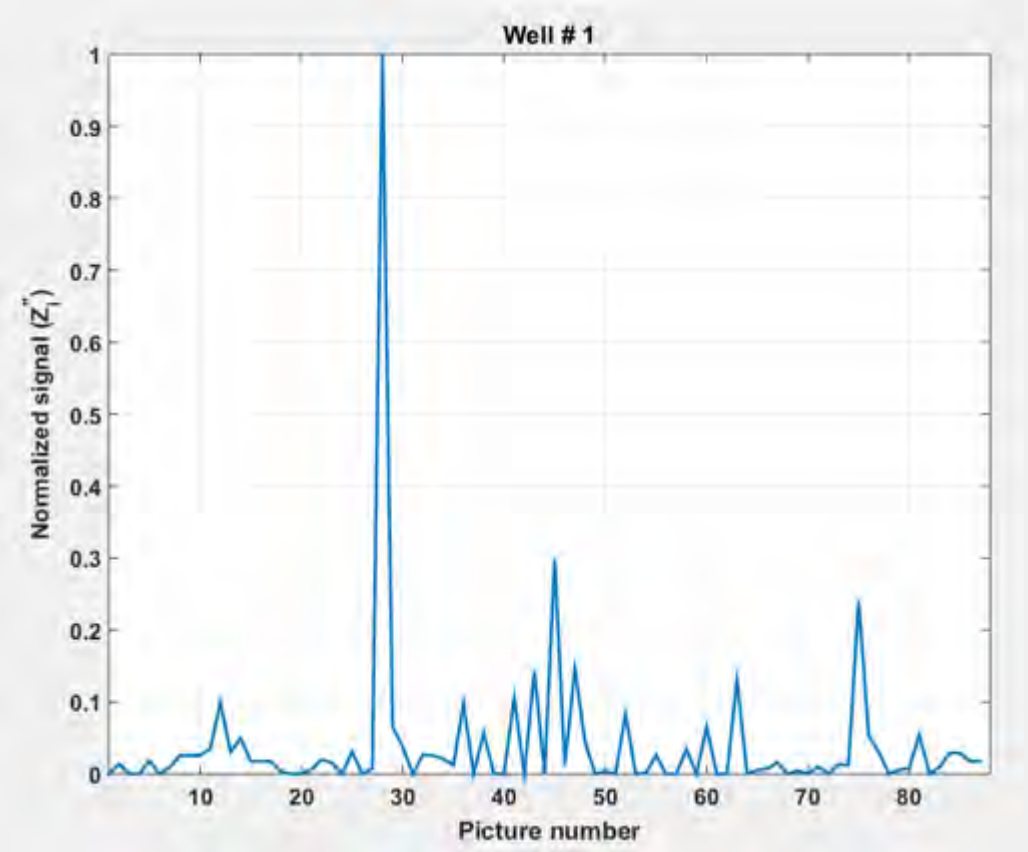

Figure A.VI.6. Normalized signal value versus the picture number for well 1.
A huge peak can be distinguished showing the sudden and sharp change in recorded light intensity, associated with ice nucleation and freezing.

The last part of the code enables me to calculate the frozen fraction (FF) for each time step and save it in a MATLAB structure.

```
FF=zeros(size(wells,1),1);
for iFF=1:size(wells,1)
   if iFF==1
      FF(iFF)=sum(Frz_Index==iFF);
   else
      FF(iFF)=sum(Frz_Index==iFF)+FF(iFF-1);
   end
end
 tname=ls('*.txt');
if isempty(tname)
   disp('No Temperature data available')
   T=NaN;
   Frz_T=NaN;
else
   [tstmp,rdata,tdata]=well_temp_load2(tname);
   tdiff=nan(length(tdata), 1);
   for k=1:length(tdata)
      if tdata(k)==0
         tdata(k)=rdata(k);
```

```
        else
            tdiff(k)=rdata(k)-tdata(k);
            continue
        end
    end

    Scan_date=datetime(Scan_time(:,:),'Inputformat','HH_mm_ss');
    Frz_date=datetime(Frz_time(:,:),'Inputformat','HH_mm_ss');

    for dt=1:length(Frz_date)
        [Frz_t_uncert(1,dt),Frz_T_index(1,dt)]=min(abs(tstmp-Frz_date(dt)));
    end

    for dt2=1:length(pcrnm)
        [t_uncert(1,dt2),T_index(1,dt2)]=min(abs(tstmp-Scan_date(dt2)));
    end

    T=tdata(T_index);
    Frz_T=tdata(Frz_T_index);
end

if nargin>=2
    data.FF=FF;
    data.T=T;
    data.Frz_T=Frz_T;
    data.Frz_Index=Frz_Index;
    data.Frz_Rank=Frz_Rank;
    assignVar(struct_name,data)
    save(struct_name,struct_name)
end
```

Appendix VII

Frozen fraction plots of tested proteins and viruses

Droplet freezing temperatures and frozen fraction data are useful for comparing ice nucleation abilities of different materials. Several example data sets are presented here to demonstrate the efficiency and appropriateness of the experimental setup used in my experiments. The freezing temperatures for droplets containing Tobacco Mosaic Virus (TMV), ice-binding protein (IBP), hydrophobins (HPA*, HPB*), albumin from bovine serum (BSA), ovalbumin and casein have been measured. For some of these materials, two different concentrations have been tested, and as expected the droplets containing more material froze at a higher temperature, except for the ice-binding protein, which exhibits opposite behavior.

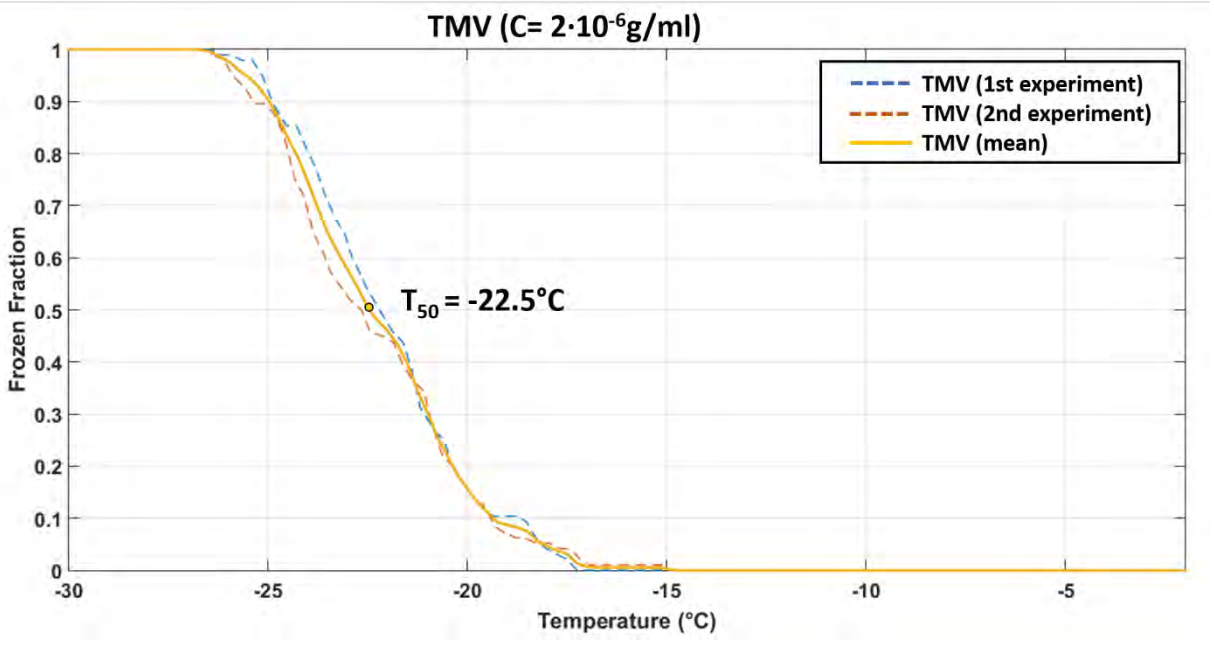

Figure A.VII.1. Frozen fraction as function of temperature for the TMV solution tested. T_{50} value is shown, which stands for the temperature at which 50% of all droplets froze (median freezing temperature).

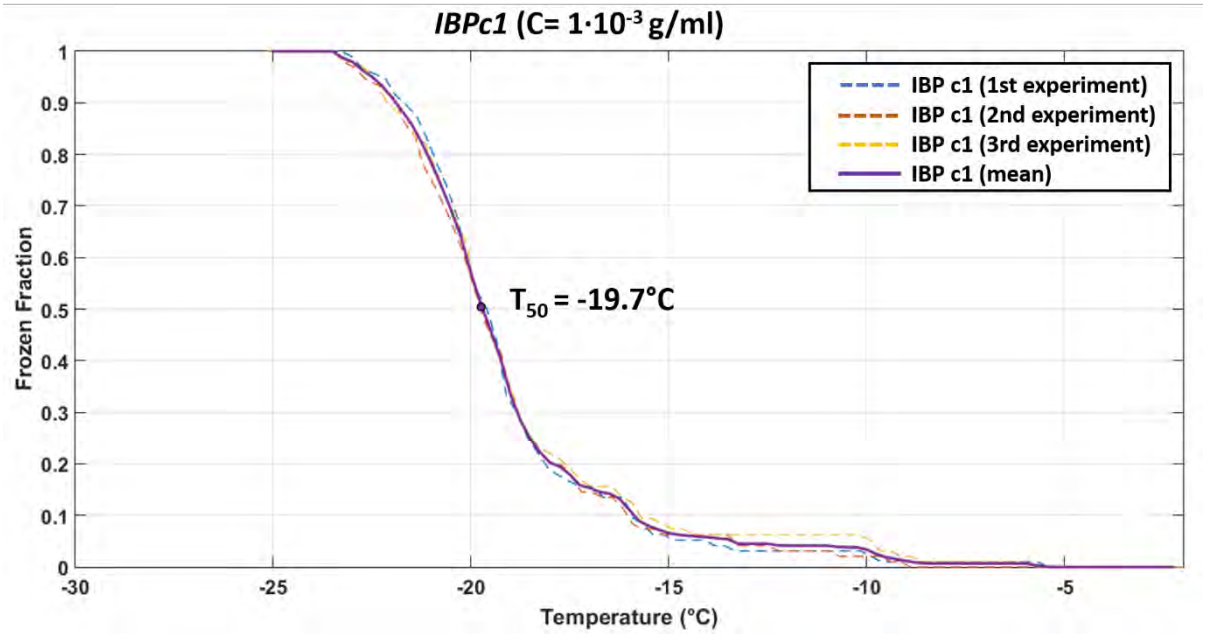

Figure A.VII.2. Frozen fraction as function of temperature for low concentration IBP solution. T_{50} value is shown, which stands for the temperature at which 50% of all droplets froze (median freezing temperature)

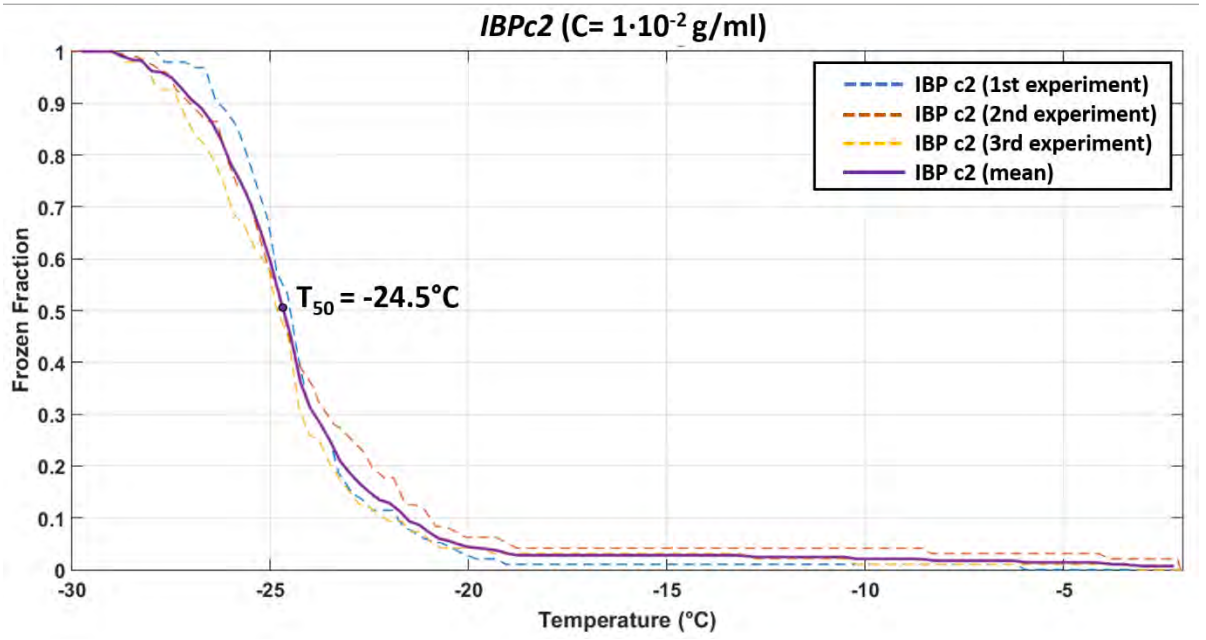

Figure A.VII.3. Frozen fraction as function of temperature for high concentration IBP solution. T_{50} value is shown, which stands for the temperature at which 50% of all droplets froze (median freezing temperature)

Appendix VII

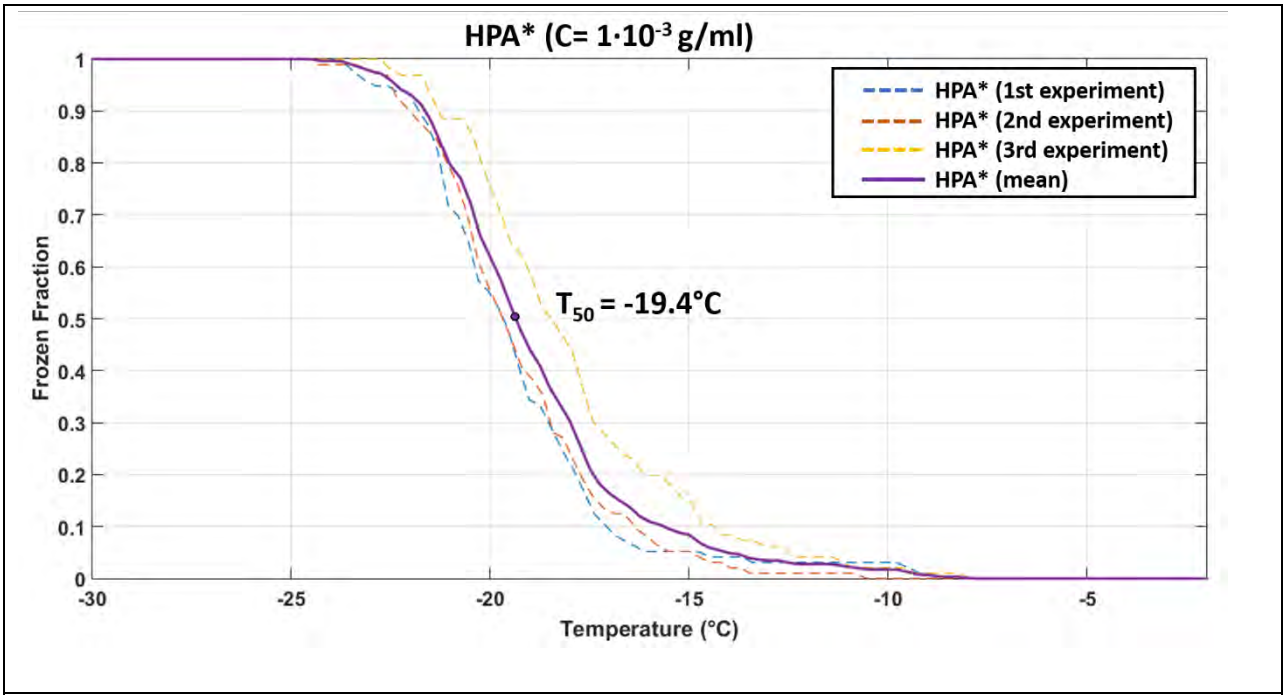

Figure A.VII.4. Frozen fraction as function of temperature for the HPA* solution tested. T_{50} value is shown, which stands for the temperature at which 50% of all droplets froze (median freezing temperature)

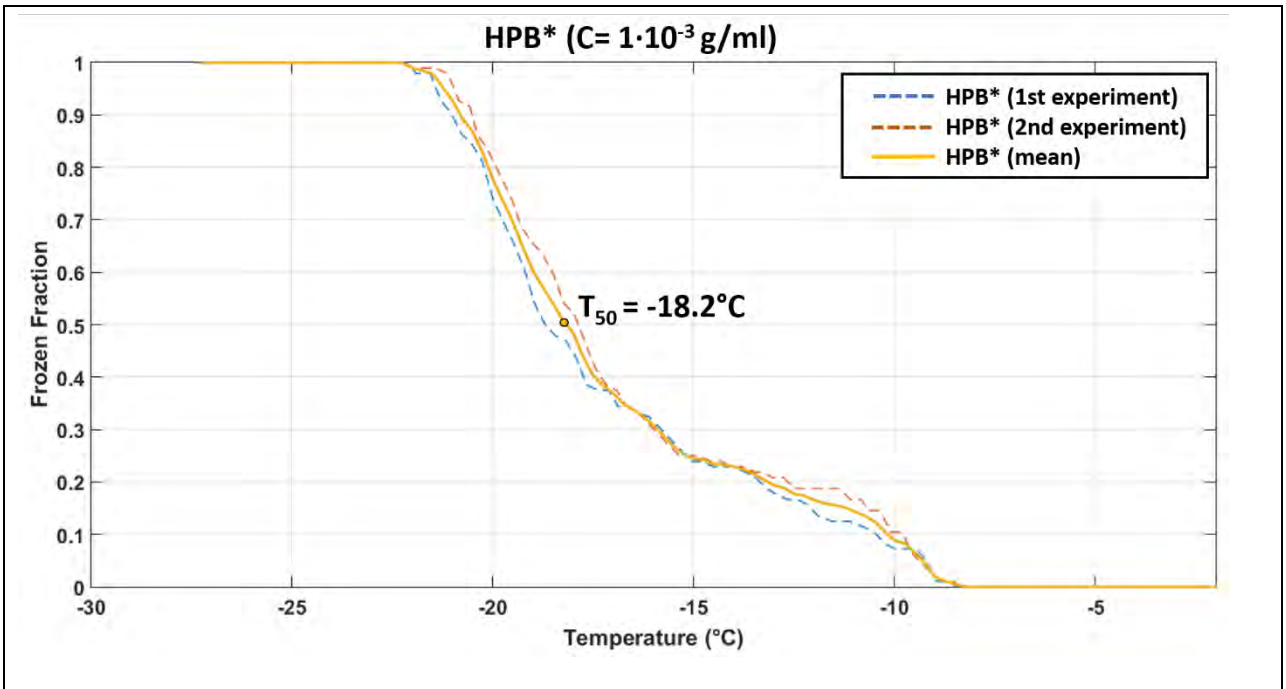

Figure A.VII.5. Frozen fraction as function of temperature for the HPB* solution tested. T_{50} value is shown, which stands for the temperature at which 50% of all droplets froze (median freezing temperature)

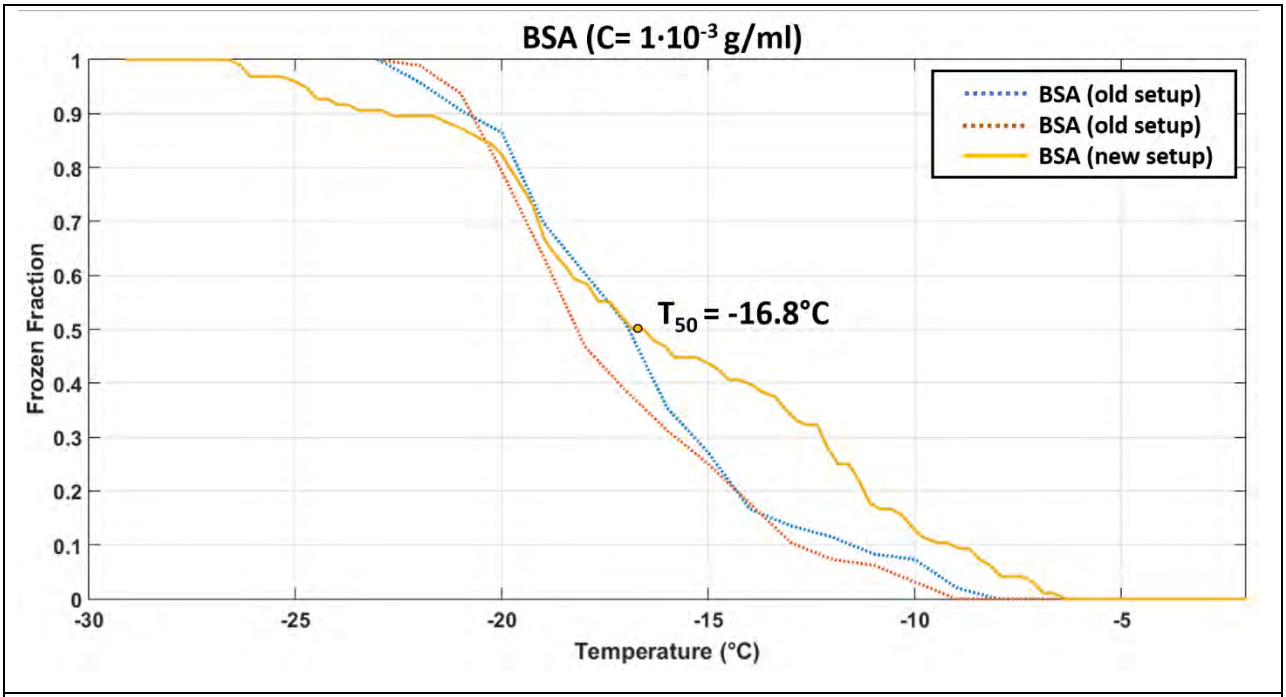

Figure A.VII.6. Frozen fraction as function of temperature for the BSA solution tested. T_{50} value is shown, which stands for the temperature at which 50% of all droplets froze (median freezing temperature)

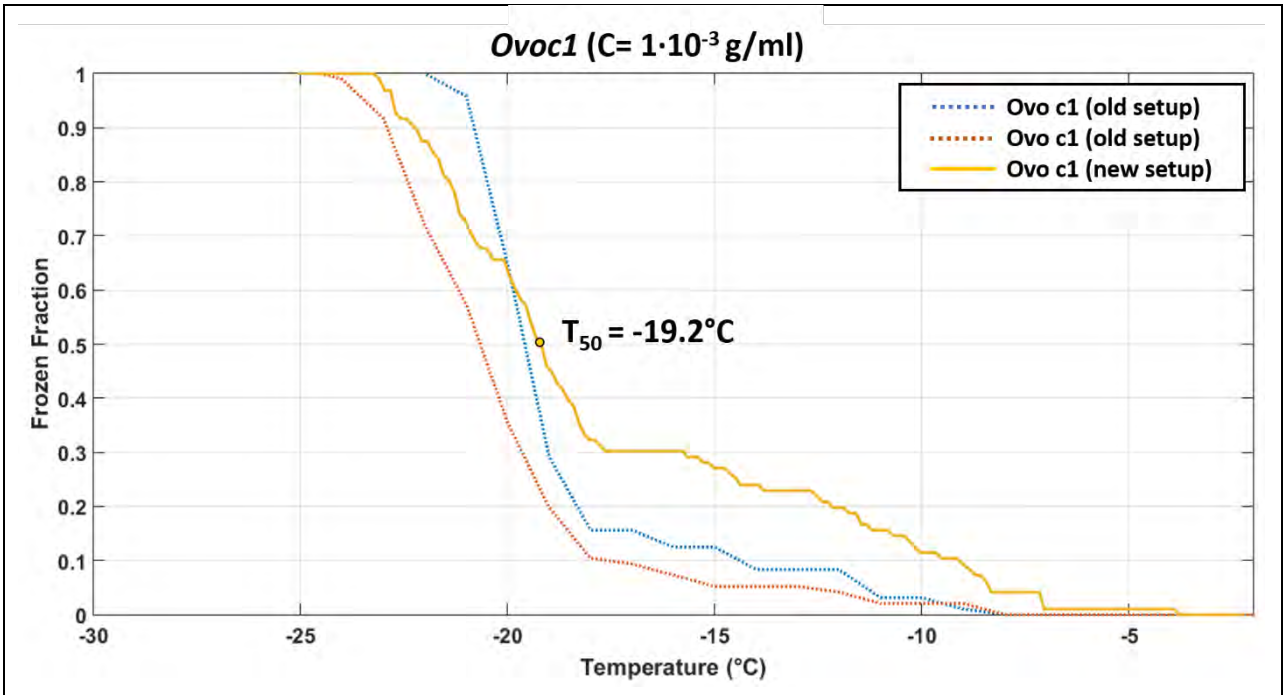

Figure A.VII.7. Frozen fraction as function of temperature for low concentration ovalbumin solution. T_{50} value is shown, which stands for the temperature at which 50% of all droplets froze (median freezing temperature)

Appendix VII

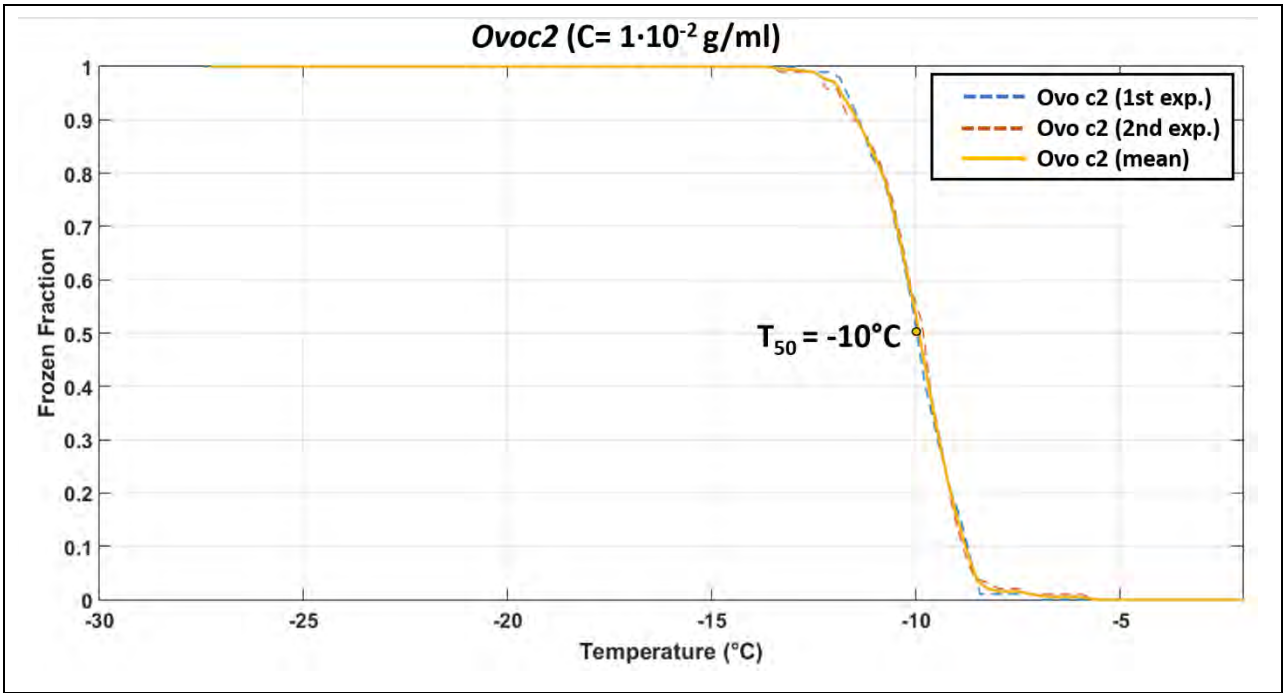

Figure A.VII.8. Frozen fraction as function of temperature for high concentration ovalbumin solution. T_{50} value is shown, which stands for the temperature at which 50% of all droplets froze (median freezing temperature)

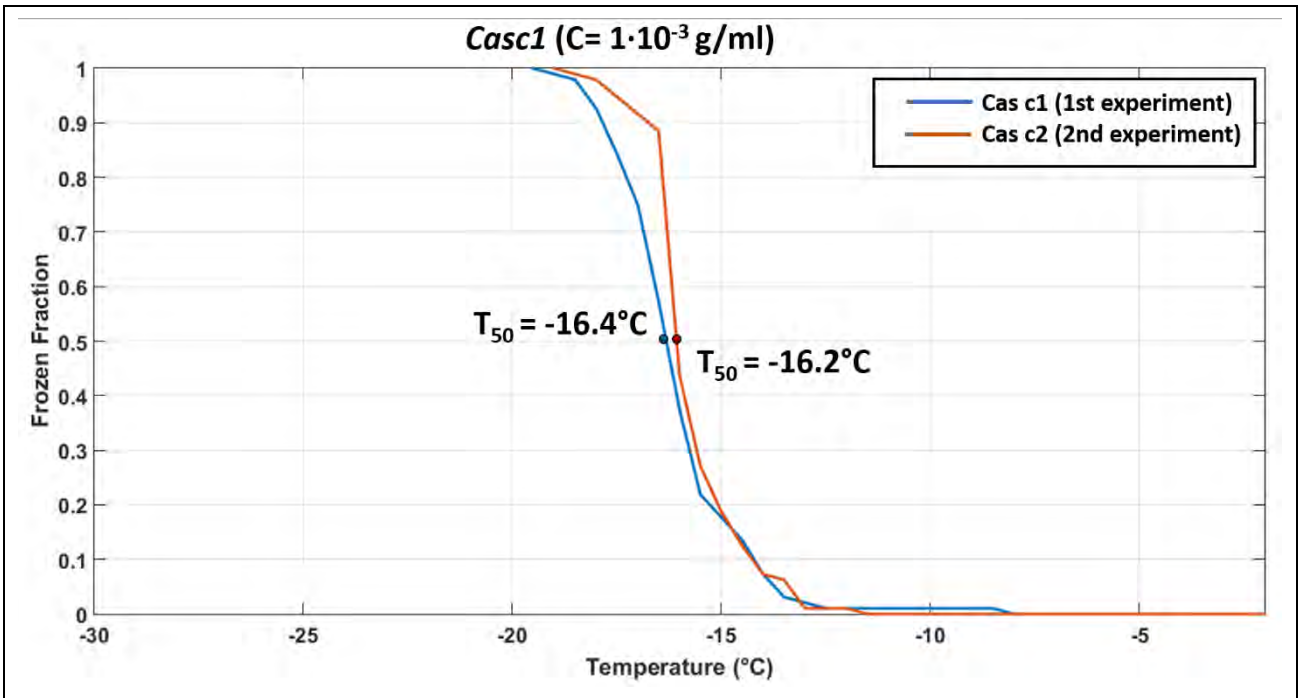

Figure A.VII.9. Frozen fraction as function of temperature for low concentration casein solution. T_{50} value is shown, which stands for the temperature at which 50% of all droplets froze (median freezing temperature)

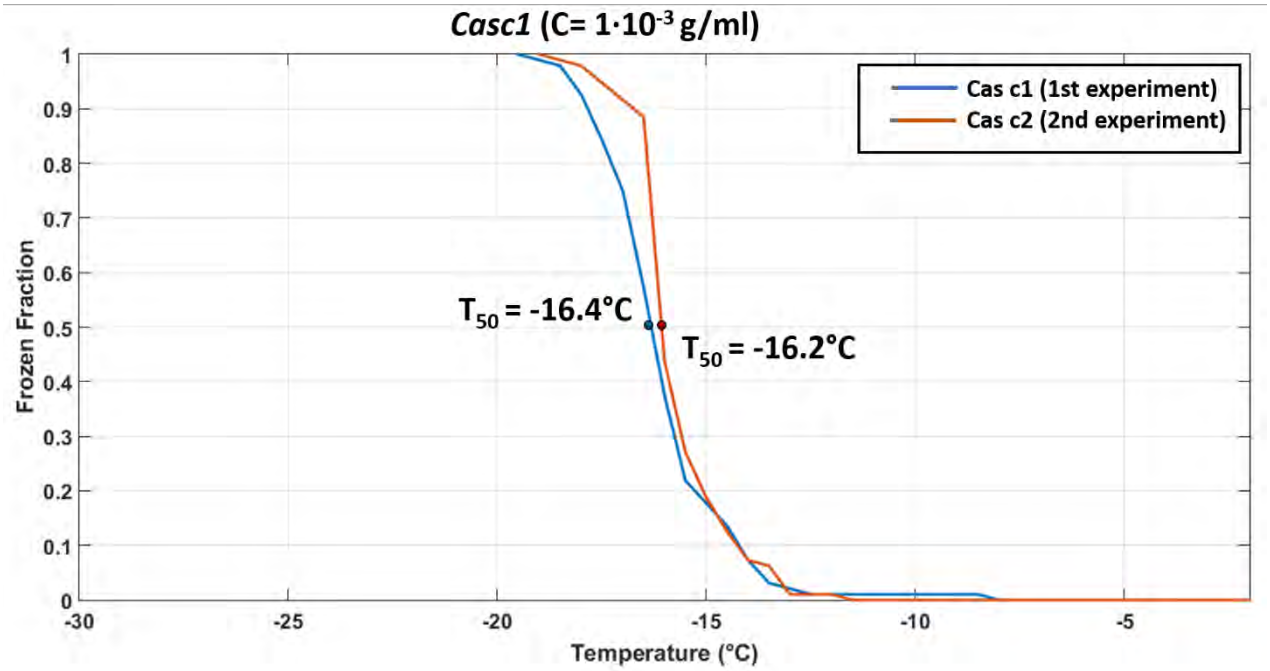

Figure A.VII.10. Frozen fraction as function of temperature for low concentration casein solution. T_{50} value is shown, which stands for the temperature at which 50% of all droplets froze (median freezing temperature)

Appendix VIII

Apoferritin and ferritin sample solutions appearance

Different apoferritin and ferritin solutions have been prepared for the different experiments that have been performed. In the following pictures one can detect physical characteristics of the different prepared solutions, like colour, turbidity…

pH variations

Different pH buffers and sample solutions were prepared to carry out the pH variation studies and the pH was measured with a pH-meter (691 pH Meter, Metrohm, Swiss) as it is shown in figure A.VIII.1.

Figure A.VIII.1. pH measurement of ferritin solution with a pH-meter.

In figure A.VIII.2 apoferritin solutions at different pH are shown. No appreciable difference can be observed between all of them since apoferritin solutions are transparent. However, it is interesting to note that at pH = 3.5 (marked with a red rectangle in figure A.VIII.2) and after an incubation time, the solution loses transparency and becomes hazy.

For ferritin solutions (see figure A.VIII.3), slight differences in colour can be detected depending on pH value and the most remarkable fact is that the same effect described for

the apoferritin solution happens to the ferritin solution at pH = 3.5 (marked with a red rectangle in figure A.VIII.3), which appears clouded compared to the other pH solutions.

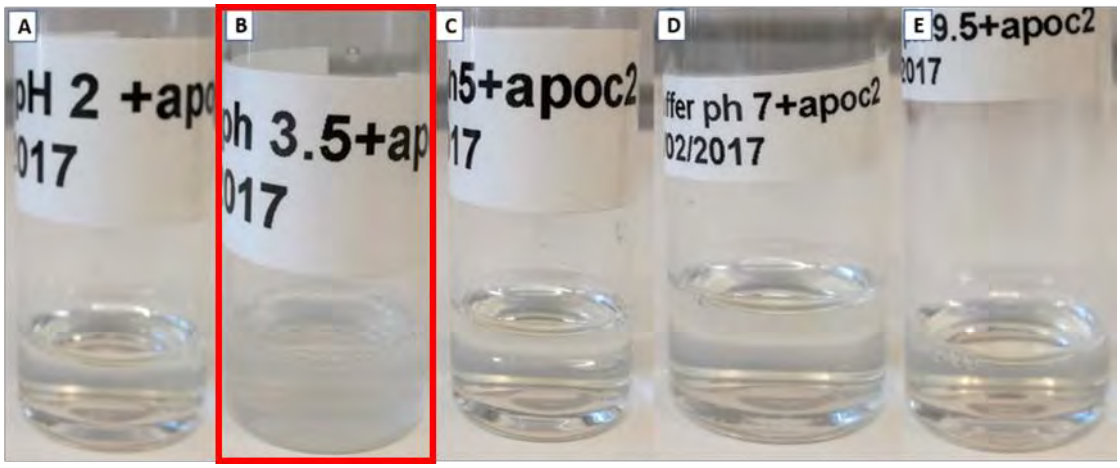

Figure A.VIII.2. Different pH high concentrated (*Apoc2*) apoferritin solutions.

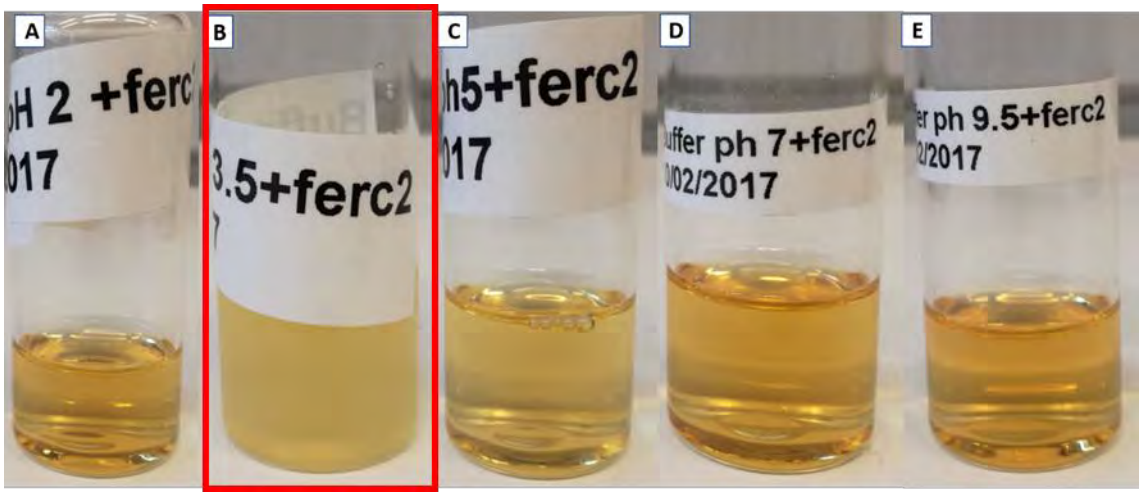

Figure A.VIII.3. Different pH high concentrated (*Ferc2*) ferritin solutions.

Apoferritin and ferritin at pH 0 suspensions were submitted to different heat treatments to reduce the presence of large aggregates suspended in the solutions. In figure A.VIII.4.A it is shown how a high concentrated (*Apoc2*) apoferritin solution becomes turbid after having been heated in the oven during three hours at 70 °C. Some of the large agreggates get dissolved but others appear sedimented at the bottom of the bottle. Further heat treatment was applied: apoferritin and ferritin solutions were heated during 5 hours at 110 °C. In figure A.VIII.4.B and A.VIII.4.C it can be appreciated how after the stronger heat

treatment aggregates dissapear completely and solutions become clearer. A noticiable effect of this heat treatment is that the ferritin solution lost its characteristic orange color completely (see figure A.VIII.4.C).

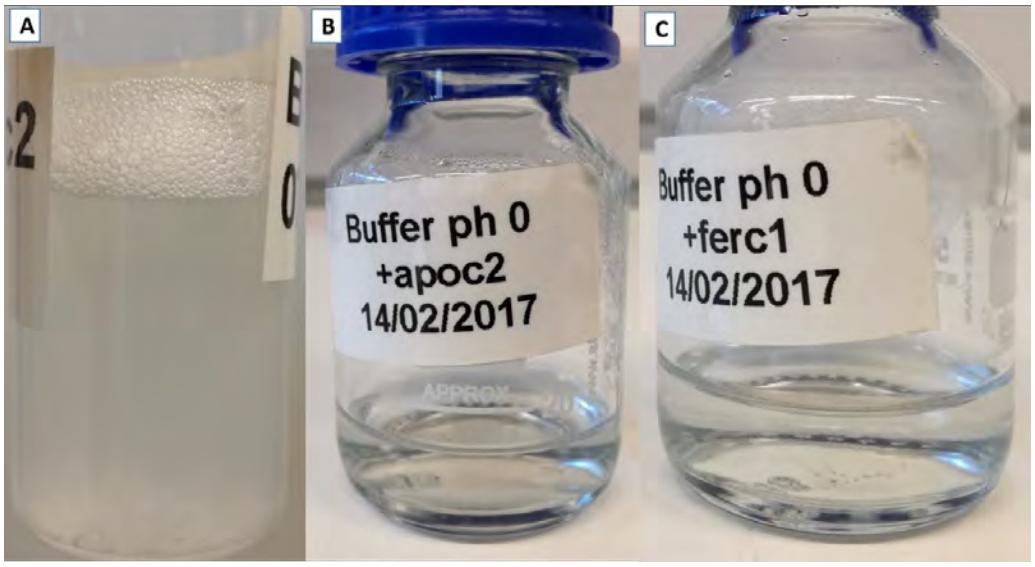

Figure A.VIII.4. A) High concentrated apoferritin (*Apoc2*) solution after having been heated during 3 hours in the oven at 70 °C. **B)** High concentrated apoferritin (*Apoc2*) solution after having been heated it during 5 hours in the oven at 110 °C. **C)** Well diluted ferritin (*Ferc1*) solution after having been heated during 5 hours in the oven at 110 °C.

Heating experiments

The effect of the concentration in the appearance of the solution (see figure A.VIII.5) is clear for the ferritin, which shows a yellow-orange colour for the high concentrated solution (*Ferc2*), but only a slightly perceptible orange colour for the well diluted solution (*Ferc1*)

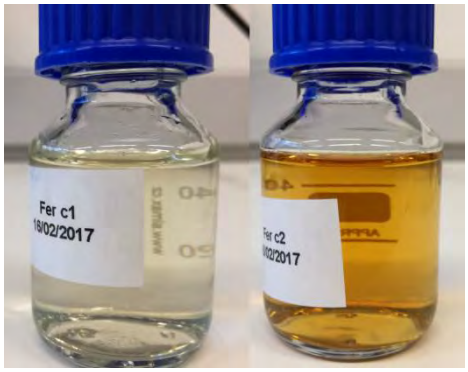

Figure A.VIII.5. Ferritin solutions before heating. The right image corresponds to the high concentrated solution (*Ferc2*), which shows a more intense colour than the well diluted solution (*Ferc1*), which corresponds to the left image.

The heated *Apoc1* solution (see figure A.VIII.6) remains as a see-through solution and a few precipitates appear at the bottom of the recipient.

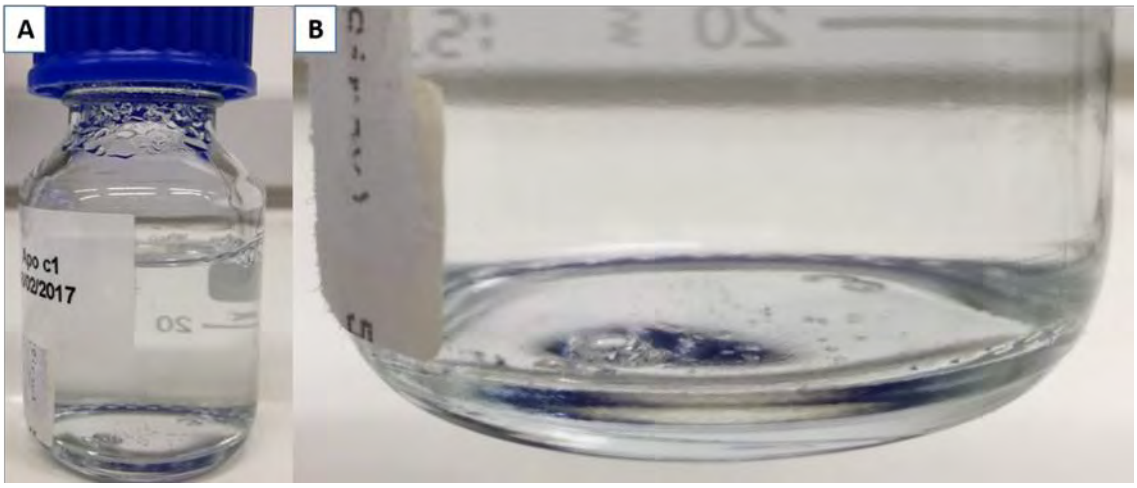

Figure A.VIII.6. A) Well diluted apoferritin (*Apoc1*) solution after having been heated during 5 hours at 110 °C. **B)** Detail of the precipitate at the bottom of the glass bottle.

However, the heated *Apoc2* solution (see figure A.VIII.7) exhibits a turbid appearance.

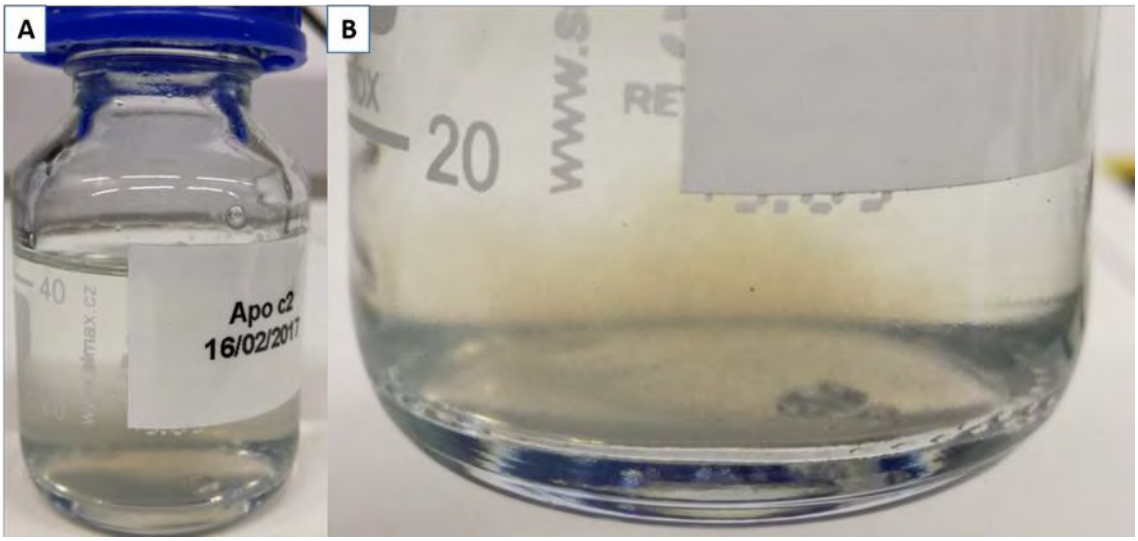

Figure A.VIII.7. A) High concentrated apoferritin (*Apoc2*) solution after having been heated during 5 hours at 110 °C. **B)** Detail of the bottom of the glass bottle, where the solution exhibits a turbid appearance.

The ferritin solutions also change its appearance after the heating treatment. Small aggregates were formed and deposited at the bottom of the recipient for the heated *Ferc1* solution (see figure A.VIII.8).

Appendix VIII

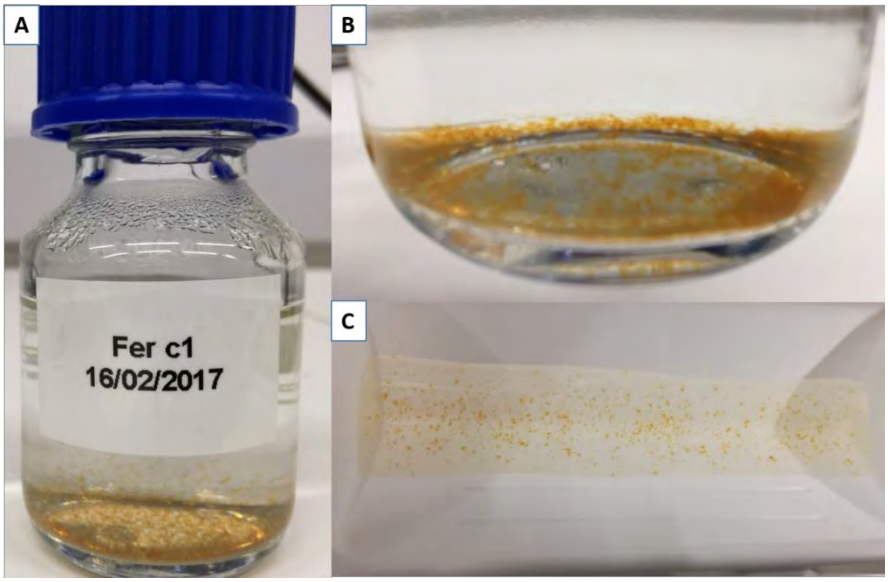

Figure A.VIII.8. A) Well diluted ferritin (*Ferc1*) solution after having been heated during 5 hours at 110 °C. **B)** Detail of the precipitate at the bottom of the glass bottle. **C)** *Fer c1* solution in the dispersion tray just before being pipetted.

Acronyms & Abbreviations

Symbol	Description
AFM	Atomic Force Microscopy
BSA	Bovine Serum Albumin
BSE	Back Scattered Electron
BSED	Back Scattered Electron Detector
CCN	Cloud Condensation Nuclei
CNT	Classical Nucleation Theory
CP	Coat protein
DSC	Differential Scanning Calorimetry
EDX	Energy Dispersive X-Ray
ESEM	Environmental Scanning Electron Microscope
ETD	Everhart-Thornley Detector
FEG	Field Emission Gun
GSED	Gaseous Secondary Electron Detector
HP	Hydrophobin
IBP	Ice binding protein
I_c	Cubic ice
I_h	Hexagonal ice
INA	Ice Nucleation Active
INP	Ice Nucleating Particle
LED	Light Emitting Diode
LFD	Large Field Detector
LV	Low Vacuum
MD	Molecular Dynamics
MSD	Mean Square Displacement
NEXAFS	Near Edge X-ray Absorption Fine Structure Spectroscopy
PBAP	Primary Biological Aerosol Particle
PCR	Polymerase Chain Reaction
PE	Primary Electron

PLA	Pressure-Limiting Aperture
PDB	Protein Data Bank
PLD	Polar Layered Deposit
PTFE	Teflon
PVC	Polyvinylchloride
QLL	Quasi-Liquid Layer
RNA	Ribonucleic acid
SAXS	Small-Angle X-ray Scattering
SE	Secondary Electron
SEM	Scanning Electron Microscope
SFG	Vibrational Sum Frequency Generation
SOA	Secondary Organic Aerosol
TEM	Transmission Electron Microscope
TMV	Tobacco Mosaic Virus
WD	Working Distance

Symbol	**Unit**	**Description**
T	K,°C	Temperature
T_f	K	Freezing temperature
T_0	K	Normal melting point
T_{50}	°C	Median freezing temperature
T_t	ºC	Water triple point temperature, 0.01 ºC
T_{melt}	ºC	Melting temperature
P	Pa	Pressure measured in the ESEM
P_{water}	Pa	Water vapor pressure
P_{ice}	Pa	Vapor pressure over ice
P_{water}^{sat}	Pa	Saturation vapor pressure over water
P_{ice}^{sat}	Pa	Saturation vapor pressure over ice
P_t	Pa	Water triple point pressure, 611.657 ± 0.01 Pa
h		Relative humidity with respect to water
s	J K^{-1} mol^{-1}	Molar entropy
R	J K^{-1} mol^{-1}	Molar gas constant, 8.31447 J K^{-1} mol^{-1}
L_{ice}	J kg^{-1}	Latent heat of ice sublimation

V	m^3	Volume
n_{solute}		Number of moles of solute
$n_{solvent}$		Number of moles of solvent
q	J mol^{-1}	Molar heat of fusion
D	m^2 s^{-1}	Diffusion coefficient
C	g/ml	Particle concentration
x	m	Position respect to axis X
y	m	Position respect to axis Y
t	s	Time
$< r^2 >$	m^2	Mean square displacement
f	kg s^{-1}	Friction coefficient
k_B	m^2 kg s^{-2} K^{-1}	Boltzmann constant, 1.381×10^{-23} m^2 kg s^{-2} K^{-1}
η	kg m^{-1} s^{-1}	Viscosity
R_H	m	Hydrodynamic radius
τ	s	Time lag
α		Parameter to characterise the diffusivity
r	m	Radius of the tracked area
Φ	µms^{-1}	Ice crystal growth rate
$P(r^2, \tau)$		Probability of finding a particle within a circle of a given radius r after a time lag τ
l_c/l_a		Length-to-width ratio in crystals
v	µms^{-1}	Crystal growth velocity normal to the surface
v_{kin}	µms^{-1}	Kinetic velocity of the molecules in the gas phase
α_w		Attachment coefficient
S_i		Supersaturation above the growing ice surface
I	nA	Beam current
U	kV	Beam voltage
κ	W $m^{-1}K^{-1}$	Thermal conductivity of ice, 1.6 W $m^{-1}K^{-1}$
R_b	µm	Beam diameter
σ_{sl}	J m^{-2}	Interfacial tension between solid and liquid
V_s	m^3mol^{-1}	Molar volume of the ice

ΔH_{melt}	J mol^{-1}	Molar enthalpy of melting
r_i	m	Radius of spherical ice with i molecules
r^*	m	Critical radius of an ice germ
σ_{sg}	J m^{-2}	Interfacial tension between solid and gas
M_n	kDa	Molecular weight

Acknowledgments

The successful completion of this PhD thesis would not have been possible without the support, guidance and encouragement of many people. At this point I would like to express my deep gratitude to professor Txema Pitarke for giving me the opportunity to join nanoGUNE. I would also like to thank my supervisor Alex Bittner for having confidence in me and giving me the opportunity to conduct a PhD in his group. I appreciated his advice and his enthusiasm for science. I thank my co-supervisor Silvina Cerdeny for teaching me so much about calorimetry studies and guiding me through my scientific work in the last stages of my thesis. I want to thank Sylvie Morin for valuable discussions during the whole year she spent in our group as a visitor and for her patient way to get me on track when I got lost in ideas.

I am also thankful to the whole group of Self Assembly. It has been a pleasure to work with all of you during these three years. I would like to especially mention my workmates Aitziber and Irma who have helped me every single time I have needed it. Many thanks to all internship students, specially to Sara. There are many things that I have learned from her and some results were also included in this thesis.

Thanks to the Advanced Electron Microscopy Laboratory at CIC nanoGUNE for the great collaboration, specially to Chris Tollan for teaching me how to use the ESEM, for eye opening explanations of complicated concepts and proof reading part of my thesis.

I also want to thank the administration of CIC nanoGUNE for their assistance beyond their duties. I cannot forget to thank the rest of the colleges working at nanoGUNE. Thank you for the great atmosphere we have at nanoGUNE and outside nanoGUNE.

Ulrike Lohmann for giving me the opportunity to come visit her group in Zurich. I was fortunate to have the chance to work with Zamin Kanji and Claudia Marcolli and I want to thank both of them for encouragement and scientific advice. I appreciated their enthusiasm for science which was the best motivation I can imagine.

I am very grateful to Robert David who introduces me in the fascinating field of atmospheric science; without his e orts my job would have undoubtedly been more

di cult. I also want to specially thank my laboratory mates the time I spent at the ETH: Fabian, Misha, Larissa, Monika, Fabiola. I have learnt lot of things from all of you and I really appreciated their friendship beyond the walls of CHN.

I would like to thank the various members of the Atmospheric Physics Group at the ETH in Zurich with whom I had the opportunity to work and have not mentioned. They provided a friendly and cooperative atmosphere at work and also useful feedback and insightful comments on my work.

I am very grateful to professors Javier Gil, Angel Alegria and Ulrike Lohmann for accepting to be in my thesis committee.

I acknowledge the financial support of my Ph.D. work from the 'Diputación Foral de Gipuzkoa' and from nanoGUNE.

Finally, and perhaps most importantly, my family, especially my parents, for promoting my curiosity, for their support in all my decisions and their encouragement in my meandering career path. My friends for just being who they are and by that always animating and encouraging.